Relativistic outflow in the galaxy M87: The first hundred parsecs

INAUGURAL-DISSERTATION

zur Erlangung des Doktorgrades der
Mathematisch-Naturwissenschaftlichen Fakultät der
Universität zu Köln

vorgelegt von
Aleksei Nikonov
aus Jakutsk, Republik Sacha (Jakutien)
Russische Föderation

Köln, 2024

I dedicate this dissertation
to my entire family,
especially to my mom and dad.

Посвящаю диссертацию
всей моей семье,
особенно моим Маме и Папе.

Диссертациябын дьиэ кэргэммэр,
ийэбэр уонна а5абар аныыбын.

Abstract

Relativistic jets from Active Galactic Nuclei (AGN) are highly collimated plasma streams (or "jets") accelerated to nearly the speed of light, extending from the vicinity of supermassive black holes (SMBH) out to megaparsec distances, into the intergalactic medium. These jets play a crucial role in the formation and evolution of galaxies. Additionally, they act as cosmic laboratories or natural particle accelerators, producing high-energy cosmic rays and neutrinos and enabling unique tests of fundamental physical models.

One of the most prominent examples of an AGN jet is the one found in the giant elliptical galaxy M87, located approximately 17 megaparsecs from Earth. Over a century ago, before modern AGN and jet theories were developed, Heber Doust Curtis discovered a "curious straight ray" in M87, now recognised as a powerful relativistic jet. The galaxy M87 harbours a supermassive black hole with a mass of around six billion solar masses—roughly a thousand times more massive than the one in our own galaxy. The proximity of M87 and the large mass of its central SMBH make it an excellent target for AGN studies. In the radio regime in particular, the technique of very long baseline interferometry (VLBI) uniquely enables the most detailed probes of the central regions in M87. Recently, the Event Horizon Telescope produced the first-ever image of a black hole "shadow" in M87, thereby, for this first time, directly imaging the vicinity of a cosmic black hole down to its event horizon scale. The superb linear resolution achieved in VLBI imaging of M87 allows for the detailed study of the collimation, acceleration, and internal structure of its relativistic jet.

This dissertation describes an investigation of the structure of the relativistic jet in M87 in linear scales spanning almost four orders of magnitude, from 0.01 to 100 parsecs. The introductory chapter explains the fundamental physical and astronomical concepts related to AGN. The first key finding, presented in Chapter 2, involves the discovery of a helical structure in the parsec-scale jet of M87, interpreted as Kelvin-Helmholtz instability (KHI) threads developing in a supersonic flow with a Mach number of around 20 and an enthalpy ratio of approximately 0.3. This was determined through the analysis of full-track dual-frequency VLBI observations conducted by the Very Large Baseline Array (VLBA), together with the Very Large Array and Effelsberg telescopes at 8 and 15 GHz, achieving a record dynamic range of about 20 000:1. Based on the two VLBI images obtained at 8 and 15 GHz, a discussion of the spectral and polarisation properties of the jet emission is presented. The 8-15 GHz spectral index map reveals a complex structure, with flattening observed in areas where the helical threads intersect, further supporting the KHI origin of the jet internal structure.

Polarisation emission is detected in the jet up to distances of 20 milliarcseconds from the VLBI core, with Faraday rotation manifesting a transverse gradient across the jet. The Faraday-corrected polarisation map indicates that the electric field position angle (EVPA) changes as a function of distance from the jet axis, suggesting the presence of a helical magnetic field.

HST-1, a knot within the conical kiloparsec-scale jet of M87, was first observed by the Hubble Space Telescope. It is the first feature to be resolved near the jet's "core" on arcsecond scales. HST-1 exhibits superluminal speeds up to 6c and significant flaring activity across multiple wavelengths, from radio to gamma rays. The transition from parabolic to linear expansion of the flow believed to occur on these scales suggests the potentially important role played by HST-1 in the jet's collimation. However, due to its distance from the jet base and smearing effects limiting VLBI's field of view, HST-1 remains a challenging feature to study in detail, with high-resolution VLBI data and spectral information still lacking. In Chapter 3, properties of the jet on hectoparsec scales are discussed, and quad-frequency observations of HST-1 at 2, 5, 8, and 15 GHz using the VLBA and EVN arrays are presented. The VLBI observations presented in Chapter 3 have allowed for accurate reconstruction of spectral index maps and, notably, for obtaining the first turnover frequency map of HST-1. The spectral index maps reveal a uniform structure with a steep spectrum slope of approximately -0.7, suggesting that HST-1 is likely part of an optically thin jet, rather than a standing shock. The turnover frequency maps also enabled the estimation of HST-1's magnetic field strength, found to be of the order of one milligauss.

Chapter 4 of the dissertation deals with specific issues pertaining to imaging sparsely sampled interferometric data. While the `CLEAN` algorithm is the standard method for image reconstruction in radio astronomy, the necessity of supervised reconstruction in the hybrid image involving CLEAN deconvolution can introduce biases, which may produce artefacts in the final image—an issue observed in the spectral index maps from Chapter 2. In order to alleviate these potential biases, in Chapter 4, a novel Bayesian image reconstruction algorithm, `resolve`, is applied to RadioAstron observations at 2 and 5 GHz. This method corrects for amplitude and phase gains for each antenna and polarisation mode by modelling the temporal correlation of the gain solutions. A variational inference method is used to estimate uncertainties in both the gain and the image. The resulting images fully reproduce the filamentary, helical structures observed earlier, providing further support for the KHI interpretation of the jet threads.

Zusammenfassung

Relativistische Jets von Aktiven Galaxienkernen (AGN) sind stark gebündelte Plasmaströme (oder “Jets”), die fast bis zur Lichtgeschwindigkeit beschleunigt werden und sich von der Umgebung supermassiver Schwarzer Löcher (SMBH) bis in Entfernungen von Megaparsecs in das intergalaktische Medium erstrecken. Diese Jets spielen eine entscheidende Rolle bei der Entstehung und Entwicklung von Galaxien. Darüber hinaus fungieren sie als kosmische Labore oder natürliche Teilchenbeschleuniger, die hochenergetische kosmische Strahlen und Neutrinos erzeugen und einzigartige Tests fundamentaler physikalischer Modelle ermöglichen.

Eines der bekanntesten Beispiele für einen AGN-Jet befindet sich in der riesigen elliptischen Galaxie M87, die etwa 17 Megaparsec von der Erde entfernt ist. Vor über einem Jahrhundert, noch bevor moderne AGN- und Jet-Theorien entwickelt wurden, entdeckte Heber Doust Curtis einen „merkwürdigen geraden Strahl“ in M87, der heute als stark relativistischer Jet bekannt ist. Die Galaxie M87 beherbergt ein supermassives Schwarzes Loch mit einer Masse von etwa sechs Milliarden Sonnenmassen – ungefähr tausendmal massereicher als jenes in unserer eigenen Galaxie. Die Nähe von M87 und die große Masse ihres zentralen SMBH machen sie zu einem ausgezeichneten Ziel für AGN-Studien. Insbesondere im Radiobereich ermöglicht die Technik der very-long-baseline Interferometrie (VLBI) einzigartige und detaillierte Untersuchungen der zentralen Regionen von M87. Kürzlich erzeugte das Event Horizon Telescope das erste Bild eines “Schattens” eines Schwarzen Lochs in M87 und ermöglichte damit erstmals die direkte Abbildung der Umgebung eines kosmischen Schwarzen Lochs bis zum Ereignishorizont. Die hervorragende lineare Auflösung, die durch VLBI-Bildgebung von M87 erreicht wurde, ermöglicht eine detaillierte Untersuchung der Bündelung, Beschleunigung und internen Struktur des relativistischen Jets.

Diese Dissertation beschreibt eine Untersuchung der Struktur des relativistischen Jets in M87 auf linearen Skalen, die fast vier Größenordnungen von 0,01 bis 100 Parsec umfassen. Das einleitende Kapitel erklärt die grundlegenden physikalischen und astronomischen Konzepte im Zusammenhang mit AGN. Das erste wichtige Ergebnis, das in Kapitel 2 präsentiert wird, ist die Entdeckung einer helikalen Struktur im Parsec-Skalen-Jet von M87, die als Kelvin-Helmholtz-Instabilität (KHI) interpretiert wird, die sich mit Überschallgeschwindigkeit mit einer Mach-Zahl von etwa 20 und einem Enthalpie-Verhältnis von ungefähr 0,3 entwickelt. Dies wurde durch die Analyse von VLBI-Beobachtungen mit zwei Frequenzen durchgeführt, die vom Very Large Baseline Array (VLBA) zusammen mit dem Very Large Array und dem Effelsberg-Teleskop bei 8 und 15 GHz durchgeführt wurden und ein Rekord-Dynamikverhältnis von etwa 20 000:1 er-

reichten. Auf der Grundlage der beiden bei 8 und 15 GHz erhaltenen VLBI-Bilder wird eine Diskussion der spektralen und Polarisationseigenschaften der Jet Emission präsentiert. Die 8-15-GHz-Spektralindexkarte zeigt eine komplexe Struktur, wobei in Bereichen, in denen sich die helikalen Fäden überschneiden, eine Abflachung beobachtet wird, was die KHI-Ursache der inneren Jet-Struktur weiter unterstützt. Polarisations-Emission wird im Jet bis zu Entfernungen von 20 Millibogensekunden vom VLBI-Kern detektiert, wobei eine transversale Gradienten-Rotation über den Jet erkennbar ist. Die Faraday-korrigierte Polarisationskarte zeigt, dass sich der Winkel des elektrischen Feldes (EVPA) in Abhängigkeit von der Entfernung zur Jet-Achse ändert, was auf das Vorhandensein eines helikalen Magnetfelds hinweist.

HST-1 ist ein Knoten innerhalb des konischen Kiloparsec-Jets von M87 der erstmals mit dem Hubble-Weltraumteleskop beobachtet wurde.. Es ist die erste Struktur, die in der Nähe des "Kerns" des Jets auf Bogensekundenskalen aufgelöst wurde. HST-1 zeigt superluminale Geschwindigkeiten von bis zu 6c und erhebliche Flaring-Aktivitäten über mehrere Wellenlängen hinweg, von Radio- bis zu Gammastrahlen. Der Übergang von einer parabolischen zu einer linearen Ausdehnung des Flusses, der auf diesen Skalen vermutet wird, deutet darauf hin, dass HST-1 eine potenziell wichtige Rolle bei der Kollimation des Jets spielt. Aufgrund der Entfernung von der Jet-Basis und der begrenzten Sichtfeldgrenze von VLBI bleibt HST-1 jedoch eine herausfordernde Struktur für detaillierte Studien, wobei hochauflösende VLBI-Daten und Spektralinformationen weiterhin fehlen. In Kapitel 3 werden die Eigenschaften des Jets auf Hektoparsec-Skalen diskutiert, und Beobachtungen von HST-1 bei 2, 5, 8 und 15 GHz unter Verwendung der VLBA- und EVN-Arrays vorgestellt. Die in Kapitel 3 vorgestellten VLBI-Beobachtungen ermöglichten die genaue Rekonstruktion von Spektralindexkarten und insbesondere die Erstellung der ersten Umschlagsfrequenzkarte von HST-1. Die Spektralindexkarten zeigen eine einheitliche Struktur mit einem steilen Spektrum von etwa $-0,7$, was darauf hindeutet, dass HST-1 wahrscheinlich Teil eines optisch dünnen Jets und kein statischer Schock ist. Die Umschlagsfrequenzkarten ermöglichten auch die Schätzung der Magnetfeldstärke von HST-1, die in der Größenordnung von einem Milligauss liegt.

Kapitel 4 der Dissertation befasst sich mit spezifischen Problemen bei der Bildgebung von mäßig geprobte interferometrischen Daten. Während der `CLEAN`-Algorithmus die Standardmethode zur Bildrekonstruktion in der Radioastronomie darstellt, kann die Notwendigkeit einer überwachten Rekonstruktion in der hybriden Bildgebung mit CLEAN-Dekonvolution zu Verzerrungen führen, die Artefakte im endgültigen Bild erzeugen können – ein Problem, das in den Spektralindexkarten von Kapitel 2 beobachtet wurde. Um diese potenziellen Verzerrungen

zu minimieren, wird in Kapitel 4 ein neuartiger Bayes'scher Bildrekonstruktionsalgorithmus, `resolve`, auf RadioAstron-Beobachtungen bei 2 und 5 GHz angewendet. Diese Methode korrigiert Amplituden- und Phasen Verstärkung für jede Antenne und Polarisationsmodus, indem sie die zeitliche Korrelation der Verstärkungslösngen modelliert. Eine Variationsinferenzmethode wird verwendet, um Unsicherheiten sowohl in den Verstärkungen als auch im Bild zu schätzen. Die resultierenden Bilder reproduzieren vollständig die zuvor beobachteten filamentären, helikalen Strukturen und liefern weitere Unterstützung für die KHI-Interpretation der Jet-Fäden.

Contents

List of Figures

Chapter 1

Introduction

Standing on the ground, humans have always looked up at the sky, fascinated by the distant stars, which they believed could influence and predict the future.

Figure 1.1: Night sky and Milky Way. The Andromeda galaxy can be seen in the upper right corner. The photo was taken on 21 June 2021 using the main camera of a Samsung Galaxy S20+ with 30 seconds exposure, F1.8, ISO3200. The field of view is 80°.

Studying the sky, deep space, and its laws has always been critical for human civilisation. First, the sky helped our ancestors determine time, like when to start the harvest and to navigate the Earth. Now, researching the sky provides tools to further our knowledge in mathematics, physics, space sciences, and engineering.

The study of the movement of stars played an essential role in the economies of the most significant civilisations, the main application of which was the navigation of merchant ships. Until the 1970s, aviation used stars in places without navigation infrastructure.

The invention of the telescope played a key role in the development of astronomy and human thinking. It turned out that not every luminous point in the sky is a star. Observations have shown that the wandering stars, known as "planets", are the same worlds as the Earth. Moreover, observations of Jupiter — the largest planet in the Solar system and its moons, have shown that not all celestial bodies orbit the Earth, which has shaken the traditional doctrine of geocentrism, which states that our planet is the immobile centre of the Universe. Galilei, in his work "Dialogue Concerning the Two Chief World Systems" (Galilei 1632), tried to explain how a person standing on a moving body may not feel its movement, and he thought that the tides were proof of this. With the advent of increasingly sensitive and accurate astronomical instruments, humanity began to find more fascinating and unusual celestial objects. Some of them looked like clouds that we see during the day, while others had unimaginably complex and, at the same time, organised structures. For some time, it was impossible to separate all the objects astronomers saw in the sky. But in the end, it became clear that there are such types of objects called galaxies and we live in one of them. Just as the Earth and other planets revolve around the Sun, stars, dust, and gas orbit around a certain centre, forming a complex disk of luminous matter (Fig. 1.2).

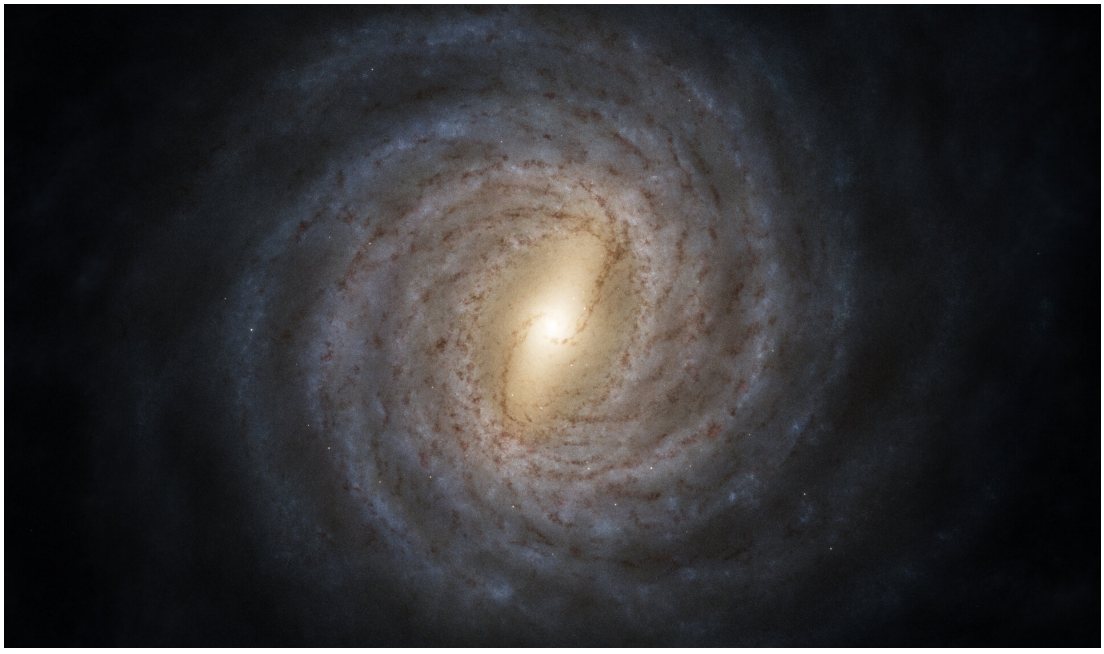

Figure 1.2: Reconstructed top-down view of the Milky Way. The image represents the data obtained by ESA's Gaia mission. Credit: ESA/Gaia/DPAC, Stefan Payne-Wardenaar.

Our galaxy, the Milky Way, is just one of countless galaxies in the universe. Its closest neighbour, the Andromeda galaxy, is visible to the naked eye on a clear, moonless night and appears similar to the Milky Way (Figure 1.1). The Hubble Space Telescope, one of the most successful telescopes of the last century, captured a remarkable image over 11.3 days. It observed a small patch of sky, seemingly empty to weaker telescopes, and discovered that it was filled with thousands of galaxies of various shapes and sizes: some resembling our Milky Way, while others looked quite different (Figure 1.3).

Figure 1.3: Left: Hubble Ultra-Deep Field. This image with a field of view (FoV) of 3 arcminutes in the Fornax constellation contains about 10,000 galaxies. Right: Zoomed in image of the Hubble Ultra-Deep Field shows individual galaxies. Credit: NASA, ESA, and S. Beckwith (STScI) and the HUDF Team.

The central part of a galaxy is called the nucleus and some galactic nuclei are active. The activity of individual stars, gas and dust clouds cannot explain the energy release of these regions. Active galactic nuclei is so bright that their luminosity can be comparable to an entire galaxy and even exceed it.

Despite this, the study of galactic nuclei was limited by the following reasons: many distant active galactic nuclei in the optical range do not visually differ from ordinary stars, and galaxies with visible nuclei may not show activity. With the advent of radio astronomy, everything changed when a new window for receiving radiation from space objects was opened. Previously invisible outflows and clouds of matter extending for kiloparsecs into intergalactic space became visible.

1.1 Radio astronomy

Radio astronomy is a branch of astronomy that studies celestial objects through radio waves. It began with Karl Jansky's pioneering experiments. In the 1930s, Karl Jansky was an engineer at the Bell Telephone Laboratories company and had been developing a trans-Atlantic wireless connection. During this project, he investigated noise and interference interrupting the radio contact. For this, Karl Jansky constructed a directional antenna (Figure 1.4) with a sensitive receiver. In addition to thunderstorms and other atmospheric effects emitting radio waves, he noticed periodic signals with timescales of Earth rotation, which was already a sign of an extraterrestrial origin. Using this antenna, Karl Jansky discovered the first radio source in the middle of the Milky Way (Jansky 1933).

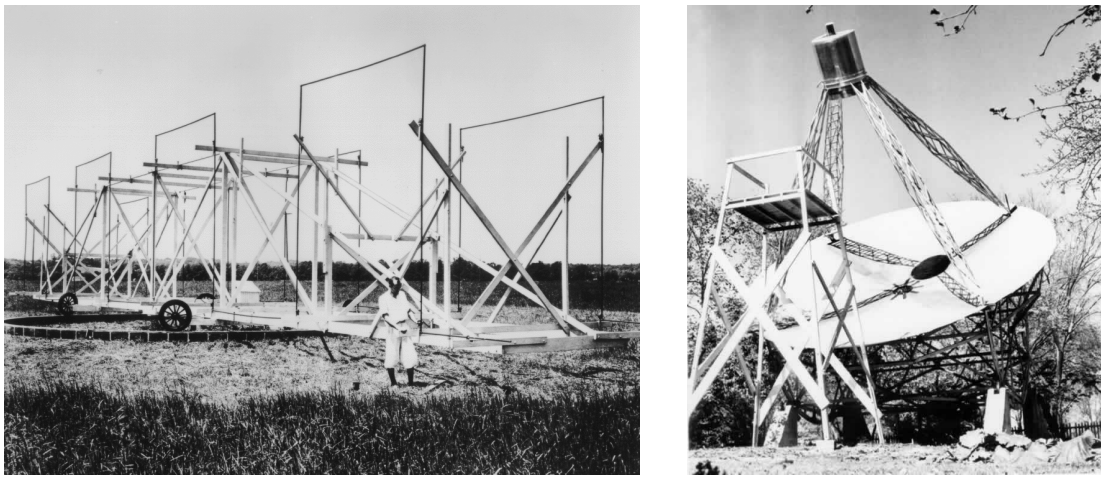

Figure 1.4: Left: Karl Jansky's directional antenna. Right: Grote Reber's 9.5-meter parabolic antenna. Credits: NRAO.

Jansky realized that careful astronomical observations would require antennas with narrower radiation patterns that could be easily oriented across the sky. The size of radiation pattern θ, or point spread function (PSF) of a radio telescope, depends on the size of the antenna, D, and the observing wavelength, λ, as $\theta \propto \lambda D^{-1}$, so he proposed the design of a large parabolic antenna with a mirror of 30.5 meters in diameter to observe at wavelengths of a few meters, but no one supported it. An off-system unit was named after him — Jansky: $1\,\mathrm{Jy} = 10^{23}\,\mathrm{erg\,s^{-1}\,cm^{-2}\,Hz^{-1}}$, which is used in radio astronomy as a unit of measurement of the spectral flux density of radiation.

Grout Reber was a radio and astronomy amateur who worked in radio manufacturing in Chicago. In 1937, he became interested in Karl Jansky's work on radio emission from the sky. He built a 9.5-meter parabolic antenna in the courtyard of his parents' house, the direction of which was fixed along the meridian (Figure 1.4, right panel). The antenna was significantly smaller than the one that Jansky

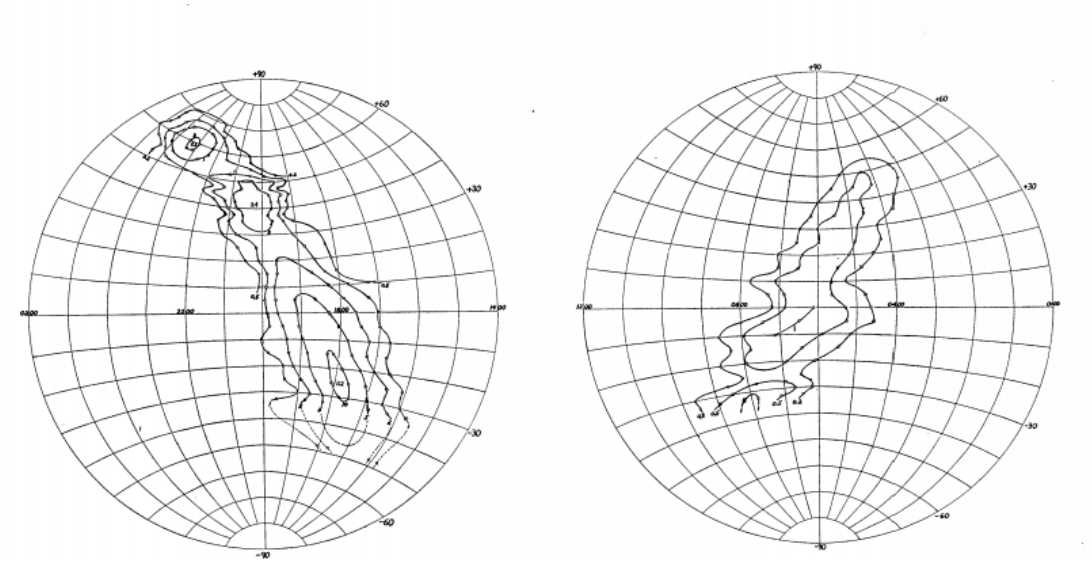

Figure 1.5: The first map of a sky in radio band (Reber 1944). The figure shows two hemispheres of the sky and intensity contours with the step of $10^{-22}\,\mathrm{W\,cm^{-2}\,deg^{-1}\,Hz^{-1}}$

proposed to use. Still, due to using a detector of significantly shorter wavelengths, the resolution was better than the expected one of the telescope of Karl Jansky himself. In 1944, Grout Reber published an article in which the first radio map of the sky (Figure 1.5) was presented (Reber 1944).

A completely new channel for studying celestial objects has opened up for astronomy. Therefore, the first radio astronomers made many discoveries, even with relatively weak instruments. On the maps in Figure 1.5, the central regions of the Milky Way and bright radio sources in the constellation Sagittarius, Cygnus A, Cassiopeia A, Canis Major, and Puppis are shown. Despite this, identification with known optical objects was required to accurately determine the nature of the radiation, which was an impossible task due to the lack of resolution of the instruments. Therefore, unique designations for the radio objects were introduced. It consist of the name of the constellation in which it is located and the letter of the Latin alphabet indicating the object's place in brightness, among others, in the constellation — for example, Sagittarius A, Cygnus A, Cassiopeia A, Virgo A, etc.

The Second World War accelerated the development of radio engineering and radio astronomy. Radar systems began to be used to detect enemy warplanes and other aircraft. Since the radar area was poorly studied, there was a problem with detecting air combat units. Flying from the direction of the setting or rising Sun, the aeroplanes could fly through undetected. It turned out that the Sun is a strong source of radio emission (Reber 1946). Radio astronomy began its rapid development after this conclusion and the advent of antennas and sensitive

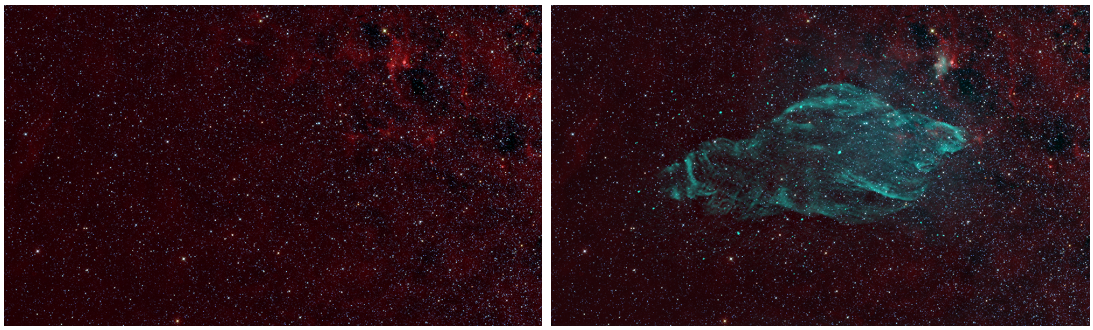

Figure 1.6: The W50 "Manatee" Nebula is shown in visible light (Left) and visible + radio light (Right). Credits: NRAO.

receivers. In the 1950s, the 21 cm radio line of neutral hydrogen was discovered (Ewen & Purcell 1951), thanks to which clouds invisible in the optical range became visible. Quasi-stellar sources of powerful radio emission, called quasars (Matthews & Sandage 1963), were also found. In the 1960s, the cosmic microwave background radiation (Penzias & Wilson 1965) and sources of rapidly varying bursts were discovered (Hewish et al. 1968), which were later called pulsars. All discoveries significantly complemented the astronomical picture of the world and added many objects invisible in the optical range. The W50 "Manatee" is a perfect example of such an "invisible" object (Figure 1.6). For a more detailed historical review, the reader is suggested to proceed with Arnold (2014); Braude et al. (2012); Thompson et al. (2017).

1.1.1 Radio light through the window

Traditionally and historically, only those astrophysical objects that emit visible light have been studied well. Of course, before the invention of special devices for detecting the "invisible" light, humans could rely only on their eyes, which biologically have a limited range of colours or wavelengths that can they register. But is it biological? Will aliens from Trisolaris in Alpha Centauri[1] have the same observable range of wavelengths? Everything is dictated by simple randomness and light transmission of our atmosphere. From Figure 1.8, we can see that the region of light transparency coincides with visible light, and indeed, we can see a lot during night sky gazing. Light in the sky at shorter wavelengths is completely invisible from Earth; exactly for that reason, the only way to observe it is to go to space. It is not surprising that the first discovery of the first cosmic gamma-ray burst (GRB) was made not by astronomers but by an American military reconnaissance satellite Vela 4 in 1967[2] (Klebesadel et al. 1973). The

[1] A planet with aliens from "The Three-Body Problem" novel by Cixin (2008)

[2] This discovery would not be made public for several years due to a military classification. `https://heasarc.gsfc.nasa.gov/docs/history/`

Figure 1.7: SOFIA (Stratospheric Observatory for Infrared Astronomy). Boeing 747-SP with a 2.5-meter infrared telescope inside. Credit: NASA/Jim Ross

satellite was built to track Soviet nuclear tests, during which gamma radiation was expected to be detected. Nowadays, ultraviolet (UV), X-ray and gamma-rays are observed by dozens of spacecrafts such as Spectr-RG, Swift, XMM-Newton, Nu-Star, etc., covering the short wavelength part of the spectrum. On the other hand, visible light in the infrared (IR) part is not opaque, and some light can reach Earth. Although it is still possible to have astronomical IR observations on Earth's surface, astronomers try to reduce the atmosphere on the way to the sky, searching for higher, dryer and better places. One of the most elegant attempts was SOFIA (Stratospheric Observatory for Infrared Astronomy), a huge double-deck airliner Boeing 747-SP with a 2.5-meter telescope inside (Figure 1.7). But the longer the wavelength of the sky is observed, the more transparent the atmosphere becomes. The next transmission window, in addition to one in the visible light, is radio waves. The vast range of wavelengths, from sub-millimetres to dozens of meters, is called the radio window.

In radio astronomy, frequencies are preferred in contrast to wavelength. Thus, the radio window has a lower frequency limit of $\nu \approx 10\,\mathrm{MHz}$ and an upper-frequency limit of $\nu \approx 1.5\,\mathrm{THz}$. The radio window is divided into several bands. The most relevant ones for radio astronomy are L (1–2 GHz), S (2–4 GHz), C (4–8 GHz), X (8–12 GHz), U (12–18 GHz), K (18–27 GHz), Q (40–70 GHz) and W (75–100 GHz) bands. Despite visual clearness from the atmosphere transmission

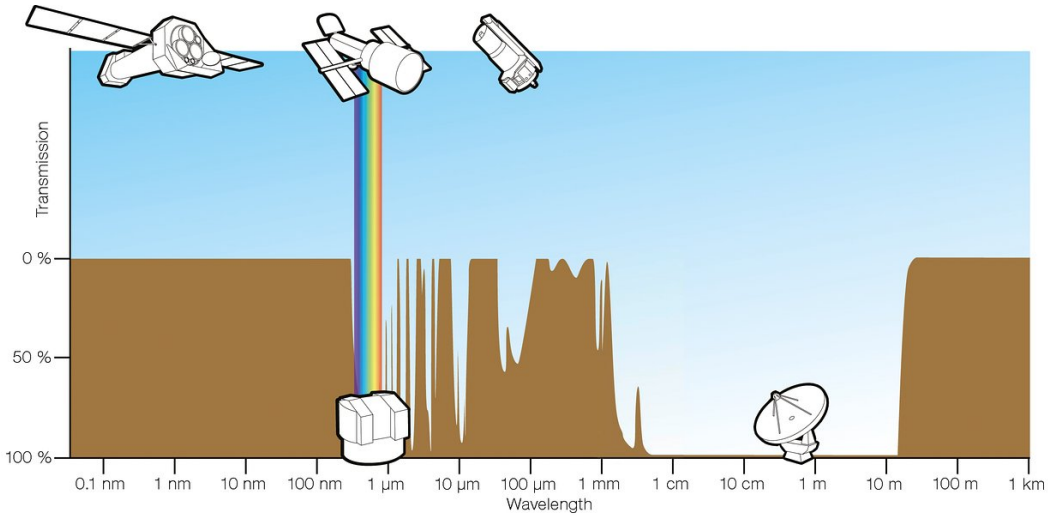

Figure 1.8: Atmospheric opacity is indicated in brown. The major windows are at visible wavelengths (marked by the rainbow) and radio wavelengths from about 1 mm to 10 m. Space telescopes shown on the top are used to mitigate the influence of the atmosphere. From left to right: XMM-Newton for X-rays, Hubble Space Telescope for optical and the Spitzer Space Telescope for infrared. Earth-based telescopes are illustrated at the bottom: Very Large Telescope (VLT) for optical and Atacama Large Millimeter/submillimeter Array (ALMA) for radio correspondingly. Credit: ESA/Hubble (F. Granato)

plot, there are absorption zones where the sky will be not transparent. This is because of the resonant absorption of the lowest rotational bands of molecules in the troposphere, with water vapour and molecular oxygen being the most impactful. Water vapour have absorption lines at $\nu = 22.2\,\mathrm{GHz}$ ($\lambda = 1.35\,\mathrm{cm}$) and 183 GHz (1.63 mm). In the case of O_2, there is a group of lines closely spaced near 60 GHz (5 mm), and a single line near 119 GHz (2.52 mm). The absorption by the other molecules like N_2 and CO_2 happens at frequencies above 300 GHz. The lower frequency limit is based on the free electrons in the Earth's ionosphere. In this case, transmission is limited to the plasma frequency, below which the light is blocked. The plasma frequency can be calculated from electron density: $\nu = 8.97\sqrt{N_e}\,\mathrm{kHz}$, where electron density N_e measured in cm^{-3}. Given electron density during night $N_e \approx 2.5 \times 10^5\,\mathrm{cm}^{-3}$, the plasma frequency $\nu_\mathrm{p} \approx 5\,\mathrm{MHz}$. During the day, the electron density rises, and in principle, it depends on space weather.

With the development of human civilization, the radio window has become more and more opaque because of radio frequency interference (RFI). Radio signals obtained from space are extremely weak. Energy collected by all observatories during the whole existence of radio astronomy is much less than the energy needed to raise a stack of paper from the floor on the table. That's why modern devices

such as cell phones, wireless networks, and Bluetooth completely dominate the signal. Even when these sources of interference can be avoided by putting a telescope in the middle of nowhere, nothing will help against satellites. From the first-ever space RFI Sputnik to Ilon Mask's Starlink, avoiding the noise produced by our electronic devices became an important task to overcome for the radio astronomy community. Despite the threatening spread of RFI, there are agencies and communities (the International Telecommunication Union (ITU), the European Science Foundation's Committee on Radio Astronomy Frequencies (CRAF), and the U.S. The National Academy of Sciences' Committee on Radio Frequencies (CORF)) which involve a list of countries that regulate the use of the radio spectrum and protect radio astronomy.

Radiative transfer

There are three fundamental interactions of light with matter: emission, absorption and scattering. To describe the first, the emissivity coefficient is introduced j_ν, which is energy emitted per unit volume, unit time and a unit frequency range in a particular direction. In the radiating matter without absorption, photons cover path $\mathrm{d}s = c\mathrm{d}t$ and the increase in intensity will be defined by the increase of the path multiplied by the emissivity coefficient $\mathrm{d}I_\nu = j_\nu \mathrm{d}s$. In non-emitting matter, part of the photons are absorbed by it. This can be defined through the absorption coefficient α_ν. If the medium can emit and absorb, then the radiative transfer equation is a sum of emissivity and absorption:

$$\frac{\mathrm{d}I_\nu}{\mathrm{d}s} = -\alpha_\nu I_\nu + j_\nu. \tag{1.1.1}$$

Since path ds is a complicated observable value, the optical depth can be introduced, a dimensionless quantity that characterises the attenuation of emission in a medium due to its absorption and scattering $\tau_\nu = \alpha_\nu \mathrm{d}s$. In the case of $\tau_\nu \gg 1$, a medium is optically thick or opaque for light. In the other case of $\mathrm{d}\tau_\nu \ll 1$, a medium is optically thin or transparent for light. Using the optical depth coefficient and source function, $S_\nu \equiv j_\nu/\alpha_\nu$, the formal solution of Equation 1.1.1 is

$$I_\nu(\tau_\nu) = I_\nu(0)e^{-\tau_\nu} + \int_0^{\tau_\nu} e^{-(\tau_\nu - \tau'_\nu)} S_\nu(\tau'_\nu)\mathrm{d}\tau'_\nu. \tag{1.1.2}$$

When the radiation passes a single optical distance, the intensity decreases by a factor of e (if the medium does not emit).

Black body radiation

The thermal movement of particles of an emitting body generates thermal radiation. It satisfies the main Kirchhoff's law, which states that the ratio of emissivity and absorptivity coefficients is the function of temperature and does not depend on the physical and geometrical structure of the body, i.e. $j_\nu/\alpha_\nu = S_\nu(T)$. The most important case of thermal radiation is the black body radiation.

In visible light, the majority of emission come from stars. Despite stars being very complex bodies with many different mechanisms play a role in the evolution of these objects, they can be described by a relatively simple model of a black body. The body's surface is black in the sense that it does not reflect any radiation but absorbs it. The only emission seen from the black body is its own, created by a random interaction of particles it consists of. The speed or energy of a random particle is lost by the interaction through emitting electromagnetic radiation. In case of a high number of particles, the average or square root mean speed is considered, and it represents the energy of the body and can be directly traced by temperature. The emission spectrum is obtained by integrating the Maxwell distribution of the particles. This is called the Plank distribution:

$$B_\nu \equiv I_\nu = \frac{2h\nu}{c^2}\frac{1}{e^{h\nu/kT}-1}, \tag{1.1.3}$$

where I_ν is the specific intensity defined as power emitted at a specific frequency, per unit area, unit frequency interval, and solid angle. The Plank distribution is presented here Figure 1.9. The spectrum does not depend on chemical content or the physical processes occurring inside the emitting body. Thus, in the case of optically thick source, the function tends to the Planks law $S_\nu|_{\tau\to\infty} = B_\nu$.

The Plank distribution can also be represented in terms of wavelength:

$$I_\lambda = \frac{2hc^2}{\lambda^5}\frac{1}{e^{hc/\lambda kT-1}}. \tag{1.1.4}$$

Taking a derivative and defining it to zero, the Wien's displacement law is obtained:

$$\lambda_{\text{peak}} = \frac{b}{T}, \tag{1.1.5}$$

where $b = 2.897771955\times10^{-3}\,\text{m K}$ is constant. Since the wavelength of a maximum is inversely proportional to the temperature, colour is a direct trace to the most important physical quantity. Even with a human eye, estimating the temperature of distant objects like stars is possible. Betelgeuse, the brightest star of the most recognised constellations, has a red colour, in contrast to Sirius, the brightest star in the sky, which has a white colour. Considering only these observational results,

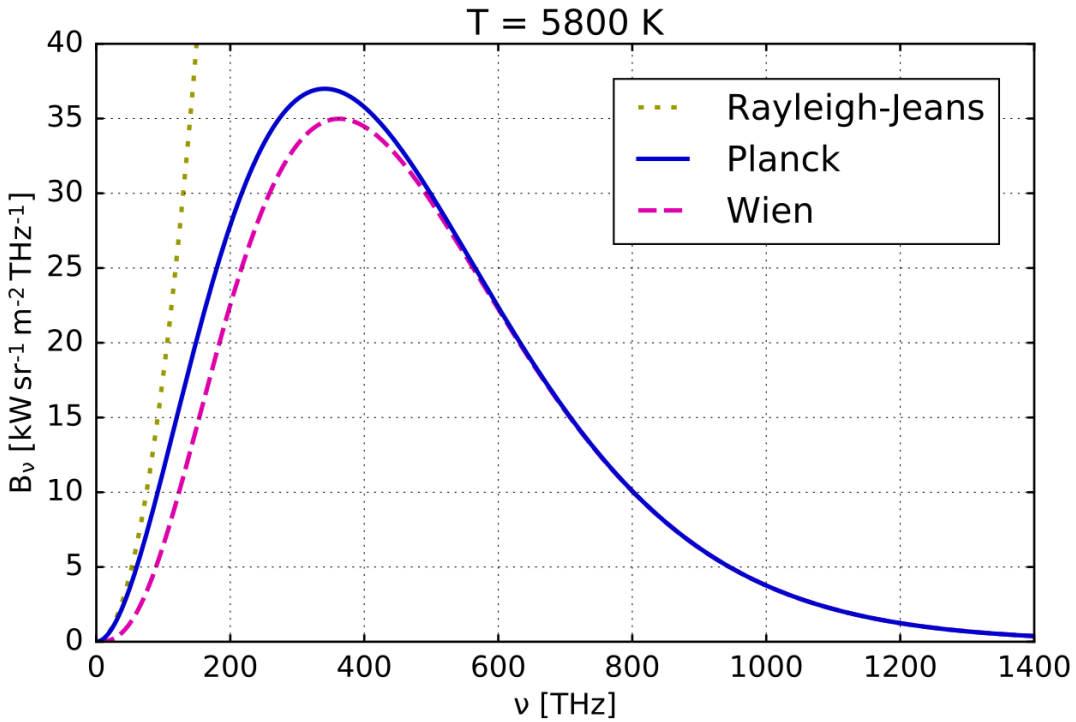

Figure 1.9: Spectrum of a black body with temperature $T = 5300\,\mathrm{K}$. The blue line shows the Plank distribution, the olive dotted line presents the Rayleigh-Jeans law, and the violet dashed line is reserved for the Wien approximation. Credits: Wikimedia, Geek3.

it is possible to deduce that Sirius' surface is hotter than Betelgeuse's.

As seen from Figure 1.9, it is a smooth function with a peak associated with a specific temperature. The higher the temperature, the higher the frequency and intensity of the peak. The total power per surface unit area deduced by integrating the spectrum is the Stefan–Boltzmann law:

$$P = \sigma T^4, \tag{1.1.6}$$

where $\sigma = 5.67 \times 10^{-6}\,\mathrm{W\,m^{-2}\,K^{-4}}$ is Stefan–Boltzmann constant. This is very convenient since the dimensions of the source can be calculated based on known temperature, brightness, and distance to a source.

Returning to radio astronomy and frequencies observed in this regime, it can also be useful to have a simpler version of Plank law in the case of $h\nu \ll kT$:

$$I_\nu = \frac{2kT\nu^2}{c^2} = \frac{2kT}{\lambda^2}. \tag{1.1.7}$$

This is the Rayleigh-Jeans (RJ) approximation. Of course, the approximation fails in high-frequency regimes with millimetre wavelengths and low temperatures. This is called the ultraviolet (UV) catastrophe. Still, for the majority of cases of

radio astronomy, it is a good instrument for estimations. The case of $h\nu \gg kT$ is the Wien approximation. Both of them are illustrated in Figure 1.9.

The other case of thermal radiation is the emission of optically thin ($\tau \ll 1$) plasma in a thermodynamic equilibrium. In contrast to the black body radiation, in this case, the emission of a body depends on its contents, ionisation and probabilities of particular processes of generations of photons. The common property of any emitting mechanism is an exponential decay at high frequencies $I \propto \exp\{-h\nu/kT\}$. However, a coefficient before the exponent is different. For example, in the case of optically thin hot plasma, the main emission mechanisms are bremsstrahlung and photo-recombination. The spectrum of the plasma will be the sum of the continuous spectrum from bremsstrahlung and lines from photo-recombination.

Synchrotron radiation

When a charged particle moves in a magnetic field, another radiation mechanism plays a crucial role in radio astronomy. This is magnetobremsstrahlung or synchrotron radiation. Typically it is a non-thermal mechanism, thus such a parameter as temperature does not make sense. Despite this, it is used to describe the brightness of an object, which is used because radio telescopes are typically calibrated in temperature units. When they detect signals, the measurements can be directly converted into brightness temperatures. The brightness temperature is obtained from Equation 1.1.7:

$$T_b = \frac{c^2}{2k\nu^2} I_\nu. \tag{1.1.8}$$

In the case of non-thermal radiation, there is no connection between the observed brightness temperature and internal energy, thus very high values up to $10^{12}\,\mathrm{K}$ can be obtained.

Electrons produce most of the observed synchrotron emission and will be considered charged particles later. Due to the Lorentz force, the particle accelerates perpendicular to the direction of motion, leading to the helical path. Accelerated charged particles generate radiation, the pattern of which is a dipole in the rest frame. Since observed particles are usually relativistic, Lorentz transformations lead to a strong beaming (Figure 1.10). Thus, a particle emits electromagnetic waves predominantly in the direction of its movement inside a cone with an opening angle of $\psi \sim \gamma^{-1}$.

Moving through the magnetic field, a particle gyrates, and an observer receives a short pulse each time the cone crosses their line of sight. The particle gyrates

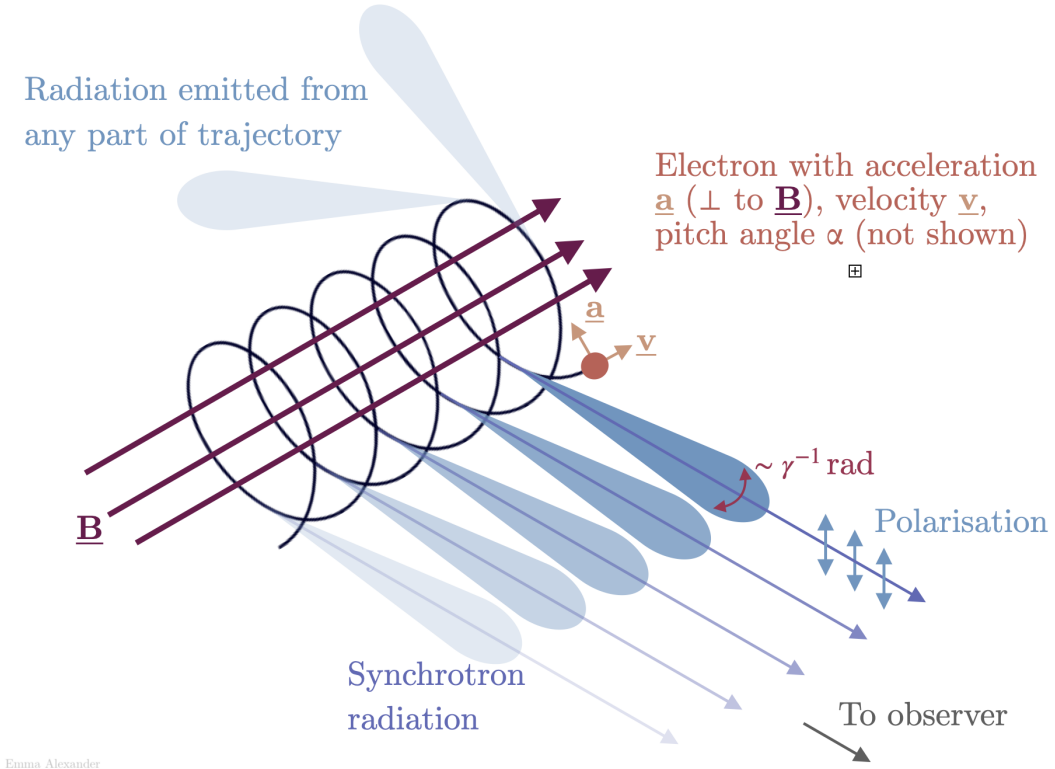

Figure 1.10: Diagram of synchrotron emission from a relativistic electron moving along a helical path around an ordered magnetic field. Credit: Emma Alexander

with the gyrofrequency:

$$\nu_g = \frac{|q|B}{2\pi mc}\gamma^{-1}, \tag{1.1.9}$$

where q is the charge of a particle, B is the magnetic field strength, $\gamma = 1/\sqrt{1-(v/c)^2}$ is the Lorentz factor. But because of the very narrow cone, the pulse duration will be much smaller than the period ν_g^{-1}. Thus, in a uniform magnetic field, the radiation would consist of periodic pulses, the Fourier series of which will describe the spectrum. The spectrum will look like the harmonics of the fundamental gyrofrequency. In reality, frequency shifts are caused by fluctuation in the path, relativistic effects, and magnetic field structure, which smear the spectrum, making it effectively continuous. The full analytical calculations give the power spectrum of the synchrotron radiation from a single particle (Ginzburg & Syrovatskii 1965):

$$P(\nu)\mathrm{d}\nu = \sqrt{3}\frac{|q|^3 B\sin\alpha}{mc^2}F(x)\mathrm{d}\nu, \tag{1.1.10}$$

where F(x) contains an integral of a modified Bessel function of order 5/3:

$$F(x) \equiv x\int_x^\infty K_{5/3}(\xi)\mathrm{d}\xi. \tag{1.1.11}$$

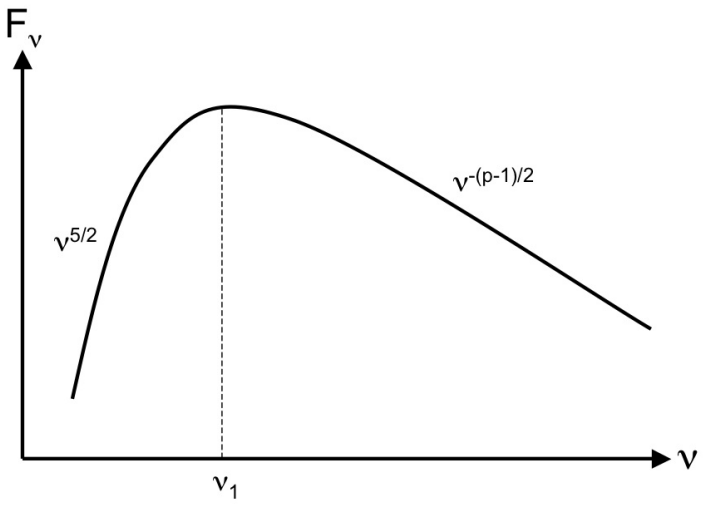

Figure 1.11: Synchrotron spectrum. The turnover frequency, ν_1, separates the optically thin and thick regimes with spectral indexes $\alpha_{\text{thin}} = -(p-1)/2$ and $\alpha_{\text{thick}} = 5/2$ correspondingly. The parameter p is a power of energy distribution of electrons (Equation 1.1.14). Credit: Jonathan Williams, University of Hawaii

Synchrotron emission is polarized, so it is convenient to describe components parallel and perpendicular to the magnetic field. For this, the we introduce:

$$G(x) \equiv x \int_x^\infty K_{2/3}(\xi)\mathrm{d}\xi. \tag{1.1.12}$$

Thus, the power spectra of the two polarised components are:

$$P_\perp \propto F(x) + G(x), P_\parallel \propto F(x) - G(x). \tag{1.1.13}$$

The difference between $P_\perp$ and $P_\parallel$ yields linear polarisation in the plane of motion of the electron. In most cases, observed synchrotron radiation is highly polarised, and the degree of polarisation can reach 70–80%.

Real astrophysical sources consist of an ensemble of charged particles. For example, a relativistic gas consisting of electrons with an energy distribution of $N(E)$. The energy distribution of many synchrotron sources is a power law (Condon & Ransom 2016):

$$\mathrm{d}N(E) \propto E^{-p}\mathrm{d}E. \tag{1.1.14}$$

The spectrum for a single particle from Equation 1.1.10 can be convolved with the energy distribution in Equation 1.1.14, resulting in a spectrum from an ensemble of charged particles (Figure 1.11):

$$I_\nu \propto B^{\frac{(p+1)}{2}} \nu^{-\frac{(p-1)}{2}}. \tag{1.1.15}$$

The resulting equation shows also a power-law $I_\nu \propto \nu^\alpha$, in which spectral index:

$$\alpha = -\frac{(p-1)}{2}. \tag{1.1.16}$$

The spectral index lies between -2 and 0 for the optically thin radiation.

When the free path length of a synchrotron photon becomes less than the size of the emitting region, the light will be absorbed by electrons from the same matter. This process is called self-absorption and leads to the formation of optically thick regions. In the spectra (Figure 1.11), it forms an inverted to optically thin regime slope of $\alpha = 5/2$. The transition area in the spectrum, where optically thin radiation is transformed into optically thick, is called turnover frequency (Figure 1.11). This very important quantity traces the density and magnetic field in a matter.

Inverse Compton scattering

Compton scattering is a process of energy transfer from a high-energy photon to a low-energy electron. The opposite situation, in which a relativistic electron transfers energy to a low-energy photon, is called inverse compton scattering. It can boost radio photons into the ultraviolet, X-ray and gamma-ray bands. An example of this is the Sunyaev–Zel'dovich effect, in which the high-energy electrons of a galactic cluster boost the energy spectrum of the cosmic microwave background (CMB). This is called the external Compton scattering (EC). The same process can be seen in the gamma-ray bursts (GRB) or relativistic jets of active galactic nuclei (AGN). As a result, radio photons, for example, are boosted to X-ray bands by synchrotron self-Compton or SSC. The spectrum of SSC is similar to the power-law synchrotron spectrum and has a spectral index of $\alpha = -(p-1)/2$. Together, synchrotron and SSC show a double peak spectrum like in Figure 1.12.

1.1.2 Polarised light

Electromagnetic waves are represented by electric $\vec{E}$ and magnetic field $\vec{B}$ vectors, which are perpendicular to each other and oscillate in the xy plane, perpendicular to the wave propagation direction z (Figure 1.13). The light is called polarised if these vectors' directions change according to a particular law. There are different states of polarisation, and each of them depends on how orthogonal components (E_x, E_y) of the electric vector $\vec{E}$ are evolving in time. Syn-phase sinusoidal evolution of the components leads to linear polarisation, showing a constant direction of the oscillation of the electric field. Usually, for the direction

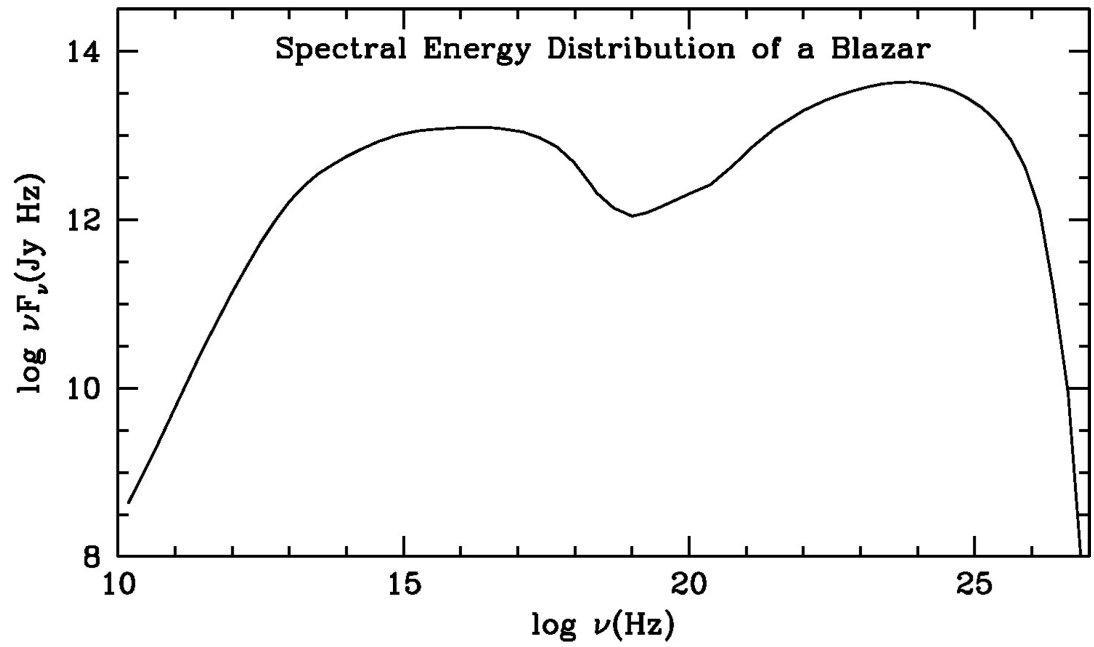

Figure 1.12: Sketch of the spectral energy distribution of a blazar. There are two peaks, one at low (infrared) and another at high (γ-ray) photon energies. Credits: Marscher & Jorstad (2022).

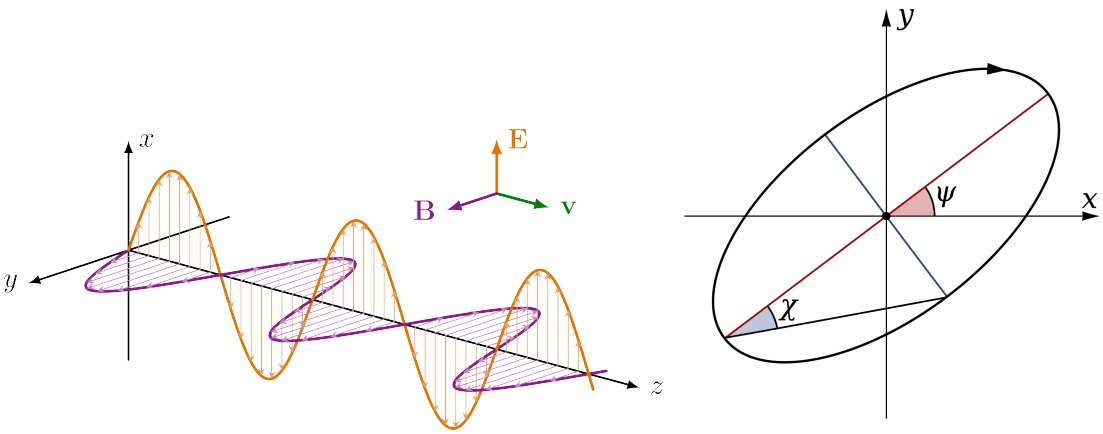

Figure 1.13: Left: A linearly polarised electromagnetic wave travelling in the z-axis, with E denoting the electric field and B, which is perpendicular to E, denoting the magnetic field. Credit: Izaak Neutelings. Right: Polarisation ellipse described by the orientation and ellipticity angles ψ and χ. Credit: Wikimedia.

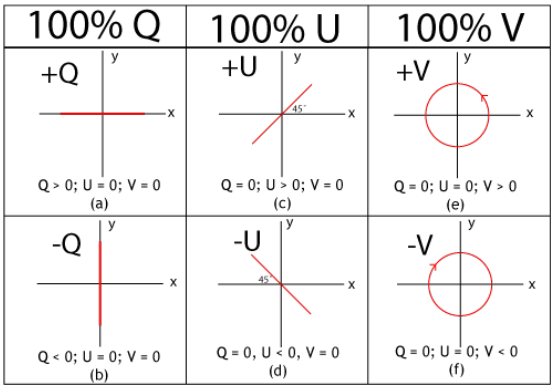

Figure 1.14: Stokes parameters in some degenerate cases. Credit: Dan Moulton.

of polarisation, the Electric Vector Position Angle (EVPA) is used and measured in the xy plane between North and the electric vector $\vec{E}$ in the direction of East. A phase shift added to the orthogonal components makes the vector oscillate in an elliptical shape. This introduces an elliptical polarisation. Depending on the direction of rotation, the polarisation state is defined as left- or right-handed. One important case appears when the phase shift equals to $\Delta\phi = 90°$. In this case, the ellipse degenerates into a circle, introducing a circular polarisation.

The circular and the linear polarization are the important cases of the elliptical polarisation. Therefore, polarised emission is defined in terms of the polarisation ellipse. In Figure 1.13, the ellipse is described by the orientation and ellipticity angles ψ and $\chi = \arctan b/a$, where a and b are the major and minor axis of the ellipse. The first parameter sets the ratio between the major and minor axis, and the other shows how the ellipse is rotated relative to the North. The polarisation ellipse is a convenient presentation of the polarised emission, but it is inconvenient to use it. Thus, the Stokes parameters were introduced to simplify the notation. George Stokes defined I, Q, U and V by the angles of polarisation ellipse and the degree of polarisation p:

$$\vec{S} = \begin{pmatrix} I \\ Q \\ U \\ V \end{pmatrix} = \begin{pmatrix} I \\ pI\cos 2\psi \cos 2\chi \\ pI \sin 2\psi \cos 2\chi \\ pI \sin 2\chi \end{pmatrix}. \tag{1.1.17}$$

Using the Stokes parameters, the fractional linear m_l, circular m_c, and total polarisation m_t are defined:

$$m_l = \frac{\sqrt{Q^2+U^2}}{I},\ m_c = \frac{V}{I},\ m_t = \frac{\sqrt{Q^2+U^2+V^2}}{I}. \tag{1.1.18}$$

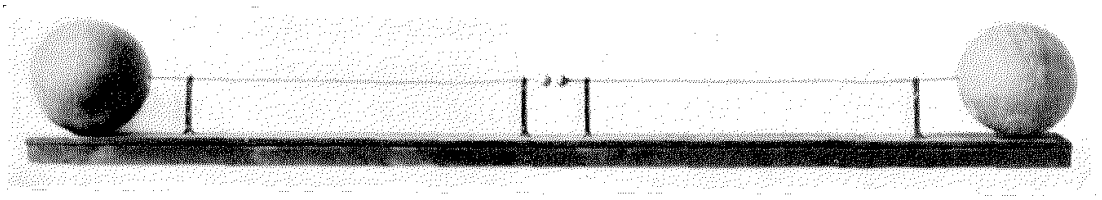

Figure 1.15: Hertz's first radio transmitter. Credit: Appleyard (1927).

The EVPA is defined as:

$$\theta = \frac{1}{2}\tan^{-1}\left(\frac{U}{Q}\right),\ 0 \leq \theta \leq \pi. \tag{1.1.19}$$

Figure 1.14 shows how Stokes parameters are connected to the particular polarisation states.

1.1.3 Radio telescope

A wide range of telescopes use charge-coupled device (CCD) or complementary metal-oxide semiconductor (CMOS) sensors. The fundamental principle of these devices is the photoelectric effect. An electromagnetic wave interacting with matter can transfer energy to an electron inside it. If the energy of a photon is higher than a particular energy called workfunction, the electron is freed and can be counted. The typical workfunction values for metals and semiconductors are around 3–5 eV, which is perfect for visible light. In the case of radio light, this energy is too high; therefore, the photoelectric effect is not working.

Heinrich Hertz, in 1887, using the dipole antenna, proved the existence of radio waves (Hertz 1887). The dipole antenna, which is presented in the Figure 1.15 represents just two conducting wires. The oscillating electric field of the radio wave makes electrons in the antenna move correspondingly, inducing an electric current. Moreover, radio emission can be generated if the oscillating electric current is present in the same antenna. Therefore, an antenna can be analysed as a transmitter or as a receiver. One of the most important characteristics of any antenna is the radiation pattern or beam pattern. It describes response or radiation level in different directions. The dipole antenna may be listed under the category of omnidirectional antennae since the beam pattern (Figure 1.16) is not very constrained. This discovery led to different types of antennas, which have the same principle. The geometry of the dipole antenna hints its sensitivity to a linearly polarised light. Indeed, two perpendicular dipoles are needed to register the whole emission. The other type of antenna is helical, and it is sensitive to a circular polarisation. This antenna is well-spread in space communications since the radiation pattern of the antenna shows a much narrower beam (Figure 1.16),

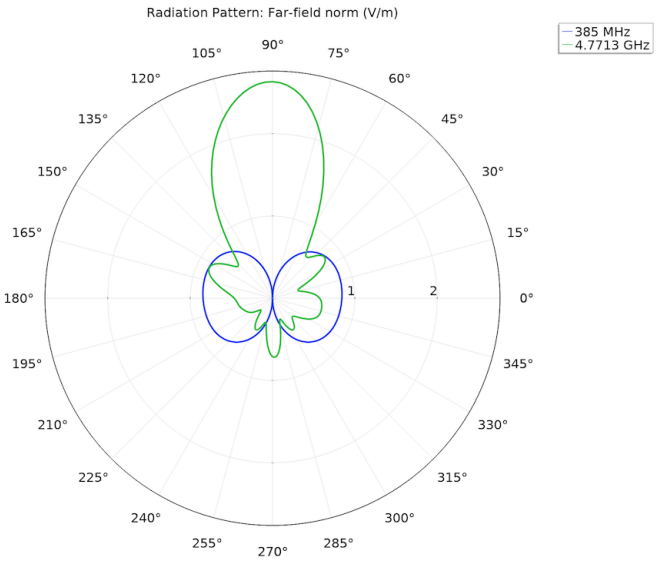

Figure 1.16: Polar plot of the beam pattern of a dipole in blue and a helical antenna in green. Credit: COMSOL/Thomas Forrister.

leading to more efficient energy transmission in contrast to a simple dipole antenna. The radiation pattern of the helical antenna shows the main component or lobe containing the majority of power. The rest components seen in the pattern are side lobes and back lobes. In the case of the directional antenna side and back lobes are undesired features and minimised. Thus, with this type of antenna an emission can be localised in the sky. The angular resolution of the antenna is defined by the angular size of the main lobe θ.

Celestial objects in the radio sky have small angular sizes and are very faint. The mentioned types of antennae cannot observe the sky and study faint objects in detail. Here, it is important to introduce one of the most important parameters of an antenna: the effective area A_{eff}. The bigger the area, the higher the sensitivity of observations. One of the ways to increase this parameter is to add a reflector or use a horn which will collect electromagnetic waves and transfer them to the receiver. These antennae are called aperture-type. In the case of the Hertzian dipole the effective area depends on the wavelength $A_{\text{eff}} = (3/8\pi)\lambda^2$ but in the other case it is proportional to area $A_{\text{eff}} \propto R^2$, where R is the size or the radius of the antenna. The term effective also indicates that the physical area of the telescope does not correspond to the real collecting area A_{eff} due to imperfection of a surface and other causes. The horn antenna is used for radio astronomical observations. For example, this type of antenna shown in Figure 1.17 helped Penzias & Wilson (1965) to discover the Cosmic Microwave Background. However, the antenna most common in radio astronomy is parabolic.

Diffraction effects, occurring on any aperture, cause the beam pattern to depend on the size of the telescope and the main lobe size $\theta \propto \lambda/D$, where λ is

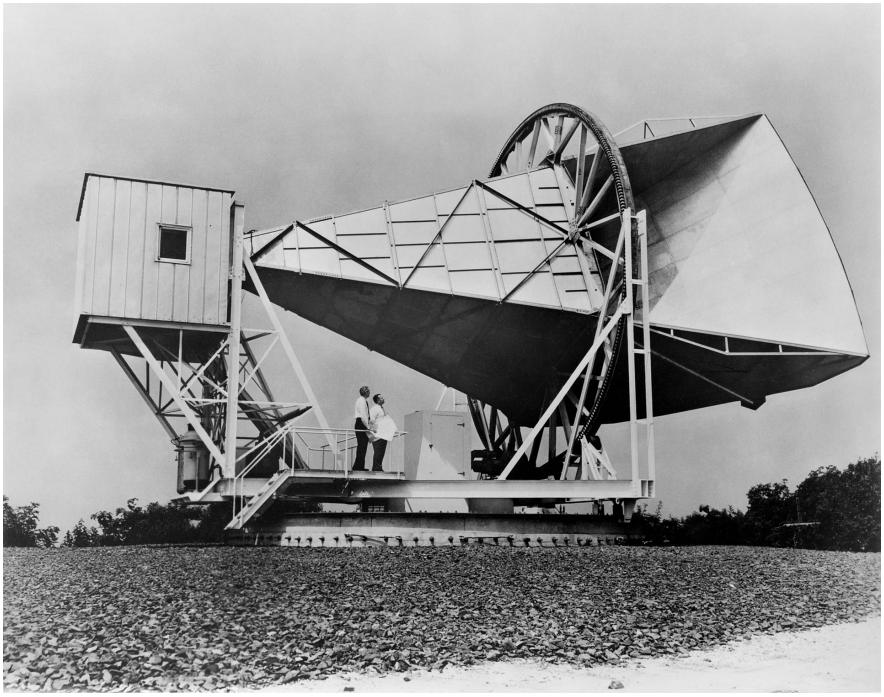

Figure 1.17: The 15-meter Holmdel horn antenna at Bell Telephone Laboratories in Holmdel, New Jersey, was built in 1959.

the wavelength and D is the aperture diameter. The beam shape depends on the particular aperture, but in the case of a filled circle, the pattern is represented by the Bessel function Figure 1.18, also known as the Airy pattern. The first null of the Bessel function defines the resolution:

$$\theta \approx 1.22\frac{\lambda}{D}. \tag{1.1.20}$$

However, in the universal case, the FWHM (full width half maximum) of the beam is used to define the resolution of an instrument. The effect of a finite resolution smoothens the real sky brightness distribution. A point source observed by a radio telescope is represented by a beam function $P(\alpha, \delta)$ as an output. In other words, the observed sky brightness distribution is a convolution of the real one with the beam. In the cases of a complex beam structure, this can be a problem, since the low surface brightness region can be contaminated by the sidelobe pickup of more intense radiation and deconvolution is needed.

The electrical current generated in the antenna by electromagnetic radiation from a blackbody source is noise, indistinguishable from the noise from a resistor of the same temperature. Warm resistors are used in radio astronomy to calibrate receivers, so the noise power per unit bandwidth is often described in terms of the Rayleigh-Jeans antenna temperature. The total spectral power generated by a

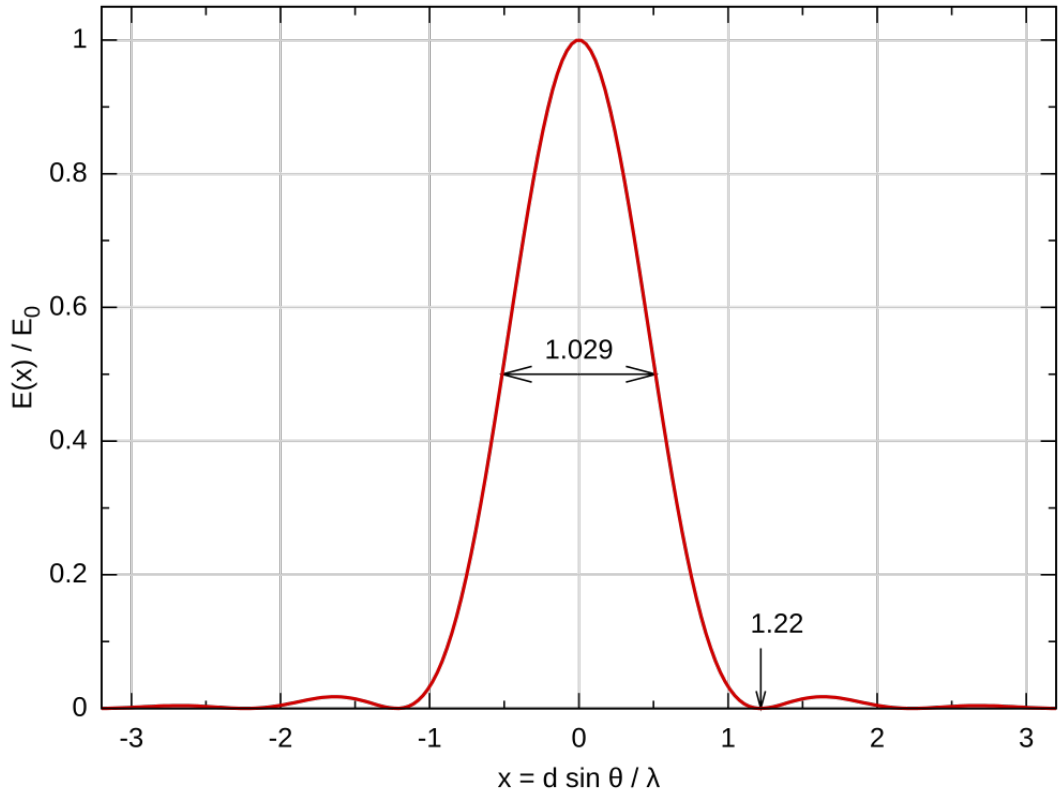

Figure 1.18: Point spread function of a telescope or the Airy pattern. Credit: Edgar Bonet.

resistor in the limit $h\nu \ll kT$ is called the Nyquist approximation:

$$P_\nu = kT. \tag{1.1.21}$$

Thus, the antenna temperature can be defined as $T_\mathrm{A} \equiv P_\nu/k$. This quantity is a convenient and practical unit for the radio astronomical observations for the following reasons:

- Antenna temperature is a convenient way to describe faint radio signals from cosmic objects. $T_\mathrm{A} = 1\,\mathrm{K}$ corresponds to $P_\nu = k = 1.38 \times 10^{-23}\,\mathrm{J\,K^{-1}}$.
- The units of receiver noise are also in K, so it is convenient to calibrate a signal and compare it with the noise power.
- Brightness temperature is equivalent to the antenna temperature. In the case of a smooth source much larger than the antenna beam, the temperatures are equal $T_\mathrm{A} = T_\mathrm{b}$. Thus, the antenna temperature can be used for a physical interpretation of an observation.

In the perfect world, the quantity measured by a radio telescope is the antenna

temperature $T_{\rm A}$, related to the flux density S_ν as

$$T_{\rm A} = \frac{A_{\rm eff}}{2k} \int I_\nu P_n {\rm d}\Omega = \frac{A_{\rm eff}}{2k_{\rm B}} S_\nu, \tag{1.1.22}$$

where I_ν and $P_n = P(\alpha, \delta)/P_{\rm max}(\alpha, \delta)$ are the intensity distribution on the sky and normalised beam pattern of the telescope, and $k_{\rm B}$ is the Boltzmann constant. The effective area term can also be represented as $A_{\rm eff} = \eta A_{\rm D}$, where the true aperture area is $A_{\rm D}$ and η is efficiency. In reality, there are a lot of noise sources and the telescope output is affected and dominated by the system temperature $T_{\rm sys} = T_{\rm ground} + T_{\rm CMB} + T_{\rm atm} + ...$, which include contributions from ground, antenna, atmosphere, CMB etc.

To detect a signal from a faint cosmic source, the total-power radiometer can be used. The simplest radiometer consists of:

- a bandpass filter that passes input noise in the desired frequency range
- a square-law detector whose output voltage is proportional to the square of the input converting it to the power
- a signal averager or integrator that smoothes fluctuating output
- a voltmeter or other device to measure and record the output voltage.

Since the radio signal is squared, the dispersion of the noise is $2T_{\rm sys}^2$, so $\sigma_{\rm T} = \sqrt{2} T_{\rm sys}$. Averaging with $N \gg 1$ independent samples gives a rms noise reduced by a factor $\sqrt{N}$: $\sigma = \sqrt{2} T_{\rm sys}/\sqrt{N}$ or in terms of bandwidth $\Delta\nu$ and integration time τ:

$$\sigma \approx \frac{T_{\rm sys}}{\sqrt{\tau \Delta\nu}}. \tag{1.1.23}$$

This is called the ideal radiometer equation for a total-power receiver. The product $\tau\Delta\nu$ can be as large as 10^8, for example. Thus, the weakest detectable signal can be as faint as $T \sim 10^{-4} T_{\rm sys}$. However, in real observations, the sensitivity can not be improved infinitely by improving the $\tau\Delta\nu$ term. In practice, receiver gain changes, erratic fluctuations in the atmosphere and the "confusion" by the unresolved background of continuum radio sources limit the sensitivity of single-dish continuum observations.

Signal chain in a radio telescope

The total power of the incoming signal received by an antenna is proportional to the antenna's effective area and the source's brightness $P_\nu = A_{\rm eff} I_\nu$. In the case of the parabolic antenna, the collected power from the reflector goes to the feed. A waveguide can be used directly as a feed. However, because there is a significant mismatch between the impedance of the waveguide and that of free

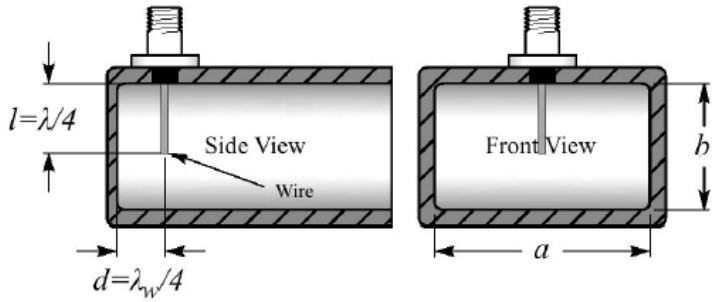

Figure 1.19: Scheme of a waveguide with a dipole antenna inside. Credit: Physicsopenlab.org.

space, much of the input radiation is reflected or scattered. Thus, the horn is needed to increase the efficiency of the receiver. The size of the horn is configured corresponding to the size of the reflector so the beam of the horn will be smaller than the angular size of the reflector to avoid signal picking from the ground. The electromagnetic wave enters the horn and goes through the waveguide where it excites current in the dipole or a monopole antenna and the coaxial coupler (Figure 1.19). Since one antenna obtains only a half polarisation, the second one oriented perpendicularly is present. In the case if circular polarisation needs to be obtained, the quarter-wavelength plate is placed. In this way, Left Circular Polarisation (LCP) and Right Circular Polarisation (RCP) are measured. The later signal chain is doubled. After the polariser, but before the monopole, the noise source with a flat spectrum is embedded. This is made to calibrate the amplitude of the incoming signal to the known value. In this case, the amplitude of the noise will not be changed relative to the signal since it goes through the same path in the instrument. A resistive load can generate the noise and the power can be calculated as $P_\nu = kT$. The obtained noise has a flat spectrum at a vast range of frequencies from Hz to THz and is called Johnson–Nyquist noise. Thus, the amplitudes of received signals are measured in temperatures, and normalised to the system temperature T_{sys}.

The signal received from a radio source is very weak. The CMB has a typical temperature of 3 K, Milky Way Galaxy show about 1K, and for a 1 Jy source observed by a 12-meter antenna with 50 % efficiency will produce an antenna temperature of $T_\mathrm{A} = 0.02\,\mathrm{K}$[3]. The presented typical values for cosmic sources are about 1000 times smaller than typical system noise. Therefore, it is important to have an amplification chain, in which the first step is required to have a very low input noise and a high gain. The latter will reduce the noise contribution at the subsequent stages. For example, in the case of two-stage amplification of

[3]EGU and IVS Training School, Bill Petrachenko. https://www.oso.chalmers.se/evga/vlbi_school_2013/VLBI-school-2013_L02_Petrachenko.pdf

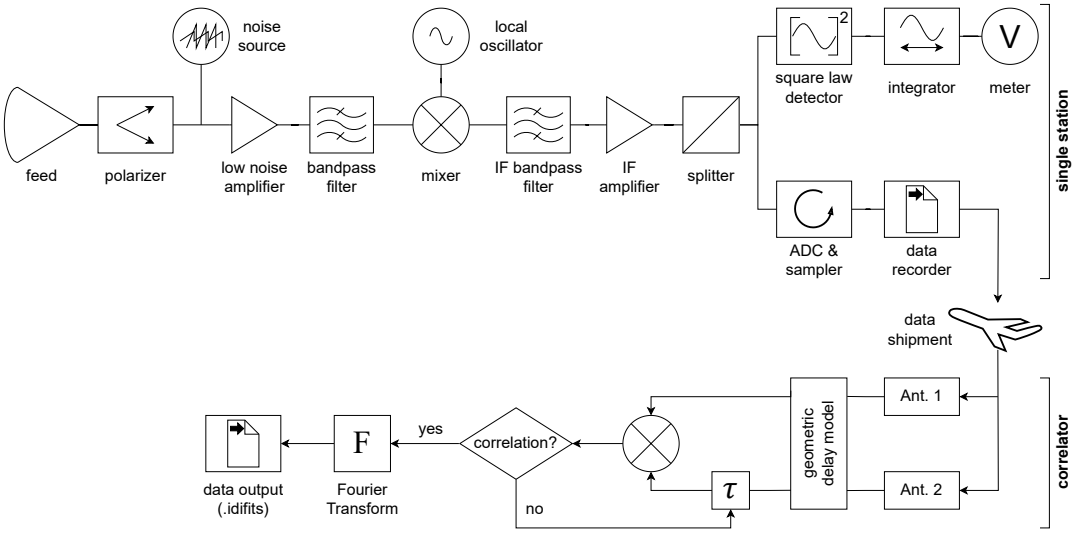

Figure 1.20: Signal chain in a radio telescope. Credit: Jan Röder.

signal S, noise N with gains G_1 and G_2 the total signal after amplification is $G_1G_2(S + N + N_1) + G_2N_2$. Hence the signal-to-noise ratio is

$$SNR = \frac{G_1G_2S}{G_1G2(N + N_1) + G_2N_2} = \frac{S}{N + N_1 + \frac{N_1}{G_1}}. \tag{1.1.24}$$

Therefore, the low-noise amplifier (LNA) with high gains is used at the beginning of the signal chain.

The next step is heterodyne, where the radio frequency (RF) signal is mixed with a local oscillator (LO). An important element of the heterodyne is the mixer, which conceptually can be considered as a multiplier producing outputs at the sum $\nu_{\mathrm{RF}} + \nu_{\mathrm{LO}}$ and difference $|\nu_{\mathrm{RF}} - \nu_{\mathrm{LO}}|$ frequencies of the inputs. If the frequency sum is selected using a filter this is referred to as an up converter. The opposite is referred to as a down converter. In radio astronomical observations it is nessesary to down-convert the input signal into a frequency low enough to transmit signals with wires, avoid interference with a receiving system and be able to digitize it. The output of the down converter is called intermediate frequency (IF). For a multiple set of IFs, multiple combinations of LOs and IF bandpass filters are used. Finally, square law detectors and integrators are used to obtain the final signal from each IF. The signal chain is also presented in Figure 1.20.

1.2 Interferometry

The resolution of a telescope is proportional to the wavelength of observation and inversely to the aperture diameter $\theta \propto \lambda/D$. The human eye has an angular

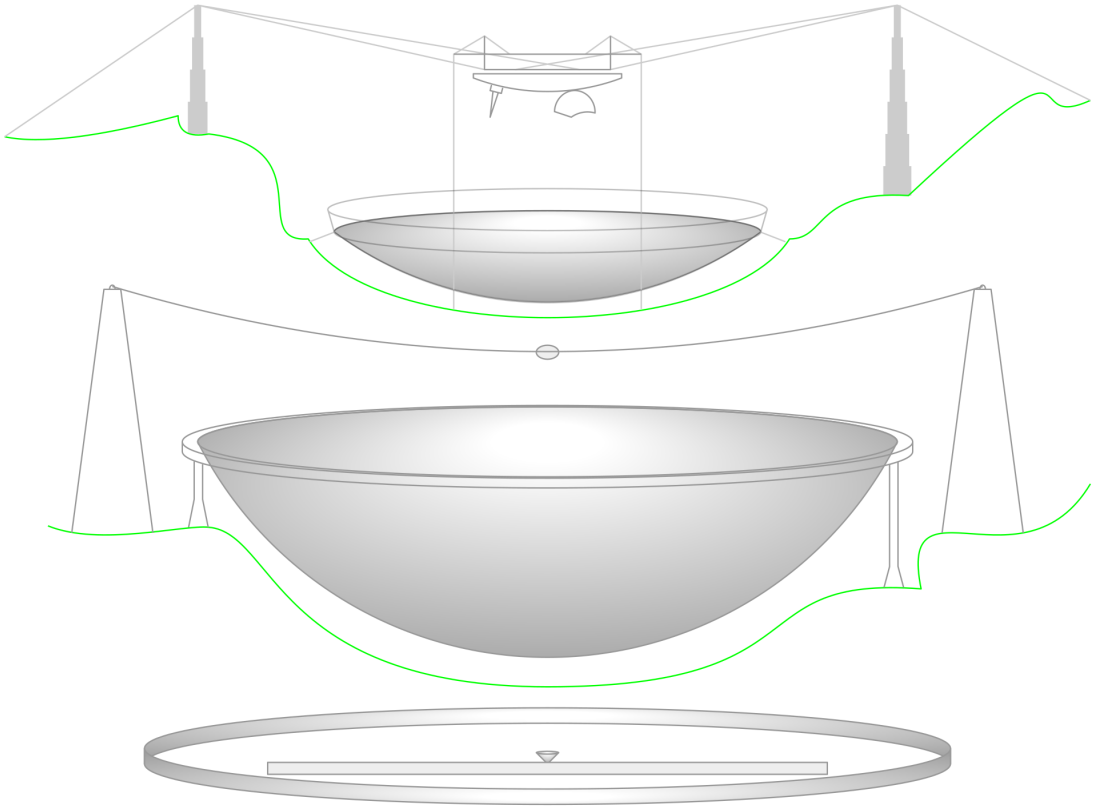

Figure 1.21: Comparison of the biggest radio telescopes. From top to bottom: Aresibo, FAST (Five-hundred-meter Aperture Spherical Telescope), and RATAN-600 (Radio Telescope of the Academy of Sciences 600). The terrain is highlighted in green colour. Credit: Wikimedia/Cmglee.

resolution of about half an arc minute. In radio bands, for example, to achieve the same resolution while observing the neutral hydrogen line at 21 cm, a 750-meter radio telescope is required. Nowadays, the biggest single-dish filled-aperture telescope is the Five-hundred-meter Aperture Spherical Telescope (FAST), built in 2016 in China (Figure 1.21). The telescope was constructed in a natural depression in the landscape; thus, the surface itself is not steerable. However, the cabin with a receiver can be moved to change the pointing. Thus, despite having a 500-meter dish, the effective diameter is 300 meters. The biggest steerable radio telescopes have a diameter of around 100 meters, like The Robert C. Byrd Green Bank Telescope (GBT) and the Effelsberg radio telescope (Figure 1.22). In the current state of materials studies, it is hard to build a telescope larger than 100 meters because of the fluidity of materials. Of course, the vast majority of radio telescopes have much lower diameters of the dish, thus poor resolution leading to the effect called confusion. The number of discrete sources is inverse to the flux, which was measured by (Franzen et al. 2019; Gower 1966; Jauncey 1975; Matthews et al. 2021; Ryle 1968). In the general case, the counts of radio sources are defined by the model of the Universe and evolution of objects (e.g. Davidson

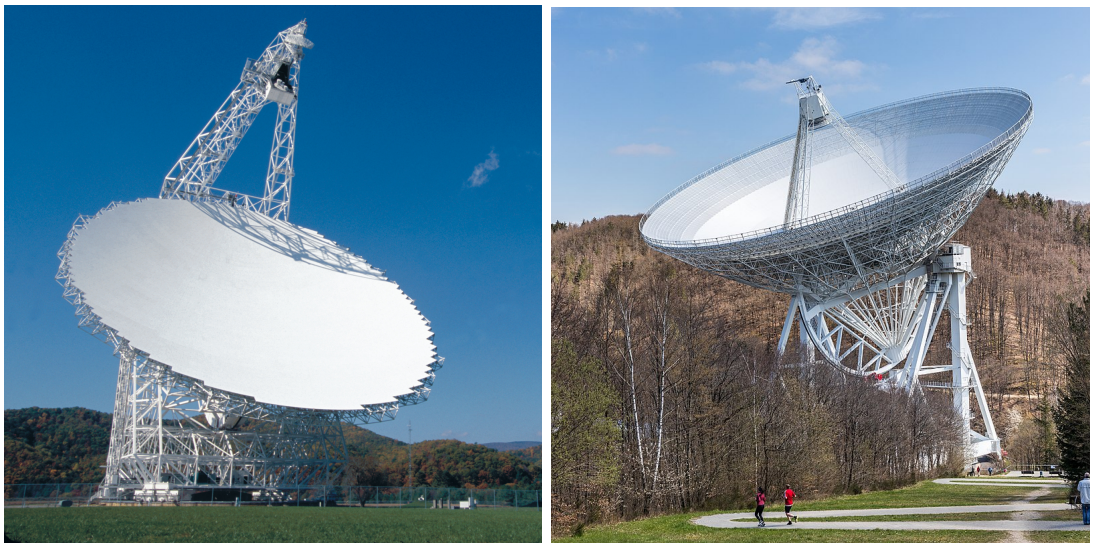

Figure 1.22: Left: The Robert C. Byrd Green Bank Telescope. Credit: NRAO/AUI/NSF. Right: Effelsberg 100-m Radio Telescope. Credit: Raimond Spekking.

& Davies (1964); Longair (1966)) and represented by the logarithmic scale plot $\log N$–$\log S$. In the case of low resolution, many different sources are observed within the same beam. Therefore, it is hard to separate the strong sources from the high number of weak sources. In this case, weak sources may be presented as confusion noise, which limits a single-dish observation. This can be avoided only by improving the resolution.

The largest individual radio telescope of any kind is the Radio Telescope of the Academy of Sciences 600 (RATAN-600), a 600-meter diameter telescope built in the 1970s in the Soviet Union (Figure 1.21). However, the engineers used a trick: instead of having a filled parabolic dish, the telescope has only the ring cut from the classical spherical or parabolic reflector shape. The radio emission from space is reflected by the ring to the conical secondary reflector (Figure 1.23) in the middle of the telescope, and to the receiver. This is called an unfilled aperture. Using this method, it is possible to dramatically increase resolution without building a very large telescope. A similar idea is used in radio interferometers, a system of more than two individual radio telescopes. The telescopes in the interferometer array represent a part of a parabola reflector that focuses light on the focal point. But in the case of the interferometer, "focusing" or combining the signals from telescopes is done by wires.

1.2.1 Astronomical interferometry

The basic experiment to demonstrate interference of light is Young's or double-slit experiment. In the experiment, a monochromatic wave $\vec{E} = E_0 \exp i(\omega t + \vec{k}\vec{r} + \varphi)$

Figure 1.23: Conical secondary reflector of RATAN-600. Credit: Vladimir Malder.

falls into an opaque screen with two narrow slits, behind which the measurement screen is placed (the scheme is presented in Figure 1.24). According to the Huygens–Fresnel principle, every point on a wavefront is itself the source of spherical waves. In the case when the width of the slits is an order of a wavelength, slits generate spherical waves, which interfere with each other and produce a fringe pattern on the measurement screen like in Figure 1.24. The intensity distribution is created by the superposition of electric vectors from the slits $\vec{E}_\Sigma$ and defined by

$$I = \langle \vec{E}_\Sigma^2 \rangle = \langle \vec{E}_1^2 \rangle + \langle \vec{E}_2^2 \rangle + 2\langle \vec{E}_1 \vec{E}_2 \rangle, \tag{1.2.1}$$

where $2\langle \vec{E}_1 \vec{E}_2 \rangle$ is an interference term. In the case, when $2\langle \vec{E}_1 \vec{E}_2 \rangle = 0$, the interference is not observed and the resulting intensity equals the sum of intensities from the slits $I = I_1 + I_2$. Intensity maximums in the pattern correspond to the in-phase amplitude sum of the waves or constructive interference, and the opposite creates minimums or destructive interference. The distance between the slits defines the width of the fringes.

The main condition for observing an interference pattern is coherence. There are two types of coherence: temporal and spatial. Temporal coherence **means** that the wave in a particular area does not change with time or have the same frequency. However, it is hardly possible to observe a monochromatic electromagnetic wave, thus a wave will be temporarily coherent only within coherence time τ_c and area defined by the coherence length $L_c = \tau_c c \propto \Delta\nu^{-1}$, where $\Delta\nu^{-1}$ is bandwidth. With an increase of bandwidth, the fringe pattern loses contrast, and the minimum intensity will not be zero $I_{\min} \gneq 0$. In this case, the term visibility arises, which is

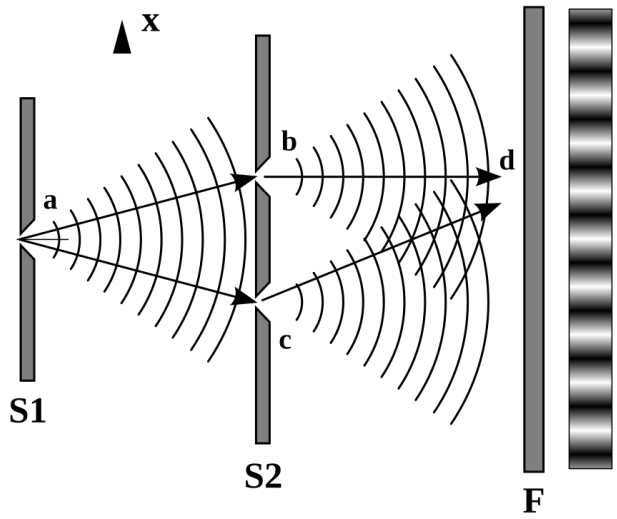

Figure 1.24: Double slit experiment. The screen **S2** with two slits **b** and **c** are illuminated by the light source **a**. According to the Huygens–Fresnel principle, **b** and **c** create spherical waves, which interfere and result in an interference pattern on the screen **F**. The pattern is illustrated on the right side of the figure as fringes. Credit: Wikimedia/Stannered.

the ratio between difference and sum of intensity maximum and minimum:

$$\mathcal{V} = \frac{I_{\max} - I_{\min}}{I_{\max} + I_{\min}}. \tag{1.2.2}$$

Visibility equals one $\mathcal{V} = 1$ when the light is coherent, and $\mathcal{V} = 0$ when there is no coherence and the fringe pattern is not visible. In the case of temporal incoherence, the visibility depends on the location on the screen and has the shape of a sinc function $\mathcal{V}(x) \propto \operatorname{sinc} x \equiv \sin x/x$ (Figure 1.25). Therefore, the interference pattern in the case of nonzero bandwidth is smeared out with the distance from the main maximum.

Spatial coherence is a synchronisation of oscillation perpendicular to the direction of wave propagation (Figure 1.26). It is important when the emitting source is extended since the difference in a wave path between different parts of the source reduces the maximum power of the fringes. The extended source consists of incoherent point sources, thus to obtain the interference result, one should sum all intensities coming from all elements. Visibility, in this case, does not depend on position on the measurement screen and is represented by a sinc function $\mathcal{V} = \operatorname{sinc}(kDd/2H)$, where $k = 2\pi/\lambda$ is the wave vector. The case of $\mathcal{V} = 0$ happens when $kDd/2H = \pi$ or angular size $\theta = D/H = \lambda/d$, $D \ll H$. The last expression is similar to the resolution of an instrument shown earlier in Equation 1.1.20. Thus, using an interferometer, it is possible to derive the angular sizes of objects increasing the distance between the slits until the fringe pattern is

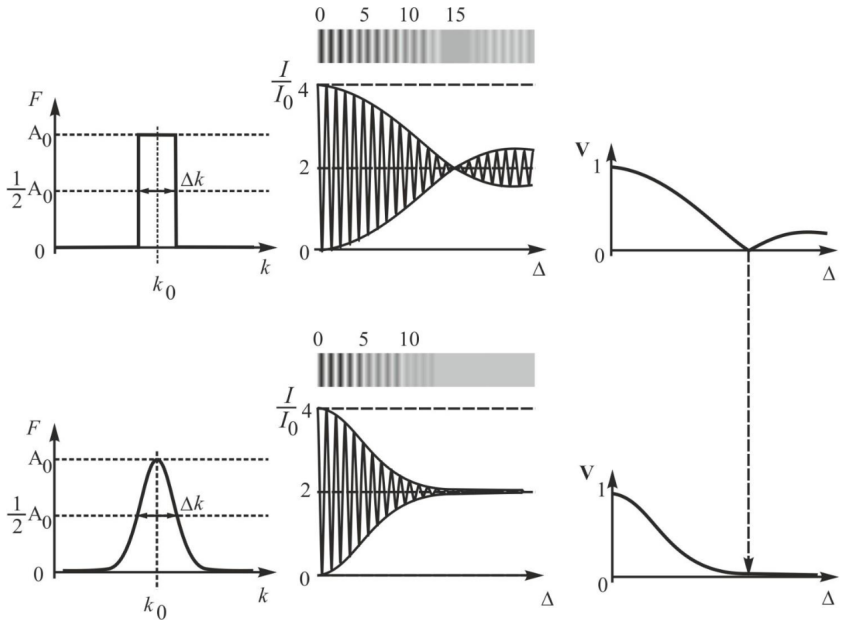

Figure 1.25: Visibility and interference pattern in the case of rectangular (top) and Gaussian (bottom) spectra. The first column shows the spectra of emission, the second column shows the interference patterns on a screen, and the third presents the visibility on a screen. Credit: Igor V. Mitin.

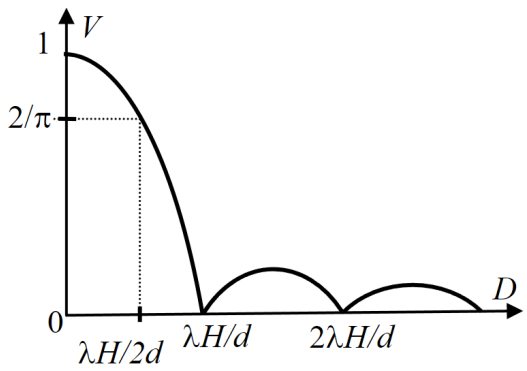

Figure 1.26: Visibility and the source size D. Credit: Igor V. Mitin.

gone. The angular size, then is calculated from Equation 1.1.20, where D is the distance between the slits.

In the general case, coherence can be described by a correlation between electric fields from the slits $\langle E_1(t)E_2^*(t+\tau)\rangle$. Complex coherence is defined as:

$$\gamma(\tau) = \frac{\langle E_1(t)E_2^*(t+\tau)\rangle}{\sqrt{I_1 I_2}}, \tag{1.2.3}$$

and can be placed as an interference term in Equation 1.2.1. Since visibility from Equation 1.2.2 contains intensities, it is connected to complex coherence as:

$$\mathcal{V} = \frac{2\sqrt{I_1 I_2}}{I_1 + I_2}|\gamma|\Bigg|_{I_1=I_2} = |\gamma|, \tag{1.2.4}$$

and is equal if the slits are identical.

The usage of Young's experiment in astronomical observations was proposed by Hippolyte Fizeau in 1867 (Bonneau 2019)[4]. The main idea is to cover a telescope aperture with a mask with two small apertures separated in a particular, better variable, distance. This type of mask was used in 1873 by Edouard Stephan to build the first astronomical interferometer using the 80 cm telescope at Marseille Observatory. In the case of Edouard Stephan's experiment, the two apertures were separated at 50 cm, which was not enough to measure star diameters. Therefore, he concluded that bigger separations are needed and obtained an upper limit for stellar diameters of $0.158''$ (Georgelin & Lequeux 2021; McLean 2008). Later, using a similar technique, Albert Michelson successfully measured the diameters of the major moons of Jupiter using a 30 cm refractor at Lick observatory (Michelson 1891). But this was not his only attempt measuring the diameters of sky objects. Michelson, inspired by Fizeau, suggested using a Michelson stellar interferometer to measure the diameter of a star. The first interferometer of this kind was built using the 2.5-meter Hooker telescope at the Mount Wilson Observatory. This time, instead of a mask, two mirrors with a variable 6-meter separation were used, effectively increasing the resolution of the host telescope. The scheme and the photograph of the stellar interferometer are presented in Figure 1.27. The instrument allowed them to measure the angular diameter of α Orionis for the first time $\beta''_{\text{Betelgeuse}} = 0.047''$ (Michelson & Pease 1921).

[4]See also: Optical Interferometry Motivation and History, Peter Lawson, 2006 Michelson Summer Workshop `https://nexsci.caltech.edu/workshop/2006/talks/Lawson.pdf`

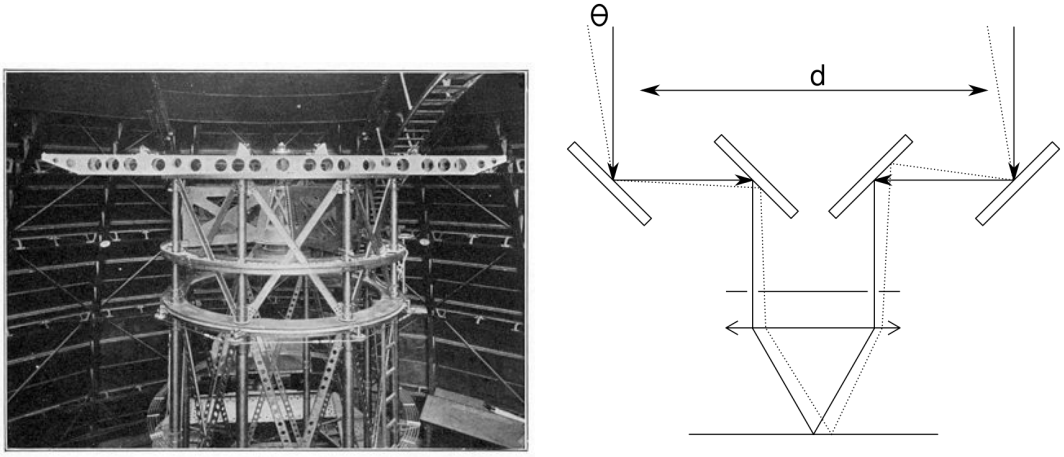

Figure 1.27: Left: The 2.5-meter Hooker telescope at the Mount Wilson Observatory. The 6-meter mirror separation device is installed on the top of the telescope. Credit: George Ellery Hale. Right: The interferometer scheme used on the Hooker telescope. Credit: Wikimedia/Alex-engraver.

1.2.2 The Two-Element Radio Interferometer

The simplest radio interferometer is a pair of radio telescopes whose voltage outputs are correlated (multiplied and averaged). The identical dishes are presented in Figure 1.28. The separation between telescopes is defined by the baseline vector $\vec{b}$ of length b from antenna 1 to 2. The direction to the source is specified by the unit vector $\vec{s}$, and θ is the angle between the direction and the baseline. Since the emitting objects are typically very far away, the light from a point source can be considered plane waves. The emission after reaching the telescope two needs to travel an extra distance $\vec{b}\vec{s} = b\cos\theta$ to reach the antenna 1. Therefore, the output of antennas is identical to the time lag called geometric delay

$$\tau_{\mathrm{g}} = \frac{\vec{b}\cdot\vec{s}}{c}. \tag{1.2.5}$$

As a simplification, a quasi-monochromatic interferometer is considered, thus the bandwidth is narrow $\Delta\nu \ll 2\pi/\tau_{\mathrm{g}}$ with central frequency $\nu = \omega/2\pi$.

Earlier in subsection 1.1.3, the signal chain of an individual telescope was described in detail. In contrast to a single-dish antenna, amplified signals from IF do not pass through square-law detectors. Instead, a correlator multiplies signals $V_1 = V\cos\omega(t-\tau_{\mathrm{g}})$ and $V_2 = V\cos\omega t$ from telescopes and averages them in time.

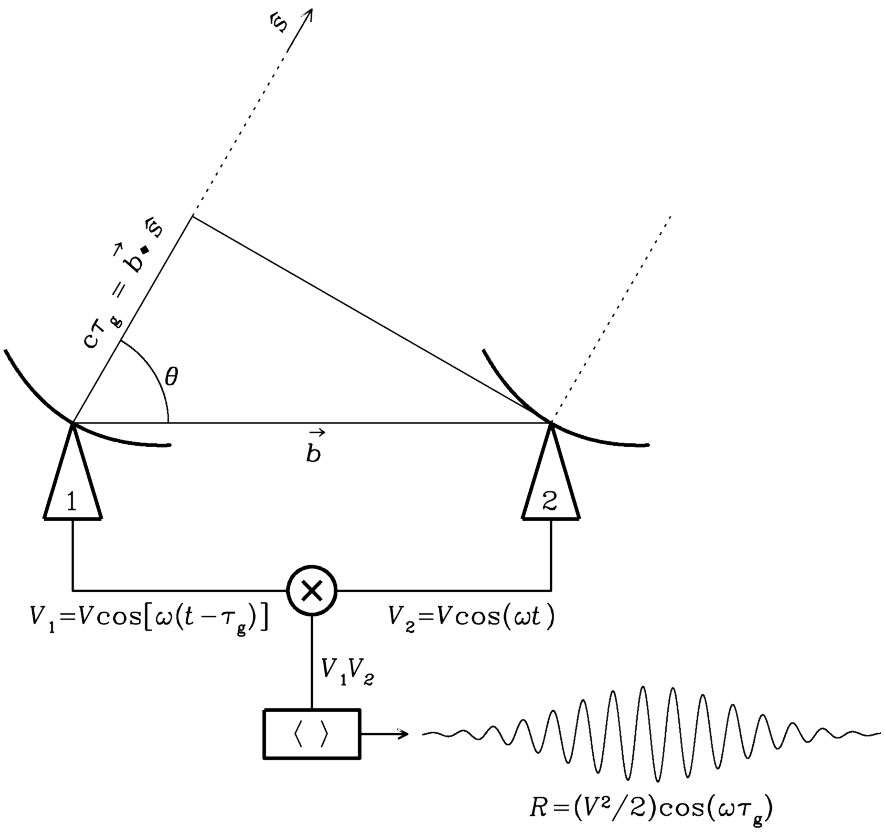

Figure 1.28: A two-element quasi-monochromatic multiplying interferometer. Credit: Condon & Ransom (2016).

The correlator response is

$$\begin{gathered} R = \langle V_1 V_2 \rangle = \\ \langle V^2 \cos\left[\omega(t-\tau_\mathrm{g})\right] \cos \omega t \rangle = \\ \langle \tfrac{V^2}{2} [\cos\left(2\omega t - \omega\tau_\mathrm{g}\right) + \cos \omega\tau_\mathrm{g}] \rangle = \\ \tfrac{V^2}{2} \cos \omega\tau_\mathrm{g}. \end{gathered} \tag{1.2.6}$$

The averaging removes $\cos\left(2\omega t - \omega\tau_\mathrm{g}\right)$ and keeps only the slowly varying term. The electric vector of the emission and the output voltages are analogous. Therefore, as an output of interferometer, the interference term from Equation 1.2.1 is obtained and one can connect the correlator response R to the visibility $\mathcal{V}$ using Equation 1.2.3.

A radio signal can be expressed as a complex exponent $V(t) = Ae^{i(\omega t+\phi)}$. At the same time, it can be decomposed into cosine and sine components $e^{i\theta} = \cos\theta + i\sin\theta$. Full information from the signal after correlation can be obtained if both components are obtained. For this reason, "cosine" and "sine" correlators are used. Outputs of the correlators are $R_\mathrm{c} = \langle V_1 V_2 \cos(\omega t)\rangle$ and $R_\mathrm{s} = \langle V_1 V_2 \sin(\omega t)\rangle$. In practice, it can be implemented by adding a 90° phase delay into the output of one antenna because $\sin\varphi = \cos\left(\varphi - \pi/2\right)$. Thus, complex visibility is defined by

$$\begin{aligned} \mathcal{V} &= Ae^{-i\phi} \equiv R_{\mathrm{c}} - iR_{\mathrm{s}}, \\ A &= \sqrt{R_{\mathrm{c}}^2 + R_2^2}, \\ \phi &= \tan^{-1}(\tfrac{R_{\mathrm{s}}}{R_{\mathrm{c}}}), \end{aligned} \tag{1.2.7}$$

where A is visibility amplitude and ϕ is visibility phase. And this is convenient since the visibility is connected to the intensity distribution by the van Cittert–Zernike theorem:

$$\mathcal{V} = \int I(\vec{s}) e^{-i\frac{2\pi\vec{b}\cdot\vec{s}}{\lambda}} \mathrm{d}\Omega. \tag{1.2.8}$$

Equation 1.2.8 shows that the visibility and the brightness distribution are connected through the Fourier transform $\hat{f}(\xi) = \int_{-\infty}^{\infty} f(x) e^{-i2\pi\xi x} \mathrm{d}x$. Thus, for simplicity, the Fourier transform operator will be denoted as $\mathbb{F}$ and Equation 1.2.8 can be rewritten as $\mathcal{V} = \mathbb{F}I$.

Bandwidth and time smearing

Previously, the monochromatic light case was reviewed, nevertheless, in reality, instruments have a particular bandwidth $\Delta\nu$ centred on frequency ν_{c}. In this case, in Equation 1.2.8 integration by frequency is needed

$$\begin{aligned} \mathcal{V} &= \int \int_{\nu_{\mathrm{c}}-\Delta\nu/2}^{\nu_{\mathrm{c}}+\Delta\nu/2} I(\vec{s}) e^{-i\frac{2\pi\vec{b}\cdot\vec{s}}{\lambda}} \mathrm{d}\nu \mathrm{d}\Omega \\ &= \int \int_{\nu_{\mathrm{c}}-\Delta\nu/2}^{\nu_{\mathrm{c}}+\Delta\nu/2} I(\vec{s}) e^{-i2\pi\nu\tau_{\mathrm{g}}} \mathrm{d}\nu \mathrm{d}\Omega \\ &\approx \int I(\vec{s}) \operatorname{sinc}(\Delta\nu\tau_{\mathrm{g}}) e^{-i2\pi\nu_{\mathrm{c}}\tau_{\mathrm{g}}} \mathrm{d}\nu \mathrm{d}\Omega. \end{aligned} \tag{1.2.9}$$

Therefore, the amplitude is attenuated by the factor $\operatorname{sinc}(\Delta\nu\tau_{\mathrm{g}})$. This can be compensated in a direction $\vec{s}_0$ called delay centre or the phase reference point by adding a delay $\tau_0 \approx \tau_{\mathrm{g}}, |\tau_0 - \tau_{\mathrm{g}}| \ll \Delta\nu^{-1}$ in the signal path of the reference antenna. Since the geometric delay τ_{g} varies with direction, the attenuation is larger with increasing the distance from the phase reference and $\Delta\tau_{\mathrm{g}} \propto \Delta\theta$, where $\Delta\theta$ is the angular radius of the usable field-of-view (FOV). From Equation 1.2.5 $|c\Delta\tau_{\mathrm{g}}| = b\sin\theta\Delta\theta$. Using $|\tau_0 - \tau_{\mathrm{g}}| \ll \Delta\nu^{-1}$ and $\theta_{\mathrm{s}} = \lambda/(b\sin\theta$ for the beam width, the size of the FOV due to the bandwidth smearing is

$$\frac{\Delta\theta}{\theta_{\mathrm{s}}} \ll \frac{\nu}{\Delta\nu}. \tag{1.2.10}$$

Using the same logic, time averaging Δt needs to be short enough so the Earth's rotation will not move the source position. In the case of the phase reference fixed

in the celestial pole, to prevent a time smearing effects, it is required

$$\frac{2\pi\Delta t}{P} \ll \frac{\theta_{\mathrm{s}}}{\Delta\theta}, \tag{1.2.11}$$

where P is the Earth's sidereal rotation period.

Smearing effects are crucial during a data analysis process, especially when the goal is to obtain a wide-field image. Thankfully, there are very useful and simple-to-use instruments which help observers and researchers calculate the effects discussed. One can use the online old EVN calculator[5] or the new EVN observation planner[6].

1.2.3 Aperture Synthesis

A pair of telescopes measures the visibility function at one spatial frequency at a time. Measurements at multiple baselines are synthesised to sample the Fourier (spatial frequency) domain with these single measurements. This is either done by combining many antennas (forming many antenna pairs), moving antennas relative to each other, or coverage is accrued over time due to Earth's rotation.

Historically, the single antennas were placed on rail tracks and moved away. One of the telescopes can be placed on the rail track and moved away to change the baseline vector $\vec{b}$, increasing the distance between the telescopes. One instrument which applied such a configuration was the One-Mile Telescope at the Mullard Radio Astronomy Observatory (MRAO), Cambridge, UK. Iteratively repeating the procedure, one can obtain visibilities at different spatial frequencies as illustrated in the example from Figure 1.29. The visibility function $\mathcal{V}(u)$ shown in Figure 1.29 reminds a spherical Bessel function; using Equation 1.2.8 or applying the inverse Fourier transform, the brightness distribution profile is obtained and presented on the right side of Figure 1.29. By changing the rail's orientation, the two-dimensional visibility $\mathcal{V}(u, v)$ can be obtained, where u and v axes point east and north and represent the components of the baseline vector in wavelength units $\vec{b}/\lambda$.

Each pair of telescopes creates a fringe intensity pattern in the image. Changing the baseline, the orientation and spacing of the pattern changes. Thus, the pair of telescopes at a given time is sensitive to a particular spatial frequency on a particular orientation. With the summation of the fringe patterns from different telescope orientations, an image of a source is obtained.

The projected baseline of an antenna pair relative to the sky plane changes with time due to Earth's rotation. Therefore, it is unnecessary to have telescopes

[5]EVN calculator `https://services.jive.eu/evn-calculator/cgi-bin/EVNcalc.pl`
[6]EVN observation planner `https://planobs.jive.eu/`

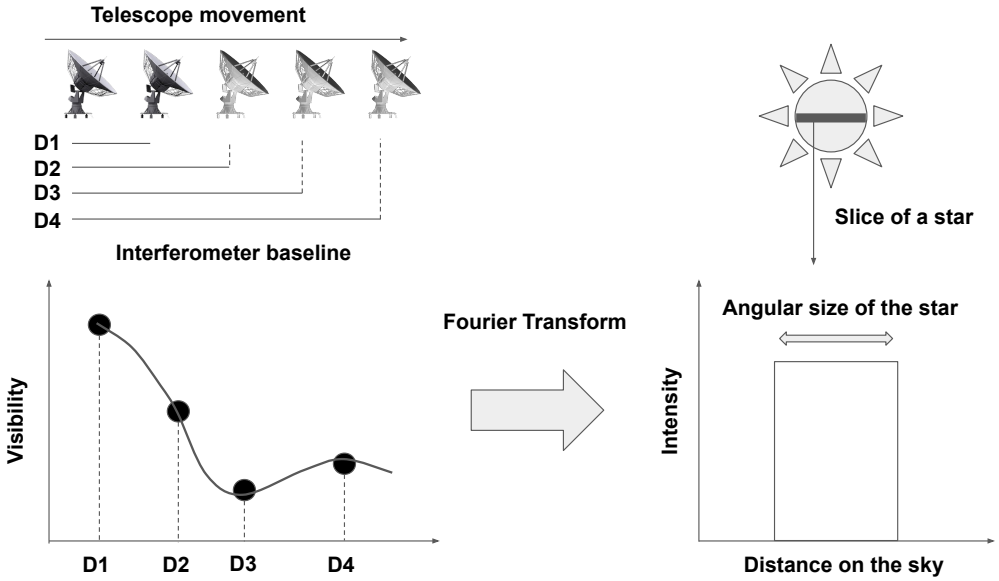

Figure 1.29: A two-element interferometer. One of the telescopes can move and change its position by rail, which can be seen on the top left of the figure by letters **D1**—**D4**. Measured visibility is presented on the bottom left. Fourier transform of the visibility function shows the intensity slice of a source on the bottom right of the figure.

on the rail to fill the uv domain. Historical examples include the Long Michelson Interferometer and the Cambridge Interferometer. A large interferometer at Cambridge used four antennas located at the corners of a rectangle 580 m east-west by 49 m north-south (Hewish & Ryle 1955). Martin Ryle and Antony Hewish received the Nobel Prize for Physics in 1974 for the development of this technique and other related work[7]. As the antennas track the source across the sky, the (u, v)-plane, in this case, is getting filled in an arc of an ellipse. The shape of the ellipse depends on the declination of the source, baseline vector and the latitude of the centre of the baseline. In Figure 1.30, various uv-coverages obtained with the Karl G. Jansky Very Large Array (VLA) are presented.

1.2.4 Very Long Baseline Interferometry

Interferometers exceed the resolution limit of a single antenna. However, this was still insufficient since the observed "radio stars" appeared to have angular sizes as small as $0.001''$ (Slish 1963). In addition, the observations of flat spectrum radio sources showed fast flux density variations with a time scale of months (Sholomitsky 1965). The causality principle suggests linear scales of less than

[7]The Nobel Prize in Physics 1974: Ryle and Hewish's Prize in Physics was the first to celebrate breakthroughs in astronomy. `https://www.nobelprize.org/prizes/physics/1974/speedread/`

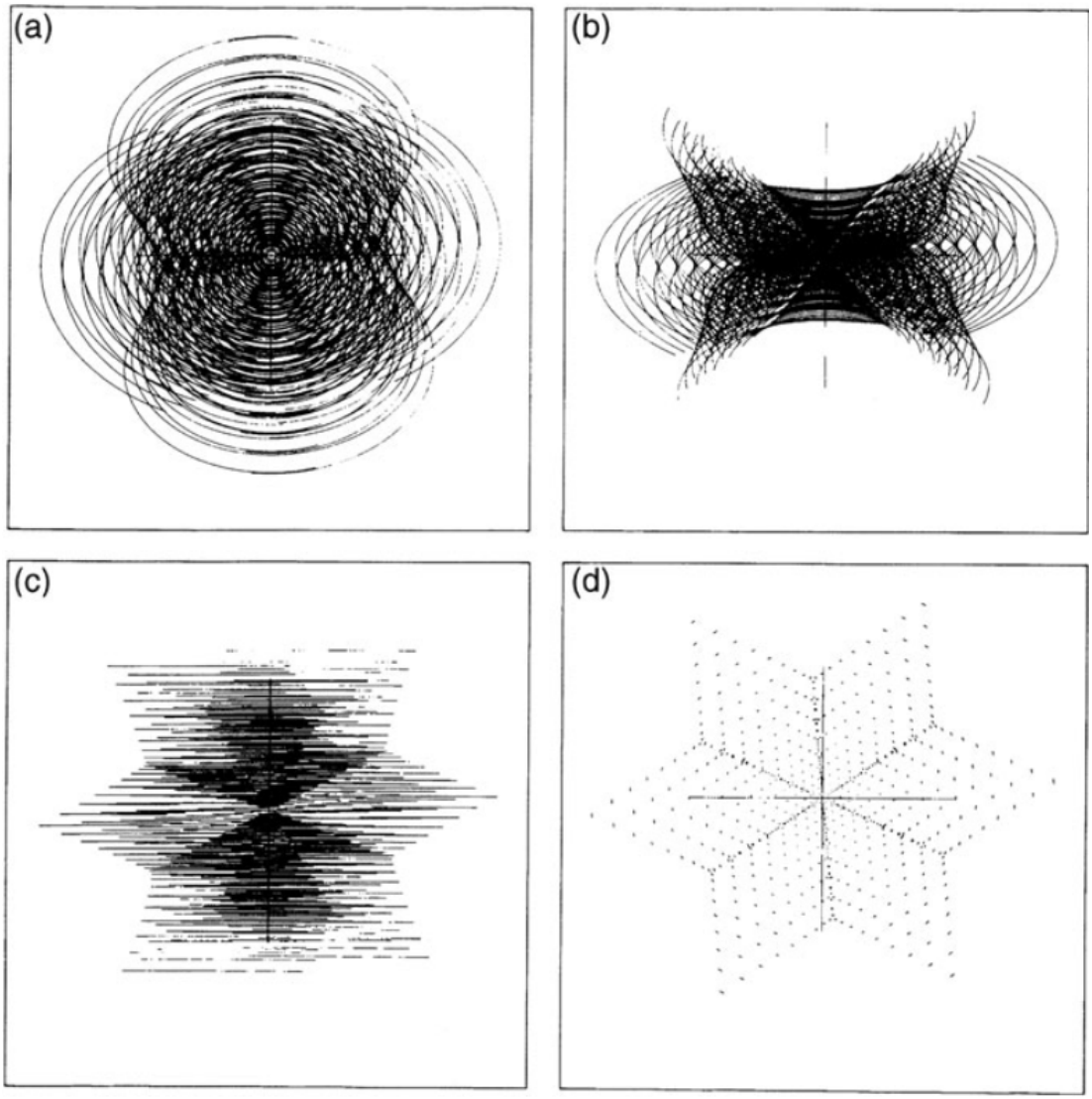

Figure 1.30: Simulated *uv*-coverage for the Very Large Array (VLA). Each plot shows the observation of a source with a particular declination: (a) $\delta = 45°$; (b) $\delta = 30°$; (c) $\delta = 0°$; (d) snapshot at zenith. Credit: Thompson et al. (2017).

one light year. Together with redshift measurements, this yield angular scales even less than 0.001″. Thus, interferometers with very long baselines of thousand kilometres were needed to determine the structure of these quasi-stellar objects (Burbidge 1967).

Early discussions to use independent oscillators and tape recorders to build an interferometer with large baselines took place at a series of seminars led by Leonid Matveyenko at the Lebedev Physical Institute in Moscow in autumn of 1962 (Kellermann & Moran 2001; Thompson et al. 2017). Later, the technical requirements for "Large base-line" radio interferometers were published (Matveenko et al. 1965; Slysh 1966). The first very long baseline interferometry (VLBI) experiments were independently conducted in 1967 in Canada (Broten et al. 1967) and the United States (Bare et al. 1967) achieving resolution of 0.02″. An early example of the extremely high angular resolution of 200 μas was achieved with the baseline Haystack (USA) – Simeiz (USSR) during observation of a maser in the giant molecular cloud W49 at 1.3 cm (Burke et al. 1972; Thompson et al. 2017). Later, radio observatory facilities collaborated to simultaneously obtain measurements of more baselines, leading, for example, to the first global radio telescope (Batchelor et al. 1976). The initiative developed into arrays consisting of inhomogeneous telescopes all around the world, such as the European VLBI Network (EVN), Global mm-VLBI Array (GMVA), and Event Horizon Telescope (EHT).

Calibration

The calibration of VLBI data is usually manually processed using standard software such as AIPS (Greisen 2003a) or CASA (CASA Team et al. 2022). Nowadays, some automatised pipelines can obtain science-ready products such as calibrated visibilities or even images like NRAO's VLBA pipeline for AIPS (Sjouwerman et al. 2005) and CASA-based `rPICARD` pipeline (Janssen et al. 2019). However, one should be careful about the output of the pipelines and look at diagnostic plots together with final results since poor data quality or unusual observation setup can make automated calibration harder. The general calibration process for a VLBA dataset is outlined in Figure 1.31. A detailed description of calibration steps is available in the AIPS cookbook [8] and CASA VLBI tutorials [9].

[8] AIPS cookbook: Calibration strategy `http://www.aips.nrao.edu/CookHTML/CookBooks e59.html`

[9] CASA VLBI tutorials `https://casaguides.nrao.edu/index.php/VLBI_Tutorials`

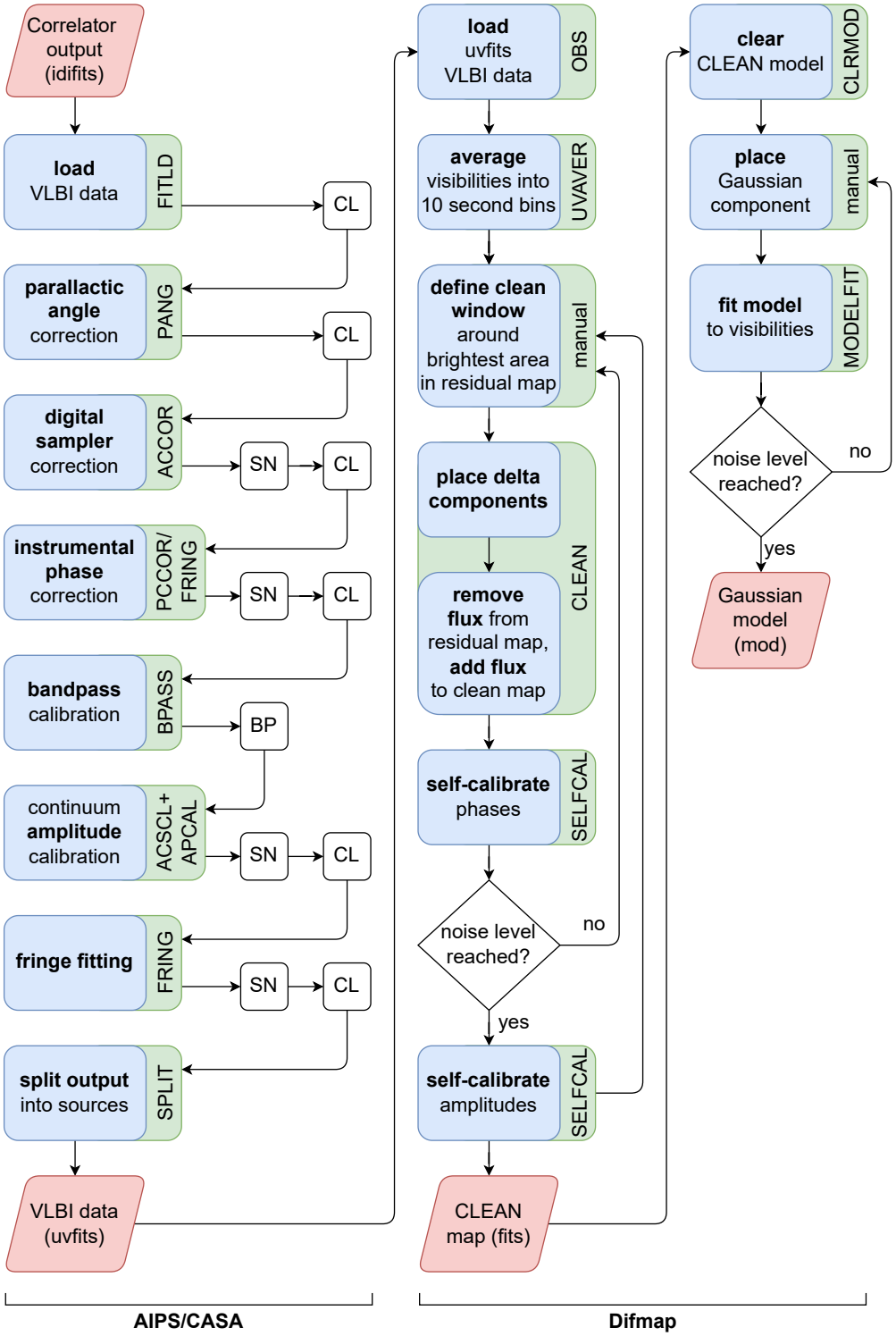

Figure 1.31: Data reduction scheme from apriori calibration to imaging and self-calibration. Credit: Jan Röder.

RIME

The radio interferometer measurement equation (RIME) is a mathematical formulation of a radio interferometer by Hamaker et al. (1996a) and Smirnov (2011). The approach provided a basis for the novel calibration methods and techniques used in the listed above software. The main idea and the fundamental assumption is linearity: all transforms and projections along the signal path are linear. The signal at a fixed point in space and time can be described by the complex vector $\vec{e}$ in the orthonormal xyz coordinate system, with z along the direction of propagation:

$$\vec{e} = \begin{pmatrix} e_x \\ e_y \end{pmatrix}. \tag{1.2.12}$$

A matrix multiplication can represent all linear transformations of a 2-vector:

$$\vec{e}' = \vec{J}\vec{e}, \tag{1.2.13}$$

where $\vec{J}$ is a 2×2 complex matrix called Jones matrix (Jones 1941). Since multiple effects can affect the signal, the signal propagation path corresponds to repeated matrix multiplications, which can be collapsed into a single cumulative Jones matrix:

$$\vec{e}' = \vec{J}_n \vec{J}_{n-1} ... \vec{J}_1 \vec{e} = \vec{J}\vec{e}. \tag{1.2.14}$$

The signal in the antenna is recorded as voltages in the antenna feed a and b (for example, two linear dipoles or left/right circular feeds). Thus the voltage vector $\vec{v}$ can be presented analogous to Equation 1.2.13:

$$\vec{v} = \begin{pmatrix} v_a \\ v_b \end{pmatrix} = \vec{J}\vec{e}. \tag{1.2.15}$$

In an interferometer voltages from different pairs of telescopes p and q are correlated, producing four pairwise correlations between the components v_p and v_q: $\langle v_{pa} v^*_{qa} \rangle$, $\langle v_{pa} v^*_{qb} \rangle$, $\langle v_{pb} v^*_{qa} \rangle$, $\langle v_{pb} v^*_{qb} \rangle$. Together it forms the visibility matrix:

$$\mathcal{V}_{pq} = 2 \begin{pmatrix} \langle v_{pa} v^*_{qa} \rangle & \langle v_{pa} v^*_{qb} \rangle \\ \langle v_{pb} v^*_{qa} \rangle & \langle v_{pb} v^*_{qb} \rangle \end{pmatrix} = 2 \left\langle \begin{pmatrix} v_{pa} \\ v_{pb} \end{pmatrix} (v^*_{qa} v^*_{pb}) \right\rangle = 2 \langle \vec{v_p} \vec{v_q}^H \rangle. \tag{1.2.16}$$

where factor 2 is defined by convention discussed in detail by Smirnov (2011). Thus, the signal from a source $\vec{e}$ is connected to the observed visibility via antenna-based Jones matrices $\vec{J_p}$ and $\vec{J_q}$: $\mathcal{V}_{pq} = 2 \vec{J_p} \langle \vec{e}\vec{e}^H \rangle \vec{J}^H_q$. Since the quantities inside the brackets are related to the definition of the Stokes parameters, they can be

defined as a brightness matrix B:

$$2\begin{pmatrix} \langle e_x e_y^* \rangle & \langle e_x e_y^* \rangle \\ \langle e_y e_x^* \rangle & \langle e_y e_y^* \rangle \end{pmatrix} = \begin{pmatrix} I+Q & U+iV \\ U-iV & I-Q \end{pmatrix} = B. \tag{1.2.17}$$

Thus, the RIME can be defined as:

$$\mathcal{V}_{pq} = \vec{J}_p B \vec{J}_p^H, \tag{1.2.18}$$

where $\vec{J}$ is a cumulative Jones matrix, each component of which is used to calibrate a particular effect.

Amplitude

A telescope uses the noise temperature diode as an amplitude measure. Therefore, the correlator outputs are the ratios of correlated power to noise power. The system equivalent flux density (SEFD) of a radio telescope is the total system noise represented in units of equivalent incident flux density above the atmosphere:

$$\text{SEFD} = \frac{T^*_{\text{sys}}}{\text{DPFU} \times \eta_{\text{h}}}. \tag{1.2.19}$$

The effective system noise temperature describes the total noise of the system attenuated for the atmospheric opacity $T^*_{\text{sys}} \simeq e^{\tau}(T_{\text{rx}} + T_{\text{atm}}(1 - e^{-\tau}))$, where T_{rx} is receiver noise temperature and τ sky opacity in the line of sight. The degrees per flux density unit (DPFU) provides a factor of conversion KJy^{-1} correcting for the aperture efficiency $\text{DPFU} = A_{\text{eff}}/2k_{\text{B}}$. In practice, it is calculated by observing planets, and $\text{DPFU} = T^*_A/S_{\text{planet}}$, where T^*_A is the antenna temperature and S_{planet} is calculated flux density of an observed planet. The gain curve η_{h} is a modelled elevation dependence of the telescope's aperture efficiency and parametrised as a second-order polynomial $\eta_{\text{h}} = 1 - B(h - h_{\max})^2$.

Visibility amplitudes are calibrated by the geometric mean of the derived SEFD of the two stations in a baseline:

$$|\mathcal{V}_{pq}| = \sqrt{\text{SEFD}_p \times \text{SEFD}_q}|r_{pq}|, \tag{1.2.20}$$

where $|\mathcal{V}_{pq}|$ is the calibrated visibility amplitude in Jy.

The data from each IF or spectral window passes through a bandpass filter, which does not have a perfect rectangular passband. Leaving it without the correction leads to incorrect relative amplitudes and spectral information. A bandpass calibration uses a strong calibrator source to obtain the amplitude and phase response as function of frequency; at least one 2-minute scan should be

scheduled on a bright source at every observing band for every 3 to 4 hours of observing [10].

Fringe fitting

In contrast to connected-element interferometry, in VLBI, the signals obtained at each telescope are post-processed: instead of the square law detector, they are converted to a digital signal and sampled in the analogue-to-digital converter (ADC) at the Nyquist-Shannon sampling rate. Along with the high-accuracy timestamps derived from GPS and the station's atomic frequency reference, the signal is recorded to a storage device. Since each station has its frequency standard, it is hard to hold the phase stability for a long time. Errors in the source or antenna position and atmospheric model also affect the phase, introducing phase errors $\Delta\phi(t,\nu) = 2\pi\nu \mathrm{d}\tau$. This creates drifts in the visibility phase $\phi(t,\nu)$ (fringe phase) and the rate of change with frequency (delay) $\mathrm{d}\phi/\mathrm{d}\nu$ and time (delay rate) $\mathrm{d}\phi/\mathrm{d}t$ from the first order expansion of the error for individual antenna:

$$\Delta\phi(t,\nu) = \phi_0 + \left(\frac{\mathrm{d}\phi(t,\nu)}{\mathrm{d}\nu}\Delta\nu + \frac{\mathrm{d}\phi(t,\nu)}{\mathrm{d}t}\Delta t\right), \tag{1.2.21}$$

where ϕ_0 is the phase error at the reference time and frequency. The delay corresponds to the geometric delay discussed earlier in Equation 1.2.5 and has values of the order of nanoseconds, and the rate is measured in mHz. Therefore, it is important to calculate the correlation function considering the time offset that maximizes the correlation. Thus, a VLBI experiment begins with a two-dimensional search for delay and delay rate to find the peak of the correlation function. This process is referred to as fringe finding. It is done in real time with a bright source as a fringe finder to determine the relative station clock offsets before the main experiment starts. This adds a correction to the initial correlator model, which accounts for the array's geometry and other parameters. After the correlation, the phases still can exhibit residual delays and rates. Thus, these residuals should be reduced by a more accurate procedure called global fringe fitting. The fringe fitting solves for the parameters of $N-1$ antennas relative to the reference antenna. After that the data can be averaged in time and frequency to obtain better SNR. However, the consequence of the phase shift applied is the loss of absolute positions of a source. More detailed insight into fringe fitting can be found in Schwab & Cotton (1983).

[10] VLBA Calibration strategies `https://science.nrao.edu/facilities/vlba/docs/manuals/obsvlba/referencemanual-all-pages`

Polarisation calibration

Many VLBI telescopes use circularly polarised feeds. Therefore, four right-hand (R) and left-hand (L) circular feed correlations are used to obtain polarisation information: RR, LL, and cross-correlations RL and LR. In the formulation of Stokes parameters discussed in subsection 1.1.2:

$$\begin{aligned} I &= (RR + LL)/2 \\ Q &= (RL + LR)/2 \\ U &= i(LR - RL)/2 \\ V &= (RR - LL)/2. \end{aligned} \tag{1.2.22}$$

Previously, using the fringe fitting, the phase was corrected for the delay and rate for each polarisation individually. There still may be R–L phase and multi- and single-band delay offsets. Since this is an antenna-based effect, it will not depend on the parallactic angle, which evolves with time in altazimuth mounts. This effect can be used in calibration, and strong polarised sources must be observed over a wide range of feed rotation angles to calibrate the cross-hand correlations (Cotton 2012). During the calibration, the absolute cross-hand phase is lost. This is crucial for the absolute EVPA reconstruction and can be calibrated using observations from a connected-element interferometer or a single-dish calibrator source, which has the same field orientation on VLBI scales. The difference in EVPA found in the calibrator source is later applied to the scientific one.

Parallel hand feeds are not ideal; the signal from one polarisation can leak to the other and vice versa. The leakage can be described by the D-terms (Conway & Kronberg 1969). It can be assumed that extragalactic synchrotron sources have negligible circular polarisation. In this case, the D-terms on a baseline pq can be modelled by a first-order approximation (Leppanen et al. 1995):

$$\begin{aligned} RL_{pq}^{obs} &= RL_{pq} + (D_p^R e^{2I\chi_p} + (D_q^L)^* e^{2I\chi_q})I \\ LR_{pq}^{obs} &= LR_{pq} + (D_q^L e^{-2I\chi_p} + (D_p^R)^* e^{-2I\chi_q})I. \end{aligned} \tag{1.2.23}$$

As can be seen from Equation 1.2.23, D-terms affect polarisation depending on the field rotation angle χ on a particular antenna. This makes the instrumental effect distinguishable from the source polarisation. Therefore, for the D-term calibration, a weak polarisation source observed at a good range of parallactic angles is needed. At high frequencies (> 15 GHz), it is hard to find a sufficiently weak polarisation source. In this case, a strong and compact polarised source is required. In `AIPS`, it is solved by `LPCAL` task (Cotton 1993; Leppanen et al. 1995). The total intensity model of a source I is first divided into sub-components. Each

of these components is assumed to have constant fractional polarisation, thus:

$$I = \sum_{i}^{N} I_i;\ Q = \sum_{i}^{N} q_i I_i;\ U = \sum_{i}^{N} q_i I_i, \tag{1.2.24}$$

where q_i and u_i are real values and defined in the interval $q_i^2 + u_i^2 \in [0, 1]$. However, `LPCAL` does not constrain these values. The least-squares minimisation obtains the D-terms $\chi^2 = \chi^2_{RL} + \chi^2_{LR}$, where

$$\begin{aligned} \chi^2_{RL} &= \sum\nolimits_k \left| \frac{V^k_{RL}}{g^p_R (g^q_L)^*} - \frac{D^p_R V^k_{LL}}{g^p_L (g^q_L)^*} - \frac{(D^q_L)^* V^k_{RR}}{g^p_R (g^q_R)^*} - \mathcal{P}_{1,k} \right|^2 w_k, \\ \chi^2_{LR} &= \sum\nolimits_k \left| \frac{V^k_{LR}}{g^p_L (g^q_R)^*} - \frac{D^p_L V^k_{RR}}{g^p_R (g^q_R)^*} - \frac{(D^q_R)^* V^k_{LL}}{g^p_l (g^q_L)^*} - \mathcal{P}_{2,k} \right|^2 w_k, \end{aligned} \tag{1.2.25}$$

where $\mathcal{P}_{1,k} = (\widetilde{Q}^k + i\widetilde{U}^k) e^{i(\psi^p + \psi^q)}$, $\mathcal{P}_{1,k} = (\widetilde{Q}^k - i\widetilde{U}^k) e^{-i(\psi^p + \psi^q)}$, and $\widetilde{Q}^k$ and $\widetilde{U}^k$ are Fourier transforms of Stokes parameters evaluated at the point of uv-space corresponding to the kth visibility; w_k are the visibility weights.

Although `LPCAL` is widely used and works well in linear regimes of D-terms, which is the case for this dissertation, it suffers from limitations originating from assumed approximations. In terms of RIME formalism, D-terms can be included in the Jones matrix for antenna a and polarisations r and l:

$$\vec{J}^a = \vec{G}^a \vec{D}^a \vec{P}^a = \begin{bmatrix} G^a_r & 0 \\ 0 & G^a_l \end{bmatrix} \begin{bmatrix} 1 & D^a_r \\ D^a_l & 1 \end{bmatrix} \begin{bmatrix} e^{i\psi_a} & 0 \\ 0 & e^{-i\psi_a} \end{bmatrix}, \tag{1.2.26}$$

where $D^a_{r,l}$ are D-terms used to model the signal leakage; $G^a_{r,l}$ are complex gains, and ψ_a is a feed rotation angle. Thus, Equation 1.2.25 is the approximation to the exact

$$\chi^2_{\mathrm{RIME}} = \sum_{k,m} w_k |[(\vec{J}^a)^{-1} \vec{V}^{ab} ((\vec{J}^b)^{-1})^H]_m - \vec{B_m}|^2, \tag{1.2.27}$$

where m runs over the RL and LR matrix elements. In recent years, new methods emerged which solve for D-terms using different approaches and software, which should improve the nonlinear terms (Chael et al. 2016; Martí-Vidal et al. 2021; Park et al. 2021).

Space VLBI

Earth limits the resolution of VLBI by the maximum baseline to the planet's diameter. Longer baselines are only achieved by connecting radio antennas launched to space to ground-based telescopes. The discussions started already in the 1960s and evolved into projects like Quasat (15-m dish), RACSAS (30-m

Figure 1.32: Left: HALCA (Highly Advanced Laboratory for Communications and Astronomy), also known for its project name VSOP (VLBI Space Observatory Programme). Credit: ISAS JAXA. Right: Spektr-R (part of RadioAstron program). Credit: Sergei Danilov.

dish) and IVS (25-m dish) in the 1970s (Gurvits 2023). Practical realisations started in the 1980s, beginning with NASA's geostationary Tracking and Data Relay Satellite System (TDRSS). Launched in 1986, it was equipped with two 4.9 m antennas. One was used to obtain the first VLBI fringes with a network of Earth-based antennas in Australia, Japan and the US. The maximum projected baseline achieved in the demonstration was around 2.2 Earth diameters (ED) (Levy et al. 1986). The experiment's success led to the VLBI Space Observatory Program (VSOP), the first space-VLBI mission (Figure 1.32). It was launched on 12 February 1997 and had an 8.8 m parabolic mirror made of wire mesh. Two receivers enabled observations at 18 and 6 cm in left-hand circular polarisation (LCP). The satellite was in an elliptical orbit with a major axis of about 28000 km with an orbital period of 6 hours (Hirabayashi et al. 2000, 1998).

RadioAstron, a VLBI mission, was launched on 18 July 2011 from the Baikonur Cosmodrome aboard the Spektr-R spacecraft. The telescope could observe full polarisation at 0.32, 1.6, 4.8, and 22 GHz. It had a highly elliptical orbit with a major axis of 360,000 km, corresponding to 30 ED. Given such a long baseline, the RadioAstron mission has achieved angular resolution records in all frequency bands, including 22 GHz, where the all-astronomy record of 7 microarcseconds was obtained. The telescope observed many compact radio-emitting objects such as pulsars, molecular clouds, and AGN jets, on probably the innermost regions inaccessible to ground-based VLBI (Kardashev et al. 2013). For example, it is observed the filamentary structure was discovered in the jet base of 3C 84 (Giovannini et al. 2018) and 3C 279 (Fuentes et al. 2023). The mission was completed in 2019 after operating in orbit for nearly 7.5 years, 2.5 times longer

than the industrial warranty of the spacecraft.

1.2.5 Imaging in radio interferometry

According to the van Cittert–Zernike theorem (Equation 1.2.8), the sky brightness distribution and the visibility function are connected via the Fourier transform

$$\mathcal{V}(u,v) = \mathbb{F}I \equiv \iint I(x,y)e^{-2\pi i(ux+vy)}\mathrm{d}x\mathrm{d}y, \tag{1.2.28}$$

where (u,v) are the Fourier and (x,y) image domain coordinates (Thompson et al. 2017). In practice, any instrument obtains only part of the visibility function. The sparse coverage in the uv-domain is essentially a mask. Thus, the observed visibility can be written as

$$\mathcal{V}_{\mathrm{obs}}(u,v) = W(u,v)\mathcal{V}(u,v), \tag{1.2.29}$$

where $W(u,v)$ is the transfer function or a mask of the visibility function. The inverse Fourier transform of the transfer function is known as the point spread function (PSF) for uniform weighting. The PSF is the response function to a point source. Similarly, we define the dirty map as the Fourier pair to the observed visibilities and reformulate problem (Equation 1.2.28) as a deconvolution problem:

$$I_{\mathrm{dirty}}(l,m) = I(l,m) * b_0(l,m), \tag{1.2.30}$$

where the asterisk is convolution, and b_0 is the PSF. The process of recovering the real intensity distribution is called deconvolution. Since the PSF is rank-deficient, the deconvolution is an ill-posed inverse problem, and naive inversion approaches will diverge in the presence of noise therefore.

Figure 1.33 shows the uv-coverage, where the *uv*-coverage of the VLBA full-track observations is presented. The sparsity of the uv-coverage creates an ill-posed inverse problem, which has an infinite number of solutions between the measurement points (Bracewell & Roberts 1954; Thompson et al. 2017), and a complicated shape PSF or a dirty beam also presented in Figure 1.34. Thus, a special treatment during deconvolution is needed.

Before the deconvolution the visibility data needs to be interpolated into a rectangular grid for convenience in Fourier transformation. This process is called gridding. The visibility $\mathcal{V}_{\mathrm{obs}}(u,v)$ is convolved with a convolution function $C(u,v)$ to produce a continuous visibility distribution. After, it is resampled in a rectangular grid with incremental spacings Δu and Δv. This process is called convolutional gridding, where $C(u,v)$ is typically a radially symmetric convolution

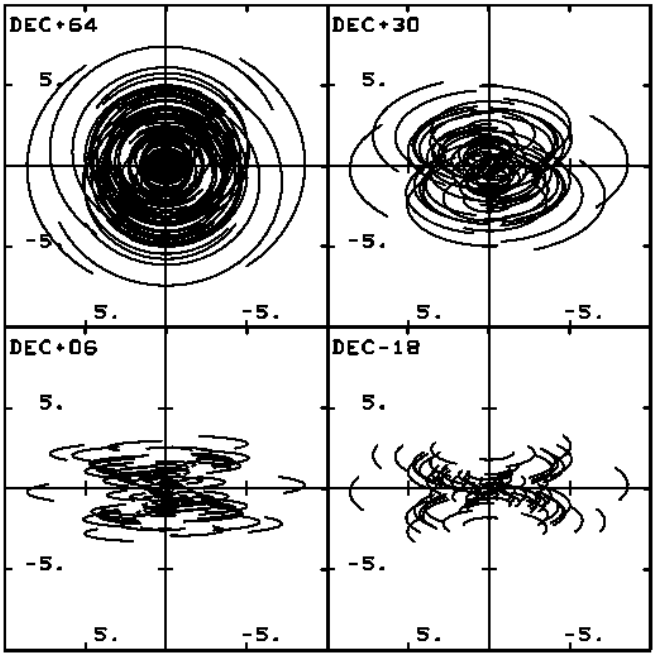

Figure 1.33: Simulated *uv*-coverage of VLBA observing sources with $\delta = 64°$, $\delta = 30°$, $\delta = 6°$, $\delta = -18°$. Credit: NRAO.

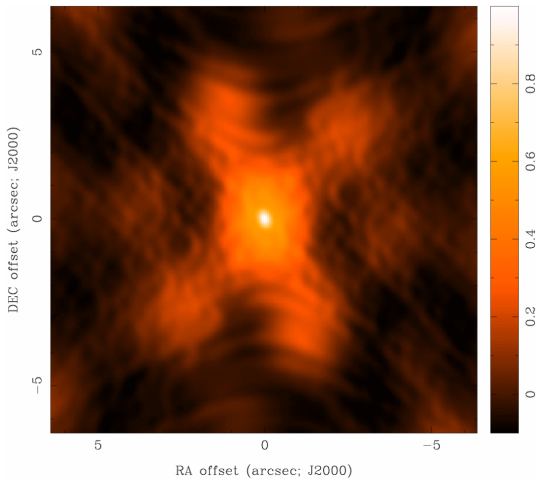

Figure 1.34: Dirty beam or a PSF of VLBA. Credit: NRAO, Jim Braatz, David Wilner, Scott Schnee, Remy Indebetouw.

kernel with a size of a few gridding cells, in the simplest case just a rectangular function. The weighting $w(u, v)$ is applied to include information on the thermal noise levels in the deconvolution. Thus,

$$\mathcal{V}_{obs}(u, v) = \frac{w(u, v)}{\Delta u \Delta v} \mathrm{III}\left(\frac{u}{\Delta u}, \frac{v}{\Delta v}\right) [C(u, v) * (W(u, v)\mathcal{V}(u, v))], \tag{1.2.31}$$

where $\mathrm{III}\left(\frac{u}{\Delta u}, \frac{v}{\Delta v}\right)$ is a shah function (Bracewell 1956; Thompson et al. 2017). Depending on the need, weighting can be set inversely to the variance or $\propto 1/\sigma^2$, which is called natural weighting. Thus, the weighting scheme highlights the effect of the highest SNR baselines leading to a big beam, and it emphasises short baselines in the case of VLBI. In the case of high SNR on long baselines, one can use uniform weighting, which weighs every point equally $\propto 1/\sigma$ and normalises the number of visibility points in every gridding cel. This improves the resolution in the cost of lower SNR.

The `CLEAN` algorithm

Högbom (1974) presented a method named `CLEAN` which iteratively removes a beam from the image. To date, it is the most common and well-tested deconvolution algorithm used in radio astronomy and other fields. The algorithm treats the sky as a collection of delta components. One can subtract dirty beams, locate the delta components, recovering the sky distribution. This can be described by a loop consisting of the following steps:

1. Compute the dirty beam and dirty image.

2. Find a maximum of dirty image $|I_{max}(x_0, y_0)|$ and subtract from the residual a dirty beam centred at maximum (x_0, y_0) and normalised to $\gamma|I_{max}(x_0, y_0)|$. The parameter γ is called loop gain.

3. Repeat the previous step until the residual map maximum will be similar to the noise value. All subtracted fluxes and locations of the components should be saved in a table called `CLEAN` model.

4. Approximate a Gaussian to the main lobe of the dirty beam creating the `CLEAN` beam. Next, convolve it with the `CLEAN` model. The resulting map with the last residual is called `CLEAN` map.

In the simple cases, the loop gain $\gamma = 1$ can show good results. However, if a source has a complicated structure, it is recommended to use small gain. In the case of a polarisation, mapping can be done by processing Q and U Stokes parameters separately.

Nowadays, a lot of new approaches and deconvolution methods have been developed. Starting from modifications of the original `CLEAN` algorithm like optimizing (Clark 1980) and implementing multi-scale capabilities (Cornwell 2008; Müller & Lobanov 2023; Wakker & Schwarz 1988) to the advanced regularized maximum likelihood (Chael et al. 2018, 2016; Müller & Lobanov 2022) and bayesian methods (Arras et al. 2021a).

Visibility model fitting

Since the beginning of the operation of the interferometry technique in astronomy, simple analytical models have been fitted into the visibility data. Even now, with a good-sampled uv-plane and the quality of the data, sometimes it is useful to fit the model directly to the visibility function. Imaging algorithms produce a model of a brightness distribution that can fit the visibility data. Analysing the obtained map can be characterised as "modelling the model". In addition, it is a very useful instrument in the determination of the changes in parameters of a source with time in the observations with not identical uv-coverage. And, of course, if the imaging is complicated and not robust, fitting the visibility with different models and comparing can help reveal the structure of an object. Since the real and imaginary parts of the visibility usually have a Gaussian noise, the χ^2 criterion is optimal for the fitting. In this case, it minimises the weighted mean-squared difference between the model and the data set with N points:

$$\chi^2 = \sum_i^N \frac{[\mathcal{V}(u_i, v_i) - \mathcal{V}_{\rm model}(u_i, v_i, \vec{p})][\mathcal{V}(u_i, v_i) - \mathcal{V}_{\rm model}(u_i, v_i, \vec{p})]^*}{\sigma_i^2}, \qquad (1.2.32)$$

where $\mathcal{V}_{\rm model}(u_i, v_i, \vec{p})$ are model visibilities with N_p parameters in $\vec{p}$, and σ_i are the measurement errors. The good fit is reached when the reduced chi-square is close to unity $\chi_{\rm r} = \chi^2/(N - N_p) \sim 1$.

Bayesian imaging

Bayesian imaging is a probabilistic approach using Bayes' theorem (Bayes & Price 1763). Using formulation Equation 1.2.33, the output of the imaging algorithm is not a single image but instead the posterior probability distribution for the sky $I(x, y)$ from the incomplete visibility data $V_{ij}(t)$. The posterior distribution of the image I given the data V can be calculated via Bayes' theorem:

$$\mathcal{P}(I|V) = \frac{\mathcal{P}(V|I)\,\mathcal{P}(I)}{\mathcal{P}(V)}, \qquad (1.2.33)$$

where $\mathcal{P}(V|I)$ is the likelihood, $\mathcal{P}(I)$ is the prior, and $\mathcal{P}(V) = \int \mathcal{D}I\, \mathcal{P}(V|I)\, \mathcal{P}(I)$ the evidence as a normalization constant. In the case of Bayesian image reconstruction, the evidence involves an integral over the space of all possible images, hence $\int \mathcal{D}I \ldots$ indicates a path integral.

Since the probability is calculated in each pixel, it is difficult to visualise $\mathcal{P}(I|V)$. Therefore, the summary statistics can be used: the posterior mean

$$m = \langle I \rangle_{\mathcal{P}(I|V)} \tag{1.2.34}$$

and standard deviation

$$\sigma_I = \sqrt{\langle (I-m)^2 \rangle_{\mathcal{P}(I|V)}}, \tag{1.2.35}$$

where $\langle f(I) \rangle_{\mathcal{P}(I|V)} := \int \mathcal{D}I\, f(I)\, \mathcal{P}(I|V)$ is the posterior mean of $f(I)$.

In Bayesian imaging, the knowledge about the source and instrument, such as the positivity of flux density, can be included in the prior. All additional information helps an algorithm to obtain reasonable images. For example, in the case when it is known that the imaged source has diffuse emission, it can be well described by a smoothness prior on the brightness of nearby pixels. In other words, we can encode the smoothness constraints in the prior, which is a reasonable assumption for diffuse emission.

The likelihood $\mathcal{P}(V|I)$ can be redefined by obtaining

$$\tilde{V}_{i,j}(t) = g_i(t) g_j^*(t) W(t) [\mathbb{F} I] + n_{ij}(t) \Leftrightarrow \tilde{V} = RI + n, \tag{1.2.36}$$

where $g_i(t)$ and $g_j(t)$ are station-based gains, R is the interferometer response function, and n is thermal noise, which is assumed to be Gaussian. Therefore, the likelihood $\mathcal{P}(V|I) = \mathcal{P}(V|\tilde{V})$. Bayes' theorem is often rewritten in terms of a statistical field theory by defining the information Hamiltonian (Enßlin 2019):

$$\mathcal{P}(I|V) = \frac{e^{-\mathcal{H}(V,I)}}{\mathcal{Z}(V)}, \tag{1.2.37}$$

where $\mathcal{H}(V,I) = -\ln\big(\mathcal{P}(V,I)\big)$ is the information Hamiltonian, which is the negative log probability, and $\mathcal{Z}(V) = \int \mathcal{D}I\, e^{-\mathcal{H}(V,I)}$ is the partition function. Since the noise is assumed to be Gaussian, uncorrelated with time and different baselines, the likelihood Hamiltonian can be interpreted as the data fidelity term:

$$\mathcal{H}(V|I) \;=\; \frac{1}{2} \sum_n \frac{|V_n - (RI)_n|^2}{\sigma_n^2} = \frac{1}{2}\, \chi^2. \tag{1.2.38}$$

Thus, the posterior information Hamiltonian

$$\mathcal{H}(I|V) \equiv -\ln\big(\mathcal{P}(I|V)\big) = \mathcal{H}(V|I) + \mathcal{H}(I) - \mathcal{H}(V). \tag{1.2.39}$$

Many methods, such as Markov chain Monte Carlo (MCMC) and Hamiltonian Monte Carlo (HMC), allow the search of the posterior. However, these methods are computationally expensive, especially in imaging. Another method is to calculate the maximum a posteriori (MAP) estimation, searching for the mode of the posterior distribution. This method is very efficient and fast. However, this method does not provide the estimation of uncertainties itself. In addition, MAP can be trapped in the local minima without exploring the parameter space. The `resolve` imaging algorithm used in this thesis is based on variational inference methods, which provide a local approximation of the posterior with a Gaussian and is able to estimate uncertainty (Frank et al. 2021b; Knollmüller & Enßlin 2019). These inference methods are a good balance between the speed of MAP and the accuracy of MCMC or HMC methods.

Self-calibration

After the calibration discussed earlier, residual gain errors remain in the data. Since the source structure and residual gains impact the visibilities of the science target, we need to take the source structure into account during the fine-calibration of the gains. This is called self-calibration. The main idea of self-calibration is minimising the difference between the observed visibility and the model visibility by tweaking complex gains:

$$\min \left| \sum_k \sum_{pq} w_{pq}(t_k)[V_{pq}^{\mathrm{obs}}(t_k) - g_p(t_k) g_q^*(t_k) V_{pq}^{\mathrm{model}}(t_k)] \right|^2. \tag{1.2.40}$$

One way to help the minimisation and constrain the search is to use closure quantities. The observed visibility can be written as $V_{pq}^{\mathrm{obs}} = g_p g_q^* V_{pq}$. First, phase relationships can be considered. Thus, in terms of phases:

$$\phi_{pq} = \phi_p - \phi_q + \phi_{vpq}, \tag{1.2.41}$$

where the minus behind ϕ_q is occurred due to g_q^* is a complex conjugate, and ϕ_{vpq} is the visibility phase $\mathcal{V}_{pq}$. For three antennas p, q, k the phase closure is a sum:

$$\begin{aligned}\phi_{Cpqk} &= \phi_{pq} + \phi_{qk} + \phi_{kp} \\ &= \phi_p - \phi_q + \phi_{vpq} \\ &\phi_q - \phi_k + \phi_{vqk} \\ &\phi_k - \phi_p + \phi_{vkp} \\ &= \phi_{vpq} + \phi_{vqk} + \phi_{vkp}.\end{aligned} \tag{1.2.42}$$

Therefore, phase closure depends only on the source structure and is independent of the atmospheric and instrumental effects represented by gains. In addition to the phase, there is a relationship for the amplitudes:

$$\frac{|r_{pq}||r_{mn}|}{|r_{mp}||r_{nq}|} = \frac{|\mathcal{V}_{pq}||\mathcal{V}_{mn}|}{|\mathcal{V}_{mp}||\mathcal{V}_{nq}|}. \tag{1.2.43}$$

In this case, four antennas are required to obtain the amplitude closure quantity. Thompson et al. (2017) is referred here for more detailed reading.

Self-calibration can be performed for data with good enough SNR; otherwise, it may produce spurious structures. For the phase self-calibration, SNR > 3 for all baselines for a single antenna is required. The main procedure consists of cycles, where: `CLEAN` model is created, phase self-calibration is applied, and the model is cleaned before starting the next iteration. To help the algorithm to deconvolve and self-calibrate only on the well-trusted areas on the map, the `CLEAN` windows are used, which are defined manually. Each cycle decreases noise, and the cycles are repeated until saturation is reached.

Typically, the noise is decreased up to this point so that amplitude self-calibration can be applied. This time, the requirement is SNR > 10. Amplitude corrections are more dangerous in terms of generating spurious structures. The self-calibration cycle is updated, and amplitude corrections are added after rounds of phase calibration. In every iteration step, the solution interval is decreased from the whole observation to minutes. The complete algorithm is also presented in the diagram of Figure 1.31. With iterations, a new structure will appear. Therefore, during cleaning, it is necessary to be cautious and put `CLEAN` windows only where the source is expected. If the source is complex and it is not trivial to understand the nature of the appeared component, it is better to avoid including it by putting windows. If the component persists at the end of the self-calibration, it is a strong indication to include this feature and repeat the self-calibration from the beginning. The knowledge about the *uv*-coverage and the dirty beam pattern can also help identify spurious features. The diagnostics of the visibilities and dirty image can be found in greater detail in Thompson et al. (2017).

1.3 Active Galactic Nuclei

At the beginning of the 20th century, astronomers started to study the origin of observed nebulae. The main question was whether all nebulae were relatively nearby gaseous objects or distant collections of unresolved stars. To answer this question, Fath (1909) conducted a series of observations at Lick Observatory with a self-made spectrograph, which could extract spectra from faint objects. The continuum spectrum of unresolved stars was found for most objects, suggesting a collection of unresolved stars. However, in the case of NGC 1068, Fath observed a spectrum with bright emission and absorption lines. Later, more observations showed spirals with stellar nuclei with a planetary nebula-type spectrum like NGC 1068, 4051, and 4151 (Hubble 1926; Humason 1932; Mayall 1934; Slipher 1917). The systematic study of galaxy nuclei started with Seyfert (1943), who obtained spectrograms of six galaxies with bright, nearly stellar point source-like nuclei showing wide emission lines superimposed on a normal Solar-like spectrum. The width of the lines suggested speeds up to 8,500 $\mathrm{km\,s^{-1}}$, which was not observed in the arms of spiral galaxies or irregular galaxies. Nowadays, galaxies with high excitation nuclear emission lines are called "Seyfert galaxies" (An example image and spectrum of a Seyfert galaxy is presented in Figure 1.35 and Figure 1.36).

The term "Active Galactic Nuclei" or AGN was first introduced by Viktor Ambartsumian in the 1950s (see historical review by Israelian (1997)). In his famous report at the Solvay Conference on Physics (Brussels 1958), Armbartsumian said that enormous explosions take place in galactic nuclei and as a result a huge amount of mass is expelled. In addition, these galactic nuclei must contain bodies of huge mass and of unknown nature. The concept of AGN seemed to be too fantastic for the scientific audience. Nevertheless, it was widely accepted a few years later. One of the students of Ambartsumian, Benjamin Markarian, completed a survey of galaxies with UV excess using the 1-m Schmidt telescope of the Byurakan Observatory. The nuclei of galaxies he observed were blue, which did not match the rest of the galaxy. Spectrum showed that continuum is produced by non-thermal mechanism (Markarian 1963, 1967).

Further development in the AGN study is tightly connected with advances in radio astronomy. In the beginning, radio telescopes' resolution was inferior compared to optical ones. The numerous point-like sources discovered in radio bands were considered radio stars. With the construction of the first interferometers, the optical identifications of radio objects were achieved (Bolton et al. 1949). The "radio stars" survey (Ryle et al. 1950) showed pretty uniform distribution in the sky, already hinting at the extragalactic origin of these "stars". Accurate position of four discrete sources by Smith (1951) allowed to make optical iden-

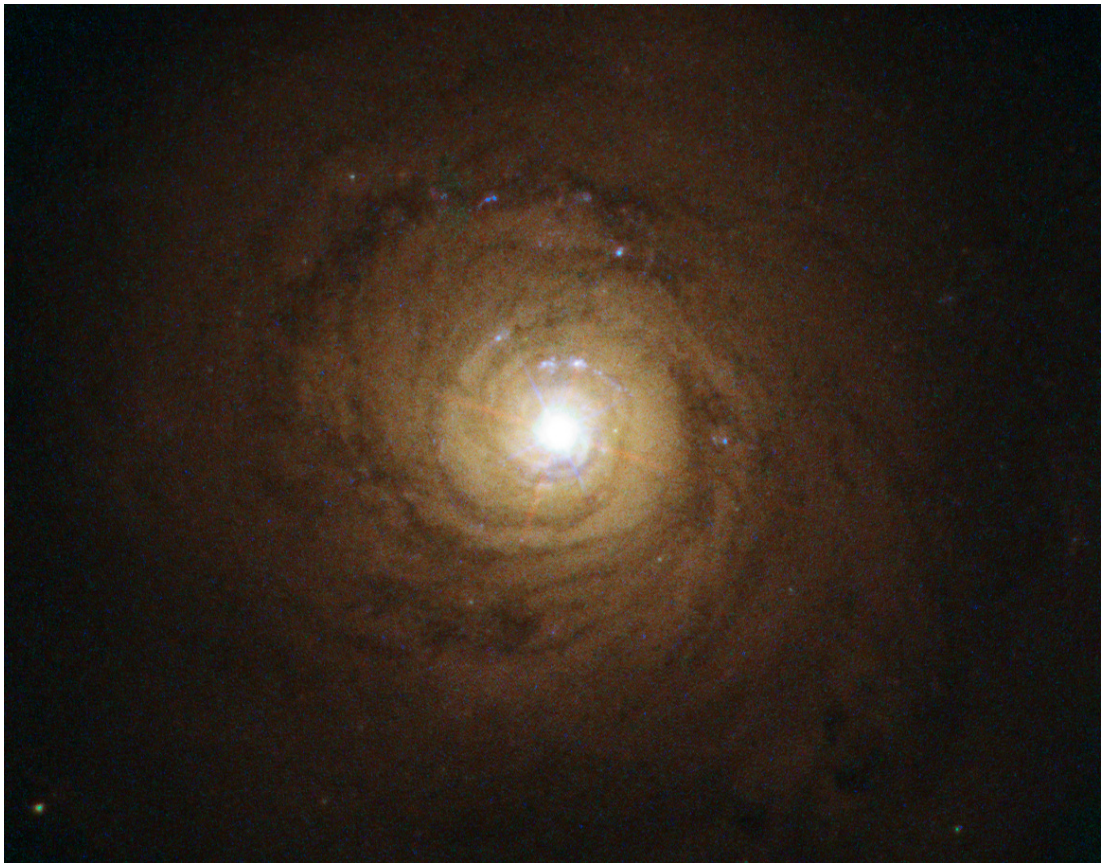

Figure 1.35: A Seyfert 1 galaxy NGC 5548, where the bright nucleus shows a stellar, point-like nature by the diffraction pattern of the telescope. Credit: ESA/Hubble.

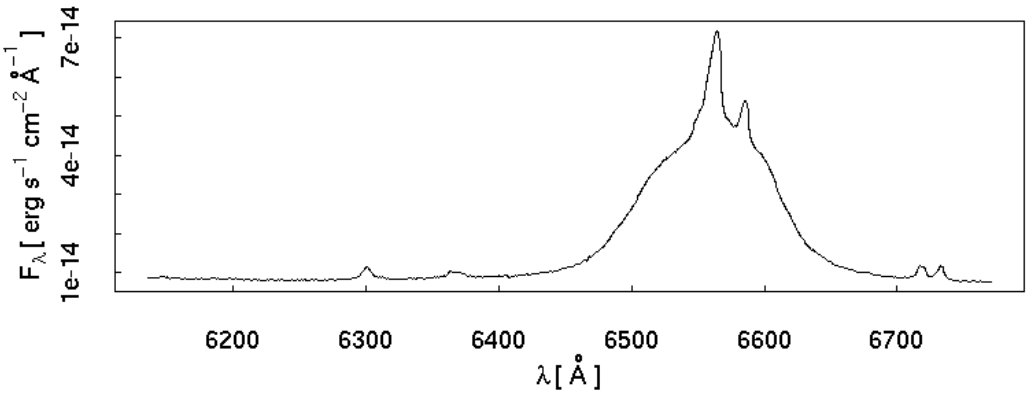

Figure 1.36: Optical spectrum of the Seyfert 1 NGC 5548 nucleus made by The Hale Telescope at the Palomar Observatory. The brightest lines in the spectrum are hydrogen and nitrogen lines H_α $\lambda = 6563\,\text{Å}$ and N II $\lambda = 6583\,\text{Å}$. The full width at half maximum (FWHM) of the broad lines is $5900\,\text{km}\,\text{s}^{-1}$, and of the narrow components, $400\,\text{km}\,\text{s}^{-1}$. Credit: NASA/IPAC Extragalactic Database, Ho et al. (1995)

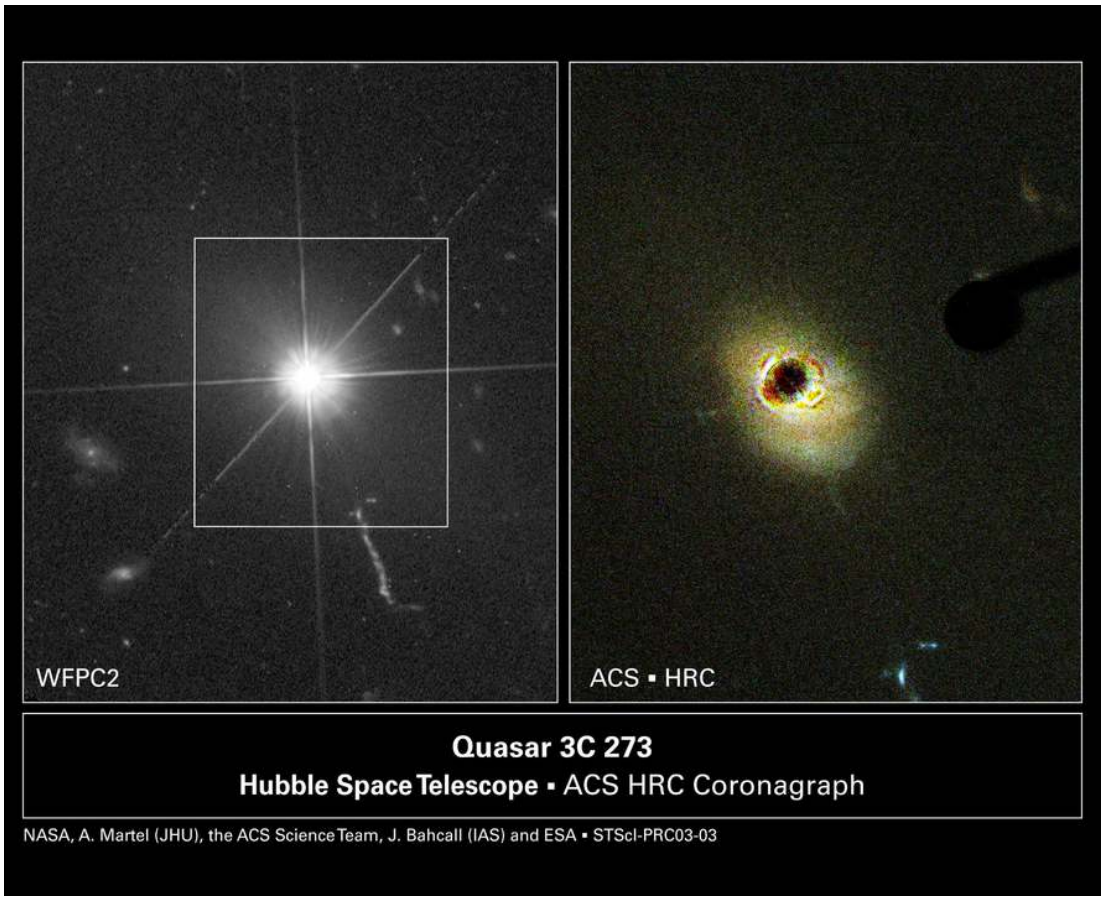

Figure 1.37: Left: Optical image of a quasar 3C 273. Right: The point-source subtracted image, which shows the host galaxy. Credit: WFPC2 image: NASA and J. Bahcall (IAS); ACS image: NASA, Martel et al. (2003), the ACS Science Team and ESA.

tifications of Cassiopeia, Cygnus A, and Puppis A (Baade & Minkowski 1954). Redshift measured for Cygnus A suggested a very large distance of 31 Mpc with a Hubble constant assumed $H_0 = 540\,\mathrm{km\,s^{-1}\,Mpc^{-1}}$. This led to the enormous radio luminosity of $L_{\mathrm{radio}} = 8 \times 10^{42}\,\mathrm{erg\,s^{-1}}$, which was larger than optical one $L_{\mathrm{optical}} = 6 \times 10^{42}\,\mathrm{erg\,s^{-1}}$. Morris et al. (1957) estimated upper limits on sizes of five radio sources, including Cassiopeia A and Cygnus A. Observed small angular sizes with an extreme brightness temperature of about 10^8 K suggested non-thermal mechanism of emission. First, the Galactic radio background was explained by synchrotron radiation (Alfvén & Herlofson 1950; Ginzburg 1951; Kiepenheuer 1950). Later, it was adopted for extragalactic discrete sources.

In some cases, an identification led to point-like optical sources named quasi-stellar objects (QSO) or quasars (quasi-stellar radio sources). Slish (1963) estimated the angular size of "radio stars", which greatly exceeded the angular diameter of stars and concluded that these objects could not be considered stars. Shklovskii (1964) estimated masses and sizes of envelopes of "radio stars" and

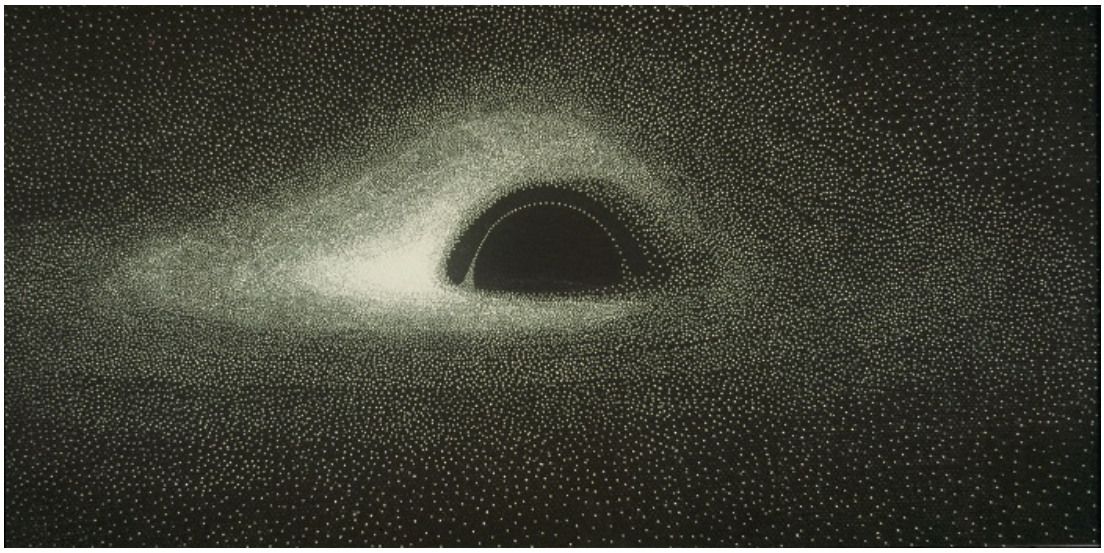

Figure 1.38: A simulated photograph of the spherical black hole with a thin accretion disc and a photon ring. Credit: Luminet (1979).

concluded that these objects are remnants of ultramassive bodies. Together with the redshift measurements, it was understood that these objects hold enormous power, orders of magnitude above that of other observed galaxies (Greenstein 1963; Greenstein & Schmidt 1964; Schmidt 1963). Observed radio components far away from the nucleus started discussions on the nature and origin of radio galaxies, according to which the components are "plasmons" that are launched from the nucleus periodically depending on the galaxy evolution state (De Young & Axford 1967; Shklovskii 1963a,b). It was hard to explain the nature of these objects by their stellar origin. Thus, an accreting black hole in the nucleus of a galaxy was suggested as a main actor producing observed emission and morphology (Lynden-Bell 1969a; Salpeter 1964; Zel'dovich 1964). Shklovskii (1966) showed that quasars and Seyfert galaxies are the same object types. Later, it was confirmed that all of them are active galactic nuclei. The host galaxy can be unrevealed after subtracting a point source from an image like in Figure 1.37. However, for a long time, astronomers only dreamed of seeing the image of the vicinity of a black hole. Surprisingly, early computer simulations were started in the late 1970s with Luminet (1979), who obtained a simulated photograph of the spherical black hole with a thin accretion disc. Figure 1.38 shows the collection of points drawn by hand from the numerical simulation results, where the points' density shows the image's brightness. Strikingly, this early result, despite the computational limitations of that time, is in remarkable agreement with today's simulations. For instance, the widely popularised artist's impression of a Black Hole in the "Interstellar" movie by Christopher Nolan, based on modern numerical simulation (James et al. 2015), is almost identical. The first indirect confirmations

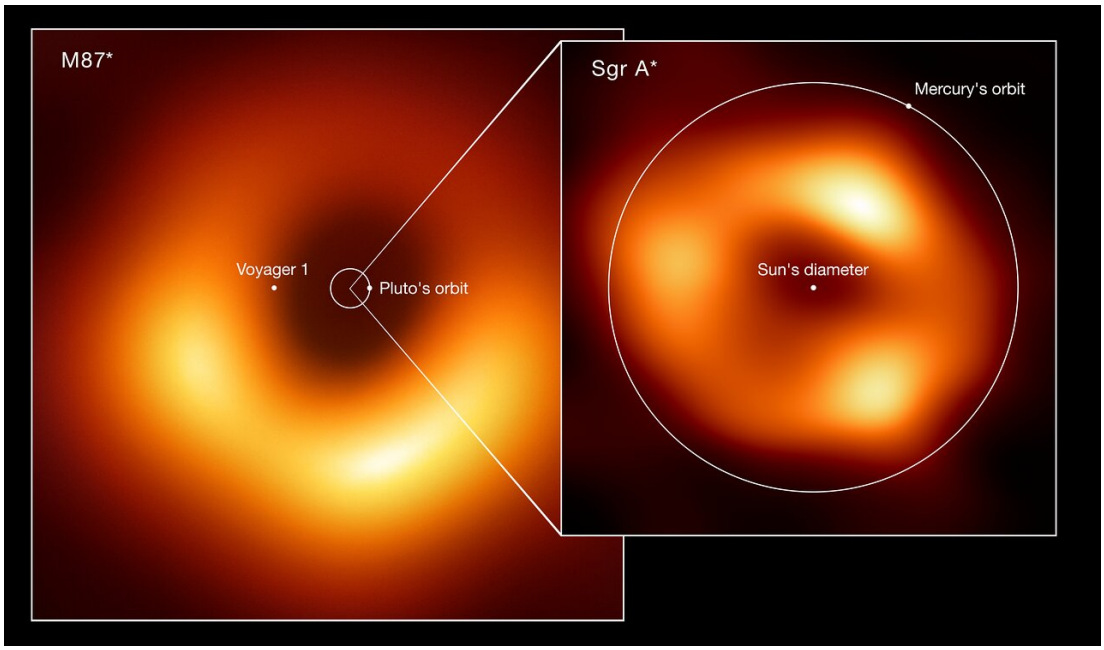

Figure 1.39: Size comparison of black hole shadows of Messier 87* (left) and Sagittarius A* (right) observed by the Even Horizon Telescope. The figure shows the scale of the shadows compared to the elements of the Solar System, such as the orbits of Pluto and Mercury, and the distance between the Sun and Voyager spacecraft. Credit: EHT collaboration (acknowledgement: Lia Medeiros, xkcd).

of the black hole's existence and location in our galaxy were done by measuring the kinematics of stars close to the gravitating centre (Genzel et al. 1997; Ghez et al. 1998). The authors of the papers obtained the Nobel Prize in Physics 2020[11] together with Roger Penrose. Twenty years later, the first-ever black hole images were observed at 230 GHz in the M87 galaxy and the centre of our galaxy (Event Horizon Telescope Collaboration et al. 2022, 2019c). The images show a black hole "shadow" predicted by the theory of relativity (Einstein 1916) with a central depression on the images (Figure 1.39). Moreover, linear and circular polarisation was detected, which constrained the magnetic field, its strength and the connection to the jet launching mechanism (Event Horizon Telescope Collaboration et al. 2024, 2023, 2021). Due to scattering effects, observing the ring at lower frequencies is complicated. For example, the RadioAstron SVLBI mission at 22 GHz can resolve the black hole shadow in the M87 galaxy but instead discovered a scattering substructure: a new type of scattering. The same was expected for 86 GHz for GMVA, but Lu et al. (2023) showed the first image of the ring with the relativistic jet (Figure 1.40).

According to Galaxy statistics, 10% of them are active and have an AGN. Galaxy evolution studies suggest that all galaxies go through an active phase, during which powerful collimated relativistic plasma outflows are produced in

[11] `https://www.nobelprize.org/prizes/physics/2020/summary/`

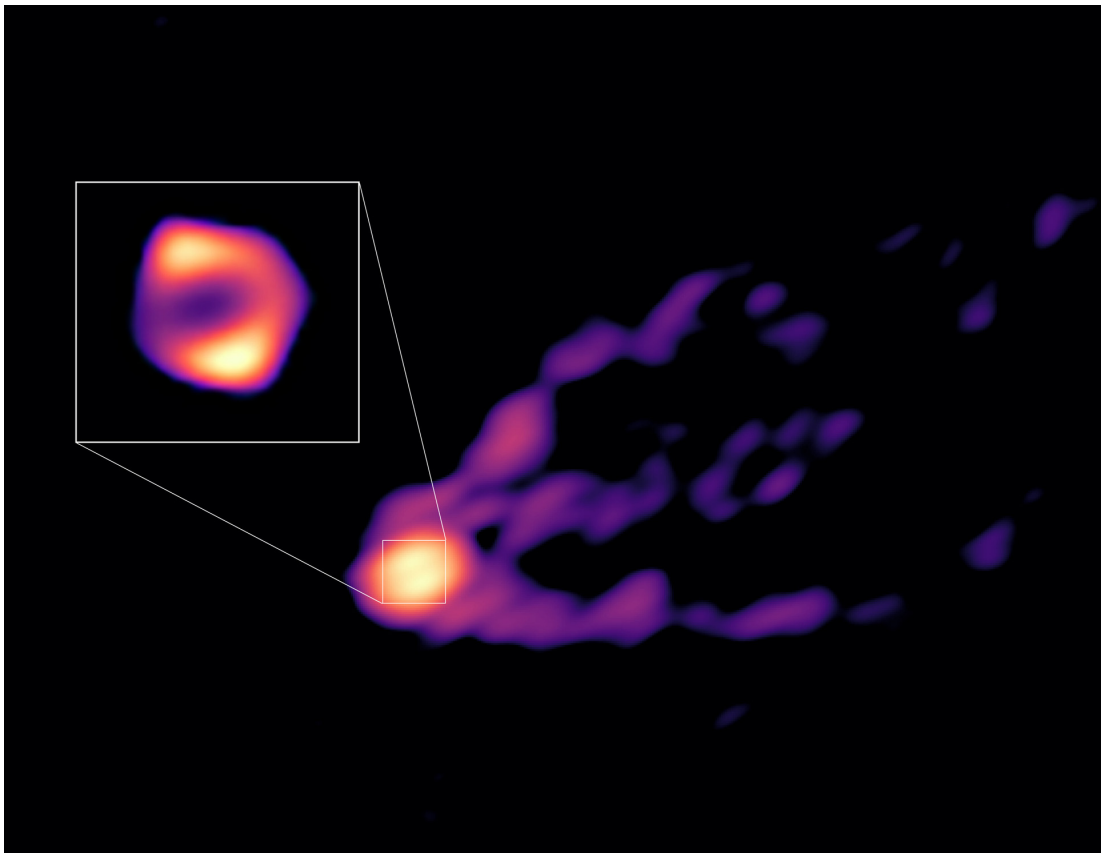

Figure 1.40: A ring-like structure in M87 connecting its black hole and jet. Credit: Lu et al. (2023), SHAO / E. Ros, MPIfR / S. Dagnello, NRAO, AUI & NSF.

the fraction of AGN. These jets play a critical role in the galaxy's evolution and intergalactic medium and propagate up to distances of kilo- and megaparsecs (Blandford et al. 2019; Morganti 2017). Recently, the largest AGN jet was discovered by the International Lofar Telescope (ILT) and upgraded Giant Metrewave Radio Telescope (uGMRT) (Oei et al. 2024). The length of the jet from the Porphyrion galaxy reaches a record 7 Mpc. The active galaxies have extreme luminosities up to $L \sim 10^{48}\,\mathrm{erg\,s^{-1}}$, which is produced by thermal and non-thermal mechanisms. Depending on the class of AGN, the dominant mechanism and frequency band can be different; nevertheless, observed spectra are broadband and cover all frequencies from radio to γ-rays. Recently, AGN was associated with neutrino events, opening a multi-messenger window. The first neutrino from AGN was observed by the IceCube observatory and associated with TXS 0506+056 (IceCube Collaboration et al. 2018). Later, a statistical study resulted in a connection of neutrino and a sub-class of AGN named blazars (Plavin et al. 2020). For a more detailed historical review, the reader is suggested to proceed with Combes (2021); Kellermann (2015); Shields (1999).

1.3.1 Classification and unification

Classification is always needed to understand and sort all knowledge about observed objects. A successful example of the approach is the Morgan–Keenan (MK) stellar spectral classification (Morgan et al. 1943). Active galactic nuclei (AGN) are a more diverse phenomenon than stars. In contrast to stars, AGN emits a vast range of frequencies from radio to gamma rays. Therefore, there are a lot of different classifications of AGN, which are based on radio luminosity, morphology, spectrum, and orientation. The main observational classification is AGN's division into two classes, "radio-loud" and "radio-quiet" (Kellermann et al. 1989; Strittmatter et al. 1980). The criteria for this division is defined by the parameter $R = f_{5\,\mathrm{GHz}}/f_{\mathrm{B}}$, where f are corresponding fluxes at 5 GHz and in the optical B band. Radio-quiet AGN, for which the parameter is below ten $R < 10$, mainly split into Seyfert galaxies of types 1 and 2 depending on the spectra, i.e. emission lines. Despite the attempt to systematise knowledge by this classification, there is a fair claim that it is not good to classify objects based on observational parameters rather than physically based one (Padovani 2017). Therefore, nowadays, the definition shifts to "jetted" and "non-jetted" AGN, first proposed by Padovani (2016).

Seyfert galaxies

Seyfert galaxies have bright quasar-like nuclei whose spectra have high-ionisation emission lines. They have very luminous nuclei with luminocities $L \sim 10^{44}\,\mathrm{erg\,s^{-1}}$.

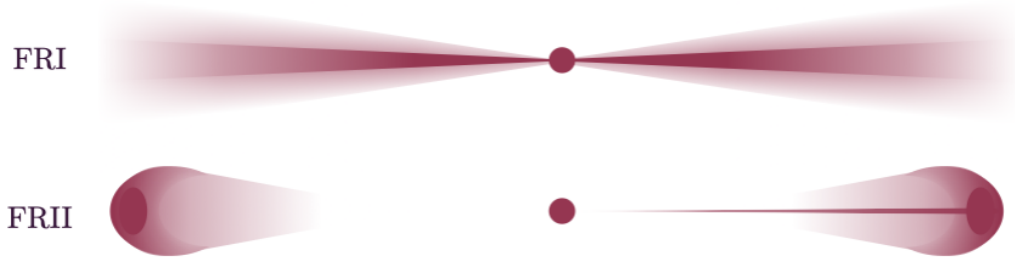

Figure 1.41: Morphological difference between Fanaroff and Riley Class I (FR I) and Class II (FR II). Credit: Emma L. Alexander.

Typically, Seyfer galaxies are non-jetted, low-redshift spiral galaxies.

- **Type 1 Seyfert galaxies** show broad and narrow emission lines. The line width is broadened due to Doppler motion. Typical width for broad lines is about $5\,000\,\mathrm{km\,s^{-1}}$. Although the spectral lines observed are narrow, they are broader than normal galaxies and show width up to $1\,000\,\mathrm{km\,s^{-1}}$. The source of broad lines is highly ionised gas above the accretion disc closer than one parsec to the supermassive black hole. The narrow lines are formed farther from the black hole in the accretion disc. In addition, they are bright at high frequencies in UV and X-rays.

- **Type 2 Seyfert galaxies** are less luminous than Seyfert 1 galaxies, showing bright infrared nuclei and only narrow lines. There is am evidence that Seyfert 2 galaxies are obscured Seyfert 1s and possibly connected via inclination angles (Blandford et al. 1990). This explained the necessity of having the intermediate Seyfert types (Osterbrock 1981).

Radio galaxies

Radio galaxies are active galaxies with powerful radio emissions produced by the relativistic jets and their interaction with the intergalactic medium on scales of megaparsecs. Typically, their host galaxies are elliptical. The first relativistic outflow was observed for the giant elliptical galaxy M87 by Curtis (1918) by an optical telescope. Unlike Seyfert galaxies, they do not show Doppler broadened lines since the emission from the broad-line clouds is obscured by a dusty torus being observed edge-on. Synchrotron radiation from the jet is observed at a vast range of frequencies. An optical jet, for example, is also visible in 3C 273 on the southwest corner of the left image of Figure 1.37. However, in the radio band, this structure is dominant. In the 1970s, when high-resolution interferometry was

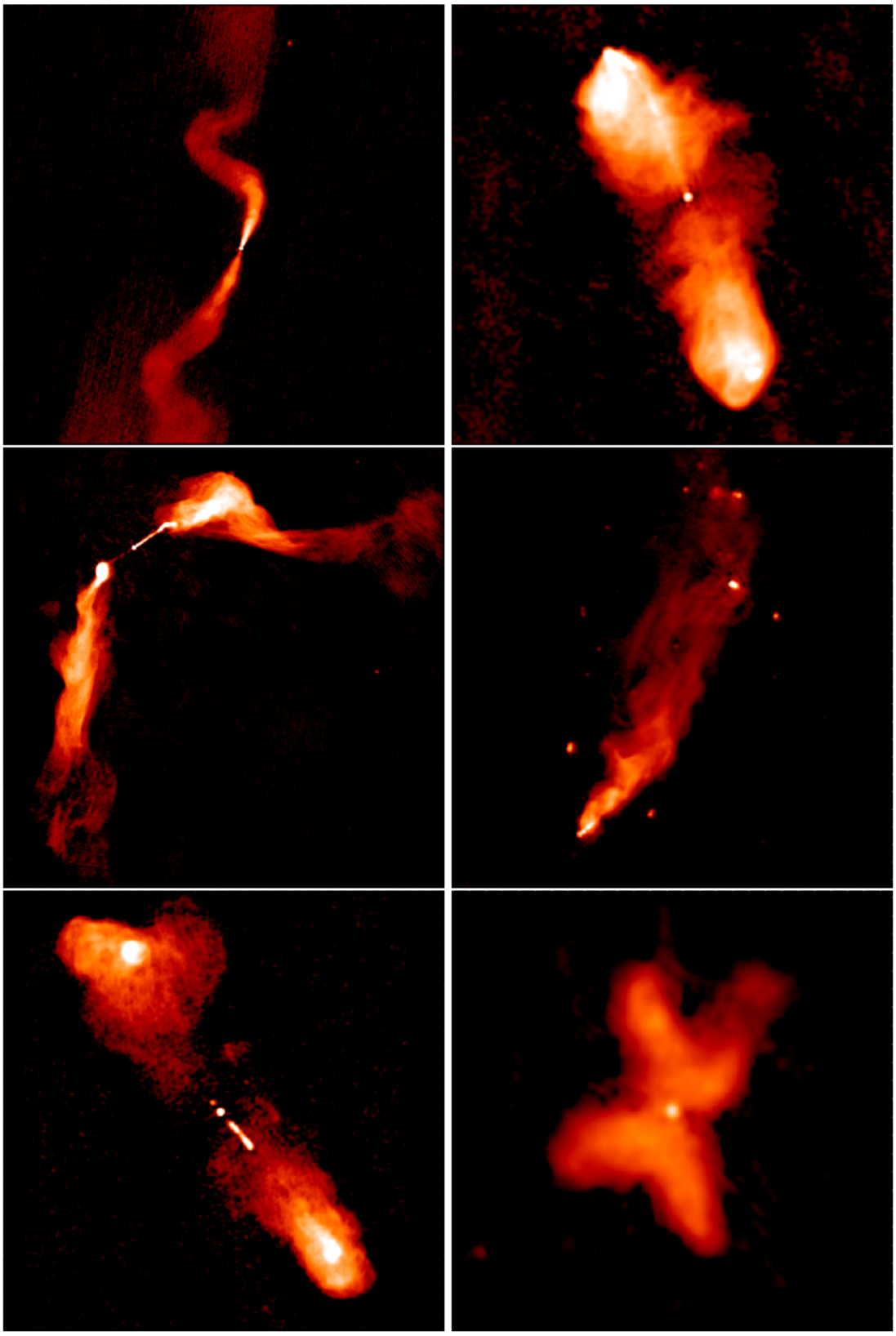

Figure 1.42: Jets of radio galaxies. The top row is the Fanaroff-Riley class I source 3C 31 (left) and the Fanaroff-Riley class II source 3C 98; the middle row is 3C 465 (left) and NGC 6109 (right); and the bottom row is 3C 219 (left), and 3C 315 (right). Credit: Robert Laing, "Atlas of DRAGNS", Emmanuel Bempong-Manful, Clarke et al. (1992), NGC 6109 and 3C 315 from unpublished LOFAR data (Hardcastle & Croston 2020).

available with NRAO Very Large Array (VLA), the morphology of radio galaxies started to be studied. Bernard Fanaroff and Julia Riley divided radio sources into two classes: Fanaroff and Riley Class I (FR I) and Class II (FR II) (Fanaroff & Riley 1974).

- **FR I**: initially strong jets that decrease in luminosity with the distance from the central engine; center-brightened, low-power radio galaxies with weak radio lobes.

- **FR II**: a bright core and low-luminosity jets; edge-brightened, high-power radio galaxies with radio lobes showing strong hotspots.

The classification was concentrated at flux at 1.4 GHz, where FR I sources are weaker than FR II galaxies, which is explained by the black hole mass and the disk accretion power (Ghisellini & Celotti 2001). The morphological differences between FR I and FR II galaxies are seen in detain in Figure 1.41 and in real examples in Figure 1.42. Recent simulations show that FR dichotomy can arise as a consequence of jet stability: powerful jets are more stable (Tchekhovskoy & Bromberg 2016).

Buttiglione et al. (2010) observed optical spectra of the 3CR sample of AGN and obtained a bimodal distribution in the proposed Excitation Index (E. I.). The spectroscopic indicator shows the relative intensity of low and high excitation emission lines. The authors of the paper speculate that this dichotomy can be related to the accretion mode. Nuclear properties separate radio galaxies into two classes:

- **Low-Excitation Radio Galaxies (LERGs)**: Relatively low luminosity provided by the kinetic energy of jets. Weak ionisation lines and the absence of high ionisation lines indicate weak and inefficient accretion occurred by Advection Dominated Accretion Flows (ADAF).

- **High-Excitation Radio Galaxies (HERGs)**: High luminosity occurs due to radiation cooling of matter surrounding the supermassive black hole. Strong high-ionisation lines indicate strong and effective accretion. The accretion is powered by "thin disc".

The connection to the morphology of these classes is not direct. All HERGs have FR II morphology, but LERGs can be FR I or FR II. Despite LERGs having lower luminosities than HERGs, some LERGs some LEGs are bright radio sources and have an FR II morphology, which can't be distinguished from HEGs. Therefore, besides the accretion mode, there should be other parameters which determine the classification of radio galaxies, like the jet interaction with the extragalactic medium (Hu 2018).

Quasars

Quasars or Quasi-Stellar Objects (QSO) are very luminous AGN sources with a high redshift. The power of the AGN is so high that it overshines the host galaxy, making it invisible without subtracting the nuclear influence like in Figure 1.37. In contrast to the radio galaxies, quasars show Doppler broadened lines (with FWHM $> 1\,000\,\mathrm{km\,s^{-1}}$, indicating that the accretion disc and the surrounding area are observed face-on with the jet aligned smaller than $\lesssim 45°$ to the line of sight.

Blazars

Blazar is an AGN with a relativistic jet oriented less than $\lesssim 20°$ to the line of sight. With such small viewing angles, the emission from the jet becomes dominant because of relativistic effects. Blazars show strong variability on timescales of month and days across the spectrum induced by the parsec-scale jets. This type of AGN emission is broadband and dominates radio and γ-ray sky (Padovani 2016). Recently, it was shown that blazars are the sources of cosmic neutrino (Plavin et al. 2020). There are two classes of blazars:

- **BL Lacertae** (BL Lac): characterised by weak emission lines. The class name was translated from the name of the source BL Lacertae, which was identified as a variable star. Later, the "star" was observed as a strong variable radio source (Schmitt 1968).
- **Flat-Spectrum Radio Quasars** (FSRQs): This class's bolometric luminosity is much higher than BL Lac objects and is characterised by strong emission lines.

Unification

The observational diversity of AGN puzzles and until the end of the 20th century, all these classes were considered different objects. Antonucci (1993) introduced a unified model for radio-quiet AGN, which successfully explained the difference between type 1 and type 2 Seyfert galaxies. Later, the proposed unified scheme was introduced to radio-loud AGN (Barthel 1989; Hardcastle et al. 1999; Urry & Padovani 1995). Today, it is believed that the different AGN are the same object observed with different viewing angles as presented in Figure 1.43.

1.3.2 AGN composition

The tremendous energy observed from the AGN arises from the gravitational energy released during the accretion, i.e., the process of a matter (gas and dust)

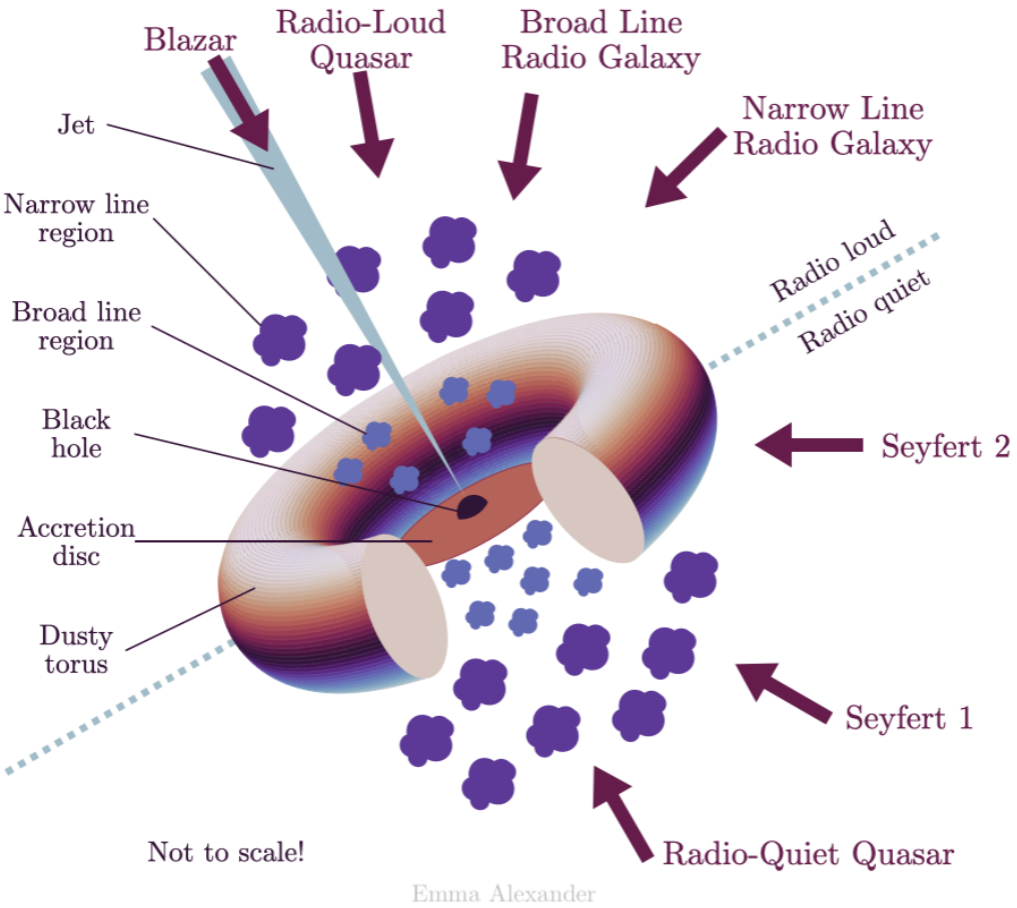

Figure 1.43: Unified scheme for AGN adapted from (Urry & Padovani 1995). The thick arrows show different viewing angles and the observed class of AGN. The upper left and lower right parts of the image, separated by a blue dashed line, represent radio loud and quiet AGN. Credit: Emma L. Alexander.

falling into the central object. Due to viscosity effects, the matter heats to enormous temperatures, forcing itself to glow by thermal radiation. The energy released due to this process is:

$$L_{\rm bol} = \eta \dot{M} c^2, \tag{1.3.1}$$

where $L_{\rm bol}$ is bolometric luminosity or luminosity across the entire spectrum, η is the efficiency of accretion, $\dot{M}$ is the mass accretion rate. Accretion is among the most effective processes of energy conversion. For example, nuclear reaction efficiency is only $\eta_{\rm nuclear} \lesssim 1\%$, when for the accretion can be up to $\eta \sim 40\%$.

However, luminosity cannot be arbitrarily high because of limits on the accretion rate $\dot{M}$. Indeed, according to Equation 1.3.1, with an increase in the accretion rate, increases luminosity and the radiation pressure will be strong enough to hold gravitational forces, limiting the accretion. The luminosity required to achieve a balance of forces is called the Eddington luminosity

$$L_{\rm Edd} \propto M, \tag{1.3.2}$$

where M is the mass of the central object. Combining Equation 1.3.2 with Equation 1.3.1, the upper limit on the mass accretion rate is

$$\dot{M} \propto M. \tag{1.3.3}$$

Therefore, the energy the AGN produces is proportional to the mass of the central massive object. Nevertheless, it is possible to observe sources with a luminosity that exceeds the Eddington limit. This is possible due to Super-Eddington accretion regimes, which exist under specific conditions, and the upper limit on accretion can be exceeded for brief periods.

As can be seen from Figure 1.43, AGN can be divided into four main parts: a supermassive black hole, the accretion disc, the torus, and the relativistic jet.

Supermassive black hole

The astonishing fact that many people forget is that the concept of a black hole was introduced in the 18th century (Montgomery et al. 2009). Michell (1784) suggested that if the star is big enough, the escape velocity on its surface is so high that the light will not escape it. As Michell stated, "..; all light emitted from such a body would be made to return towards it, by its own proper gravity." He called these objects "dark stars". Independently, Laplace (1799) introduced the concept of black holes and proved if mathematically (Laplace 1813). In their works, Michell and Laplace considered light to consist of "corpuscles" or particles which

behave and interact with gravity as usual bodies. However, after the discovery of light acting like a wave (Young 1802), it became unclear how gravity would affect the waves.

Only a century later, with Albert Einstein's General Relativity Theory (Einstein 1916) and the solution for a non-rotating and uncharged point mass proposed by Karl Schwarzschild (Schwarzschild 1916). This solution showed the presence of two singularities in the equations, one of which is at $R = 0$ and another one at the area now called the Schwarzschild radius:

$$R_{\rm S} = \frac{2GM}{c^2}. \tag{1.3.4}$$

Later, Eddington (1924) showed that the singularity disappeared after a change of coordinates. In 1933, Lemaître (1933); Lemaître & MacCallum (1997) showed that "the singularity of the field is not real and arises simply because one wanted to use coordinates for which the field is static." Despite the studies and solutions that were obtained, because of a lack of observational evidence, nobody believed in this concept, not even Einstein. Right before the Second World War started, Oppenheimer & Snyder (1939) published a paper where the authors apply the equations of general relativity to prove that a large enough star will continue contracting until it transforms into a black hole. In this paper, the authors interpreted the Schwarzschild radius as a boundary where time is stopped for an external observer but not for the infalling observer. Later, Finkelstein (1958) identified this surface as an event horizon. These collapsed stars were called "frozen stars". Today, this paper is considered to have one of the most significant impacts on the black hole study, but due to the War, culture and conceptual belief system of that time, the scientific community ignored the work until the late 1950s (Ortega-Rodríguez et al. 2017): the start of the Golden Age of black hole study. The work of Penrose (1965) was one of the classical papers which demonstrated that black holes are a direct consequence of general relativity. For this work, Roger Penrose, with Reinhard Genzel and Andrea Ghez (for discovering the black hole in the centre of our Galaxy), was awarded the Nobel Prize in Physics 2020[12].

A black hole is believed to have no hair. According to the hypothesis named "the no-hair theorem", a black hole can be completely characterized by only three independent parameters: mass, angular momentum, and electric charge (Carter 1971; Hawking 1972; Israel 1967; Robinson 1975). The total angular momentum J_a of the black hole can be parametrised via the dimensionless spin

$$a = \frac{cJ_a}{GM^2}. \tag{1.3.5}$$

[12] `https://www.nobelprize.org/prizes/physics/2020/summary/`

This parameter is defined from 0 to 1 for a non-spinning and maximally spinning black hole. The rotating black hole forces the surrounding space-time to move with it (Lense & Thirring 1918), creating an "ergosphere". Because of this effect, an object that appears stationary to an observer far away must have a speed higher than the speed of light. The surface, where the speed is equal to the speed of light, is called ergosurface. It has the shape of an ellipse, with a minor axis coinciding with the rotation axis of the black hole. Thus, the ergosphere coincides with the event horizon at the poles, and the distance increases between surfaces and the equatorial plane. From ancient Greek, the word "ergon" means "work". Its ergosphere is named like it because, theoretically, one can extract energy from a black hole from this region. This effect is relevant for AGN, where a particle can enter the ergosphere and escape with higher energy obtained from the black hole. In the case of strong magnetic fields, the ergosphere is the key to the formation of relativistic jets via the Blandford-Znajek process (Blandford & Znajek 1977a). Depending on their rotation and electric charge, there are different black hole configurations:

- **Schwarzschild black hole:** non-rotating object with no electric charge.
- **Kerr black hole:** rotating object with no electric charge,
- **Reissner-Nordström black hole:** non-rotating object with electric charge,
- **Kerr-Newman black hole:** the most general solution, with both rotation and electric charge

It is quite understood how stellar mass black holes are formed. It is either the collapse of a star or Tolman–Oppenheimer–Volkoff limit for neutron stars (Landau 1932; Oppenheimer & Volkoff 1939; Tolman 1939). However, these mechanisms do not explain the supermassive black holes observed in AGN. Shadows of two of them were observed for the first time in the M87 galaxy and the centre of our galaxy (Event Horizon Telescope Collaboration et al. 2022, 2019c). Typical black hole mass obtained from stars range from $\sim 5\,M_\odot$ to $\sim 20\,M_\odot$, when masses of supermassive black holes span from $\sim 10^5\,M_\odot$ to $\sim 10^{10}\,M_\odot$. It is believed that massive black holes are formed through two main channels: black hole merging and accretion. Today, these two channels are confirmed and observed. The black hole merger is directly observed by the detection of gravitational waves (Abbott et al. 2016), and signatures of accretion are even more prominent. Nevertheless, it still does not explain the formation of the most massive ancient black hole. For example, SDSS J0100+2802 with mass $M = 1.2 \times 10^{10}\,M_\odot$ and redshift $z = 6.236$ (Wu et al. 2015). To date, the question of supermassive black hole creation is one of the mysteries in astronomy. Even the accretion of Population III stars, which

are expected to be much larger than modern-age ones, does not help. The other possibility is the hypothetical class of primordial black holes, which is expected to be formed right after the Big Bang (Zel'dovich & Novikov 1967). But there is still no evidence of the existence of primordial black holes.

Accretion disk

In the simplest case, when an object propagates through a medium, it attracts the matter, which will fall into it. The process called Bondi accretion was formulated by Bondi (1952) and Bisnovatyi-Kogan et al. (1979); Hoyle & Lyttleton (1941); Salpeter (1964). However, when the inflowing matter has significant angular momentum, it will prevent the matter from falling directly into the object, but instead, gas spirals inward, creating an accretion disc. Gravitational energy of the matter can be released due to viscosity, and the amount of energy liberated that way is enormous (Bardeen 1970; Lynden-Bell 1969b; Salpeter 1964; Zel'dovich 1964). For example, Shklovsky (1967) explained X-ray emissions from Sco X-1 as accretion of matter from a companion onto a neutron star. The accretion discs model was later developed by accounting magnetic fields and viscosity by so-called "α-parameter" in the standard accretion disk model or simply the α-disk model (Lynden-Bell & Pringle 1974; Novikov & Thorne 1973; Shakura & Sunyaev 1973). It is interesting that all listed soviet authors (Shakura, Sunyaev, Novikov), pioneers in the development of the accretion theory, were collaborators of Y.B. Zel'dovich, whose influence was of extreme importance even if his name does not appear in these classical papers (Montesinos 2012). Being a thin accretion disc model, the Shakura-Sunyaev disc is radiatively efficient. Later, radiatively inefficient accretion flow and super-Eddington class discs were examined.

- **Thin Accretion Disc (Standard Shakura-Sunyaev Disc):** The disc is relatively cold ($\sim 10^2$–10^5 K), which means the effective transformation of energy into radiation. In addition, it is optically thick and geometrically thin (i.e., its vertical height is much smaller than its radial extent).

- **Radiatively Inefficient Accretion Flow (RIAF):** This is a broad term that refers to any accretion flow where most energy is not efficiently radiated away. It includes the following sub-classes:

  Advection-Dominated Accretion Flow (ADAF): The gas is so hot that it fails to radiate away most of the heat produced by accretion. Instead, most energy is advected (carried inward) toward the black hole with the accreting material. (Abramowicz & Lasota 1995; Narayan & Yi 1994).

Convection-Dominated Accretion Flow (CDAF): Energy is transported by convection rather than advection (Narayan et al. 2002; Quataert & Gruzinov 2000).

Outflow-Dominated: A large fraction of the energy is lost in outflows rather than being advected inward or radiated.

- **Slim discs:** Slim discs are optically and geometrically thick. They form when the accretion rate exceeds the Eddington limit. The radiation is inefficient since radiation is trapped inside (Abramowicz et al. 1988).

The main target source of this thesis is the M87 galaxy, which has a radiatively inefficient ADAF mode of accretion (Feng & Wu 2017; Lucchini et al. 2019; Prieto et al. 2016). Thus, it is important also to consider modes of accretion in hot, radiatively inefficient discs, which are based on magnetic field properties and orientation. The most favoured models in this case are:

- **Standard and Normal Evolution (SANE):** The accretion disk has relatively weak and disorganized magnetic fields.
- **Magnetically Arrested Disk (MAD):** The accretion disk is highly magnetised, and the magnetic field is so strong that it can resist the flow of accreting material.

Despite the magnetic field partly blocking matter from infalling to the black hole, turbulence and instabilities locally weaken the magnetic field, allowing the matter to accrete. However, globally, these effects increase magnetic fields, making them significantly stronger than the SANE scenario. A strong magnetic field achieved in MAD mode created a much more powerful jet, like the M87 (Event Horizon Telescope Collaboration et al. 2019a; Kino et al. 2022; Yuan et al. 2022).

Masers

In the thin molecular layer of the accretion disc of an AGN, some conditions form naturally occurring sources of stimulated spectral line emission. This is called a maser (an analogy to a laser) and is observed in the microwave part of the spectrum. The VLBI technique can resolve separate maser sources in the accretion disc, giving an opportunity to study their kinematics by measuring positions and Doppler shifts of the components. Together, all information can reveal the shape of the accretion disc and even the supermassive black hole mass. For example, water masers in the galaxy NGC 4258. In Figure 1.44, the best-fit model suggests a warped disk geometry. The Keplerian rotation curve traced by these masers requires a supermassive black hole of $M_{\rm SMBH} = (3.9 \pm 0.1) \times 10^7 M_\odot$

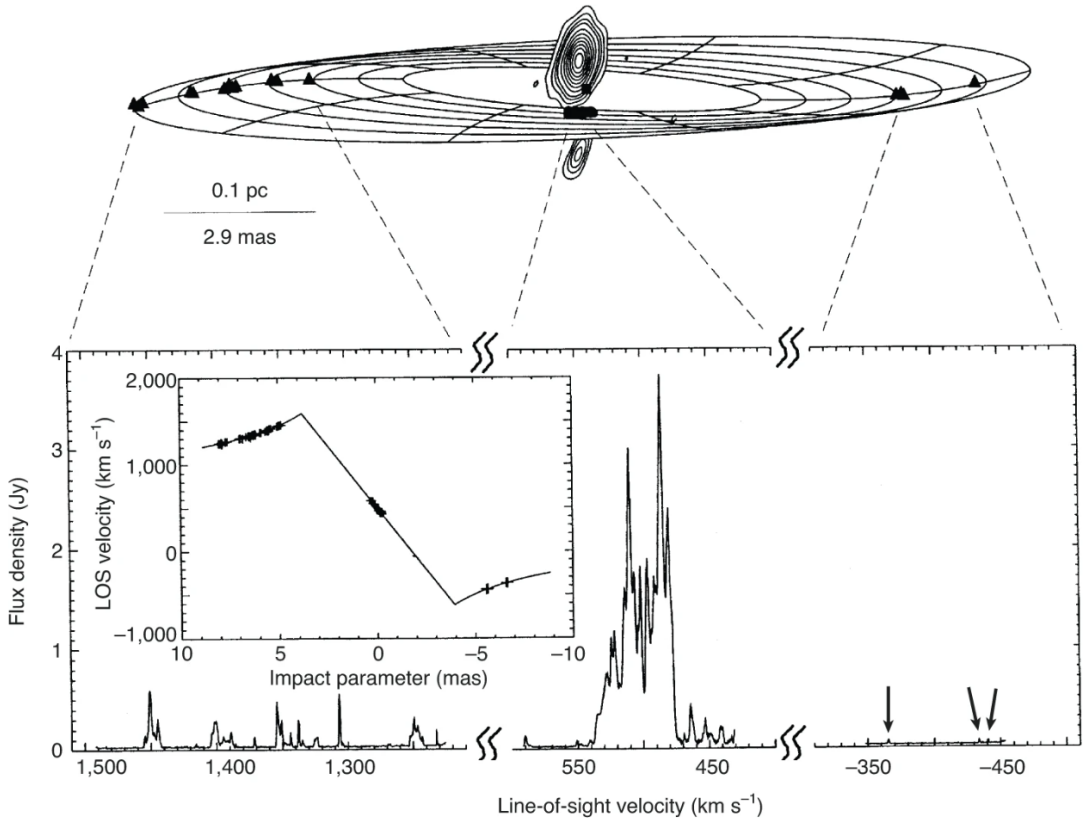

Figure 1.44: The NGC 4258 water maser. The upper panel shows the best-fit warped-disk model superposed on maser positions measured by the VLBA. Contours show the continuum image of the sub-parsec scale jet at 22 GHz. The filled triangles show the positions of the high-velocity masers with speed of around $\sim 1\,000\,\mathrm{km\,s^{-1}}$ with respect to the galaxy systematic velocity $\approx 470\,\mathrm{km\,s^{-1}}$. The lower panel show the apparent in the VLBA total power spectrum. The inset shows line-of-sight (LOS) velocity versus impact parameter for the best-fitting Keplerian disk. Credit: Herrnstein et al. (1999).

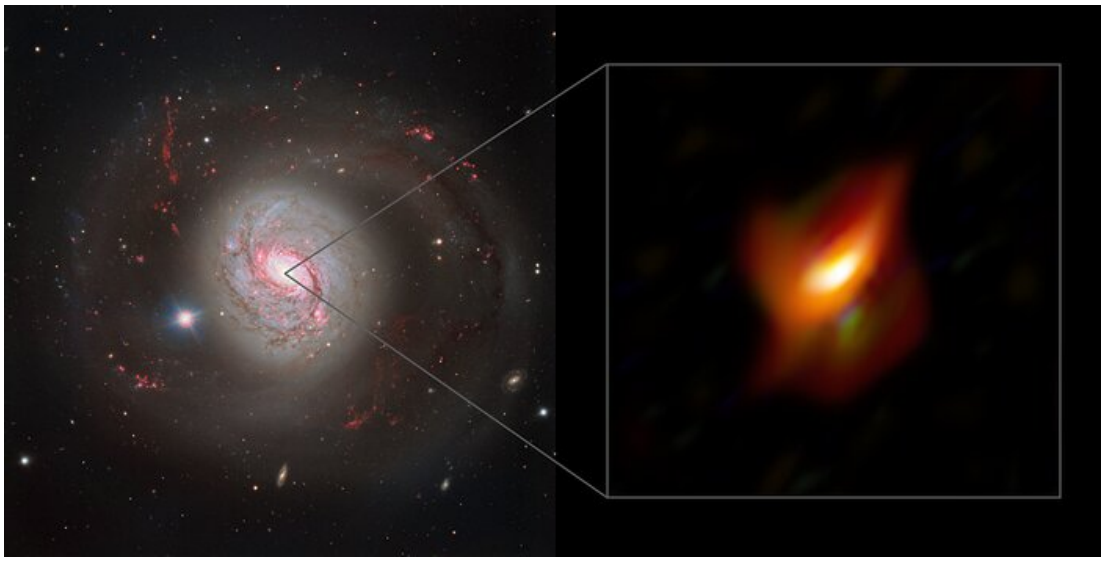

Figure 1.45: Left: NGC 1068 galaxy by Very Large Telescope (VLT). Right: Zoom in into the dusty torus of the galaxy nucleus observed by the MATISSE instrument on ESO's Very Large Telescope Interferometer (VLTI). Credit: ESO/Jaffe, Gámez Rosas et al. (2022).

(Herrnstein et al. 1999). In addition, masers in NGC 4258 indicate assurance of magneto-rotational instability (MRI), which supports the idea of shear-driven instability to be an agent for generating the viscosity in the disc as proposed nearly 50 years ago by Shakura and Sunyaev (Baan et al. 2022).

Dusty torus

The detection of polarised broad lines in the type 2 Seyfert galaxy NGC 1068 validated the unified model (Antonucci & Miller 1985). The emission from a type 1 Seyfert galaxy hidden from direct view will show the type 2 observational properties. But it is important to note that obscuration may arise not in the torus but on a large scale in the host galaxy (Goulding et al. 2012). The primary emission mechanism of the torus is thermal, which is why it is observed in the infrared (IR) bands.

The size of a torus is relatively small, and the first upper limit of less than $r < 2\,\mathrm{pc}$ was observed in the Circinus galaxy (Packham et al. 2005). This means that high-resolution observations better than $\sim 0''.3$ angular resolution are needed, which can be achieved by interferometry. Recently, the dust hiding the black hole in NGC 1068 was imaged with a resolution as high as three milliarcseconds by the MATISSE instrument on Very Large Telescope Interferometer (VLTI) (Gámez Rosas et al. 2022). The result of image reconstruction can be seen in Figure 1.45. Thermal radiation of the observed structure shows temperature as high as $684 \pm 17\,\mathrm{K}$. SED fitting revealed a chemical composition inconsistent

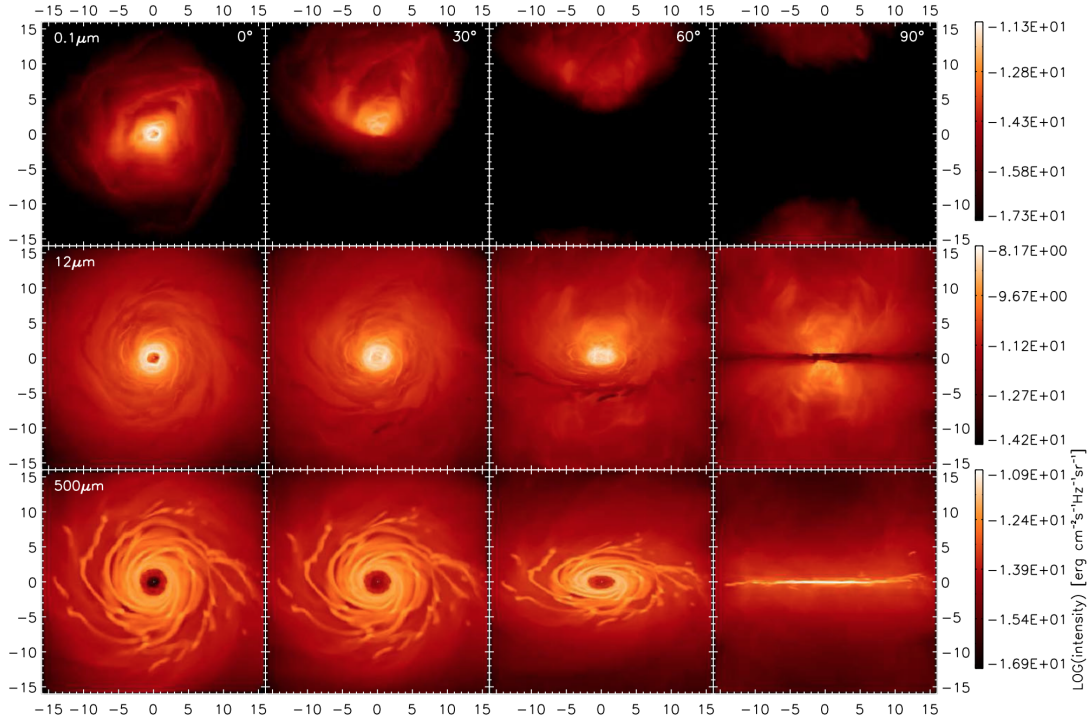

Figure 1.46: Logarithmic-scale images of a 3-D hydrodynamics model of an AGN dusty torus reconstructed using radiative transfer code RADMC-3D. The rows correspond to wavelength 0.1 (upper row), 12 (middle row) and 500 μm (lower row). The columns correspond to the inclination angle of 0°, 30°, 60° and 90° (from left to right). Credit: Schartmann et al. (2014).

with the "standard interstellar" in the galactic centre. In this case, dust particles comprised primarily of amorphous olivine with an admixture of up to 20% by weight of carbonaceous dust. If the grains get too hot ($\sim 2000\,\mathrm{K}$), they will change from a solid to a gas in a process known as sublimation. Where this happens is called the Sublimation Radius, which is the expected inner boundary of the torus. Near-IR interferometry and reverberation mapping show that the inner radius of the torus depends on luminosity as $\propto L^{0.5}$ (Kishimoto et al. 2011), which supports consistency between the torus boundary and the sublimation radius (Barvainis 1987).

In the schematic figures of the unification schemes of AGN, the torus looks like a continuous torus, which is not quite the correct representation of reality today. The picture was evolving in time. To describe the observed emission from AGN, Pier & Krolik (1992) proposed an emission model from an dust ring. Later, (Efstathiou & Rowan-Robinson 1995) showed that the torus with increasing high and opening angle of 45° is the most successful representation of observations. The evolution of models led to the clumpy tori (Nenkova et al. 2002), which is supported by the X-ray eclipse events observed in several AGN (Markowitz et al. 2014). In contrast, Fritz et al. (2006) found that a smooth distribution of dust is

also capable of recreating the observed emission. A recent 3-D hydrodynamics model of an AGN dusty torus shows that it has a complex quasi-smooth structure with clumps (Schartmann et al. (2014), see Figure 1.46).

Finally, it is important to understand that the torus is dynamic. It may consist of material flowing toward or away from the black hole. In addition, it lives with the central engine and depends on the AGN luminosity evolution (Kishimoto et al. 2013).

Relativistic jets

Astrophysical jets are one of the most spectacular and beautiful phenomena. They can be described as highly collimated outflows (Figure 1.47), which are observed in the vast range of scales of different astronomical objects and play an important role in the evolution of young stellar objects (YSOs), X-ray binaries (XRBs), active galactic nuclei (AGN), and -ray bursts (GRBs). Despite different scales and environments, all jets have similar mechanisms based on transforming the gravitational energy of accreting matter to the power of outflows (Meier 2003). Wildly outrageous are the AGN jets, which can expand megaparsecs to the extragalactic medium, playing a crucial role in cosmological scales (Oei et al. 2024).

The first observation of an astrophysical jet was done by Curtis (1918). In his work, he spotted a "curious straight ray" from the centre of the galaxy M87 (then referred to as a "nebula"). However, Curtis did provide only an observational description of what he saw without any physical explanation. Nevertheless, this was the first big step in the jet study. At that time, "nebulas" were still not associated with extragalactic objects; Einstein and Schwarzschild had just published their work on black holes, which was not taken seriously yet. Therefore, it is not surprising that there were not a lot of advances in jet research until the 1960s. In addition, as was mentioned previously in section 1.3 and section 1.3.2, only with advances in interferometry techniques in the 1950s did it become possible to associate strong radio emission with host galaxies. The first concepts and interpretations discussing high-energy particles and outflows from the galaxy's central regions were again connected to the M87 jet discovered by Curtis. Shklovsky (1957a) explained the radio emission of the jet in the galaxy M87 (NGC 4486) by synchrotron radiation and concluded that the jet was formed by an enormous explosion in the nucleus hundreds and millions of times greater than a supernova or by collision of massive aggregates. However, later, Shklovsky criticises a colliding galaxy hypothesis Shklovskii (1961). The interpretation was inspired by the discovery of synchrotron radiation being the main emission mechanism in the Crab Nebula (Shklovsky 1957b) and cosmic ray production in supernovas (Shklovsky 1954). That is why

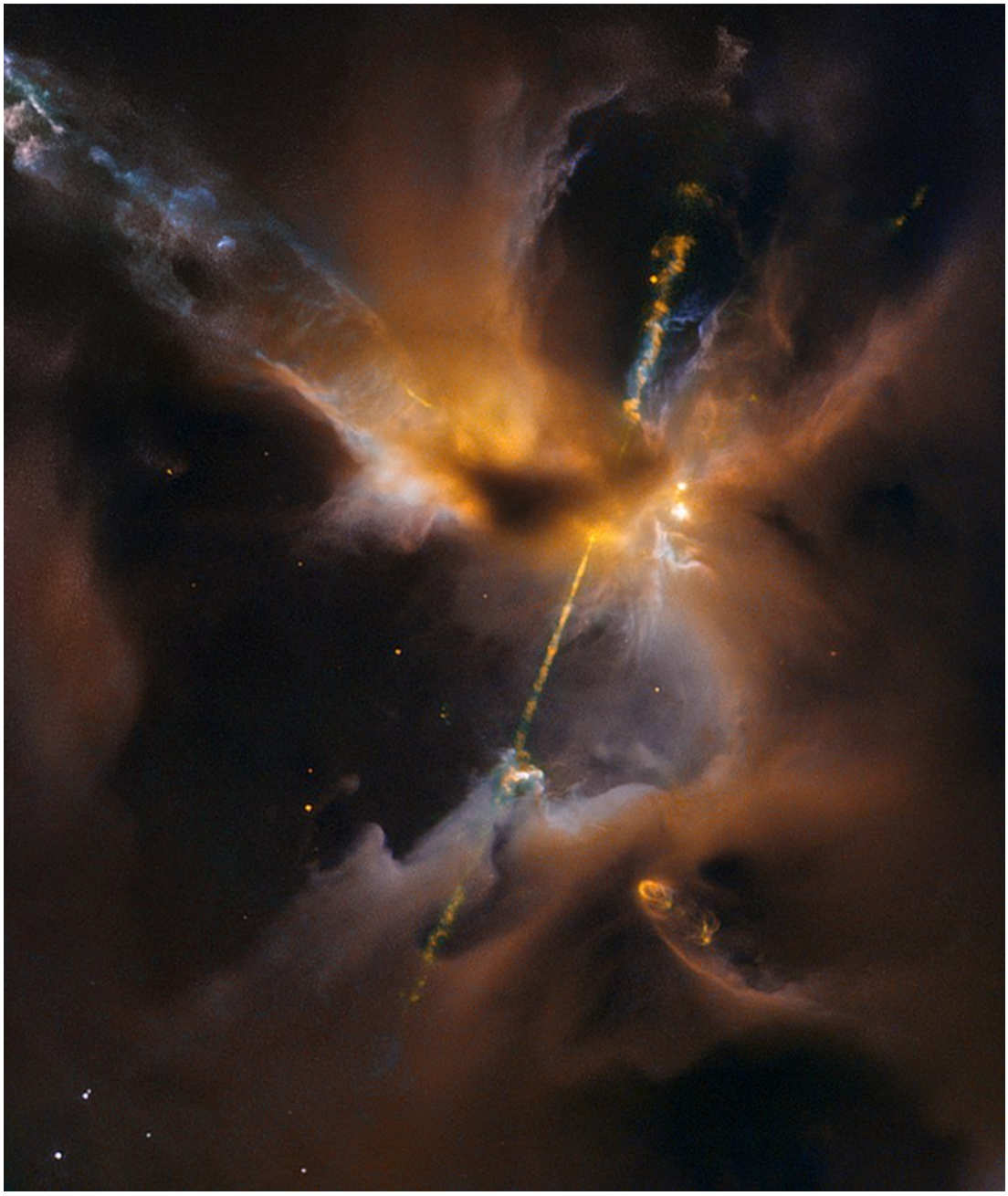

Figure 1.47: Star forming region of a molecular cloud HH 24-26 observed by NASA's Hubble Space Telescope. The image shows the region with the highest concentration of astrophysical jets in the sky. Credit: ESA/Hubble & NASA, D. Padgett (GSFC), T. Megeath (University of Toledo), and B. Reipurth (University of Hawaii).

the conclusion on the jet formation was connected to an explosion similar to a supernova. During this time, black hole study entered its golden age. At this time, it was already widely assumed that most extragalactic radio sources are formed in the vicinity of a spinning supermassive black hole (Lynden-Bell 1969a; Zeldovich & Novikov 1971). In addition, synchrotron radiation was theorised (Ginzburg & Syrovatskii 1965). From the perspective of active galaxy evolution, van der Laan & Perola (1969), to explain observed phenomena, considered burst, quasi-continuous particle ejection and multiple bursts scenarios. The fundament was ready for the theoretical description of AGN jets. Several other attempts later were made to explain extended radio sources, for example, Rees (1971), Longair et al. (1973) and Scheuer (1974). But neither model explained the observations fully. Blandford & Rees (1974) proposed a "twin-exhaust" model for double radio sources such as Cygnus A. In the paper, the authors understood that relativistic plasma cannot escape from an AGN isotropically if the nucleus is surrounded by too much dense thermal gas. An equilibrium flow is possible if the plasma escapes along two oppositely directed channels or "exhausts". These "exhausts" can be considered fluids with properties like different instabilities (Rayleigh–Taylor and Kelvin–Helmholtz) and shocks, which are particle acceleration regions. They also interpret Cygnus A "hot spots" as an interaction between the jets and an extragalactic medium.

Relativistic effects

Relativistic effects are observed in the AGN jets because of their extreme speed, which is close to the speed of light (Rees 1966). This led to very beautiful and seemed very unnatural observational phenomena.

- **Superluminal motions**
  First, proper motions observed in kilo-parsec, especially parsec scale jets, are superluminal. Typical proper motions observed by VLBI imply velocities up to $\sim 30c$ (Vermeulen & Cohen 1994). The effect is happening due to the high speeds of the jet matter and the projection effects. In Figure 1.48, the scheme explaining the superluminal motion is shown. The radio telescope observes a jet with a viewing angle θ at a distance D. At a time t_1 light is emitted from the jet component. In some time $t_2 = t_1 + \Delta t$, the same region that travelled a distance $v\Delta t$ emits another portion of light. Since the distance between the observer and the jet is big, two distances marked with D can be considered equal. The observer receives corresponding light at times $t'_2 = t_2 + D/c$ and $t'_1 = t_1 + (D + v\Delta t \cos\theta)/c$, since the first one need to pass an additional distance until the point P. Thus, $\Delta t' = t_2 - t_1 - v\Delta t \cos\theta/c = \Delta t(1 - \beta\cos\theta)$,

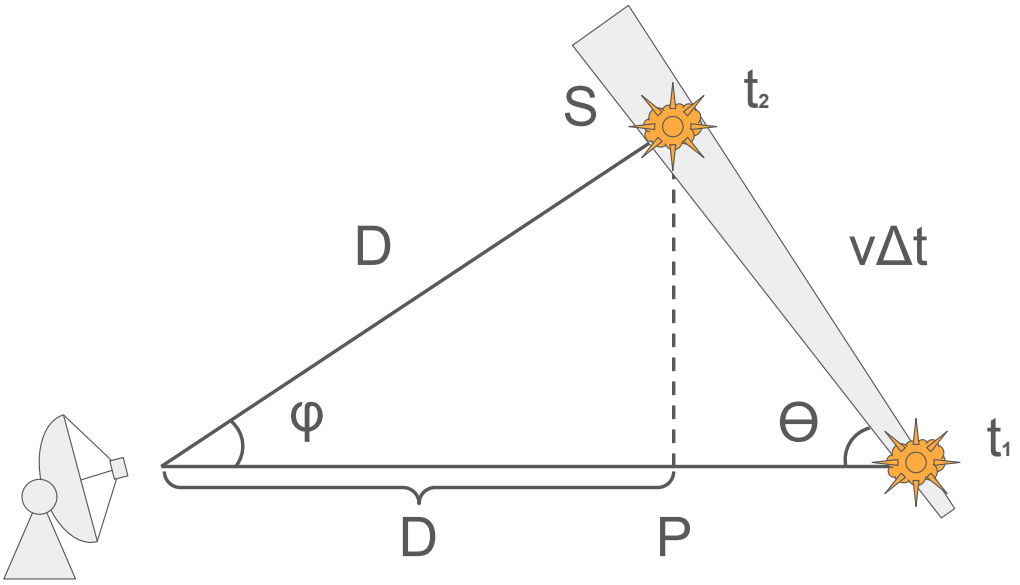

Figure 1.48: Scheme explaining superluminal motion in a jet.

where $\beta = v/c$. The observer sees transverse velocity, with is the projection into the sky plane $\beta_{\rm T} = v_{\rm T}/c = SP/\Delta t' = v\Delta t \sin\theta/[c\Delta t(1-\beta\cos\theta)]$. This leads to

$$\beta_{\rm T} = \beta_{\rm app} = \frac{\beta \sin\theta}{1-\beta\cos\theta}, \tag{1.3.6}$$

or inverse form:

$$\beta = \frac{\beta_{\rm app}}{\sin\theta - \beta_{\rm app}\cos\theta}. \tag{1.3.7}$$

- **One-sided jets**

  Observed jets are often one-sided, and for high-luminosity AGN, this type of structure is more frequent (Bridle et al. 1994). Moreover, VLBI observations of parsec scale jets showed predominantly one-sided structure (Cawthorne 1991a), even at the base of the symmetric jets in low-luminosity objects (Bridle & Perley 1984). The one-sided jet structure is also seen in the main target source of the thesis, M87 (Eichler & Smith 1983; Shklovskii 1977). The effect is explained by the relativistic beaming or Doppler boosting. Since the jets are propagating at velocities close to the speed of light, they emit whole energy into a cone oriented along the direction of travel. In this case, the brightness of observed emission depends on the viewing angle and Lorentz factor $\Gamma = 1/\sqrt{1-\beta^2}$ through the Doppler factor

$$\delta = \frac{1}{\sqrt{\Gamma(1-\beta\cos\theta)}}. \tag{1.3.8}$$

Thus, the emitted (S_e) and received (S_r) flux densities are related as

$$S_\mathrm{r} = S_\mathrm{e}\delta^{3-\alpha}, \tag{1.3.9}$$

where α is the spectral index. Therefore, the approaching jet is boosted, but the preceding jet is de-boosed. This explains the selection effect appearing with strong AGN being predominantly one-sided. Nevertheless, with the increased sensitivity, the counter-jet of these one-sided jets is observed, like in M87 (Kovalev et al. 2007; Sparks et al. 1992; Stiavelli et al. 1992). Detecting a counter-jet allows obtaining intrinsic physical jet parameters such as the speed of the flow or viewing angle of a jet, which is demonstrated in subsection 2.3.3.

- **Stratified structure**
  An increase in resolution allowed to resolve jets transversely. There are a lot of examples where a jet shows limb-brightening (Bruni et al. 2021; Giovannini et al. 2018; Janssen et al. 2021a; Kim et al. 2018; Kovalev et al. 2007; Lu et al. 2023; Paraschos et al. 2024; Park et al. 2024). The origin of this effect is not settled yet. According to one of the models proposed to explain the morphology, the jet has a "spine-sheath" structure, where the fast spine is Doppler deboosted relative to the slow sheath or, it can just have an opacity effect Hirotani et al. (2024); Punsly (2022). In some cases, a triple-ridge structure can be observed (Frolova et al. 2023; Ogihara et al. 2019). Other models discuss different launching mechanisms or structures of the magnetic fields as a trigger of the limb-brightening (Kramer & MacDonald 2021; Sob'yanin 2017). In the end, Limb-brightening structures can be confused with more complex structures like double or triple-helix because of lack of resolution and sensitivity like it was observed in 3C 279 with RadioAstron in Figure 1.49 (Fuentes et al. 2023; Pasetto et al. 2021a).

1.3.3 Jet formation and propagation

Four regions demonstrated in Figure 1.50 can describe relativistic jet in AGN (Blandford et al. 2019; Boccardi et al. 2017). The jet is born in a launching region of about $\sim 100R_\mathrm{S}$ from the black hole. Strong magnetic fields dominate the dynamics of the area and pump the plasma with energy extracted from the surroundings of the supermassive black hole. Propagating further from the black hole, the jet accelerates to relativistic velocities ($\Gamma \sim 50$). Since the magnetic field still dominates plasma, the jet collimates and shows a quasi-parabolic geometry ($w \propto z^{\sim 0.5}$). The transition from parabolic to conical ($\propto z^{\sim 1}$) shape, observed in

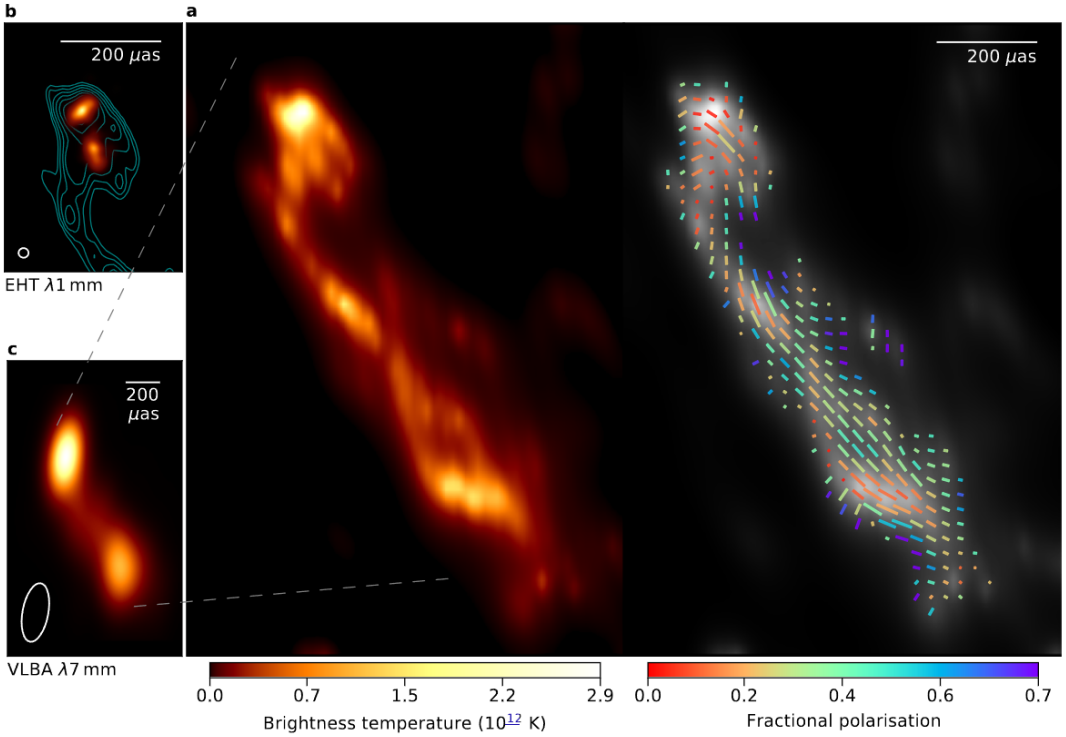

Figure 1.49: Helical structure of Kelvin-Helmholz instability theads in 3C 279 discovered by RadioAstron. The main image shows total intensity (left) and linearly polarized (right) RadioAstron image at 1.3 cm obtained on 10 March 2014. The top left image is the 1:1 scale 1.3 mm EHT image obtained in April 2017. The image is overlaid by RadioAstron image contours, which start at 90% of the peak brightness and decrease by successive factors of 3/2 until they reach 5%. The bottom left image is the 7 mm VLBA-BU-BLAZAR program image obtained on 25 February 2014. Credit: Fuentes et al. (2023).

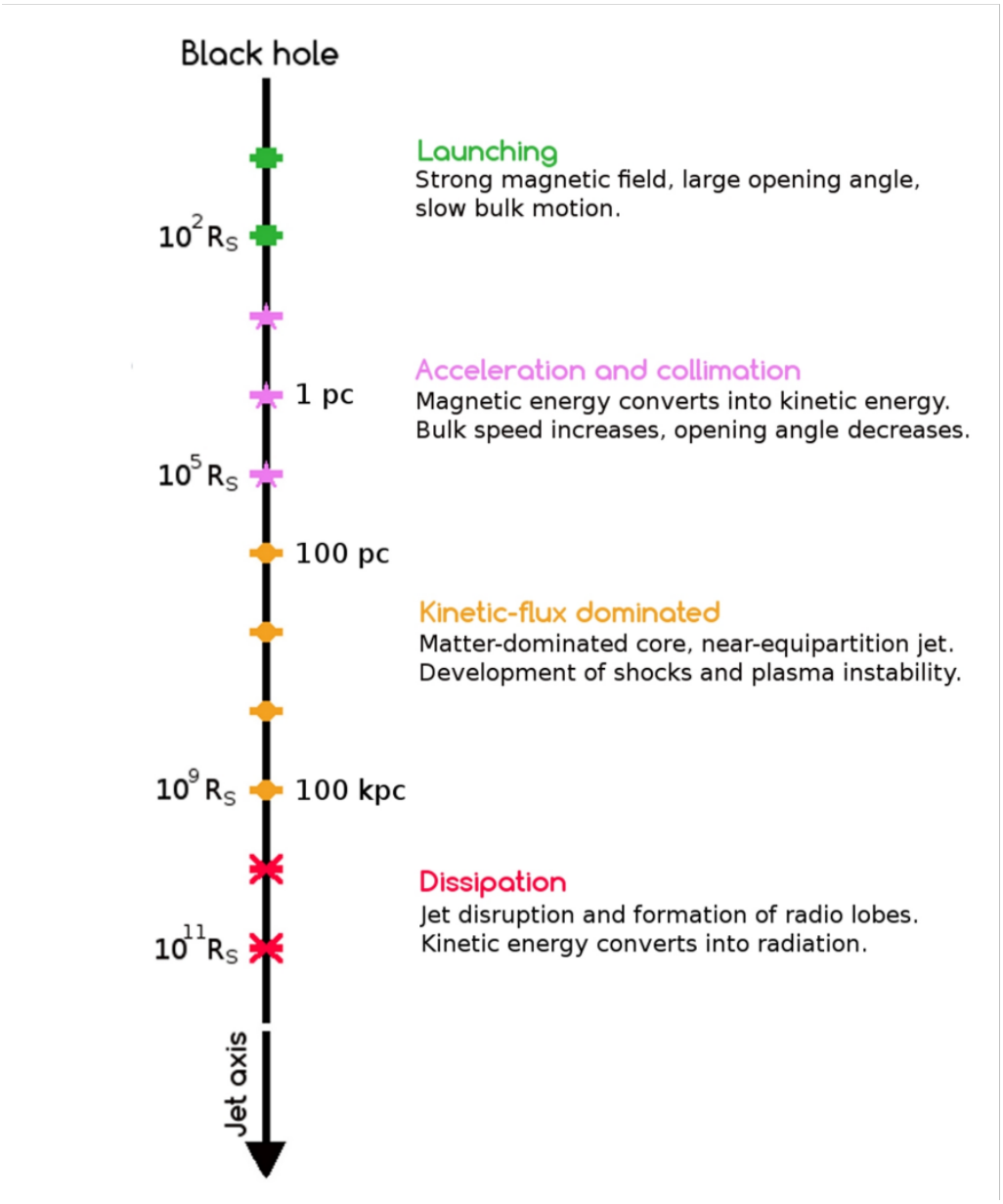

Figure 1.50: Scheme showing regions of an AGN jet. The distance on the axis is shown in a logarithmic scale. Credit: Boccardi et al. (2017).

a lot of AGN jets (Kovalev et al. 2020a), signalises the start of the particle or kinetic-flux dominated region, where gas dynamics can describe the jet. Starting at $\sim 10^5 R_{\rm S}$, it can spread in kiloparsecs or even megaparsecs before ending in the dissipation region. The VLBI technique used in this thesis studies the first two regions.

Launching region

The main actors in the launching region are a black hole, an accretion disc and a strong magnetic field. Even though several aspects of the particular mechanism of jet generation are still unclear, the scientific community agreed to concepts from the classical papers by (Blandford & Payne 1982; Blandford & Znajek 1977b). According to the papers, two main mechanisms create a jet:

- **Blandford & Znajek (BZ) mechanism:** the rotational energy of the black hole powers the plasma,
- **Blandford & Payne (BP) mechanism:** the accretion disc powers the plasma.

A strong magnetic field threading the accretion disc and ergosphere is crucial since it is the central mediator of the jet launching mechanisms. Because of rotation, a poloidal magnetic field in the accretion disc gets twisted, resulting in a helical and toroidal one in a jet. Wrapped magnetic field lines create pressure or a "magnetic spring" effect, pushing plasma along the rotation axis. In addition, this field geometry can be one of the main reasons for a jet's collimation and stability over large distances. The evolution of the magnetic field geometry is illustrated in Figure 1.51. A jet can also be formed by a Penrose process (Penrose 1969), which could extract energy from the black hole's ergosphere. In contrast to the BZ mechanism, matter plays a crucial role in this process, not the magnetic field. Particles from matter enter the ergosphere and split into two, one of which escapes the region with the additional energy from the black hole's rotation.

While the BZ mechanism is associated with high-energy jets, the BP mechanism is associated with the weaker ones. However, according to the current studies, these two mechanisms can co-exist. In this case, the jet can be represented as a multi-layer flow with an internal spine formed by BZ and the slower external winds that envelope the jet made by BP (Hardee et al. 2007). The disk-jet relation can be examined through VLBI by extrapolating the jet geometry to the black hole vicinity, directly observing it or tracing a magnetic field. This was analysed by (Boccardi et al. 2016; Paraschos et al. 2024; Ricci et al. 2022). The unprecedented resolution obtained by Space VLBI presents the direct image of the jet base of 3C

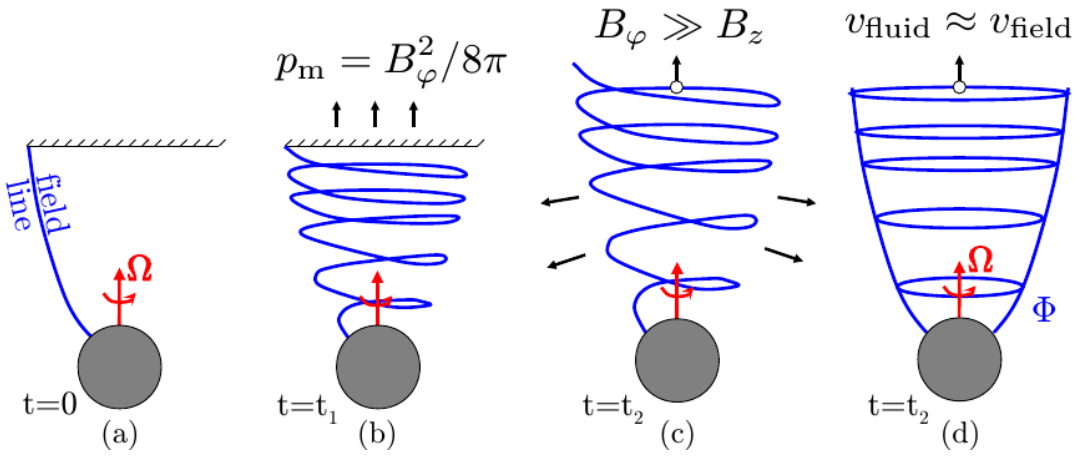

Figure 1.51: Magnetic field evolution and the concept of a "magnetic spring" which launches a jet. A single field line (a) is twisted during the accretion (b), creating the "magnetic spring". The azimuthal field strength far exceeds that of the axial direction (c). In the end, the magnetic field line will be twisted so tightly that the field becomes effectively poloidal (d). Credit: Davis & Tchekhovskoy (2020).

84 (Giovannini et al. 2018; Savolainen et al. 2023), which shows relatively large sizes and indicates the work of the BP mechanism (see Figure 1.52).

The mechanisms of jet generation are closely connected to the accretion mode in the disc (see subsection 1.3.2). Tchekhovskoy et al. (2011) showed in numerical simulations that in the case of MAD accretion disc, the efficiency of jet creation can be more than a hundred per cent and reach $\eta \sim 140\%$. This means that the energy obtained by the jet is not limited by the energy of the accretion disc but also originates from the rotational energy of the black hole. Strong magnetic fields from MAD make the BZ process effective, producing the most powerful jets. In the case of SANE accretion, the BZ process is possible, but it is less effective due to relatively weak magnetic fields. BP mechanism also plays a role in the jet creation in both cases, but in the MAD scenario, BZ is dominant.

Acceleration and collimation region

After launching, magnetic fields dominate relativistic jets. In other words, outflows are Poynting-flux dominated. The geometry of a jet in this region is quasi-parabolic, meaning collimation or the decrease of the opening angle with the distance reaching values of a few degrees. This phenomenon is observed in many nearby AGN because of the possibility of observing and resolving these relatively close to the central engine regions (Baczko et al. 2022; Boccardi et al. 2021; Giovannini et al. 2018; Janssen et al. 2021b; Junor et al. 1999; Pushkarev et al. 2017a). Asada & Nakamura (2012b) showed that the geometry of the M87 jet has a transition from parabolic to conical, tracing the end of the collimation zone. Kovalev et al. (2020a) studied a sample of AGN jets and concluded that the

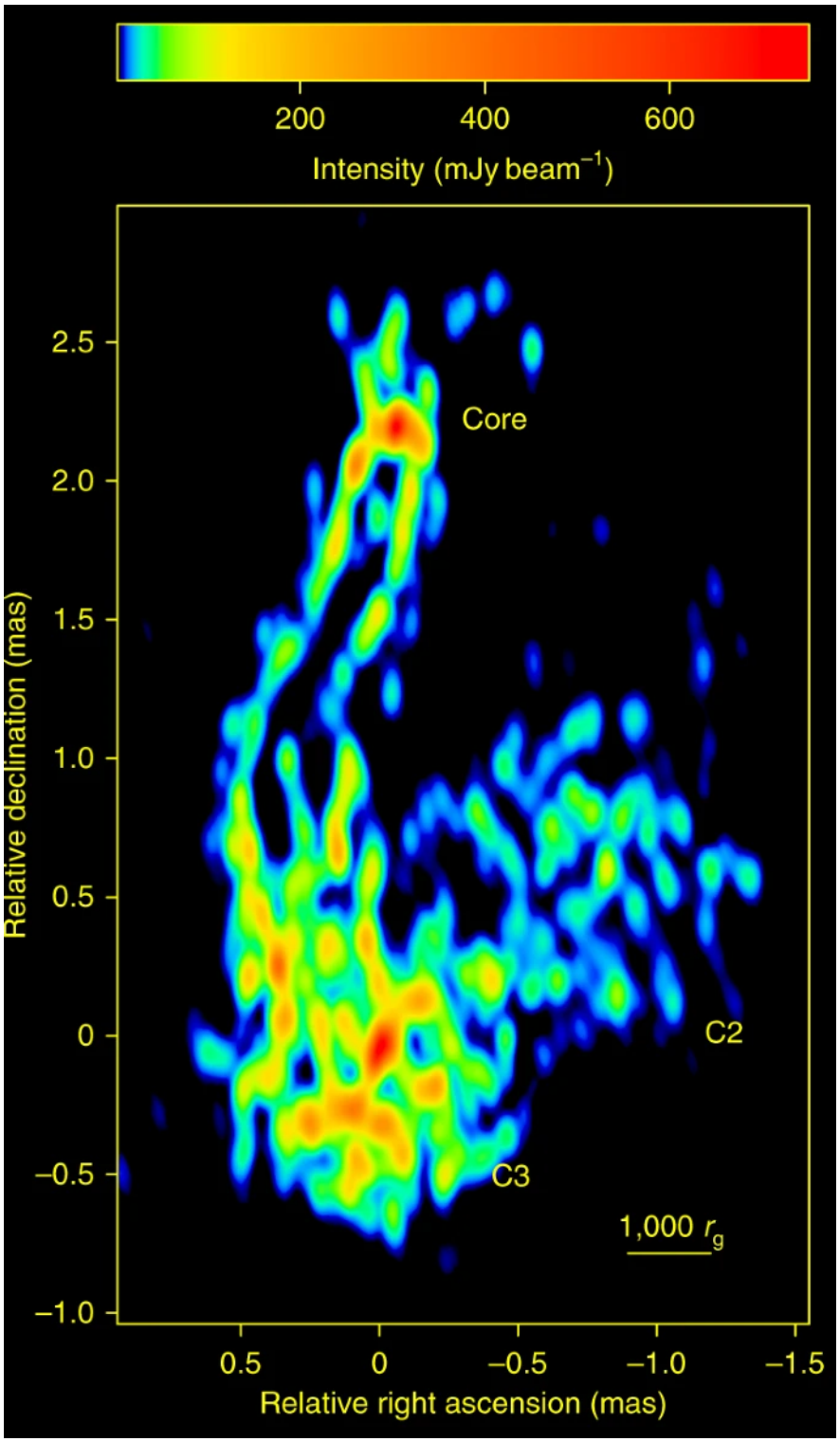

Figure 1.52: Jet of 3C 84 observed by RadioAstron Space-VLBI. The measured jet base width is about $\gtrsim 250R_S$, meaning the jet went through a rapid expansion or was produced from the accretion disc. Credit: Giovannini et al. (2018).

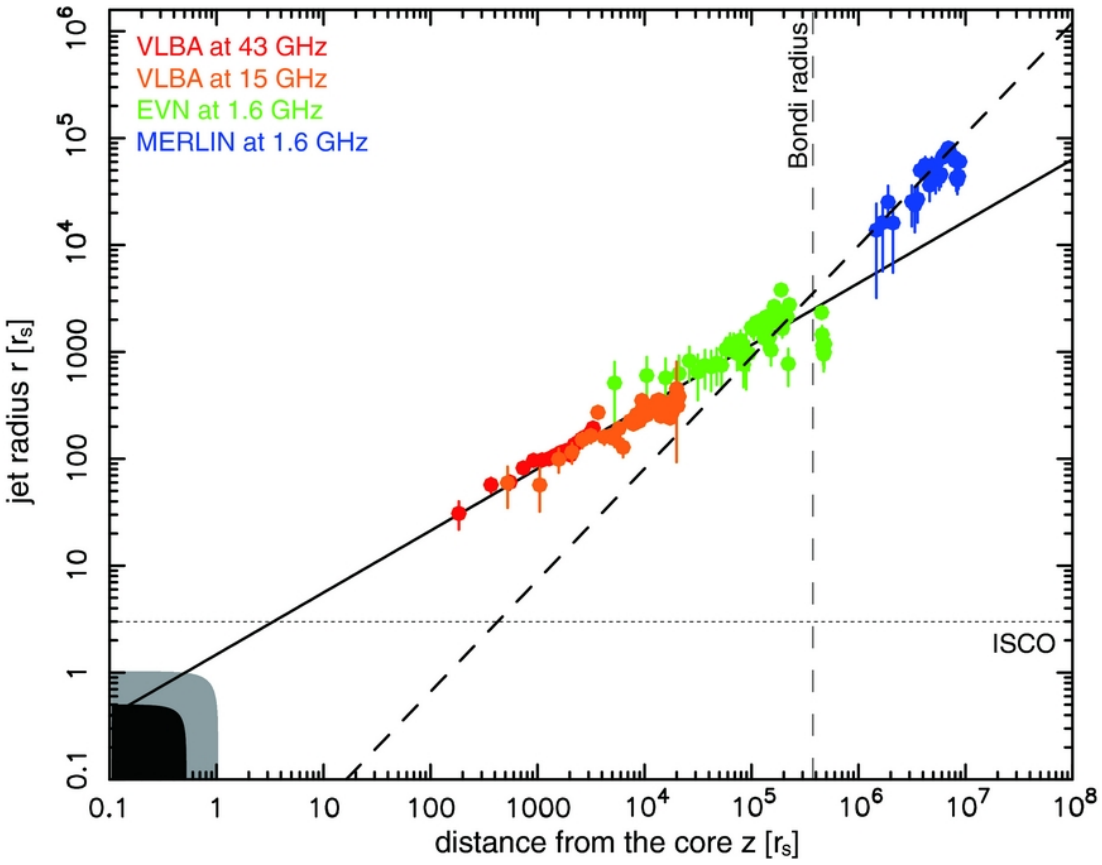

Figure 1.53: Geometry profile of the M87 jet. Different colours show measurements from different interferometers: VLBA at 43 GHz (red circles) and at 15 GHz (orange circles), EVN at 1.6 GHz (green circles), and MERLIN at 1.6 GHz (blue circles). The solid line indicates a best-fit parabola with a power-law index of $k \approx 1.7$, while the dashed line indicates a conical structure with a of $k = 1$. The dashed line shows the Bondi radius. The black area represents the size of the minor axis of the event horizon of the spinning black hole with maximum spin. The gray area indicates the size of the major axis of the event horizon. The dotted line indicates the size of the inner stable circular orbit (ISCO) of the accretion disk for the Schwarzschild black hole. Credit: (Asada & Nakamura 2012a).

geometry transition is widely observed in various sources by the VLBI technique.

The nature of collimation depends not only on the magnetic field of the jet itself but also on the external medium. In Figure 1.53, the geometry profile of the M87 jet is presented. It is seen that the transition coincides with the Bondi radius, thus the change of the external pressure profile. Kovalev et al. (2020a) found similar behaviour in several AGN. However, this is an unclear correspondence and depends on the properties of the jet. For example, shape transitions can happen before the Bondi radius (Nakahara et al. 2020; Park et al. 2021). Studies (e.g., Beskin & Nokhrina (2006)) propose that the geometry transition depends on the internal changes in a bulk flow, which would change from a magnetically dominated state to an equipartition state between the plasma kinetic and magnetic

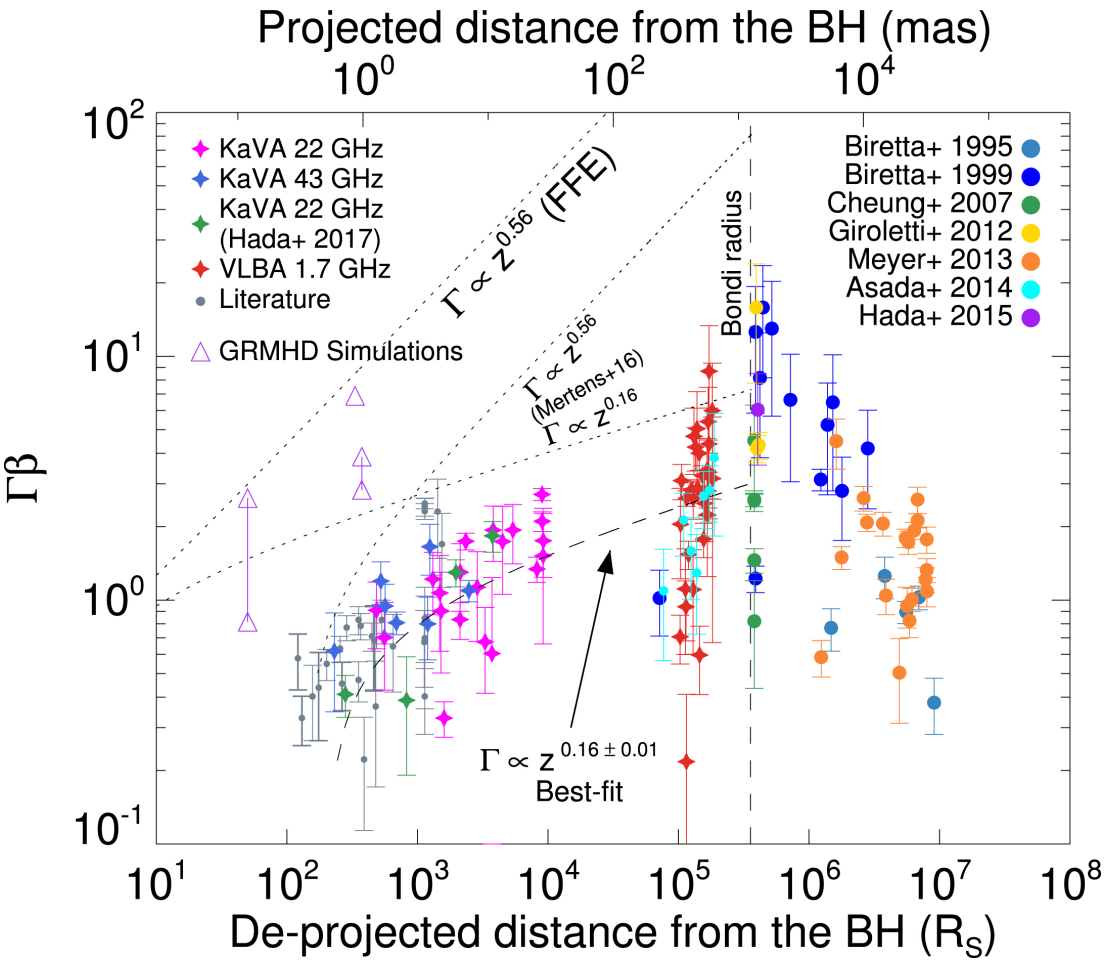

Figure 1.54: Velocity $\Gamma\beta$ is calculated from the measured apparent speeds with the adopted jet viewing angle of 17°, as a function of deprojected distance from the black hole in units of $R_{\rm S}$. Credit: Park et al. (2019).

energy. Based on this, Nokhrina et al. (2020) discussed an opportunity to estimate intrinsic jet parameters and even black hole spin from the jet brake position. However, the picture is not fulfilled since BZ and BP mechanisms can create a jet together. Therefore, the central spine and the shear layer can have different collimation scenarios.

Collimation discussed earlier is important for acceleration since magnetic acceleration is effective during collimation (Komissarov et al. 2007). Magnetic acceleration plays a crucial role in relativistic jets since thermal one is significant only in the vicinity of the jet base Vlahakis & Königl (2003a,b, 2004). When the magnetic acceleration prevails, the acceleration and collimation regions are expected to coincide. This is observed, for example, in the M87 jet (Mertens et al. 2016a; Park et al. 2019). Figure 1.54 shows the velocity profile peak of around $\beta_{\rm app} \approx 6c$ coinciding with the Bondi radius.

One of the main distinctive features of jets in VLBI images is a "VLBI-core." Being the brightest component in the image, it is often used as the centre of the

image because of a loss of absolute positions in VLBI. Although the jet base is expected to be the brightest in the jet, the core position does not coincide with it. Moreover, the position of the core is frequency-dependent, so images should be aligned before analysing multi-frequency observations (Croke & Gabuzda 2008). The nature behind the core is based on the opacity effect. Far from the central engine, the jet is transparent and can be observed easily in a broad range of frequencies. Closer to the jet base, the density of emitting electrons becomes high enough to absorb the radiation they produce. This is called synchrotron self-absorption. Thus, the core can be characterized by a flat spectrum and interpreted as the transition between synchrotron self-absorbed and optically thin regions. The effect of position change of the core is called core shift and is useful for magnetic field investigation. The core shift was predicted by Blandford & Königl (1979) in the case of a conical jet, and Lobanov (1998a) formulated the estimation of a magnetic field strength based on the core shift offset parameter. The amplitude of a core shift follows a power law $\Delta r \propto \nu^{-1/k_r}$, where k_r is a measure for the divination of the plasma from the equipartition of energy between the magnetic field and radiating particles. It was shown that, in general, VLBI sources show $k_r \approx 1$ (Sokolovsky et al. 2011). The core shift is widely used to estimate magnetic fields in relativistic AGN jets (Pushkarev et al. 2012). However, this estimation is not accurately applicable in the case of parabolic jets, such as M87. Nokhrina & Pushkarev (2024) described a methodology for estimating magnetic field strength in parabolic jets, which was successfully used in the case of NGC 315 (Ricci et al. 2022). It is important to note that the core shift does depend on the environment, so the position of the core can physically shuttle up and downstream the jet (Lisakov et al. 2017; Plavin et al. 2019). Other spectral properties, such as the turnover frequency of a synchrotron spectrum, can reveal the magnetic field strength profile, which was shown by Lobanov & Zensus (1999) in the case of 3C 345, and this thesis in the case of the HST-1 feature (see chapter 3).

Some objects do not show an appreciable core shift (Pushkarev et al. 2012). In this case, a VLBI core can be associated with a stationary feature, which is the first and brightest standing shock developing in the flow (Marscher 2008). Stationary features near the black holes can play an important role in producing a high-energy emission Arshakian et al. (2010); León-Tavares et al. (2010). In addition, they are sites of efficient particle acceleration through the Fermi mechanism (Bell 1978) and empowering magnetic fields. Last, make shocks identified by increased polarisation and perpendicular to the jet direction magnetic field. But not all observed transverse magnetic fields are shocks (Gabuzda 2003; Lyutikov et al. 2005). Shocks are present when there is an imbalance between the jet and

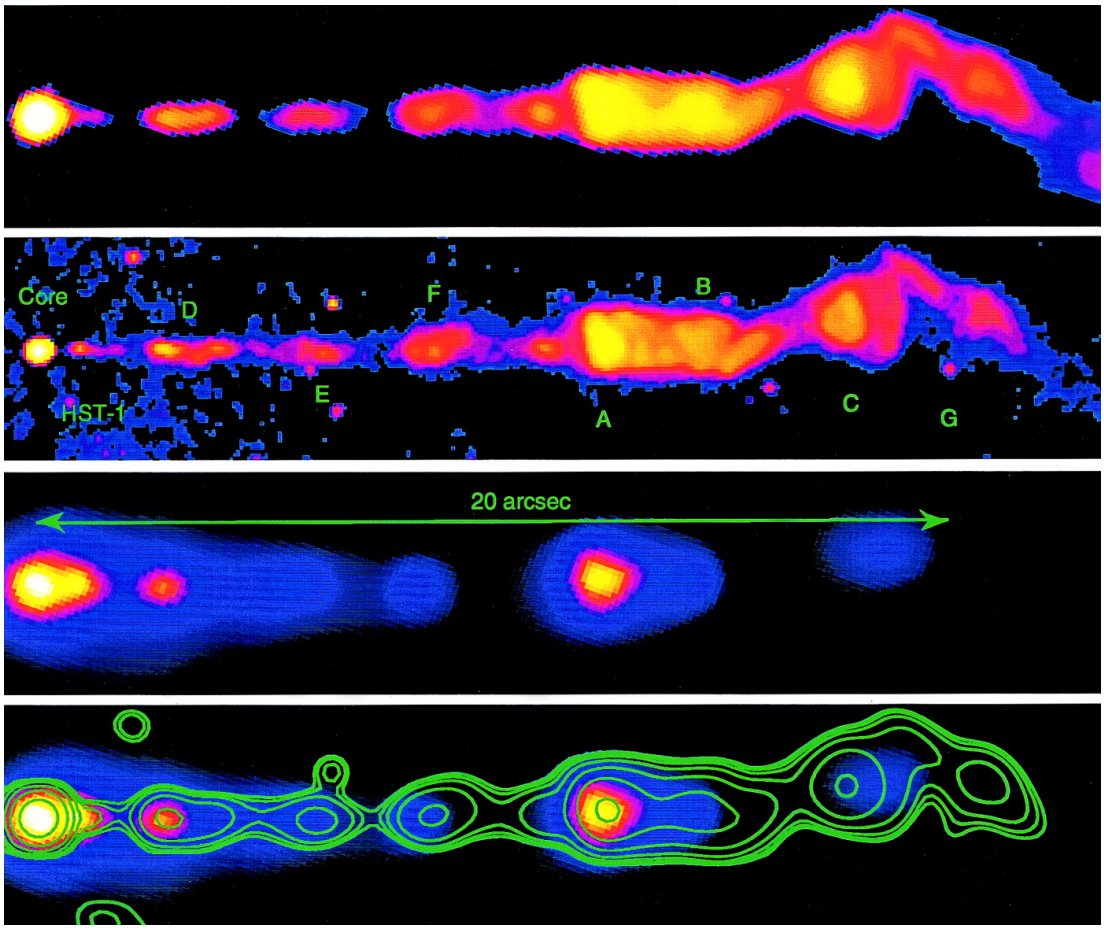

Figure 1.55: Jet in M87 in three different bands: radio by VLA, optical by HST Planetary Camera, X-Ray by Chandra. The last row shows the Chandra image overlaid with contours of a Gaussian-smoothed version of the HST image, designed to match the Chandra PSF. Credit: Marshall et al. (2002), Perlman et al. (2001).

external medium pressure or from internal jet mismatches in velocities, for example. Sometimes, it can form a series of bright, knotty structures. A recollimation shock may be expected at the end of the acceleration and collimation region, especially near the Bondi radius (Cohen et al. 2014; Polko et al. 2010). It is speculated that the HST-1 feature is the recollimation shock of the M87 jet since it is located in the Bondi radius area and the jet geometry transition area (Asada & Nakamura 2012a). Moreover, the HST-1 feature shows broad flaring activity from radio to γ-rays (Cheung et al. 2007; Harris et al. 2003, 2009; Stawarz et al. 2006).

Sometimes, the jet's knotty structure is due to a telescope's limited sensitivity and resolution. For example, M87, at first glance, indeed show a knotty structure (Figure 1.55). These images and knots were interpreted as clouds or shocks (Blandford & Koenigl 1979; Qian 1983; Sulentic et al. 1979). However, recent more sensitive images of the same region of the jet show a more complex filamentary structure similar to a double helix from a DNA, which can be seen in Figure 1.56 (Pasetto et al. 2021a). In this image, knots appear to be the intersections of

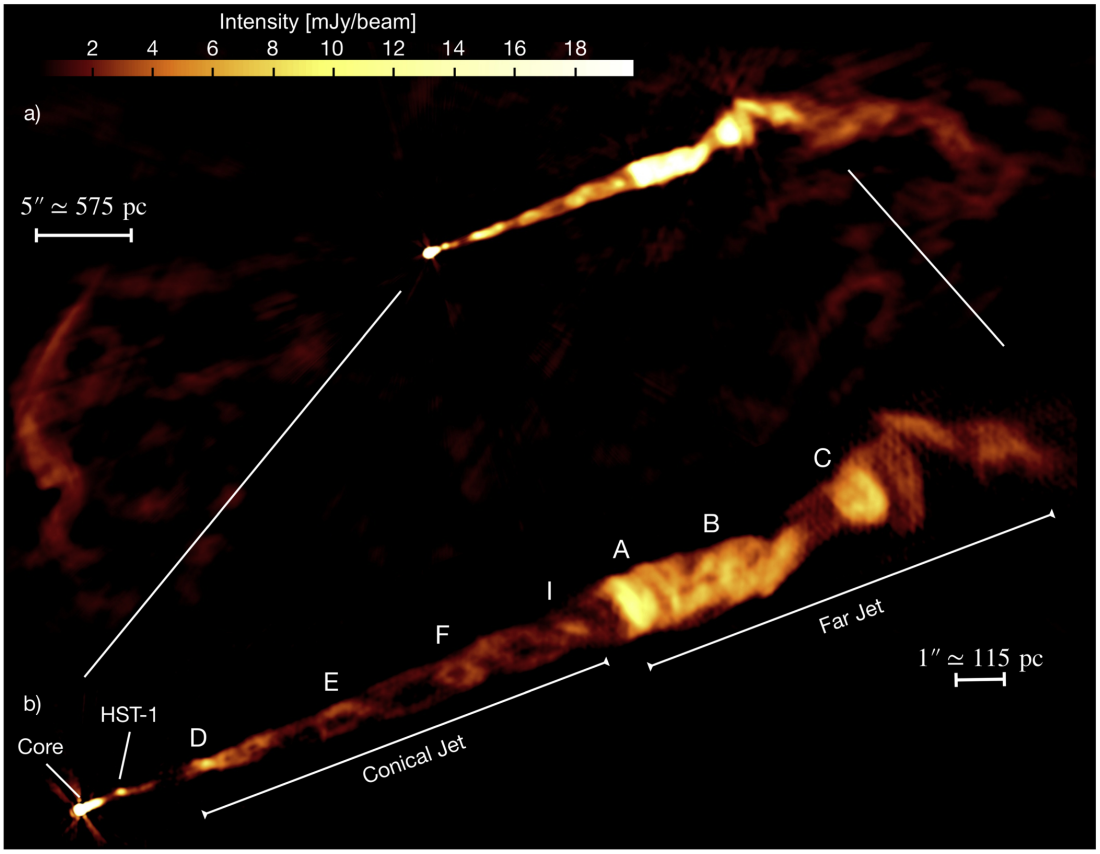

Figure 1.56: The M87 VLA radio jet combines all of the available frequencies (from 4 to 18 GHz). The top of the image robust = 1 weighted image with an angular resolution of 0.”2. It is sensitive to large-scale emission, so the jet appears as known from previous observations (Figure 1.55). The bottom image is a uniform weighted image, thus has a higher angular resolution of 0.”09. Several knots, previously identified in optical images, are labelled. This image shows a clear double-helix structure in the conical jet. Credit: Pasetto et al. (2021a).

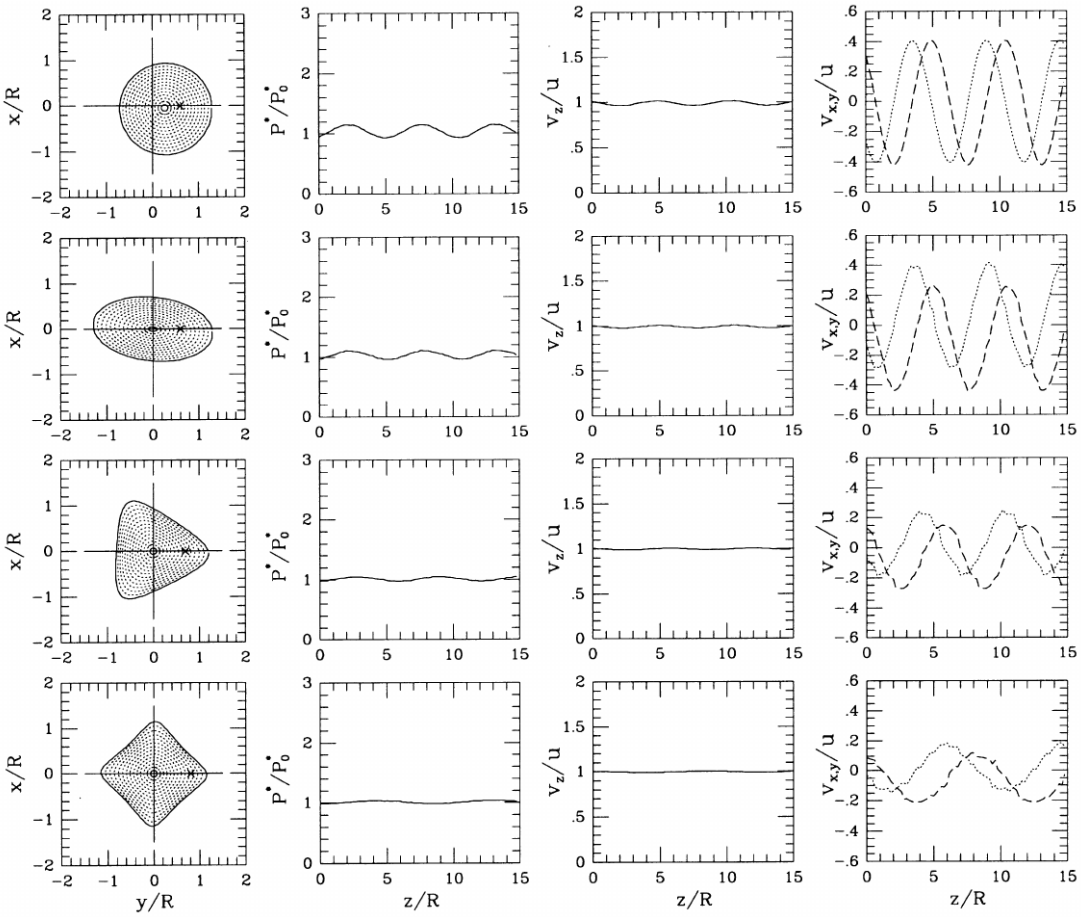

Figure 1.57: First column: Displacement cross sections for helical, elliptical, triangular, and rectangular surface waves. Second, third and fourth column: The one-dimensional pressure and velocity slices are taken at positions on the y-axis indicated by the crosses in the displacement cross sections. Credit: Hardee & Rosen (1999).

a helical structure. Lobanov et al. (2003) suggested that Kelvin-Helmholtz instability (Gerwin 1968) plays the main role in the jet structure and identified the corresponding Helical and Elliptical modes observed in the images. The instability appears when two fluids have different speeds. Small fluctuations in the jet can induce instability, which will grow and eventually destroy the jet. To analyse the instability growth and properties, Hardee (2000, 2003); Hardee & Eilek (2011); Hardee & Norman (1988); Norman & Hardee (1988) proposed and used linear analysis to describe the instability in a jet. In this approach, the instability is considered to consist of Fourier components $f(\vec{r}, \phi, z) = f(\vec{r}) \exp\{i(kz \pm n\phi - \omega t)\}$, each of which deforms a jet so that a cross-section of a jet can show different shifts and shapes like in Figure 1.57. In this form, k is the longitudinal wavenumber, n is an integer azimuthal wavenumber or a normal mode. In this case, $n = 0$, 1, 2, 3, 4, etc., correspond to pinching, helical, elliptical, triangular, rectangular, etc., normal-mode distortions of the jet, respectively. Each normal mode has surface ($m = 0$) and body modes ($m = 1, 2, 3...$). For example, E_s is an elliptical surface mode ($n = 2$, $m = 0$) or E_{b1} is an elliptical first body mode ($n = 2$, $m = 1$). One of the important observational properties of the instability is its wavelength. From the mentioned linear analysis, the wavelength is directly connected to the jet's physical parameters, such as the Mach number and the ratio of the jet to the ambient density η:

$$\begin{aligned} M_{\rm j} &= \frac{\lambda^*(1 - \beta_w \cos\theta)}{8R\gamma(1 - \beta_w/\beta_{\rm j})\sin\theta}, \\ \eta &= \frac{M_{\rm j}^2}{M_{\rm ext}^2}, \end{aligned} \tag{1.3.10}$$

where $\lambda^* = \lambda_{nm}(n + 2m + 0.5)$ is a characteristic wavelength. The Mach number of external meduim $M_{\rm ext}$ and intrinsic jet pattern β_w are calculated with

$$\begin{aligned} M_{\rm ext} &= \frac{\lambda^*\beta_{\rm j}(1 - \beta_w \cos\theta)}{8R\beta_w \sin\theta}, \\ \beta_w &= \frac{w_{\rm app}}{\sin\theta + w_{\rm app}\cos\theta}, \\ \beta_{\rm j} &= \frac{\beta_{\rm app}}{\sin\theta + \beta_{\rm app}\cos\theta}. \end{aligned} \tag{1.3.11}$$

1.3.4 Target source: M87

M87 (Virgo A, NGC 4486, 3C 274) is a giant elliptical galaxy which has an Active Galactic Nucleus (AGN) and an extended relativistic jet powered by a supermassive black hole (SMBH). The combination of proximity and SMBH makes M87 a prime target to study the outflow nature. The distance and the redsift for M87 are D =16.7 Mpc (Mei et al. 2007) and $z = 0.00436$ (Smith et al. 2000)

correspondingly, which correspond to the angular scale of 1 mas $\approx 0.08\,\mathrm{pc}$. The supermassive black hole mass obtained from the Event Horizon Telescope image analysis is $(6.5 \pm 0.2|_{\mathrm{stat}} \pm 0.7|_{\mathrm{sys}}) \times 10^9 M_\odot$ (Event Horizon Telescope Collaboration et al. 2019b). Thus, the Schwarzschild radius $R_\mathrm{s} \equiv 2GM/c^2 \approx 1.9 \times 10^{15}$ cm, which corresponds to 1 mas $\approx 130 R_\mathrm{s}$. Moreover, it is the first source in which, for the first time, the image of a black hole region shows not only the ring but a relativistic jet together (Lu et al. 2023).

The relativistic jet in M87 is frequently observed with the Very Long Baseline Interferometry (VLBI) technique. The images typically show an edge-brightened structure and a faint feature on the counter-jet side, south-east of the core. The full track 15 GHz observations which were done using the Very Large Baseline Array (VLBA) clearly show this feature (e.g. Kovalev et al. 2007; Ly et al. 2007); see also the collection of MOJAVE images (Lister et al. 2018). This structure is believed to be the counter-jet deboosted by relativistic aberration effects. However, there is no spectral information to support this idea. Spectral index maps could also help to understand better the nature of the edge-brightened (e.g. Kovalev 2008) and triple-ridge jet structure (e.g. Asada et al. 2016; Hada 2017; Savolainen 2021). The high-fidelity Very Large Array (VLA) radio images of the kiloparsec (kpc) scale jet of M87 clearly show a helical pattern (Pasetto et al. 2021b). This structure can also be seen in other jets, like 3C 273 (Lobanov & Zensus 2001) or S5 0836+710 (Vega-García et al. 2019). The oscillatory pattern of the kpc-scale jet of M87 was studied in Lobanov et al. (2003), where the observed threads were identified with the Kelvin-Helmholtz (KH) instability happening in the jet.

Kovalev et al. (2007) also showed an extended high linear polarisation region, but the absence of Faraday rotation maps did not allow the authors to reconstruct a magnetic field direction. Deep observations can significantly complement the polarisation studies of the M87 jet and reveal new regions not visible on Zavala & Taylor (2002), Park et al. (2019) and Pushkarev et al. (2023) polarisation maps.

One of the most intriguing features of the M87 jet is the HST-1 knot, located about $0.9''$ arcseconds from the central engine. HST-1 was first identified through observations by the Hubble Space Telescope (HST) as the closest knot to the core in the kiloparsec scale. The observations revealed superluminal speeds of the knot $\beta \approx 6c$ (Biretta et al. 1999; Perlman et al. 1999). In addition, HST-1 showed significant flaring activity not only in optical (Madrid 2009; Perlman et al. 2003) but across all bands from radio to X-rays and even γ-rays (Abramowski et al. 2012; Avachat et al. 2016). The observations by Chandra X-Ray Observatory of the knot showed a flaring activity that increased intensity by a factor of 50 by five years (Harris et al. 2003, 2006). There is also evidence that a γ-ray flare detected from the M87 galaxy occurred in the same date range as the flare reported earlier

and may be associated with the HST-1 knot (Aharonian et al. 2006).

Previous Very Long Baseline Interferometry (VLBI) observations showed that the HST-1 feature at sub-parsec scales exhibits structural changes and dynamics with detected velocities $0.25c < \beta_{app} < 4c$. (Chang et al. 2010; Giroletti et al. 2012). The geometry of the M87 jet demonstrates a brake between parabolic and conical shapes Asada & Nakamura (2012a) suggesting a change of an external pressure profile in this region, in contrast to a recollimation shock origin of the HST-1 feature claimed in previous studies (Bromberg & Levinson 2009; Cheung et al. 2007; Stawarz et al. 2006), which also were supported by the semi-analytical and numerical Magneto-Hydrodynamic (MHD) models (Casadio et al. 2013; Gracia et al. 2009; Nakamura et al. 2010). But it is still a place for discussions since recently, a new interpretation emerged, in which the HST-1 feature is a relativistic jet spine (Punsly 2023).

Chapter 2

Properties of the jet in M87 revealed by its helical structure imaged with the VLBA at 8 and 15 GHz

Parts of this Chapter were published in Monthly Notices of the Royal Astronomical Society (Nikonov et al. 2023).

2.1 Observations and imaging

Full Stokes, full track dual-frequency observations of M87 were made in May 2009 using the Very Large Baseline Array (VLBA) involving the Karl Jansky Very Large Array (VLA) single antenna (Y1) and the 100-m Effelsberg Radio Telescope (Eb). The project code from the NRAO archive is BK145. We used Y1 to obtain the shortest baseline possible with this array, thereby improving the extended flux sensitivity, which is crucial in the case of the M87 jet. The Effelsberg was used to obtain higher sensitivity to weak and compact structures. Observations were performed on three consecutive days. This included U-band with a central frequency 15.4 GHz (later 15 GHz) on 22 and 24 May as well as X-band with a central frequency 8.4 GHz (later 8 GHz) on 23 May. The length of each day's observation was 12 hours. The data were recorded in 16 baseband channels (intermediate frequencies, IFs), each of 8 MHz bandwidths using 512 Mbps recording rate and 2-bit sampling. Both right- and left-hand polarisations were recorded simultaneously, giving a total observing bandwidth of 32 MHz in each polarisation.

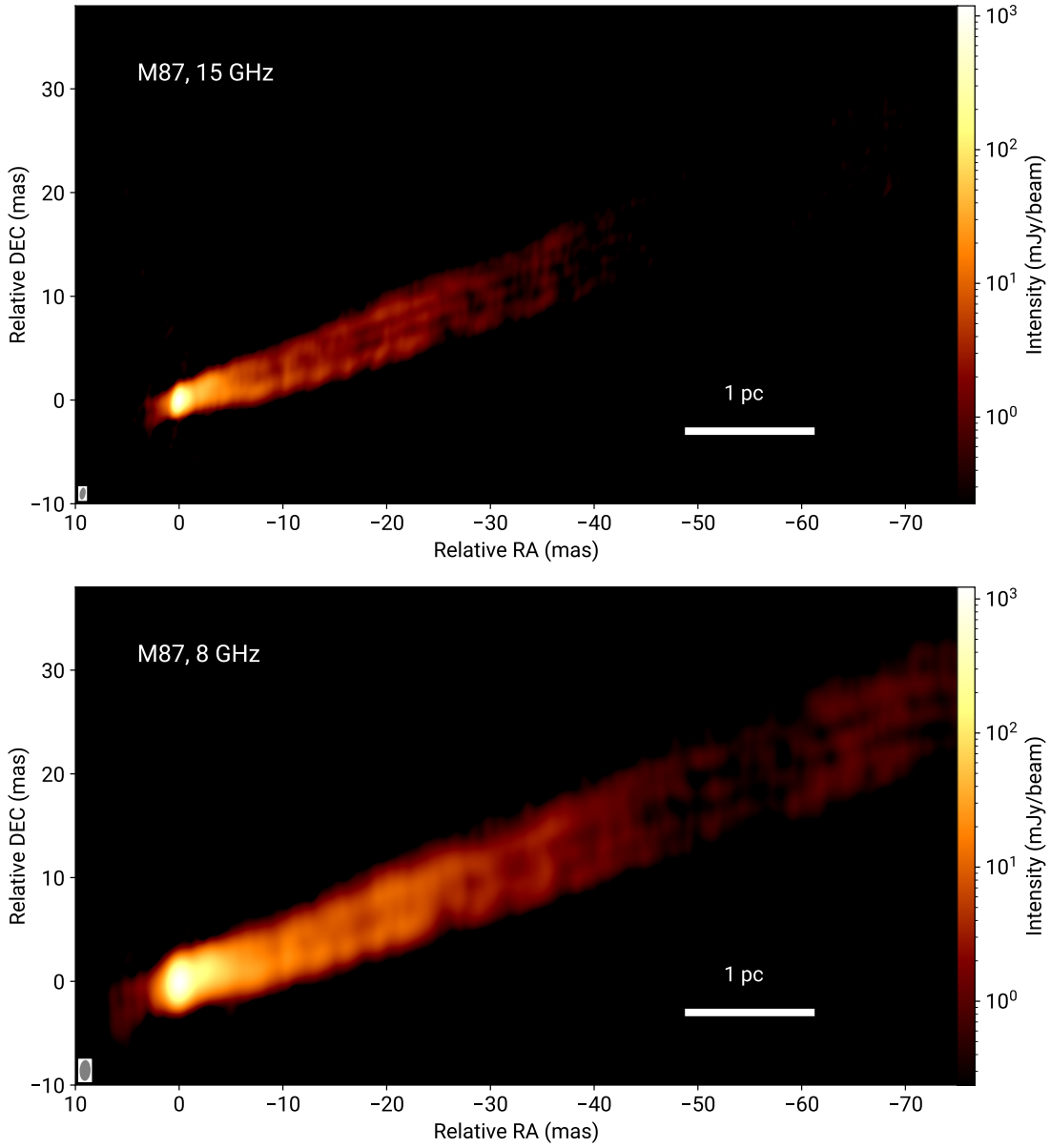

Figure 2.1: Total intensity `CLEAN` images of the jet in M87 at 15 GHz (top panel, combined data from May 22 and 24, 2009) and 8 GHz (bottom panel, data from May 23, 2009) with VLBA+Y1 configuration. Both images are reconstructed with a natural weighting of the visibility data. The peak flux densities are 1.23 Jy/beam and 1.22 Jy/beam, at 15 and 8 GHz, respectively. The elliptical restoring beams (full width at half maximum, FWHM) shown at the bottom left corner of each panel are 1.2×0.6 mas, PA $= -10°$ at 15 GHz, 2×1 mas, PA $= -2°$ at 8 GHz.

2.1.1 A priori data calibration

The data were edited and calibrated following traditional methods[1] in AIPS (Greisen 2003b). The quasar 0923+392 was used as a fringe finder. Polarisation leakage was calibrated with the AIPS task LPCAL using a 1308+326 calibrator. The electric vector polarisation angle (EVPA) was calibrated by comparing the measured EVPAs of OJ 287, 0923+392 and 1308+326 with the values obtained from the UMRAO database[2] and the VLA polarisation database[3] at 8 and 15 GHz. Due to a paucity of measurements, the values for the exact day of VLBA observations were found by linear interpolation of the UMRAO EVPAs from nearby dates. The final visibility data were averaged over 10 seconds. The AIPS task UVMOD was applied to the 22 and 24 May visibility data sets, creating a combined (u, v)-file at 15 GHz, to provide comparable to 8 GHz data sensitivity and, consequently, a higher quality of spectral index reconstruction.

2.1.2 Imaging

We used the Caltech DIFMAP (Shepherd et al. 1994) software to obtain Stokes I, Q and U maps from the calibrated visibility data using hybrid mapping in combination with super-uniform, uniform and natural weighting with pixel sizes of 0.08 mas at 15 GHz and 0.16 mas at 8 GHz. The final imaging results yielded >20,000:1 dynamic range at each frequency. The noise level is estimated (Hovatta et al. 2014) as $\sigma = (\sigma_{\rm rms}^2 + (1.5\sigma_{\rm rms})^2)^{1/2} \approx 1.8(\sigma_{\rm rms})$, where the first term is connected with the off-source rms noise level of the image $\sigma_{\rm rms} \simeq 35$ μJy beam^{-1}, and the second term is connected with the uncertainties of the `CLEAN` (Clark 1980) procedure.

We created two datasets: with and without data on baselines to Eb. All analysis in this paper was done with both datasets. For convenience, the final results in each section of the paper represent an average between results obtained with and without Eb baselines. In sections, where the difference between datasets is significant, the results of only one dataset are shown. For example, the resulting spectral index maps with the Effelsberg data show higher uncertainties as compared to the VLBA + Y1 configuration. Thus, the images presented in this paper use the conservative VLBA + Y1 configuration only as the "Atlantic gap" gives poor (u, v)-coverage between the main array and the Eb, which makes the image reconstruction process more complicated, which can be seen in the spectral index map. In addition, this makes a Kelvin–Helmholtz thread analysis more complicated. The resulting

[1] `http://www.aips.nrao.edu/CookHTML/CookBookch4.html`
[2] `https://dept.astro.lsa.umich.edu/datasets/umrao.php`
[3] `https://www.aoc.nrao.edu/~smyers/calibration/2009/`

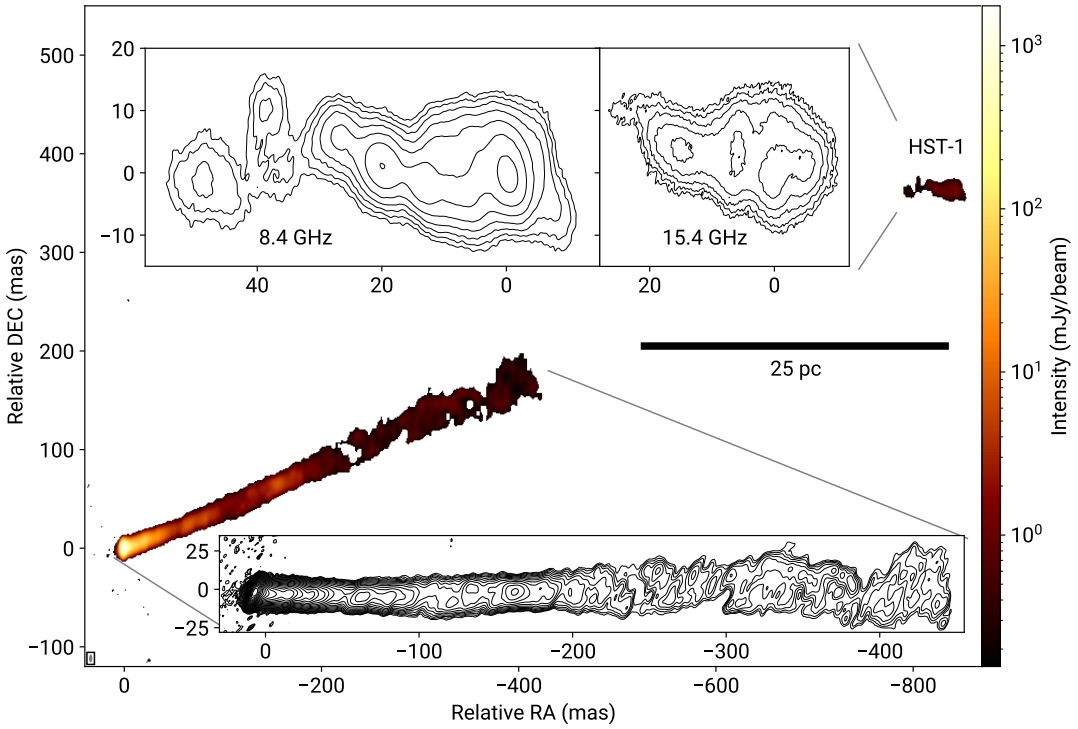

Figure 2.2: Total intensity image of the jet in M 87 at 8 GHz (colour) restored with an elliptical beam of 8×3 mas, PA $= 0°$ approximately equivalent to the restoring beam of a VLBA observation of M 87 at 18 cm. The peak flux density in the image is 1.7 Jy/beam. The HST-1 feature is located at ≈ 850 mas from the core. The insets show the contour image of the inner 450 mas of the jet at 15 GHz (bottom) and the HST-1 region at 8 GHz (top left) and 15 GHz (top right), with the lowest contour level at 156 μJy/beam and successive contour levels increasing by a factor of $\sqrt{2}$. The HST-1 feature has a peak flux density of 1.4 mJy/beam and 0.8 mJy/beam at 8 GHz and 15 GHz, respectively.

Stokes I images at 8 and 15 GHz are shown in Figure 2.1.

The lack of short baselines leads to a significant loss of flux from faint and extended features far from the core, especially at relatively high frequencies such as 8 and 15 GHz. Nevertheless, the data allowed reconstruction of the jet image until ≈ 450 mas and detect an HST-1 feature located at ≈ 850 mas from the core. To achieve a better dynamic range and to compare the results with the previous VLBA and EVN (European VLBI Network) HST-1 detections (Chang et al. 2010; Cheung et al. 2007; Giroletti et al. 2012), the images were convolved with an 8×3 mas beam, corresponding to a VLBA beam at λ 18 cm (Figure 2.2).

2.2 The M87 jet structure

2.2.1 Jet shape

Jet morphology provides crucial information for understanding the formation and propagation of relativistic outflows. The observed shape of an AGN jet depends on a number of parameters describing physical conditions in the jet plasma and in the ambient medium. So the knowledge of the shape and geometry of the flow can help us estimate intrinsic jet parameters (Algaba et al. 2017; Kovalev et al. 2020b; Nokhrina et al. 2019, 2020; Pushkarev et al. 2017b).

In M87, the jet manifests a complex and asymmetric triple-ridge internal structure developing in a predominantly straight, expanding flow. To analyse this structure, we first determine the direction of the jet axis by estimating the overall jet position angle (PA). To avoid potential uncertainties and errors due to the local curvature of the jet near its origin, we estimated the general PA of the jet position of the knot HST-1 in the large-scale image of the jet obtained from our data and presented in Figure 2.2. Using the intensity maximum of the HST-1, we obtained P.A. $= 293\overset{\circ}{.}3 \pm 0\overset{\circ}{.}5$. Note the significant difference of several degrees from results by (Plavin et al. 2022) due to the different utilized methods of P.A. measurements.

To simplify the further analysis, we rotate the jet images clockwise by $\psi = 23\overset{\circ}{.}3$ to coincide the jet axis and relative right ascension and obtain transverse profiles of brightness distribution in the jet. In order to highlight the triple-ridge structure, a stack profile is shown in Figure 2.3. It was made by averaging all individual profiles with a step of 0.05 mas at 15–25 mas from the VLBI core. In the jet images produced with the nominal restoring beam, the jet structure up to ≈ 40 mas and ≈ 80 mas, in the 15 GHz and 8 GHz image, respectively can be traced. The 8 GHz image can be further convolved with a larger beam $\approx 1/3$ of the jet width in the outer parts (3 mas), which allows us to trace the jet structure with the transverse brightness distribution profile measured up to ≈ 200 mas separation from the jet origin.

Below, we apply the transverse profiles to measure the evolution of the jet width and quantify the properties of the internal structure of the flow. For both of these tasks, we fitted the obtained profiles with multiple Gaussian components defined as:

$$I(x) = \sum_i A_i e^{-(x_i - b_i)/2c_i^2}, \tag{2.2.1}$$

where x is a transverse distance, the i-th component is described by A_i peak amplitude, b_i peak location, and FWHM full width at half maximum, calculated from $\mathrm{FWHM}_i = 2(2\ln 2)^{1/2} c_i$.

The number of Gaussian components used in fitting of each profile was chosen using an χ^2 analysis. Each profile was fitted by a multi-Gaussian function with a different number of components, where the maximum quantity is 3. Afterwards, the reduced χ^2 with q degrees of freedom for all fits for a given intensity profile were compared according to Avni (1976). The number of degrees of freedom $q = n - p$, where n is the number of beams which can be fitted inside the transverse profile, and p is the number of the fitting parameters. Using a cumulative distribution function of χ^2, the theoretical value of $\Delta(q, \alpha) \geq \chi^2$ can be calculated, where the probability of this expression equals $\alpha = 95\%$ (the confidence level). In this method, the $q + 1$ degrees of freedom model is preferred if the following ratio is satisfied:

$$\frac{\chi^2_q}{\chi^2_{q+1}} \geq \frac{\Delta(q+1, \alpha)}{\Delta(q, \alpha)}. \tag{2.2.2}$$

The width of the jet in a particular image profile was defined as a Full Width at a Quarter Maximum (FHQM) of the fit of the profile. The quarter maximum level was chosen because of the complex and asymmetric transverse structure of the M87 jet, where multiple components can have more than twice the brightness difference. In this case, the usage of the half maximum level can be misleading by measuring the width of one component instead of the whole jet.

After obtaining the jet width as described above, we deconvolved it with the beam projected onto a transverse profile. In our case, one-dimensional (1D) deconvolution procedure was done according to $w = (\mathrm{FWQM}^2_{\text{jet width}} - \mathrm{FWQM}^2_{\text{beam}})^{0.5}$, where w is the deconvolved jet width. In this case, a 1D deconvolved profile can be distorted by a two-dimensional (2D) elliptical beam which influences several profiles asymmetrically. In our data, the major axis of a beam is oriented roughly perpendicular to the jet direction, thus the distortions should be negligible. At the same time, in addition to restoring elliptical beams, we reconstructed images using equivalent area circular beams. Such maps should deliver even less biased results and be easier to analyze. Indeed no significant difference was found between the geometry obtained with circular and elliptical beams.

To investigate the jet geometry, we follow Kovalev et al. (2020b) fitting the expansion profile by a power-law function $w \propto (r + r_0)^k$, where r is the distance from the apparent VLBI core, r_0 is the distance from the core to the jet base, the expansion index k shows the jet geometry. In Figure 2.4 the fitting results of the expansion profile are presented. For this, we used the jet images convolved with a circular beam of the FWHM-size 0.86 and 1.56 mas having an equivalent area of 15 and 8 GHz elliptical beam, respectively. In addition, the geometry of the 200 mas long jet image at 8 GHz convolved with 3 mas circular beam is also presented in Figure 2.4. Jet geometry parameters were obtained for images with

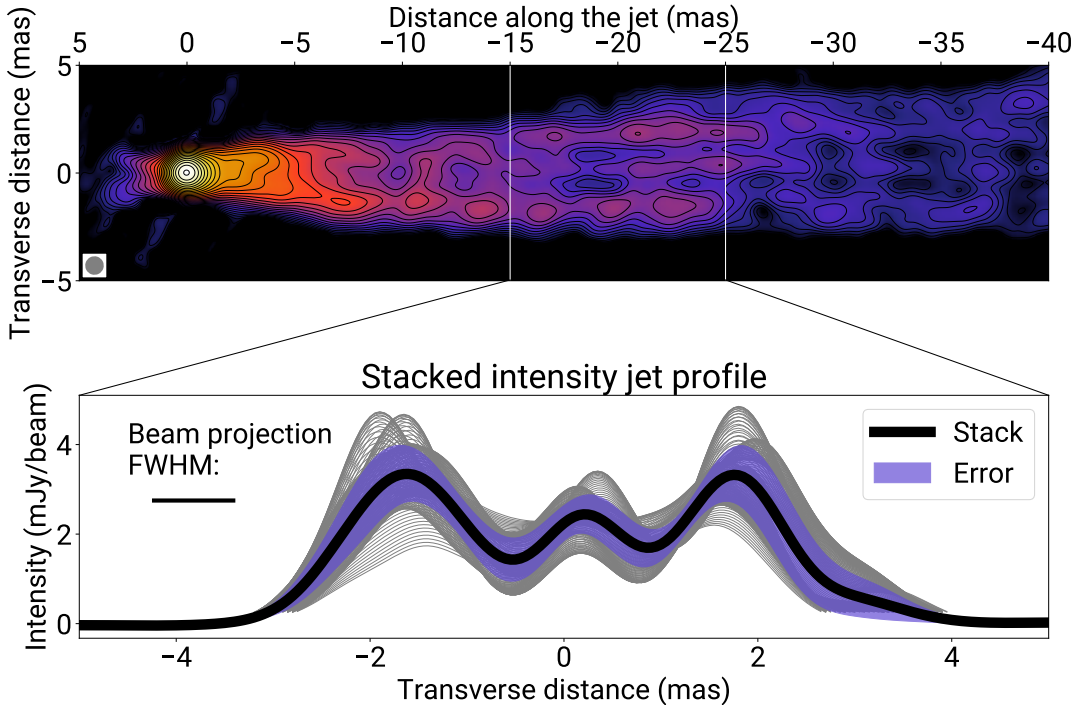

Figure 2.3: Top: Total intensity image of the jet in M87 at 15 GHz, restored with a circular beam of 0.84 mas FWHM (equivalent in area to the elliptical restoring beam used in Figure 2.1). The peak flux density is 1.23 Jy/beam. The intensity contours start at 190 μJy/beam and successive contour levels increase by a factor of $\sqrt{2}$. Bottom: The stacked profile of the jet brightness obtained by averaging all individual transverse profiles measured with a step 0.05 mas in the jet at 15–25 mas separations from the core (solid black line) and its statistical error (violet filling).

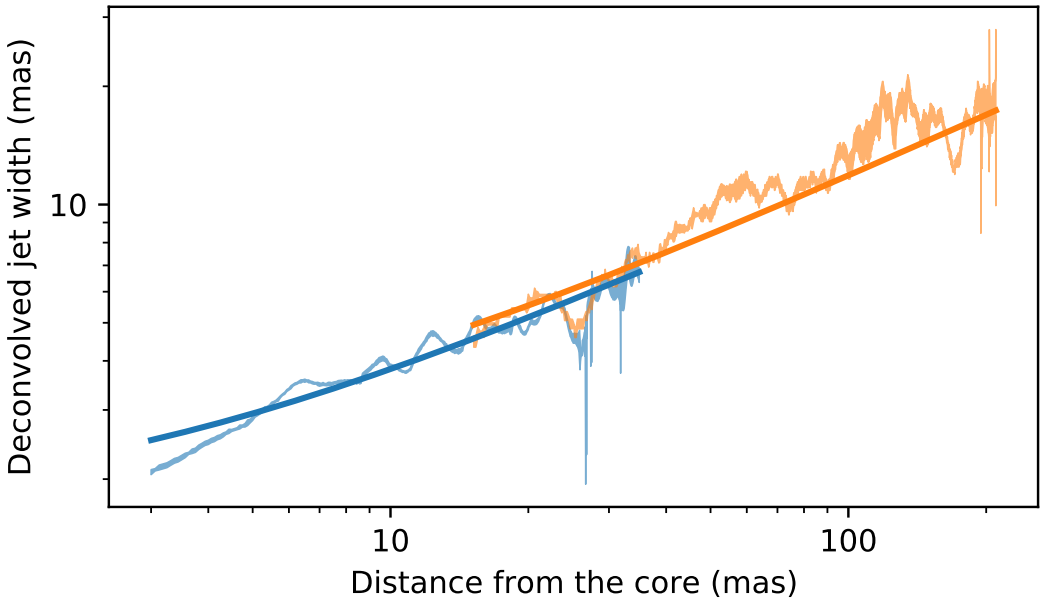

Figure 2.4: Expansion profile of the M87 jet at 15 and 8 GHz. The measurements of a jet width and uncertainties are shown as semi-transparent plots. The best-fit results are shown by solid lines. The blue colour represents the measurements taken with the 15 GHz intensity model convolved with a circular beam of 0.86 mas FWHM which has an equivalent area of a 15 GHz elliptical beam. The orange colour displays jet widths measured in the 8 GHz intensity model convolved with a 3 mas circular beam. This beam size was used to have the ability to trace extended up to 200 mas faint jet, that is barely visible with the conservative beam (subsection 2.2.1).

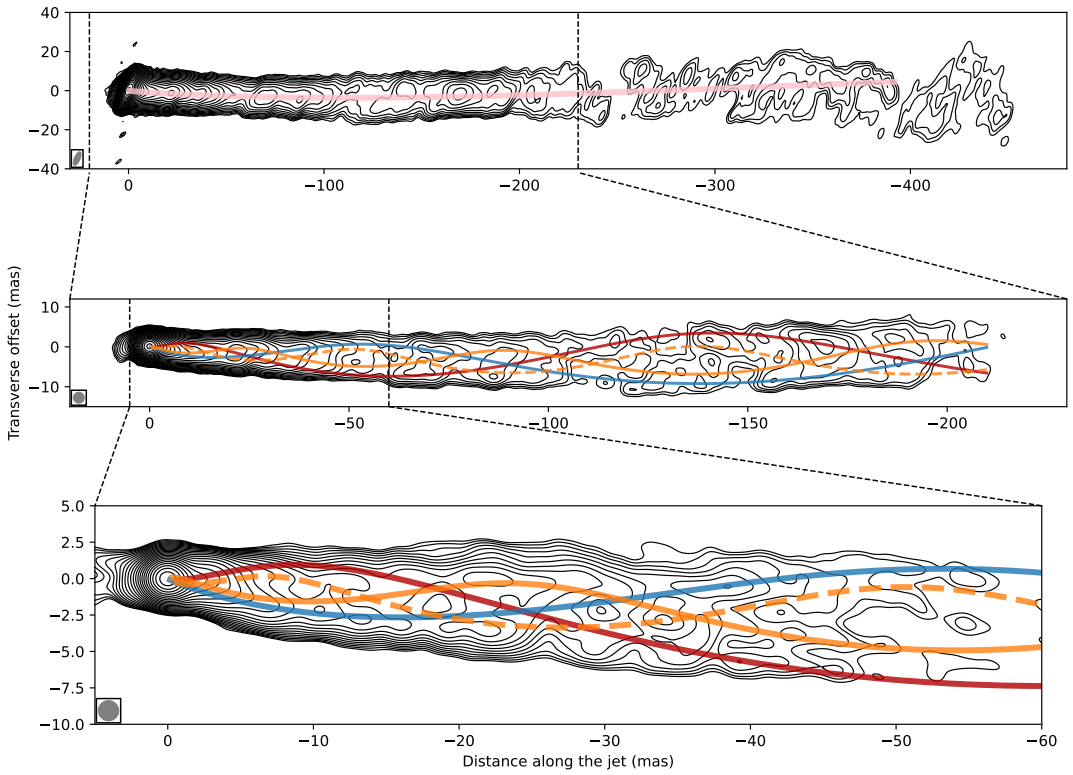

Figure 2.5: Modelling the transverse profiles of the jet brightness with oscillatory patterns. Semi-transparent curves represent the respective KH model. The dashed orange curve shows the model of the same colour but with the 180° phase offset, indicating the approximate trajectory of the anticipated secondary thread of the elliptical body mode. All Stokes I images shown in contours represent the same data restored with a different beam. Top panel: the beam (8×3 mas, PA $= 0°$) is shown at the bottom left corner. The map peak flux density is 1.7 Jy/beam. The intensity contours start at 260 μJy/beam level. Middle: the image is convolved with 3 mas circular beam and has a peak flux density of 1.7 Jy/beam. The intensity contours start at 360 μJy/beam level. Bottom: the innermost 60 mas section of jet. The image is convolved with a circular beam of 1.56 mas in diameter, which has an equivalent area of the elliptical beam used in Figure 2.1. The image peak flux density is 1.3 Jy/beam, and the intensity contours start at 494 μJy/beam level. In all panels, successive contour levels increase by a factor of $\sqrt{2}$. The jet images were rotated by the $\psi = 23.^{\circ}3$, which was estimated in subsection 2.2.1.

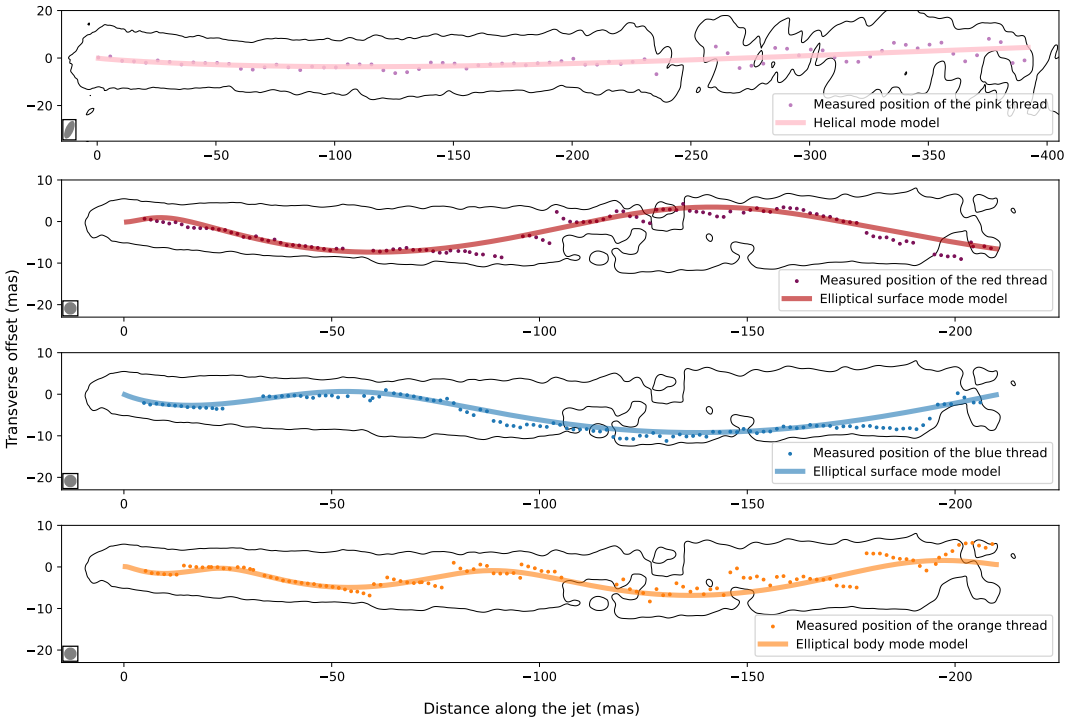

Figure 2.6: Jet decomposition by the oscillatory modes. Each extracted thread from the jet intensity images is presented in a separate sub-figure as a dotted plot with the corresponding colour according to the values listed in Table 2.1. To improve clarity, every tenth data point is plotted. A fitted KH model is displayed here as a curve with a corresponding colour. All plots show the lowest contour of the corresponding intensity image from Figure 2.5. Top panel displays the intensity contour at 260 μJy/beam level. The beam (8×3 mas, PA $= 0°$) is indicated at the bottom left corner. The remaining sub-figures display intensity contour at the 360 μJy/beam level, where the image was convolved with a 3 mas circular beam. The jet images were rotated by an angle of $\psi = 23.^{\circ}3$, which was estimated in subsection 2.2.1.

Table 2.1: Identification of Kelvin-Helmholtz plasma instability modes.

Thread (1)	A_0 (mas) (2)	λ_0 (mas) (3)	ϕ_0 (°) (4)	Mode (5)
Pink	0.42 ± 0.06	126 ± 30	188 ± 18	H_s
Red	0.64 ± 0.02	33.2 ± 1.4	340 ± 14	E_s
Blue	0.53 ± 0.06	32.7 ± 1.2	156 ± 11	E_s
Orange	0.308 ± 0.002	16.8 ± 0.2	66 ± 7	E_{b1}

The table shows: (1) thread name by colour according to Figure 2.5, (2) amplitude and (3) wavelength of an oscillatory pattern in $R_{jet} = 1$ mas area, (4) phase of a helix, (5) identified instability modes: E_s (Elliptical surface mode), E_{b1} (First-order elliptical body mode), H_s (Helical surface mode).

different array configurations (VLBA+Y1; VLBA+Y1+Eb), frequencies (8 and 15 GHz), and for extended 200 mas jet at 8 GHz. Finally, all obtained results were averaged to obtain the final M87 jet geometry parameters: $k = 0.532 \pm 0.008$, $r_0 = 3.8 \pm 1.1$ mas. The r_0 estimate by this method has a large uncertainty and is higher than expected; compare with Hada et al. (2011a), where the VLBI core separations are about 0.2 mas for 8 and 15 GHz. A possible r_0 overestimation may result from methodological complications. First, the r_0 value in the fitting procedure is sensitive to the absolute value of the jet width in contrast to k, which is sensitive to the relative width. The uncertainty of absolute values is mainly driven by the deconvolution procedure. Second, physical conditions in the jet can change geometry locally, leading to over- or underestimations in r_0 estimates. In order to improve future measurements, a dedicated study of a possible deconvolution bias and geometry variations is needed on a large sample of AGN jets (e.g. Kovalev et al. 2020b).

2.2.2 Kelvin-Helmholtz instability

Transverse oscillations in the M87 jet were analysed in previous studies. The 17-year observations at 43 GHz by VLBA show a shift of the transverse position of the jet on a quasi-periodic 10-year timescale that is consistent with the Kelvin-Helmholtz instability (Walker et al. 2018). Recent studies of the M87 jet show a 1-year period wiggles in multi-epoch 22 GHz KaVA VLBI observations (Ro et al. 2023b). It is still unclear what is the origin of these fast oscillations, but current-driven instability (CDI) was chosen as a preferable mechanism. Cui et al. (2023) analysed the periodicity of the P.A. of the jet using 22-43 GHz EAVN, VLBA and EATING VLBI observations, where the phenomenon was interpreted as the jet nozzle precession with a period of ≈ 11 years.

The data analysed in this article provide the most prominent, sensitive and extended pc-scale jet structure. In Figure 2.1 the brighter jet limb changes from the northern to the southern edge of the jet at a relative RA ≈ -10 mas and vice versa at a relative RA ≈ -25 mas), and this effect is observed in both the 8 GHz and the 15 GHz maps (Figures 2.1–2.3). Similar behaviour (changes of the brighter limb and multiple threads inside the jet) can be seen in the pc scales VLBA and RadioAstron observations (Savolainen 2021; Walker et al. 2018), the kpc scales in the VLA (Owen et al. 1989; Pasetto et al. 2021b) and the HST (Sparks et al. 1996) images. The pattern was interpreted as resulting from the KH instability in the flow (Lobanov et al. 2003).

At the distances within 15-25 mas from the core a triple-ridge structure is observed in 15 GHz map (Figures 2.1, 2.3). The central filament has been observed before in several studies both in proximity to the radio core (Asada et al. 2016; Kim et al. 2018; Walker et al. 2018) and downstream (Hada 2017) and associated with the spine in the 'spine-sheath' jet model (Mertens et al. 2016b). The simulations done by Pashchenko et al. (2023) show that the central filament might be found in an edge-brightened model due to a `CLEAN` imaging artefact. At 15 GHz the jet width coincides with three beam sizes in that region. This can cause an overlay of beam sidelobes, creating the apparent central filament. This hypothesis is supported by the absence of a prominent central ridge at 8 GHz image, where the jet width is about two beams. For this purpose we use 8 GHz maps for this analysis.

In subsection 2.2.1, the jet transverse profiles were modelled by Gaussian components. The positions of the peaks of those components obtained for the inner and outer parts of the jet were superimposed together on the intensity image (bottom plots of Figure 2.5), thus allowing us to trace the development of the jet structure on scales of up to $\sim$200 mas from the observed jet origin. The revealed jet pattern suggests the presence of up to three intertwining helical threads inside the jet, which can be related to the development of KH instability inferred for the kpc-scale jet.

Identifications of each of the individual threads were made by requiring a continuous and smooth evolution of thread parameters, such as position, intensity, and width along the jet. Using this approach, a self-consistent picture of the evolving thread-like patterns inside the jet was reconstructed.

In addition to the rich evolution of the internal structure, the jet exhibits a slight bend $\approx$80 mas which is clearly visible in Figure 2.2. To quantify the position and the magnitude of this bent, the 400 mas jet image with 18 cm VLBA beam was used. The image was rotated 23.°3 clockwise, and all transverse intensity profiles were fitted by a single Gaussian, obtaining the ridgeline (the blue line in

the top of Figure 2.5).

Both, the observed bent and the pronounced internal structure observed in the jet can result from the development of the KH instability in the flow (Hardee 2003; Lobanov et al. 2003). The changes in the ridge line and the evolution of the individual threads identified inside the flow can be well described by a three-dimensional (3D) helix in a Cartesian coordinate system (x, y, z):

$$[x, y] = A[\sin, \cos]((2\pi/\lambda)z + \phi), \tag{2.2.3}$$

where z is the distance from the jet origin, ϕ is the phase, and the amplitude and the wavelength depend on the jet radius $A \propto R_{\rm jet(z)}$, $\lambda \propto R_{\rm jet(z)}$ (Hardee 2000).

First, we fitted the global jet curvature by a 3D helix projected onto the sky plane, for which the jet angle to the line of sight $\theta = 17.^{\circ}2$ (Mertens et al. (2016b)) was used. The resultant mode can be associated with the helical surface mode ($\rm H_s$) of the KH instability as it apparently leads to oscillations of the entire jet around its average propagation direction. In order to measure more accurately the parameters of the modes affecting the internal structure of the flow, this mode was subtracted from the component positions before the fitting procedure. A robust identification of the other modes can be obtained using the characteristic wavelength $\lambda^* = \lambda_{nm}(n + 2m + 0.5)$, where λ^* is the characteristic wavelength, λ_i is the observed wavelength, n is the azimuthal wavenumber and m is the order of the mode. The pinch ($n = 0$), helical ($n = 1$) and elliptical ($n = 2$) modes are expected to be most prominent in relativistic jets. The order of the mode m determines whether the corresponding perturbation affects the surface ($m = 0$) or the interior ($m > 0$) of the jet. The characteristic wavelength depends only on the physical conditions in the jet; thus, should have a similar value for different modes (Lobanov & Zensus 2001). The final fitting results are presented in Figure 2.5 and Figure 2.6 by semi-transparent thick pink, red, orange and blue curves. A zoom into the innermost 60 mas section of the jet is shown in the bottom panel of Figure 2.5. The identification criteria discussed earlier were applied to the extracted individual threads resulting in one plausible combination of KH modes shown in Table 2.1. The red and blue threads have nearly equal wavelengths and $\approx 180^{\circ}$ phase difference, which is expected to result from the two regions of increased pressure and density produced in the jet by the elliptical surface ($\rm E_s$) mode of instability (Hardee 2000). The orange thread has a much shorter wavelength with a smaller amplitude, which is expected in the case of the body mode. In the case of a first-order elliptical body mode ($\rm E_{b1}$), one should observe the accompanied thread. For illustration purposes, the thread with the same parameters, but with the 180° phase difference was plotted as a dashed curve of

the same colour in Figure 2.5. Due to the lack of high-enough resolution, the accompanied thread was not identified robustly and extracted from the data since it is blended with the other modes. However, it is observed that the dashed curve plotted in Figure 2.5 complements the KH model well, describing the intensity images better.

To verify the robustness of the fitting procedure, we generated a synthetic dataset reproducing the internal structure with the parameters of all fitted modes. For this, we first created a model image using the parabolic jet model threaded by the KH modes obtained from the fits to the 8 GHz image. Then we created artificial uv-data using the same uv-coverage and thermal noise, as in the original 8 GHz data set. The same algorithms of the image reconstruction and the KH modes fitting were applied to the artificial data set. The derived parameters of the KH modes were found to be consistent with the ground truth values within 25%. First, this demonstrates that our approach can reconstruct the parameters with the accuracy required to distinguish between two modes (surface and body). Second, the obtained accuracy of the method shows that two threads of the elliptical surface mode are consistent with having the same observed wavelength and the 180° phase offset.

2.3 Spectral index map

The main mechanism of AGN radio jet emission is synchrotron radiation. Assuming a power-law particle energy distribution $N(E)dE \propto E^{-p}dE$, the jet spectrum for the optically thin regions is then described by a distribution $I_\nu \propto \nu^\alpha$ with a spectral index $\alpha = (1-p)/2$. Therefore, the spectral index distribution provides important information about the physical conditions of different jet regions. Due to phase self-calibration, the information about absolute celestial coordinates is lost. Thus, images at different frequencies need to be well aligned to determine spectral index distributions. For this reason, the normalised 2D cross-correlation (2DCC) method was used (Croke & Gabuzda 2008; Fromm et al. 2013; Hovatta et al. 2014; Lewis 1995; Walker et al. 2000). The method uses optically thin parts of a jet as a reference. Due to their transparency, these parts can be assumed to be located in the same place at both frequencies. So choosing the jet image regions far away from the core and applying a normalized 2DCC, we can align the images at different frequencies.

The spectral index of the M87 jet obtained between 8 and 15 GHz is shown at the top of Figure 2.7. Note that the two used images have comparable sensitivity. Due to the sparsity of the visibility plane coverage, a bias in the resulting spectral index image might be significant; see analysis in Pashchenko et al. (2023). Thus,

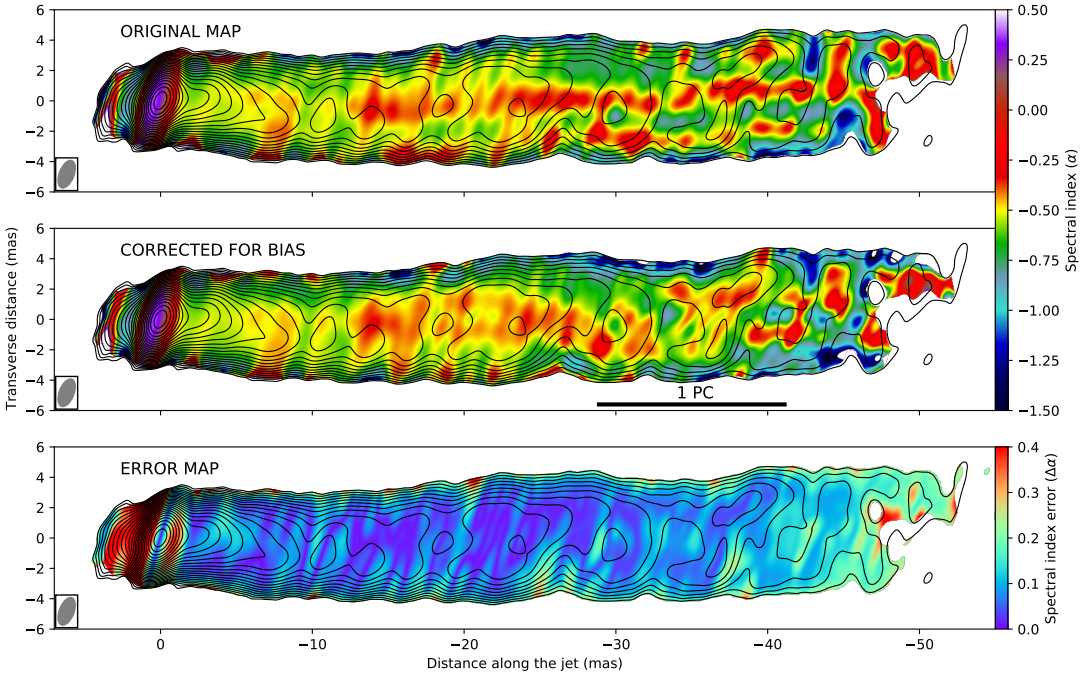

Figure 2.7: Spectral index map between 8 and 15 GHz, shown as a false-colour image before correction (top), after correction (middle) and error (bottom) map. All images are rotated 19° clockwise. The rotation of the map applied here does not correspond to the global jet PA to follow the local curvature of the jet. The size of the common 8 GHz restoring beam is displayed at the bottom left corner and is equivalent to 2×1 mas at PA $= -2°$ ellipse. The contours represent the 8 GHz total intensity map, starting from 360 μJy/beam level and increasing by a factor of $\sqrt{2}$. Only the inner 50 mas of the jet is shown due to the large spectral index errors in the outer regions.

we estimated the effect of the bias and corrected for it, see details in section 2.3.2. The final unbiased spectral index maps are shown in Figures 2.7 and 2.10. The spectral index profile along the jet axis is presented in Figure 2.8.

Quasi-periodic oscillations of width along the jet are observed in the geometry profile Figure 2.4. Additionally, Figure 2.8 shows deviations of a measured jet width at 8 and 15 GHz from the fitted 15 GHz power-law model. The oscillations exhibit quasi-periodic deviations from the parabolic shape with an amplitude up to 0.7 mas. This result cannot be an imaging effect since the oscillations are seen at both observing frequencies with equal periodicity and at the same distances. Moreover, the contraction near 5 mas is also observed at different epochs (Mertens et al. 2016b; Walker et al. 2018, and Kravchenko et al. *in prep.*). We suggest that this is caused by stationary recollimation shocks. The spectral index map profile in Figure 2.8 supports this assumption. There is evidence that recollimation shocks are seen in VLBI observations. In addition, a simulated VLBI total intensity map obtained by computing the radio continuum synchrotron emission using the relativistic magnetohydrodynamic (RMHD) model shows similar periodic contractions (Gómez et al. 2016). Periodic oscillations are also seen in other RMHD simulations (Fuentes et al. 2018; Mizuno et al. 2015). Our results are qualitatively consistent with other observations and simulations, but individual simulations are needed for a detailed comparison.

The M87 jet spectral index analysis results at 8–15 GHz obtained by Hovatta et al. (2014) show a moderate steepening of the spectra within 10 mas down to $\alpha \approx -1.5$. The recent results, observed at 22–43 GHZ show a rapid steepening down to $\alpha \approx -2.5$ within 10 mas from the VLBI core (Ro et al. 2023a). However, in this paper, there is no significant steepening in the same region. The interesting part of all these data is they all have a similar resolution, thus it is not a consequence of a resolution effect. In order to explain this discrepancy, several reasons are proposed. If the effect is intrinsic, then it can be caused by synchrotron radiation losses (Kardashev 1962; Pacholczyk 1970). This interpretation can be used in the case of NGC 315, where a similar effect was observed in two papers Park et al. (2021) and Ricci et al. (2022). For this source in the same region, the spectral index steepens with the frequency. The other reasonable interpretation is the temporal variations of the spectral index in combination with the multi-layer jet structure. The last can produce several electron plasma populations with different energy distributions that will create a broken power-law spectrum. If the effect is instrumental, it can be caused by high-frequency flux losses due to `CLEAN` bias (Pashchenko et al. 2023). In this case, the residuals of the high-frequency image are convolved with a high-frequency beam, that is smaller than the lower-frequency beam. Thus, if `CLEAN` is not deep enough, this will reduce the flux value in the

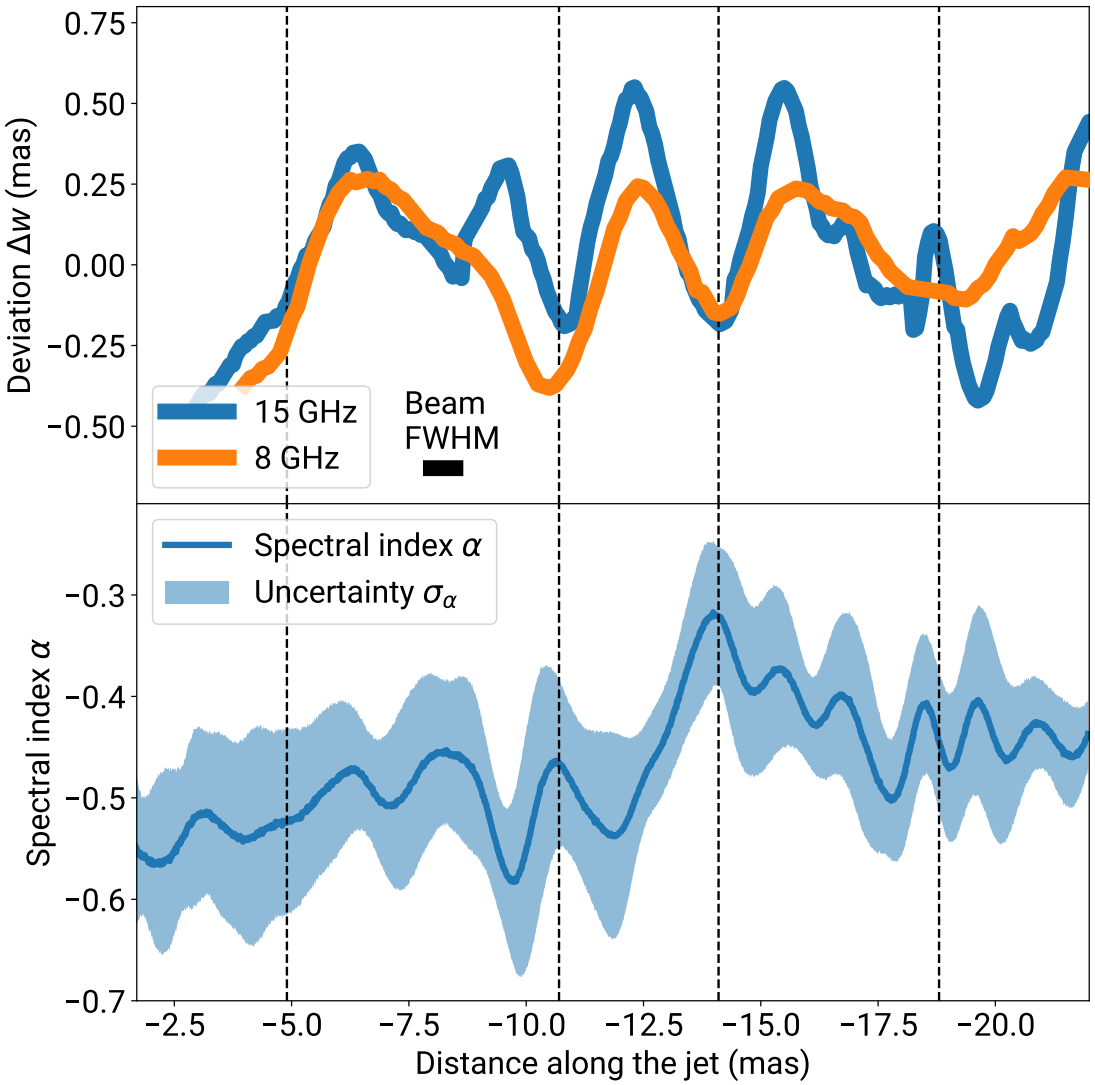

Figure 2.8: Deviations $\Delta w = w_i - w(r)_{\rm model}$ between the measured jet widths w_i and the fit by a power law curve $w(r)_{\rm model} \propto (r + r_0)^k$ (top). The blue lines represent 15 GHz data, the orange lines represent the 8 GHz data. The spectral index longitudinal profile is obtained from Figure 2.7 and presented here as a light-blue filled plot (bottom). The plot shows quasi-periodic oscillations at both frequencies indicated by the black dashed lines.

extended regions of the high-frequency image. In this paper, to avoid this effect, deep `CLEAN` was performed. In addition, the unique feature of the data in this paper is twice the difference in exposure time between 8 and 15 GHz. It was done to reduce the noise in 15 GHz data to make it correspond to the 8 GHz data. Thus, the spectral index map produced in this paper may be less affected by this effect, which is observed as the absence of the significant spectral index steepening along the jet.

2.3.1 Core shift

Due to synchrotron self-absorption, the location of the VLBI core depends on the frequency of observations as $\vec{r}_c(\nu) \propto \nu^{-1}$ (the so-called 'core shift' effect), under the assumption that the jet is expanding freely, and there is equipartition between the particle kinetic and the magnetic field energy (Lobanov 1998c). The observations show that the core shift in the many AGN jets indeed follows dependence $\vec{r}_c(\nu) \propto \nu^{-1}$ (Sokolovsky et al. 2011). Moreover, using the phase-referencing multi-frequency observations of M87, Hada et al. (2011b) show that the core shift is described by $\vec{r}_c(\nu) \propto \nu^{-0.94\pm0.09}$. Assuming $\vec{r}_c(\nu) \propto \nu^{-1}$, we can estimate the distance from the 15 GHz core ν_{15} to the jet origin as:

$$\vec{r_c}(\nu_{15}) = \frac{\Delta\vec{r}}{\frac{\nu_{15}}{\nu_8} - 1}, \tag{2.3.1}$$

where $\Delta\vec{r}$ is the core shift vector. To obtain the core shift vector, we measured the core positions and the alignment shift. To find the core positions, we used the MODELFIT function in DIFMAP: the M87 image was fitted with a model consisting of 2D Gaussian components. The coordinates of the model components, which have the highest brightness, were used as the core position relative to the phase centre ($\vec{r}_8$ for 8 GHz and $\vec{r}_{15}$ for 15 GHz). The shift between images $\vec{r}_{8\rightarrow15}$ was obtained using 2DCC at the beginning of section 2.3, where images were aligned for constructing the spectral index map. Finally, we calculate the core shift vector as $\Delta\vec{r}_{8\rightarrow15} = \vec{r}_8 - \vec{r}_{15} - \vec{r}_{8\rightarrow15}$.

Averaging the results of the measurements for all restored images with different beams and antenna configurations, we estimated $|\vec{r}_c(\nu_{15})| = 0.2 \pm 0.1$ mas. This result is consistent with the phase-referencing core shift measurements Hada et al. (2011a). Neglecting the distance from the central SMBH to the jet origin (which is predicted to be about 2.5–4 R_g (Doeleman et al. 2012)), $|\vec{r}_c(\nu_{15})|$ represents the separation of the 15 GHz VLBI core from the central SMBH. Finally, using $\theta = 17.^{\circ}2 \pm 3.^{\circ}3$ (Mertens et al. 2016b) (subsection 2.3.3), we obtained the deprojected distance from the 15 GHz VLBI core to the black hole: $r_{\rm deprojected} = 0.7 \pm 0.3$ mas

or $(5 \pm 2) \times 10^{-2}$ pc.

2.3.2 Uncertainties

Statistical error of the map

The lower the intensity, the lower the signal-to-noise ratio and the larger the errors in the resulting spectral index map. The errors can also be influenced by uncertainties of image shift correction. To estimate the accuracy of the spectral index measurement, a spectral index error map was made. The error consists of the error caused by the uncertainty of the intensity measurement σ_{I} and the uncertainty of the alignment of the image σ_{cs}, thus the spectral index random error is $\sigma_\alpha = (\sigma_{\mathrm{I}}^2 + \sigma_{\mathrm{cs}}^2)^{1/2}$.

For the errors caused by the intensity measurement uncertainties:

$$\sigma_{\mathrm{I}} = \frac{1}{\log(\nu_{\mathrm{U}}/\nu_{\mathrm{X}})} \sqrt{\left(\frac{\sigma_{\mathrm{X}}}{I_{\mathrm{X}}}\right)^2 + \left(\frac{\sigma_{\mathrm{U}}}{I_{\mathrm{U}}}\right)^2}, \tag{2.3.2}$$

where $\sigma_{\mathrm{X}}, \sigma_{\mathrm{U}}$ are the intensity maps errors, and I_{X}, I_{U} are the intensity maps at 8 and 15 GHz, respectively. The errors caused by the uncertainty of the image alignment σ_{cs} were obtained with the help of the algorithm:

1. Define the uncertainty of alignment. In this case, the error is 2 pixels or 0.025 mas.

2. Shift the map in the alignment uncertainty value in four different directions and obtain spectral index maps.

3. Subtract modulo for each of the four obtained maps with the original spectral index map.

4. Average all four maps.

The bottom image of Figure 2.7 displays the final spectral index error map. The error rises to the edges discussed earlier. Also, one can see that the error grows dramatically near the VLBI core. This is caused by the large gradient in intensity images near the core region, so the image alignment uncertainties produce significant errors. If the difference between neighbouring pixels along the jet axis in intensity images is high, then even a 1-pixel shift can dramatically change the resulting spectral index value. The rapid decrease of intensity in images southeast of the core is caused by the synchrotron self-absorption of a jet base and the transition from Doppler boosted to deboosted emission of the jet and the counter-jet. The region of a relatively large error ends at ≈ 0.5 mas southeast of

the core, and the counter-jet area errors are significantly lower. This is another indication that the faint feature southeast to the core is counter-jet. The errors in the regions further than ≈ 50 mas are high, so we decided to show a spectral index map within 50 mas.

Effects of the sparsity of visibility plane

Since the (u, v)-coverage is sparse, the restored beam takes a complicated shape with notable side lobes. The `CLEAN` algorithm is unable to completely remove them because the flux is subtracted not only from the regions of maximum intensity but elsewhere. This creates a bias on a residual image, and artefacts can appear. After that, a `CLEAN` model is convolved with a `CLEAN` beam or a 2D Gaussian function approximation of a dirty beam. Thus, the side lobes are not taken into account, and convolution errors (bias) can appear. A spectral index map is especially sensitive to this effect.

The coverage of the visibility plane depends on frequency. Even in the case of the same antennae configuration in dual-frequency observations, the pattern of the obtained (u, v) coverage will be the same, but the size will be different. So the coverage at 8 GHz will look like a stretched version of the 15 GHz (u, v) data. Thus, initially, the (u, v)-ranges do not correspond to each other, and it can cause errors or imaging artefacts which can become significant in spectral index maps, such as a steepening of the spectral index along a jet (Hovatta et al. 2014).

To test how inconsistency of the (u, v)-ranges affects the spectral index map, the (u, v)-coverage was clipped to be the same in both bands. Surprisingly, a comparison of original and (u, v)-clipped data made an insignificant difference. Thus, uv-clipping was not applied to obtain the final spectral index map, shown in the paper. The sparsity effects are much more difficult to check since it is based on the fundamental problem of deconvolution. However, it is possible to estimate the influence of this effect on the spectral index map. Here are the steps of bias checking applied in the paper:

1. Create an artificial model out of the `CLEAN` components whose structure is similar to the real jet in its form and intensity.

2. Create visibility functions with the same model but different (u, v)-coverage (at 8 and 15 GHz), using the UVMOD task in AIPS.

3. Do imaging in DIFMAP.

4. Obtain a spectral index map.

The obtained spectral index map should have zero values in a range of all maps, in the absence of a bias. In the real-intensity image, we can see the edge-brightening effect. To describe the jet and create a synthetic model, we assumed that the jet is hollow and used simple geometrical shapes. Since the edge-brightened jet is transparent and the core is opaque, we can define the core as a circle and the limbs as two expanding rails. The overall jet model was also inclined in a corresponding P.A. This model was chosen to bring the simulation closer to the observations.

Analysing the results with different beams, we conclude that the spectral index map convolved with the 8 GHz elliptical beam has minimal influence on the convolution effect with the error $\Delta\alpha \lessapprox 0.13$ in the central ridge region. Since, in the case of the VLBA+Y1+Eb dataset, the long-baseline coverage is poor, the problem of the convolution effect is more significant compared to the data with flagged Eb. It is seen that with increasing the resolution, the bias amplitude increases too. But its pattern is not truly aligned to the flattened spectrum in a ridge which was noticed in the spectral index map (Figure 2.7). The results of modelling also showed that the amplitude of the bias is less than the flat spectrum region values. Thereby, according to the analysis done above, the convolution effects do not affect the spectral index map.

Spectral index within the inner 6 mas

To examine in detail the spectral index distribution in the inner 6 mas we used a circular beam obtained from an average of 8 and 15 GHz elliptical beams equivalent area. The resultant image revealed a double structure. The flattening of the spectral index in the image coincides with the peaks of total intensity at 8 and 15 GHz, while the spectral index steepens toward the jet edges.

We also made use of recent VLBA observations performed on 2018 April 28 simultaneously at 24 and 43 GHz, which are presented in Kravchenko et al. (2020a). The full-intensity images at two frequencies were convolved with a common 24 GHz equal-area circular beam and were aligned using a 2DCC procedure. Besides, the (u, v)-coverage was matched for this pair of frequencies. The resultant spectral index map revealed a two-humped structure which corresponds well to the result at 8-15 GHz observations.

These two independent maps reveal a similar structure, see for details Figure 1 in Pashchenko et al. (2023), but is it real? A detailed analysis was performed to check its significance and concluded that the two-humped structure is actually a product of an imaging bias. Due to its importance, the analysis was presented in a dedicated paper Pashchenko et al. (2023).

Bias correction of the spectral index images

Pashchenko et al. (2023) employed a series of simulations with various jet brightness models and dual-frequency VLBI data sets. They found that the spectral index maps of the M87 parsec scale jet are heavily affected by systematical effects. For the data set analysed in this paper, these effects flatten the spectrum in a series of stripes along the jet. This is similar to the observed image: two stripes near the core turn into the central and two outer stripes of the spectral flattening further out at $r \approx 10$ mas. The outer stripes are shown at the top of Figure 2.7 by red horizontal stripes at 3 and -3 mas from the central stripe. The simulations of the data set reveal that the systematic spectral index effects trace the bias of the low frequency (8 GHz) Stokes I image. At the same time, the bias of the 15 GHz Stokes I image is down-weighted by convolving with a lower frequency `CLEAN` beam. This made it possible to successfully compensate the spectral index bias in simulations by re-creating such effects in the high frequency (15 GHz) Stokes I image. Indeed, assuming that the Stokes I bias is small and does not heavily depend on the brightness distribution, which follows from the simulations, it cancels out in the expression for the spectral index. The procedure of the spectral index bias correction consists of three steps. First is an interpolation of the original `CLEAN` model at the 15 GHz on the uv-points of the 8 GHz data set, creating visibility data of the 15 GHz model with 8 GHz (u, v)-coverage. Next, the resulting data set is imaged in the same way as the original 8 GHz data set. In the final step, a bias-compensated spectral index map is produced (Figure 2.7). These results heavily contradict previous conclusions. It is evident, that simple intensity models, as they are used in section 2.3.2, are insufficient, and a more sophisticated approach is required to analyse the convolution effects and correct the bias in the spectral index map.

2.3.3 Jet to counter-jet flux ratio

The jet-to-counter-jet flux density ratio is a direct measurable value useful for estimating the basic physical parameters of relativistic jets such as viewing angle θ and Lorenz factor Γ. We measured the flux density of the counter-jet in the following way. The jet structure was modelled with several 2D Gaussian components, the brightest and closest to the phase centre was identified as the core. The core component only was convolved with the restoring beam. Then the obtained core image was subtracted from the original one, giving us well-separated jet and counter-jet structures. To get the flux ratio, we obtained fluxes from geometrically corresponding regions. For this, the length of the detected counter-jet was measured using the estimated in subsection 2.2.1 distance to the central

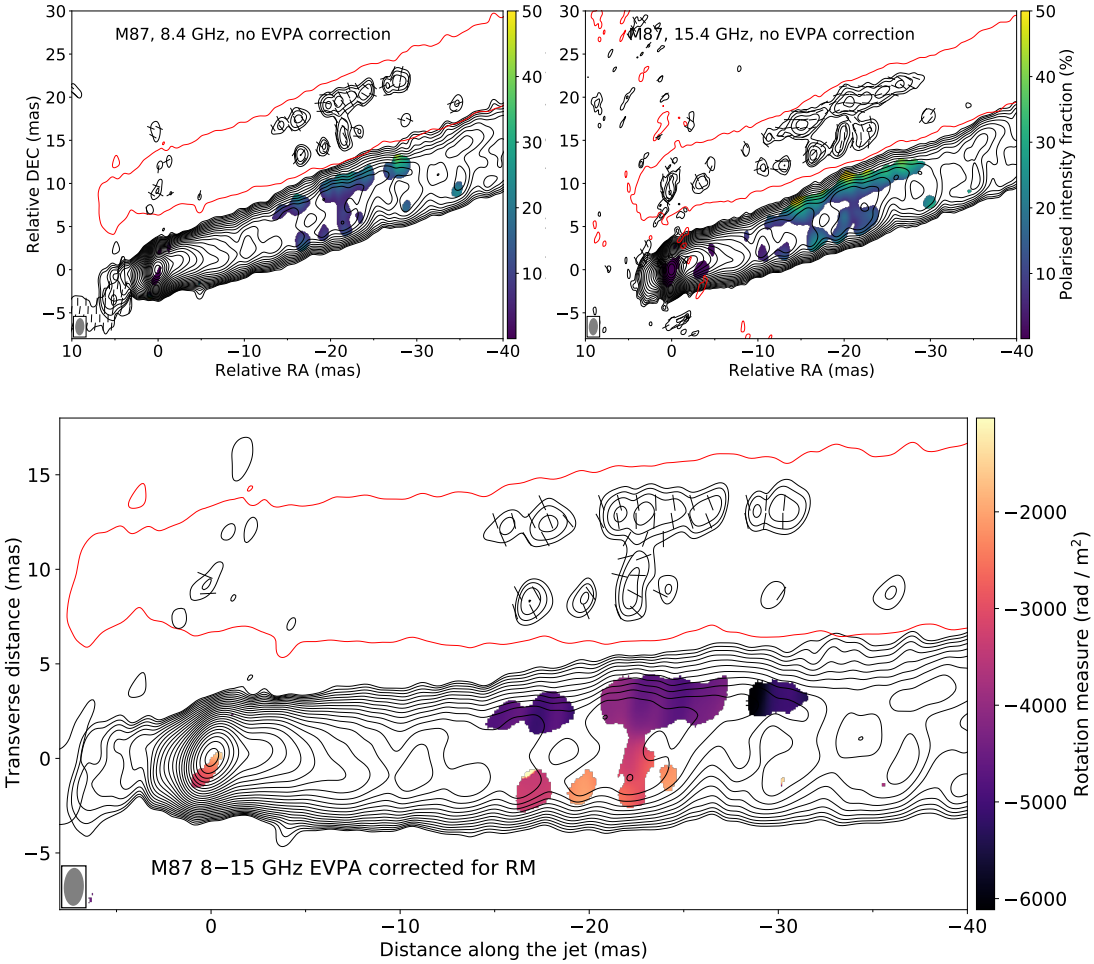

Figure 2.9: Polarisation images of M87 at 8 GHz (upper left), at 15 GHz (upper right) and Rotation Measure map between corresponding frequencies (bottom). The tick marks represent the polarisation position angle before (top) and after (bottom) correction for Rotation Measure. The black contours show the full intensity image levels which start from 260 μJy/beam at 8 GHz, 190 μJy/beam at 15 GHz and increase by a factor of $\sqrt{2}$. All full intensity images convolved with 2×1 mas, PA $= -2^{\circ}$ elliptical beam with peak 1.22 Jy/beam at 8 GHz and 1.23 Jy/beam at 15 GHz. The single red contour represents the lowest full intensity level. The black contours inside the single red contour show polarisation intensity with peak 1.5 mJy/beam at 8 GHz and 1.8 mJy/beam at 15 GHz. The polarisation contours start at 440 μJy/beam at 8 GHz, 430 μJy/beam at 15 GHz and increase by a factor of $\sqrt{2}$. The colours show polarised intensity fraction (top) and Rotation Measure (bottom).

SMBH. Thus, the boundary between the jet and the counter-jet was defined.

To measure viewing angle θ and Lorenz factor Γ, we used

$$\begin{aligned} \theta &= \arccos\left(\frac{\xi - 1}{\sqrt{(4\beta_{\rm app}^2 + (\xi-1)^2}}\right), \\ \Gamma &= \frac{\xi + 1}{\sqrt{2(\xi - \beta_{\rm app}^2)}}, \\ \xi &\equiv \frac{\delta_{\rm jet}}{\delta_{\rm cjet}}, \end{aligned} \tag{2.3.3}$$

where $\delta_{\rm jet}$, $\delta_{\rm cjet}$ are the Doppler factors of the jet and the counter-jet, $\beta_{\rm app}$ is the apparent jet speed (Boettcher et al. 2012). In the obtained images, continuous emission is observed, thus $\delta_{\rm jet}/\delta_{\rm cjet} = (F_{\rm jet}/F_{\rm cjet})^{\frac{1}{2-\alpha}}$, where $F_{\rm jet}$ and $F_{\rm cjet}$ are the fluxes of the jet and the counter-jet (Scheuer & Readhead 1979). The estimations require a spectral index and apparent velocities. Since the length of observed counter-jet is roughly 4 mas, the corresponding 4 mas downstream the jet were considered. We take the spectral index of the jet from this region ($\alpha = -0.5 \pm 0.2$), which is the median value of the distribution in the map (section 2.3). The jet speed was chosen as $\beta_{\rm app} = 0.34 \pm 0.35$, which was estimated as an average of the apparent velocities of the jet features within 4 mas from the core (Mertens et al. 2016b). Finally, we obtained results with different array configurations (VLBA+Y1; VLBA+Y1+Eb) and `CLEAN` beams (elliptical; round). The averaged outcome is summarized here:

$$\frac{F_{\rm jet}}{F_{\rm cjet}} = 18 \pm 5,\ \theta = 17^\circ \pm 8^\circ,\ \Gamma = 1.2 \pm 0.1\,.$$

2.4 Linear polarisation and Rotation Measure

Polarised emission moving through magnetized plasma can be affected by Faraday rotation. The effect can depolarise the light and change its EVPA. A relativistic jet is surrounded by a slow cocoon, optically active matter located in the magnetic field (Savolainen et al. 2021), thus, in order to investigate the magnetic field in a jet, the effect should be taken into account (Burn 1966; Hovatta et al. 2012). The rotation measures RM of extragalactic sources and can be used as a probe of the intergalactic medium to correct EVPA for Faraday rotation. The RM has been determined by the linear fit:

$$\phi_{\rm obs} = \phi_0 + RM\lambda^2, \tag{2.4.1}$$

where $\phi_{\rm obs}$ is the observed polarisation angle, ϕ_0 is the intrinsic EVPA and RM is the rotation measure. The $n\pi$ ambiguity of the $\phi_{\rm obs}$ measurements leads to uncertainties in RM estimations. Thus,

$$RM = \frac{\phi_2 - \phi_1 + n\pi}{\lambda_2^2 - \lambda_1^2}\,. \tag{2.4.2}$$

To solve the $n\pi$ problem successfully, at least three frequencies are needed (Simard-Normandin et al. 1981). Unfortunately, in our case, there are only two of them, so the problem of the $n\pi$ ambiguity is especially important. In Park et al. (2019), it was shown that the rotation measure of the jet within 15 mas is changing in time though slowly, as compared to the measurement errors. So one can assume the stability of RM over a long period of time, at least 20 years. Since the only unknown parameter in Equation 2.4.2 is n, it can be selected to match RM obtained using our data with the average value of RM, according to Zavala & Taylor (2002) and Park et al. (2019). The average RM value for the period of 1995–2015 is ≈ -4500 rad/m^2. In addition, we calculated the RM value, which provides full depolarisation with the condition of the π EVPA rotation. This makes an upper bound for $|n|$. Finally, the average RM and the maximum $|n|$ were used to solve the $n\pi$ ambiguity. For the case of $n = 0$, the resulting mean $RM \approx -4000$ rad/m^2 is consistent with previous measurements (Park et al. 2019; Zavala & Taylor 2002). We assess the significance of selecting the integer value of n by comparing the shift ΔRM associated with a change of $\Delta n = 1$ with the errors $\sigma_{\rm RM}^{\rm old} \approx 1000$ rad/m^2 in the average $RM \approx -4500$ rad/m^2 value reported in the literature, which we use as a reference point. The errors $\sigma_{\rm RM}^{\rm old}$ should be less than the shift ΔRM, otherwise, multiple integer solutions for n would exist, leading to ambiguity. In our particular case, a change of $\Delta n = 1$ corresponds to a shift of $\Delta RM \approx 2600$ rad/m^2, which leads to a change of EVPA by $\Delta\phi \approx 60°$. This supports the choice of n, since the errors of RM measurement in Zavala & Taylor (2002) and Park et al. (2019) are two times smaller. The galactic RM correction was not applied to the M87 RM map, since it is negligible for 8 and 15 GHz (Kravchenko et al. 2017). We present the reconstructed deep M 87 dual-frequency polarisation images and the Rotation Measure map in Figure 2.9. Assuming that the linear polarisation angle lies in the emitting particle orbit plane, i.e. perpendicular to the magnetic field lines, it is possible to reconstruct the magnetic field lines direction. In Figure 2.9, we observe that EVPA is oriented perpendicular to the jet direction near the edges, so the magnetic field lines are parallel to the jet axis. The opposite can be seen in the central jet regions. These results are consistent with the observations made by Zavala & Taylor (2002) and Park et al. (2019), where the perpendicular orientation of EVPAs in the northern

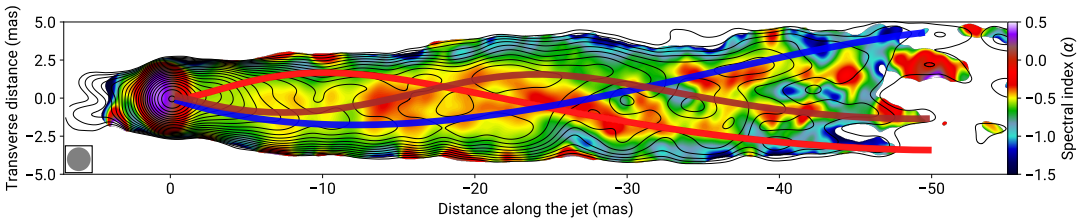

Figure 2.10: Threads identified from the Kelvin–Helmholtz instability modelling (red, blue and orange thick curves) overlaid on the bias-corrected spectral index map from Figure 2.7 and the 8 GHz intensity map, shown in contours which start from 450 μJy/beam increasing in a factor of $\sqrt{2}$ up to the peak value of 1.35 Jy/beam. The 1.56-mas circular beam used for restoring both images is displayed in the bottom left corner at its FWHM level.

edge of the M87 jet is observed.

The Rotation Measure map (Figure 2.9) shows the difference between the northern and the southern limb of the jet. The value changes from approximately -5000 to -2000 rad/m^2. Having the mean value of -4070 ± 1030 rad/m^2, the individual pixel errors are smaller ~ 300 rad/m^2. The significance of the RM gradient should be carried out carefully. Previous studies proposed several criteria for RM gradient establishment (Kravchenko et al. 2017; Taylor & Zavala 2010). Thus, the gradient of RM in the map can be considered significant, since several criteria are satisfied:

1. The M87 jet has a rich resolved transverse structure: more than three `CLEAN` beams across the jet.
2. A change in RM is more than three times greater than the typical error.
3. The gradient is located in an optically thin region.
4. The RM change is monotonic and smooth.

Although the results show a smooth distribution of RM, it is important to note that the conclusion of the significance of the RM gradient was made under the assumption of a uniform value of n across the whole jet due to the limited frequency coverage.

2.5 Discussion

2.5.1 Jet morphology, spectral index distribution, and KH instability

Morphological and spectral properties of the jet can be compared by overlaying the KH model threads from subsection 2.2.2 onto the spectral index map from

Figure 2.7. This overlay is shown in Figure 2.10 where one can see that the locations of the KH threads generally coincide with the regions of the flatter spectrum. This positional coincidence is in agreement with the theoretical expectation (Hardee 2000; Perucho et al. 2006) for the elliptical surface mode and different body modes of KH instability to produce higher pressure regions near the jet boundary and in its interior. In these regions, the combination of intrinsic heating (Hardee & Eilek 2011; Lobanov et al. 2003) and decreasing optical depth at higher frequencies should manifest itself with an apparent flattening of the synchrotron spectrum.

Basic physical parameters of the jet and ambient medium can be derived from the mode identification described in Table 2.1 by applying linear analysis of the KH instability (Hardee 2000). This allows us to estimate the jet Mach number, $M_{\rm jet}$, the ratio, $\eta = h_{\rm jet}/h_{\rm ex}$ of specific enthalpy in the jet and the external medium, and the respective speeds of sound in the external medium and the jet, $a_{\rm ex}$, $a_{\rm jet}$. In these calculations, we use the estimates of the jet viewing angle, $\theta = 17\overset{\circ}{.}2 \pm 3\overset{\circ}{.}3$, apparent speed $v_{\rm app} = (2.31 \pm 0.14)c$ and the pattern speed of instability $v_w/c = 0.34 \pm 0.21$ (Mertens et al. 2016b) and obtain $\mathrm{M_{jet}} = 20 \pm 17$, $\eta = 0.3 \pm 0.5$, $a_{\rm jet} = 0.05 \pm 0.03$, $a_{\rm ex} = 0.03 \pm 0.01$. The resulting estimated Mach number and the enthalpy ratio are higher than what is typically expected in relativistic jets (Rossi et al. 2008), for example in a relativistic jet simulation for 3C 273 and 3C 31 show $\mathrm{M_{jet}} \sim 3$, $\eta \sim 0.02$ (Perucho et al. 2005; Perucho & Martí 2007). Conversely, the respective sound speed in the jet plasma is lower than expected from those models. This apparent discrepancy may be explained by the effect of the dynamically important magnetic field which may affect the instability pattern (Hardee 2007) but is not included in the plain KH models. Alternatively, it can result from underestimating the true jet speed from the apparent measured speed. At the viewing angle of the jet in M 87, the detection of plasma motion at Lorentz factors $\gtrsim 3.38$ may be hindered by the differential Doppler boosting. Allowing for this effect, we can adopt the highest detected speed in M87 ($v_{\rm app} \approx 6c$; Biretta et al. 1999) for our estimates, which results in $\mathrm{M_{jet}} \approx 5$, $\eta \approx 0.014$, and $a_{\rm jet} \approx 0.24$. These values are in good agreement with the estimates obtained for the kiloparsec-scale jet in M87 (Lobanov et al. 2003).

The edge brightening of the jet which can be seen in Figure 2.1 and also has been reported previously (Asada et al. 2016; Janssen et al. 2019; Kim et al. 2018; Walker et al. 2018) can be explained by the stratification of a jet in velocity, density, and internal energy (Bruni et al. 2021; Walker et al. 2018) or by the presence of dynamically important magnetic field (Janssen et al. 2021b; Kramer & MacDonald 2021). Each of these effects should also provide a flattening of the spectrum toward the geometrical axis of the jet. In the first case, an interaction between layers in a velocity-stratified jet can heat the plasma, increasing the

internal energy and the spectral index in the spine region. In the second case, the spectral index can increase due to opacity variations induced by the magnetic field (Clausen-Brown et al. 2011). A combined action of these factors is also plausible (Kim et al. 2018), but our present results do not warrant a more detailed assessment of the physical conditions causing the observed edge brightening of the jet.

The observed spectral index distribution presented in Figure 2.7 indicates that the emission in the compact region at the base of the jet is optically thick at frequencies below 15 GHz, most likely due to synchrotron self-absorption. The estimated errors of the spectral index are high in this region, making it difficult to locate the transition from optically thick to thin emission. With these errors taken into account, the transition may be occurring in the jet anywhere between ≈ -1.1 mas and $\approx +1.5$ mas axial separation from the coordinate origin. On the counter-jet side, the spectral index is reliably measured at separations exceeding ≈ 1.5 mas, allowing for comparison of the emission properties in the jet and the counter jet. The median values of the spectral index distribution for the jet and the counter-jet regions are $\alpha_{\rm j} = -0.5 \pm 0.2$, $\alpha_{\rm cj} = -0.8 \pm 0.2$. The spectral index can also be estimated for the HST-1 feature, using the measured integral flux densities $F_{\rm 8GHz} \approx 19$ mJy and $F_{\rm 15GHz} \approx 8$ mJy, which yields $\alpha_{\rm HST-1} \approx -1.4$. Although this estimate should formally indicate pronounced synchrotron ageing of the emission, it should be viewed with extra caution because, at the location of HST-1, the 15 GHz flux density may be underestimated which would cause spurious steepening of the measured spectral index.

2.5.2 Magnetic field structure

Similarly to the total intensity maps, the images of fractional linear polarisation in Figure 2.9 are also edge brightened. For the optically thin emission, this effect can result from apparent or true depolarisation in the central regions of the jet caused by a helical magnetic field (Gabuzda 2021) or a turbulent plasma flow (Marscher 2014). The possibility for such a structure to result from a `CLEAN` imaging artefact due to the residual uncleaned polarized flux (Pushkarev et al. 2023) is not likely, as we employed a deep `CLEAN` in this work section 2.3.

The variations of the EVPA shown in Figure 2.9 can be reconciled with in a hollow, edge brightened jet (Frolova et al. 2023) seen at a viewing angle $\sim 1/\Gamma$ and threaded by a large scale helical magnetic field with the pitch angle $> 45^\circ$ in the plasma frame (Lyutikov et al. 2005). Similar EVPA morphology can be obtained for the force-free reverse field pinch (Clausen-Brown et al. 2011) and pure helical magnetic field model, both analytically (Butuzova & Pushkarev 2023;

Murphy et al. 2013) and numerically (Kramer & MacDonald 2021).

Some indications in favour of the presence of a substantial regular magnetic field in the jet may also be found in the transverse gradient of the Faraday rotation measure observed in the jet. Although transverse gradients of the rotation measure may as well be produced by the differences in the density of a Faraday screen of thermal electrons, which surrounds the jet, the polarization images of the large jet in M 87 (Pasetto et al. 2021b) also suggest the presence of a helical magnetic field. The observed anti-correlation between the side of the jet with higher degrees of polarization and the side with higher RM magnitude Figure 2.9 could also point at the helical magnetic field (Gabuzda 2021).

2.6 Summary

This paper presents an investigation of the physical properties of the parsec-scale jet in M 87 obtained from imaging the jet with augmented VLBA at 8 and 15 GHz. The main observational results of this work are:

1. Images of total and polarised intensity are obtained at each frequency. The total intensity images, reaching a record dynamic range >20000:1 show edge-brightening, faint counter-jet, HST-1 knot and reveal helical threads in the jet.

2. `CLEAN` bias, which strongly affects a spectral index map obtained from the individual total intensity images, is identified and corrected for. The bias-corrected spectral index map demonstrates a complex pattern.

3. The linear polarisation maps uncover the change of magnetic field lines from edges to the jet's centre.

4. The rotation measure map shows a significant gradient perpendicular to the jet direction.

A detailed analysis of the observational information obtained from the VLBA data yields the following conclusions:

1. The helical threads observed in the jet can be explained by the Kelvin–Helmholtz instability in the jet. This interpretation is also supported by the spectral index map, where the flattening of the spectra traces well the observed helical threads.

2. The edge brightening observed in the total intensity and fractional polarisation can be interpreted either by transverse velocity stratification of relativistic plasma or by a large-scale helical magnetic field.

3. The faint structure southeast to the core is confirmed as the counter-jet. According to the spectral index map analysis, this feature is optically thin $\alpha_{\rm cj} = -0.8 \pm 0.2$ and hence this region cannot be the jet origin.

4. Intrinsic physical jet parameters are estimated from modelling the observed jet structure: the jet viewing angle $\theta = 17^\circ \pm 8^\circ$, Lorenz-factor $\Gamma = 1.2 \pm 0.1$, expansion index $k = 0.532 \pm 0.008$, Mach number $M_{\rm jet} = 20 \pm 17$, jet to ambient medium density ratio $\eta = 0.3 \pm 0.5$ and the deprojected distance from the VLBI core to the SMBH $r_{\rm c} = (5 \pm 2) \times 10^{-2}$ pc.

Our results reveal that Kelvin-Helmholtz instability starts to develop in the regions relatively close to the central engine of the jet ($\sim 10^2$–$10^4 R_g$). This specific region corresponds to the jet's formation and collimation zone (e.g., Kovalev et al. 2020b; Nakamura et al. 2018), emphasizing the significant role of plasma instability in the jet morphology and evolution. Consequently, it is crucial to consider plasma instability when studying jet properties. The next step for the investigation will be the study of the temporal evolution of the helical pattern in the jet. However, due to the limited sensitivity of modern telescopes, it is challenging to track the helical pattern in survey mode. Thus, only rare full-track observations can be utilized for the analysis. The situation for M87-type jet studies will be greatly improved by ngVLA (Murphy et al. 2018; Selina et al. 2018). In addition to the sensitivity, short baselines will provide an opportunity to close the gap between parsec and kilo-parsec scale jets.

Chapter 3

Spectral properties of the HST-1 knot of the M87 jet with high-resolution VLBI observations

3.1 Observations and data reduction

Observations of the M87 jet presented and reduced in Giroletti et al. (2012); Nikonov et al. (2023) were observed within May-June 2009. Given the variability of the HST-1 feature and a relatively far distance from the VLBI core, these observations can be considered quasi-simultaneous. For the observations, we used the European VLBI Network (e-EVN) and Very Large Baseline Array (VLBA) involving the Karl Jansky Very Large Array (VLA) single antenna (Y1) at 1.7, 5.0, 8.4 and 15.4 GHz (later 2, 5, 8 and 15 GHz or L, C, X and U bands). The observations from (Giroletti et al. 2012) (project codes: VLBA bc186c, eEVN eg040) were carried out on 21 May 2009 at 2 GHz with 6 hours of observing time, and on June 1st 2009 at 5 GHz with 5 hours and by and VLBA eEVN correspondingly. The full-track 8 and 15 GHz observations from (Nikonov et al. 2023) (project code: bk145) were made involving a VLA single antenna (Y1) on May 23 for 8 GHz and May 22, 24 for 15 GHz 2009. For clarity reasons, we address the original papers for more detailed information.

The initial data calibration was performed in NRAO AIPS based on the standard reduction procedures. The data were averaged at short intervals (5 s in time, 1 MHz in frequency for 2&5 GHz, and 2 s in time, 16MHz in frequency for 8&15 GHz) to minimize smearing effects. All images were made with iterative phase and amplitude self-calibration using DIFMAP. The resulting image rms noises in the HST-1 region are $0.1 - 0.3$ mJy/beam.

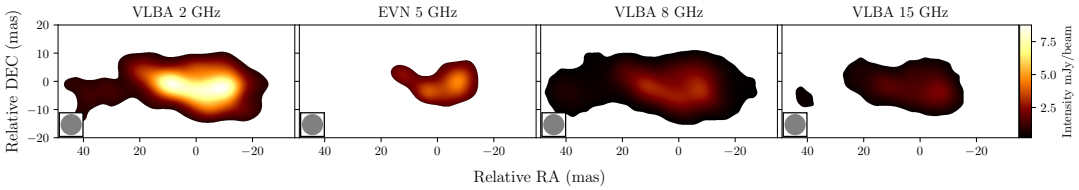

Figure 3.1: Intensity maps of the HST-1 knot at 2, 5, 8 and 15 GHz from left to right respectively. The color of the presented images represents an intensity level according to the color bar located at the right of the figure. All *uv*-coverages were clipped to have a similar range. The images are convolved with 7.5 mas circular beam, equivalent to the biggest beam obtained from the multi-frequency measurements after *uv*-clipping. The size of the beam is illustrated at the left bottom corner of each plot.

3.2 Results

On the Figure 3.1 the results of imaging are presented. All frequencies present a similar structure. The 5 GHz image repeats the relatively high-intensity regions of the other frequencies but lacks sensitivity to fully correspond 2 and 8 GHz images due to sparse eEVN *uv*-coverage and shorter observing time. Since, later in the paper we are going to discuss spectral properties of the HST-1 knot, all data were *uv*-clipped and restored with 7.5 mas circular beam, which is an equivalent for the biggest beam within the set after *uv*-clipping. It is important to note that the shortest baseline within all frequencies is approximately $3\,M\lambda$, which was taken as a reference for *uv*-clipping. Although, this coincides with the gap in *uv*-raduis at 15 GHz, in which the closest to that point is $5\,M\lambda$ baseline. Nevertheless, in the next subsection, we prove that it is enough to restore the full flux of a source and proceed with a spectral analysis.

3.2.1 Synthetic test of *uv*-coverage effects

Since HST-1 is located on the marginal distance for VLBI observations, it is important to ensure that the smearing effects will not play a significant role in the analysis. The synthetic visibility data for each observation was created using the `AIPS UVMOD` task to test the flux loss. As a model, we used two instances. First is the 8 GHz CLEAN model from the real observation (Figure 3.1). Second is an elliptical Gaussian component with two times larger size. In addition, to check the influence of sensitivity, we generated visibility data without and with noise from real data using `FLUX` parameter. The imaging was done in `DIFMAP` similar to the real data including *uv*-clipping. In the case of low noise data, we could recover all flux put into the mock visibility data at all frequencies. The result is opposite to the Gaussian model case, in which only 50% of a total flux was recovered at 15 GHz. This coincides with estimation of the largest detectable size $l_{\rm max} \approx b_{\rm min}^{-1} \approx 70$ mas,

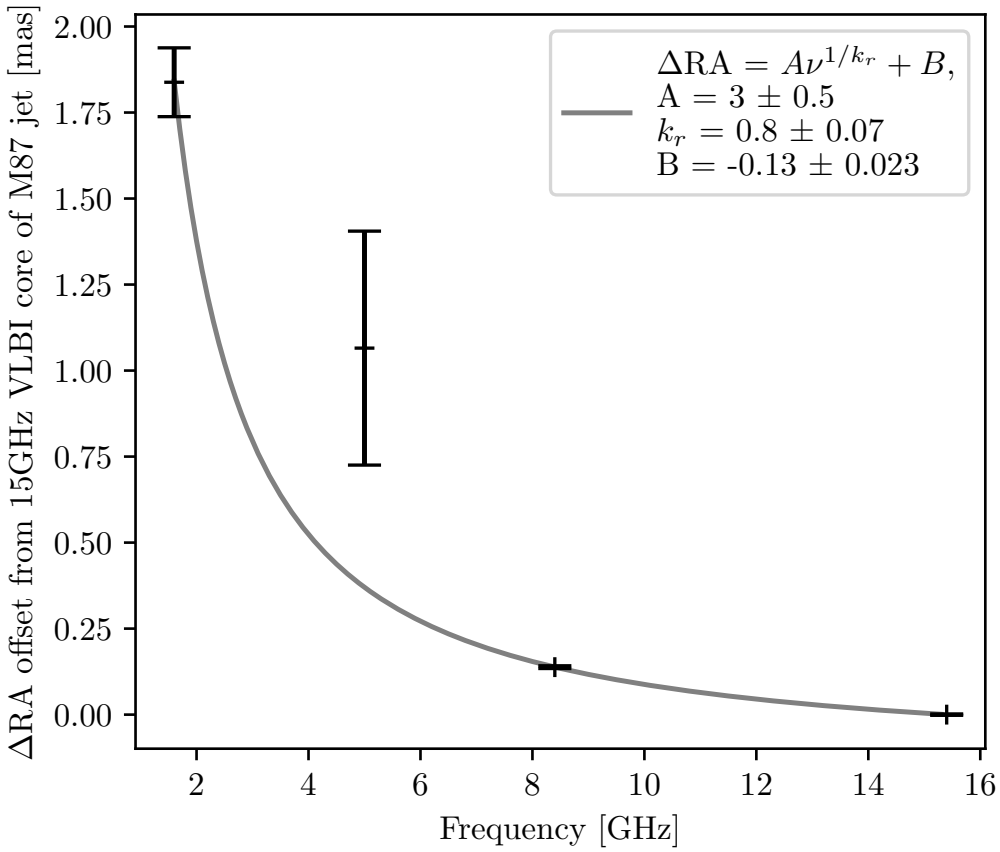

Figure 3.2: Core shift measurements in right ascension for M87 as a function of observing frequency of 2, 5, 8 and 15 GHz. Each measurement with uncertainty is shown by an error bar. The line represents a best fit by a power law $\Delta\mathrm{RA} = A\nu^{1/k_r} + B$, where $A = 3 \pm 0.5$, $k_r = 0.8 \pm 0.1$, $B = -0.13 \pm 0.023$.

where b_{min}^{-1} is the shortest projected baseline. This means, uv-coverage does not limit the analysis, but sensitivity. In the real noise simulation data, all frequencies recovered more than 98% total flux of the ground-truth model. In the image domain, the most problematic are 5 and 15 GHz data showing a significant loss of intensity on the edges and large scales. A flux loss ratio was calculated by dividing each pixel of a synthetic image intensity by the corresponding real 8 GHz image. After averaging, we multiplied each image pixel by this ratio. This procedure was done for 5 and 15 GHz images.

3.2.2 Core shift

The synchrotron nature of emission makes the jet base hardly dimmed and almost not visible at low radio frequencies due to the effect of synchrotron self-absorption. Therefore the brightest jet region on the image or a VLBI core at different frequencies represents different regions of the physical jet. Thus, the position of

the core depends on frequency creating a core shift effect $r_{\rm core} \propto \nu^{-1/k_r}$ (Konigl 1981; Lobanov 1998c), where core shift index $k_r \approx 1$ in the many AGN jets (Sokolovsky et al. 2011). In addition, the absolute positions are lost during image reconstruction, thus, before analysing multi-frequency data, it is important to align images at different frequencies.

The VLBI cores can be off-centred in the image. To correct this, we used the MODELFIT function in DIFMAP and fitted the data with 2D-Gaussian components. The brightest component is assumed to be a VLBI core and all images were shifted so the core position in each image will be in the phase center. By doing that, the shift between images starts to represent the core shift. The shift was found by applying 2D cross-correlation (Croke & Gabuzda 2008) on optically thin regions of the jet. In our case, there is a sufficient optically thin jet structure in the first ≈ 100 mas from the VLBI core, which was used for the alignment. Uncertainties were defined as a sum in quadrature of core component position error and image shift error $\sigma_{\Delta \rm RA} = (\sigma^2_{\rm core} + \sigma^2_{\rm shift})^{0.5}$.Having offsets in Right Ascension (RA) at different frequencies, we fitted the power law $\Delta \rm RA = A\nu^{-1/k_r} + B$. The results are presented at Figure 3.2, where $k_r = 0.8 \pm 0.1$, $A = 3 \pm 0.5$, and the RA offset from 15 GHz core to the jet origin is $B = -0.13 \pm 0.02$. The core shift power index does not coincide with measurements made by Hada et al. (2011b) using a phase reference, where the authors obtained $k_r^{-1} = 0.94 \pm 0.09$ or $k_r = 1.06 \pm 0.01$. Figure 3.2 show that the measurement at 5 GHz is located far away from the fitted curve. Poor sensitivity and *uv*-coverage resulted in high uncertainty, which is not enough to explain the inconsistency. It is important to note that 5 GHz observations were done with a one-week difference from the rest frequencies. Taking into account the kinematics of the jet (Mertens et al. 2016a), the distance jet components could cover in a week is about 0.1 milliarcsecond. Despite this rough estimation was already implemented into the measurements shown in Figure 3.2, there is still inconsistency with the fit, which creates high uncertainty and systematic effects. We suggest that the inaccuracy of the location of the 5 GHz core is raised due to poor sensitivity and *uv*-coverage of the observations, the absence of correct and precise jet kinematics information and the core shuttle effect (Hodgson et al. 2017; Kovalev et al. 2008; Lisakov et al. 2017; Lister et al. 2009). Nevertheless, this effect does not influence spectral analysis dramatically.

3.2.3 Spectral index and turnover frequency maps

After obtaining shifts between images, the phase shifts were applied to each image to coincide with the 15 GHz image. The resulting spectral index maps are shown in Figure 3.3. The spectral index maps show relatively uniform distribution with

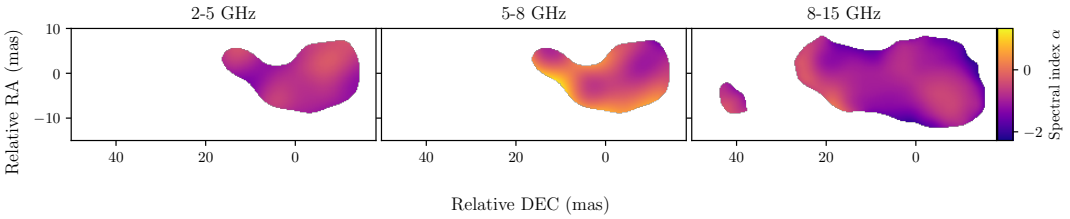

Figure 3.3: Spectral index maps of the HST-1 knot. The color of the presented images represents a spectral index level according to the color bar located at the right of the figure. Image alignment on the transparent parts of the jet was performed before obtaining of the spectral index maps.

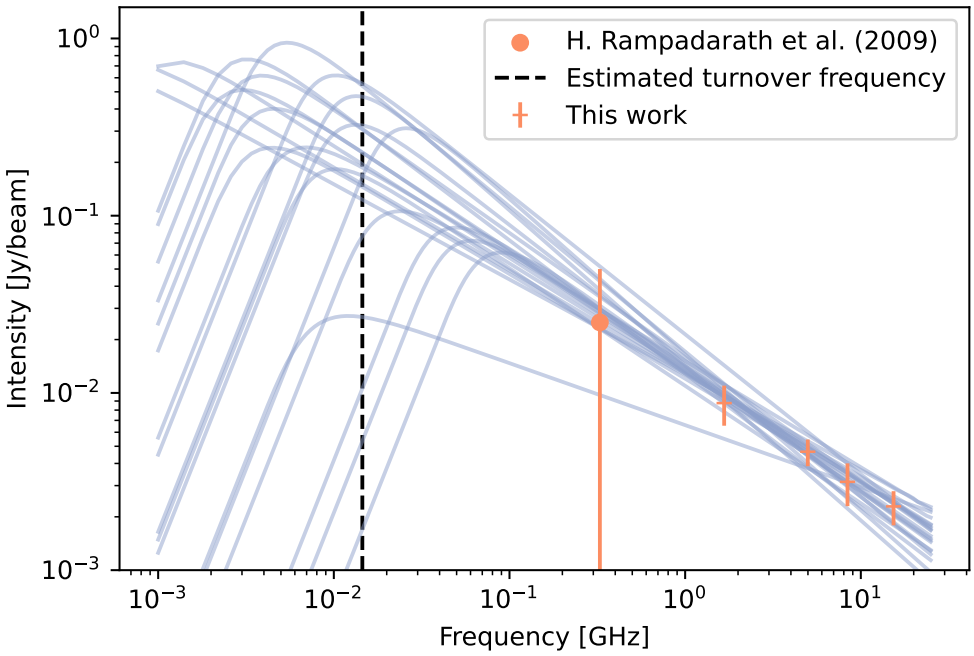

Figure 3.4: MCMC posterior predictive for HST-1 spectrum. Blue lines represent posterior sample of MCMC fit. Data points are presented here by orange circles. Crosses represent frequency cutoff points. The additional data point at 327 MHz was taken from survey.

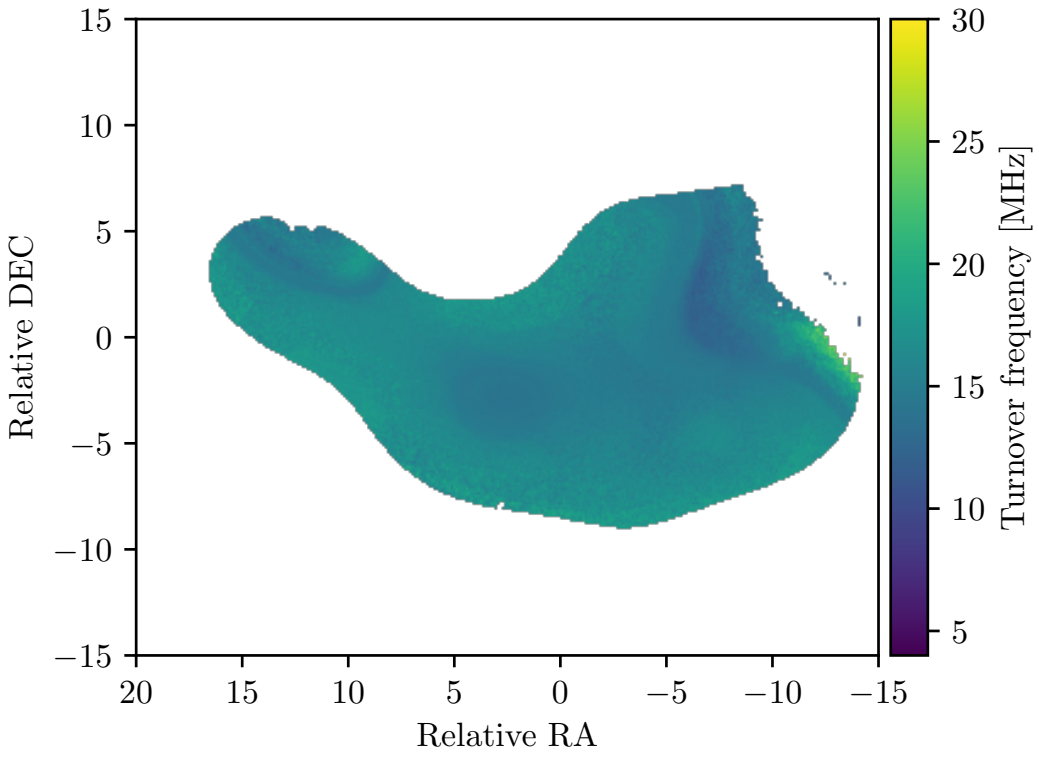

Figure 3.5: Turnover frequency map (left) and fit uncertainty map (right). The map was obtained by fitting a synchrotron spectrum to the data points.

mean value $\alpha = -0.7$ with a standard deviation of $\sigma_\alpha = 0.3$. The 5-8 GHz map shows a flattening to the edges, which could be indicated by the low sensitivity of the 5 GHz data. Our synthetic tests in subsection 3.2.1 predicted this behaviour. Overall, the spectrum in this area is steep, with the value expected from optically thin jets.

A turnover frequency map is a good measure to study the magnetic field in a jet. In the ideal case, each pixel of a data cube will have measurements of intensities at different frequencies that will follow the synchrotron spectrum Boettcher et al. (2012); Ginzburg & Syrovatsk (1969); Pacholczyk (1970). In our case, we consider synchrotron emission from a homogeneous plasma with isotropic pitch angle distribution and power law energy distribution $n(\gamma)\mathrm{d}\gamma = n_{\gamma_0}\gamma^{-s}\mathrm{d}\gamma$ for electron Lorentz factors $\gamma_\mathrm{L} < \gamma < \gamma_\mathrm{H}$ like in Lobanov (1998b). In this case, it will be enough to model the emission within the range of frequencies $\nu_\mathrm{L} < \nu < \nu_\mathrm{H}$, where $\nu_\mathrm{L,H} = \gamma_\mathrm{L,H}\Omega_e\pi^{-1}$ and Ω_e is the electron gyro–frequency. The map is obtained by fitting the synchrotron spectrum model (Equation 3.2.1) in each pixel and assigning the turnover frequency value from the fit:

$$I_\nu \propto \left(\frac{\nu}{\nu_0}\right)^{\alpha_t} \left(1 - \exp\left\{\left[-\left(\frac{\nu_0}{\nu}\right)^{\alpha_t-\alpha_0}\right]\right\}\right). \tag{3.2.1}$$

Unfortunately, we have only four frequencies in our case, and spectral index maps did not show a direct transition from optically thin to thick regions of the spectra or a turnover frequency. However, having data from the four frequencies, we can examine the bend in the spectrum and, thus can extrapolate the turnover value by the fitting process. To make estimations more robust, additional information will be needed, especially about the low-frequency part. Unfortunately, there are no observations by LOFAR (LOw-Frequency ARray) VLBI (van Haarlem et al. 2013) at the moment of year 2009 with sufficient resolution. However, Rampadarath et al. (2009) analyzed and presented the 2006 VLBA observation at 327 MHz of the M87 jet with the HST-1 knot. Since there is a considerable difference in time, the observation is not suited for using it in constructing a turnover frequency map, but it is good enough to be used as a hint or a reference point for the fitting, that will help estimate the turnover frequency. For the additional data point in spectra, a maximum intensity of the HST-1 feature was extracted from Rampadarath et al. (2009). To coincide with intensity values in our paper, the value was converted to intensity value with 7.5 mas circular beam we used in section 3.1. Since this data point is not used for structure information, a large error, that is equal to the intensity value, was added in the fitting process. A good initial guess of the fitting parameters helps the fit process. Because of this,

we conducted an MCMC fit of the HST-1 spectra given an average intensity within the knot. The posterior predictive for HST-1 spectrum is presented in Figure 3.4. Obtained parameters indicate the overall spectral index $\alpha = -0.7 \pm 0.1$ with a turnover frequency of $\nu_{\rm t} = 14 \pm 16\,{\rm MHz}$. Using these parameters as an initial guess, the spectra in each pixel of the data cube were fitted by least squares. The final turnover frequency map is displayed in Figure 3.5.

3.3 Discussion

3.3.1 Magnetic field strength

In subsection 3.2.2 we estimated the core shift, which can be used to retrieve the magnetic field strength near the VLBI core region. The standard approach to estimate it was the method suggested by Lobanov (1998c), where the conical geometry of a jet was the main assumption. In our case, the VLBI core of the M87 jet is located in a parabolic jet region, that's why a more general approach is needed. For that reason, we use a method suggested and used by Nokhrina & Pushkarev (2024); Ricci et al. (2022), which can be used in parabolic accelerating jets. Thus, the magnetic field strength at a particular distance from the jet origin:

$$B_{*\zeta} = 0.0137 \left[\left(\frac{\Omega_{r\nu}}{r_\zeta} \right)^{6k} \left(\frac{1+z}{\delta} \right)^2 \frac{1}{\sin^{6k-1}\theta} \times \frac{\rho^2 d_{br}}{\eta \Gamma_{\rm max} d_\zeta^2} \right]^{1/4} {\rm G}, \tag{3.3.1}$$

where r_ζ is a distance from the jet origin, d_ζ and d_{br} jet diameters at a distance from the jet origin and the jet brake distance $r_{br} \approx 2 \times 10^5 R_g = 770\,{\rm milliarcseconds} = 62\,{\rm parsecs}$ (Asada & Nakamura 2012a), $\theta \approx 17^\circ$ is the viewing angle adopted from Mertens et al. (2016a); Nikonov et al. (2023), $\Gamma_{\rm max} = (1-\beta^2)^{-0.5} \approx 10$ (Biretta et al. 1999) is a bulk Lorentz factor, $\delta = [\Gamma(1 - \beta\cos\theta)]^{-1}$ is a Doppler factor, $\rho \approx 0.33$ is a slope of Lorentz factor versus jet radius correlation (Nokhrina et al. 2019, 2022; Nokhrina & Pushkarev 2024), $\eta = 0.01$ is an assumption on the ratio of the jet which emits (Frolova et al. 2023), $k \approx 0.53$ is a jet geometry power index (Nikonov et al. 2023). The core shift offset is defined by Lobanov (1998c):

$$\Omega_{r\nu} = 4.8 \times 10^{-9} \frac{\Delta r_{\rm mas} D_{\rm L}}{(1+z)^2} \frac{\nu_1^{1/k_r} \nu_2^{1/k_r}}{\nu_2^{1/k_r} - \nu_1^{1/k_r}} {\rm pc\ GHz}^{1/k_r}, \tag{3.3.2}$$

where $\Delta r_{\rm mas}$ is a core shift in milliarcseconds, and for the core shift index we use results from Hada et al. (2011b) $k_r = 1.06 \pm 0.01$ since it is more precise than our results. The calculations revealed the magnetic field strength of about $B_{\rm core} \approx 1\,{\rm G}$ in the region of the 15 GHz VLBI core, and about $B_{R_g} \approx 75\,{\rm G}$ at the

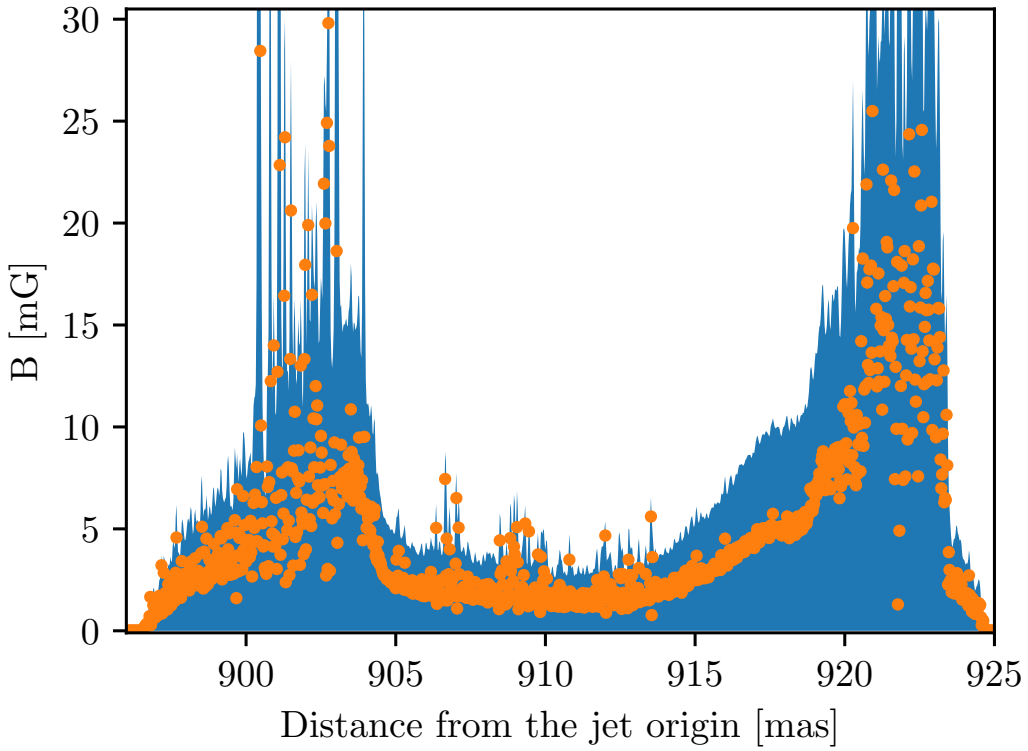

Figure 3.6: Magnetic field strength profile in the HST-1 knot showed as orange dots. The uncertainty is shown by blue filling.

Schwarzschild radius in the vicinity of the supermassive black hole.

The turnover frequency map obtained in subsection 3.2.3 can help us reconstruct a jet's magnetic field profile in the HST-1 region. As a consequence of the magnetic origin of synchrotron emission, the magnetic field strength in every pixel can be calculated as (Cawthorne 1991b; Lobanov 1998b):

$$B_{\rm pix} = C_0 \nu_{\rm m,pix}^5 S_{\rm m,pix}^{-2} \left(\frac{r_{\rm pix}}{r_{\rm core}} \right)^3, \tag{3.3.3}$$

where $\nu_{\rm m,pix}$ and $S_{\rm m,pix}$ are turnover frequency and flux in a particular pixel, $r_{\rm core}$ is the distance from the jet origin to the VLBI core, and $C_0 = B_{\rm core} S_{\rm m,\,core}^2 \nu_{\rm m,\,core}^{-5}$ is a normalization factor. The final magnetic field strength profile is presented in Figure 3.6 with a median value of around $B_{\rm HST\text{-}1} \approx 3\,{\rm mG}$. The profile was obtained by averaging all measurements perpendicular to the jet direction with P.A. $= 293.3^\circ$ Nikonov et al. (2023). Despite the double peak structure, shown in Figure 3.6, uncertainty in these regions is high. Thus, it is hard to claim the presence of the profile features.

3.3.2 Origin of the HST-1 knot

The origin of the HST-1 knot as a recollimation shock was proposed by Bromberg & Levinson (2009); Casadio et al. (2013); Cheung et al. (2007); Stawarz et al. (2006), since the position of the feature is consistent with the expected one in the jet $\approx 100\,\mathrm{pc}$ from the jet base. Detailed geometry analysis of the parsec and kiloparsec scales of the jet indeed revealed that the HST-1 feature shows a size of $\approx 40\,\mathrm{mas}$, which is smaller than the expected width of the jet Asada & Nakamura (2012a); Nikonov et al. (2023). Moreover, the region appeared as a transition region between a parabolic parsec scale jet and a conical kiloparsec scale jet. In contrast to previous works, Asada & Nakamura (2012a) proposed that such geometry law change is produced by a change of an external pressure profile $p_{\mathrm{ISM}} \propto r^{-2}$ to $p_{\mathrm{ISM}} \propto r^{-1}$ outside of the Bondi radius, which position is consistent with the location of the transition region. Later, Kovalev et al. (2020b) showed that the similar geometric transition from parabolic to colical shape is common within AGN jets and can be described by an internal flow transition from magnetically-dominated to particle-dominated regime, not only by the external medium pressure.

In this work, we confirm the over-collimation of the jet reported by Asada & Nakamura (2012a). Obtained spectral index map of the HST-1 feature shows a steep spectrum in a range of frequencies from 327 MHz up to 15 GHz. In addition, the structure of the maps looks uniform. Altogether, this hints that the HST-1 feature is an optically thin part of the jet rather than a recollimation shock. The magnetic field obtained and showed in Figure 3.6 demonstrate high values of about 3 mG, which is consistent with the X-Ray variability estimates (Harris et al. 2009; Perlman et al. 2003). This high value leads to the jet being overpressured, since magnetic pressure in this case, is about 30 times higher than the interstellar medium pressure (Allen et al. 2006; Asada & Nakamura 2012a).

Observational results show that HST-1 is rather not a reclamation shock itself, but maybe a plasma component compressed after passing a transition region thus emitting more than the surrounding jet. As a speculative interpretation, we can also suggest HST-1 being an intersection of the helical threads produced by the Kelvin-Helmholtz instability seen from parsec scale (Nikonov et al. 2023) up to the kiloparsec scale jet (Lobanov et al. 2003; Pasetto et al. 2021a). This can explain non-ballistic superluminal motion, variability and small sizes of the feature in comparison to the expected jet width. In addition, it can describe several other bright spots in the jet, starting from 100, 200, 400 mas up to knots D, E, F, and I in a kiloparsec scale jet (Pasetto et al. 2021a) as a helical threads intersections.

3.4 Conclusions

1. Physical properties of the knot HST-1 have been studied for the first time using quasi-simultaneous multifrequency VLBI observations.

2. The HST-1 show a steep spectrum in a range of frequencies from 327 MHz up to 15 GHz, with an average spectral index $\alpha = -0.7 \pm 0.1$. The spectral index maps show a uniform distribution across the entire region of HST-1, indicating the emitting plasma is optically thin.

3. The evolution of magnetic field along the jet is traced up to a distance of about 70 parsecs, with the field strength reaching $B \approx 75$ G on the horizon scale of the supermassive black hole and dropping down to $B \approx 1$ mG at the HST-1 region. The estimated magnetic field strength at the location of HST-1 implies that the magnetic field pressure in this region is about 30 times larger than the particle pressure in the surrounding interstellar medium.

4. Analysis of the spectral properties of HST-1 shows no evidence of a recollimation shock. Thus, the knot can be a plasma component passed through the transition region, where the shape of the jet changes from parabolic to conical.

5. A speculative interpretation of the knot HST-1 as an intersection of Kelvin-Helmholtz instability threads is proposed since it can explain the emission variability and apparent motions observed in this region well.

Chapter 4

Chromatic study of Kelvin-Helmholtz instability in the M87 jet with Bayesian self-calibration

Parts of this Chapter are based on several publications:

- Bayesian self-calibration and imaging in Very Long Baseline Interferometry (accepted to Astronomy & Astrophysics, Kim et al. (2024)).
- RadioAstron space-VLBI imaging of the jet in M87: II. The parsec-scale structure at 4.8 GHz (in preparation E. V. Kravchenko, T. Savolainen, **A. S. Nikonov** et. al)
- RadioAstron Space-VLBI Imaging of the Jet in M 87: III. Helical Jet Structure inside the Acceleration and Collimation Zone (in preparation T. Savolainen, ... **A. S. Nikonov** et al.)

4.1 Observation and data reduction

This Chapter presents an application of the Bayesian image reconstruction algorithm `resolve` on the RadioAstron data of the M87 jet observations at 1.7, 4.8 and 22. GHz (later 2, 5 and 22 GHz) analysed in Savolainen et al. (in prep), Kravchenko et al. (in prep) and Kim et al. (2023) correspondingly. The 2 GHz observations were carried out on 4 June 2014, while 5 GHz on 4-5 February 2014 simultaneously with 22 GHz (Kim et al. 2023). Maximum baselines used in the observations are $7D_{\oplus}$ and $12D_{\oplus}$ Earth diameters for 2 and 22, and 5 GHz correspondingly. It is important to note that for the 5 and 22 GHz observations, only

left circular polarisation (LCP) was observed. The recorded data were correlated at the Max-Planck Institute for Radio Astronomy using a modified version of the DiFX software correlator (Deller et al. 2011), adjusted for space VLBI and taking into account parameters of the orbiting antenna and both special and general relativistic effects (Bruni et al. 2020). The post-correlation calibration was performed within the AIPS software package (Greisen 2003a) in the RadioAstron specific approach (see e.g. Gómez et al. (2016); Kravchenko et al. (2020b)). The apriori calibrated data from Savolainen et al. (in prep), Kravchenko et al. (in prep), and Kim et al. (2023) were used for the imaging and self-calibration further.

4.2 The image reconstruction algorithm

4.2.1 `resolve`

The self-calibration approach developed in this paper is realized using the package `resolve`[1], which is an open-source Bayesian imaging software for radio interferometry. It is derived and formulated in the language of information field theory (Enßlin 2019). The first version of the algorithm was presented by Junklewitz et al. (2015, 2016). Arras et al. (2019b) added imaging and antenna-based gain calibration with Very Large Array (VLA) data. Dynamic imaging with closure quantities was implemented in Arras et al. (2022). In `resolve`, imaging and calibration are treated as a Bayesian inference problem. Thus from the data, `resolve` estimates the posterior distribution for the sky brightness distribution and calibration solutions. To obtain the posterior distribution and to define prior models, `resolve` builds on the a Python library NIFTy[2] (Arras et al. 2019a). In NIFTy, variational inference algorithms such as Metric Gaussian Variational Inference (Knollmüller & Enßlin 2019, MGVI) and geometric Variational Inference (Frank et al. 2021b, geoVI), as well as Gaussian process priors, are implemented.

4.2.2 Sky brightness distribution prior model

We expect the Stokes I sky brightness distribution $I(\vec{x})$ to be positive, spatially correlated, and to vary over several orders of magnitude. We encode these prior assumptions into our sky brightness prior model. More specifically, to encode the assumption of positivity and variations over several orders of magnitude, we model the sky as

$$I(\vec{x}) = \exp\big(\psi(\vec{x})\big)\,, \tag{4.2.1}$$

[1] `https://gitlab.mpcdf.mpg.de/ift/resolve`
[2] `https://gitlab.mpcdf.mpg.de/ift/nifty`

where $\psi(\vec{x})$ is the logarithmic sky brightness distribution.

To also encode the spatial correlation structure into our prior model we generate the log-sky ψ from a Gaussian process

$$\psi \curvearrowleft \mathcal{G}(\psi, \Psi)\,, \tag{4.2.2}$$

where Ψ is the covariance matrix of the Gaussian process.

The covariance matrix Ψ represents the spatial correlation structure between pixels. Since the correlation structure of the source is unknown, we want to infer the covariance matrix Ψ, also called the correlation kernel, from the data. However, estimating the full covariance matrix for high-dimensional image reconstructions is computationally demanding since storing the covariance matrix scales quadratically with the number of pixels. To overcome this issue, the prior log-sky ψ is assumed to be statistically isotropic and homogeneous. According to the Wiener-Khinchin theorem (Khinchin 1934; Wiener 1949), the spatial covariance S of a homogeneous and isotropic Gaussian process becomes diagonal in Fourier space, and is described by a power spectrum $P_\Psi(|\vec{k}|)$,

$$\Psi(\vec{k}, \vec{k}') = \langle \psi(\vec{k}) \psi(\vec{k}')^\dagger \rangle = (2\pi)^{d_k} \delta(\vec{k} - \vec{k}') P_\Psi(|\vec{k}|), \tag{4.2.3}$$

where d_k is the dimension of the Fourier transform.

The power spectrum $P_\Psi(|\vec{k}|)$ scales linearly with the number of pixels. Thus, inference of the covariance matrix assuming isotropy and homogeneity is computationally feasible for high-dimensional image reconstructions. In our sky prior model, the power spectrum is falling with $|\vec{k}|$, typically showing a power law shape. The falling power spectrum encodes smoothness in the sky brightness distribution I. Small-scale structures in the image I are suppressed since high-frequency modes have small amplitudes due to the falling power spectrum. The correlation kernel in the prior can be interpreted as a smoothness regularizer in the RML method and vice versa.

The log-normal Gaussian process prior is encoded in `resolve` in the form of a generative model (Knollmüller & Enßlin 2018). This means that independently distributed Gaussian random variables $\xi = (\xi_\Psi, \xi_k)$ are mapped to the correlated log-normal distribution:

$$I(\vec{x}) = \exp(\psi(\vec{x})) = \exp(\mathbb{F}[\sqrt{P_\Psi(\xi_\Psi)}\xi_k]) = I(\xi), \tag{4.2.4}$$

where $\mathbb{F}$ is the Fourier transform operator, all ξ are standard normal distributed, $P_\Psi(\xi_\Psi)$ is the spatial correlation power spectrum of log-sky ψ, and $I(\xi)$ is the standardized generative model.

In `resolve`, the power spectrum model P_Ψ is modeled non-parametrically. In the image reconstruction, the posterior parameters ξ_Ψ modeling the power spectrum are inferred simultaneously with the actual image. More details regarding the Gaussian process prior model in `resolve` can be found in the methods section of Arras et al. (2022).

We note that we can mitigate strong biasing since the reconstruction of the correlation kernel is a part of the inference process instead of assuming a fixed correlation kernel or a specific sky prior model. As an example, in `CLEAN`, the sky brightness distribution is assumed to be a collection of point sources. However, it is not a valid assumption for diffuse emission, and it therefore might create imaging artifacts, such as discontinuous diffuse emission with blobs. In `resolve`, the correlation structure in the diffuse emission can be learned from the data. As a result, the diffuse emission can be well described by the sky prior model. Furthermore, the Gaussian process prior model with non-parametric correlation kernel can also be used for the inference of other parameters, such as amplitude and phase gain corruptions, in order to infer the temporal correlation structure and to encode smoothness in the prior.

4.2.3 Antenna-based gain prior model

In this Chapter, it is assumed that the residual data corruptions can be approximately represented as antenna-based direction-independent gain corruptions. The measurement equation (Eq. 4.2.5) can be generalized for polarimetric visibility data with sky brightness distribution matrix including right-hand circular polarisation (RCP) and left-hand circular polarisation (LCP) antenna-based gain corruptions for antenna pair i, j (Hamaker et al. (1996b), Smirnov (2011)):

$$\mathbf{V}_{ij} = G_i(t) \left(\int_{-\infty}^{\infty} \int_{-\infty}^{\infty} \mathbf{I}(x,y)\, e^{-2\pi i(u_{ij}x + v_{ij}y)} dx\, dy \right) G_j^\dagger(t) + \mathbf{N}_{ij}, \tag{4.2.5}$$

where $\mathbf{V}_{ij}$ is the visibility matrix with four complex correlation functions by the right-hand circularly polarized signal R and the left-hand circularly polarized signal L:

$$\mathbf{V}_{ij} = \begin{pmatrix} R_i R_j^* & R_i L_j^* \\ L_i R_j^* & L_i L_j^* \end{pmatrix}, \tag{4.2.6}$$

$\mathbf{I}(x, y)$ is the sky brightness distribution matrix of the four Stokes parameters (namely, I, Q, U, and V):

$$\mathbf{I} = \begin{pmatrix} I+V & Q+iU \\ Q-iU & I-V \end{pmatrix}, \tag{4.2.7}$$

$\mathbf{N}_{ij}$ is the additive Gaussian noise matrix, and $G_i(t)$ is the antenna-based gain corruption matrix:

$$G_i(t) = \begin{pmatrix} g_i^R(t) & 0 \\ 0 & g_i^L(t) \end{pmatrix}. \tag{4.2.8}$$

We model the complex gain $g(t)$ via the Gaussian process prior to the model described in the previous section. For instance, the ith antenna RCP gain $g_i^R(t)$ can be represented by two Gaussian process priors λ and ϕ:

$$g_i^R(t) = \exp(\lambda_i^R(t) + i\phi_i^R(t)), \tag{4.2.9}$$

where λ is the log amplitude gain, and ϕ is the phase gain.

The Gaussian process priors λ and ϕ are generated from multivariate Gaussian distributions with covariance matrices Λ and Φ:

$$\lambda \curvearrowleft \mathscr{G}(\lambda, \Lambda)\,, \phi \curvearrowleft \mathscr{G}(\phi, \Phi)\,. \tag{4.2.10}$$

The temporal correlation kernels Λ and Φ are inferred from the data similarly to the inference of spatial correlation of the log-sky ψ (see Section 4.2.2). The gain prior g is represented in the form of a standardized generative model

$$g(\xi) = \exp\Big(\mathbb{F}\Big[\sqrt{P_\lambda(\xi_\Lambda)}\xi_{k'} + i\sqrt{P_\phi(\xi_\Phi)}\xi_{k''}\Big]\Big), \tag{4.2.11}$$

where $\xi = (\xi_\Lambda, \xi_{k'}, \xi_\Phi, \xi_{k''})$ are standard normal distributed random variables, $P_\lambda(\xi_\Lambda)$ is the temporal correlation power spectrum for log amplitude gain λ, and $P_\phi(\xi_\Phi)$ is the temporal correlation power spectrum for phase gain ϕ.

As we discussed before, in `resolve`, power spectra are modeled non-parametric. Therefore, the temporal correlation structure of the amplitude and phase gains is determined automatically from the data. In `CLEAN` self-calibration, the solution interval of the amplitude and phase gain solutions characterizes the temporal correlation. However, the user chooses a fixed solution interval without objective criteria; it might induce biases and create imaging artefacts from the noise in the data (Martí-Vidal & Marcaide 2008; Popkov et al. 2021). This issue can be

mitigated in Bayesian self-calibration by inferring the temporal correlation kernels for amplitude and phase gains from the data.

In this paper, only the total intensity image is reconstructed. Therefore, non-diagonal terms in the visibility related to linear polarisation can be ignored. The visibility matrix is approximated as

$$\mathbf{V}_{ij} \approx \begin{pmatrix} R_i R_j^* & 0 \\ 0 & L_i L_j^* \end{pmatrix}. \tag{4.2.12}$$

Similarly, Stokes Q, U, and V can be ignored in the sky brightness distribution:

$$\mathbf{I}(\vec{x}) \approx \begin{pmatrix} I(\vec{x}) & 0 \\ 0 & I(\vec{x}) \end{pmatrix}. \tag{4.2.13}$$

Therefore, the visibility matrix model is

$$\tilde{\mathbf{V}}_{ij}(t) = \begin{pmatrix} g_i^R(t) & 0 \\ 0 & g_i^L(t) \end{pmatrix} B(t) \left[\mathbb{F} \begin{pmatrix} I(\vec{x}) & 0 \\ 0 & I(\vec{x}) \end{pmatrix} \right] \begin{pmatrix} g_j^R(t) & 0 \\ 0 & g_j^L(t) \end{pmatrix}^\dagger, \tag{4.2.14}$$

where $B(t)$ is the sampling operator (see Eq. 1.2.36).

The visibility matrix model $\tilde{\mathbf{V}}_{ij}(t)$ can be calculated from the standardized generative sky model $I(\xi)$ and the gain model $g(\xi)$. We note that we aim to fit the model $\tilde{\mathbf{V}}_{ij}(t)$ in Eq. 4.2.14 containing the RCP and LCP gains and Stokes I image to the visibility matrix data $\mathbf{V}_{ij}$ in Eq. 4.2.12 directly in a probabilistic setup. As a result, we can perform self-calibration (gain inference) and imaging simultaneously. In the next section, we describe the variational inference algorithm we use to approximate the posterior distribution of the gain and sky parameters given the data.

4.2.4 Inference scheme

Bayes' theorem allows us to infer the conditional distribution of the model parameters $\xi = (\xi_\Psi, \xi_k, \xi_\Lambda, \xi_{k'}, \xi_\Phi, \xi_{k''})$, also called posterior distribution, from the observed data. From the posterior distribution of ξ, we can obtain the correlated posterior distributions with inferred correlation kernels for the sky emission $I = I(\xi)$ and the gains $G = G(\xi)$. In order to estimate the posterior distribution for the high-dimensional image reconstruction, the MGVI algorithm (Knollmüller & Enßlin 2019) is used. In MGVI, the posterior distribution $\mathcal{P}(\xi|V)$ is approximated as a multivariate Gaussian distribution $\mathcal{G}(\xi - \bar{\xi}, \Xi)$ with the inverse Fisher information metric Ξ as a covariance matrix.

The posterior distribution is obtained by minimizing the Kullback-Leibler (KL)

divergence between the approximate Gaussian distribution and the true posterior distribution:

$$D_{KL}(\mathcal{G}(\xi-\bar{\xi},\Xi)||\mathcal{P}(\xi|V)) = \int d\xi\, \mathcal{G}(\xi-\bar{\xi},\Xi)\, \ln\left(\frac{\mathcal{G}(\xi-\bar{\xi},\Xi)}{\mathcal{P}(\xi|V)}\right). \quad (4.2.15)$$

The KL divergence measures the expected information gain from the posterior distribution to the approximated Gaussian posterior distribution. By minimizing the KL divergence, we can find the closest Gaussian approximation to the true posterior distribution in the variational inference sense.

The KL divergence in the MGVI algorithm can be represented by the information Hamiltonians:

$$D_{KL} = \langle \mathcal{H}(\xi|V)\rangle_{\mathcal{G}(\xi-\bar{\xi},\Xi)} - \langle \mathcal{H}(\xi-\bar{\xi},\Xi)\rangle_{\mathcal{G}(\xi-\bar{\xi},\Xi)}, \quad (4.2.16)$$

where $\mathcal{H}(\xi|V)$ is the posterior Hamiltonian and $\mathcal{H}(\xi-\bar{\xi},\Xi)$ is the approximated Gaussian posterior Hamiltonian.

We can express the posterior Hamiltonian in terms of the likelihood and prior Hamiltonians (see Eq. 1.2.39):

$$D_{KL} \cong \langle \mathcal{H}(V|\xi) + \mathcal{H}(\xi)\rangle_{\mathcal{G}(\xi-\bar{\xi},\Xi)}. \quad (4.2.17)$$

The evidence Hamiltonian $\mathcal{H}(V)$ can be ignored because it is independent of the hyperparameters for the prior model. We note that the KL divergence contains the likelihood Hamiltonian, which is equivalent to the data fidelity term (see Section 1.2.5), ensuring consistency between the final image and the data.

The MGVI algorithm infers samples ξ of the normal distributed approximate posterior distribution. The posterior mean and standard deviation of the sky I and the gain G can be calculated from the samples of the normal distributed posterior distribution and those sky and gain posterior are consistent with the data. MGVI allows us to capture posterior correlations between parameters ξ. However, multimodality cannot be described, and the uncertainty values tend to be underestimated since it provides a local approximation of the posterior with a Gaussian (Frank et al. 2021a). In conclusion, high-dimensional image reconstruction can be performed by the MGVI algorithm by striking a balance between statistical integrity and computational efficiency. A detailed discussion is

provided in Knollmüller & Enßlin (2019).

4.3 Image reconstruction: synthetic data

4.3.1 Synthetic data

In order to validate the method, it is crucial to test the Bayesian self-calibration algorithm by applying it to synthetic visibility data with a known ground truth image. The synthetic data test is conducted in a semi-blind way. The metadata, including *uv*-coverage, frequency, and the error associated with each visibility point, was imported from the real observation data of M87 at 43 GHz (Walker et al. 2018). For the ground truth image, we chose the 15 GHz intensity image obtained by `resolve` using full-track VLBA May 2009 observations used in Nikonov et al. (2023). The ground truth image shows a great variety of scales from small and bright filaments to extended faint structures. Such choice of the synthetic image and the *uv*-coverage fits well with the observations (see section 4.1) we will analyse since it has structure at different scales with different *uv*-coverage. The ground truth image is displayed in Figure 4.1. The *uv*-data was created from this image using `ehtim` software (**?**). We corrupted the data with periodic time-dependent complex antenna gains using CASA software to simulate the atmospheric, pointing, and other antenna-based errors. The periods of the gain functions for an individual antenna are defined between 1 and 12 hours to mimic inhomogeneous statistics, which is commonly found in data from inhomogeneous arrays. The degree of gain variation was chosen based on the real observations, where one can observe the change of amplitude gain approximately 20% and for the phase around 10°.

4.3.2 Reconstruction by `CLEAN` and `resolve`

The `CLEAN` and `resolve` images with the synthetic data are depicted in Figure 4.1. All obtained images show a helical structure. Visual inspection and comparison with the results obtained in chapter 2 cross-identify the same instability modes. Interestingly, high frequencies, 5 and 22 GHz, show the presence only of an elliptical body mode.

For `CLEAN` reconstruction, we used `DIFMAP` (Shepherd 1997) software to reconstruct a Stokes I image using hybrid mapping in combination with super-uniform, uniform and natural weighting with a pixel size of 0.03 milliarcsecond (mas). To facilitate a direct comparison with the results obtained by the `resolve` software, we convert the standard `CLEAN` image intensity unit, originally in $\mathrm{Jy\,beam^{-1}}$, to $\mathrm{Jy\,mas^{-2}}$. This conversion involved dividing the `CLEAN` output in $\mathrm{Jy\,beam^{-1}}$ by

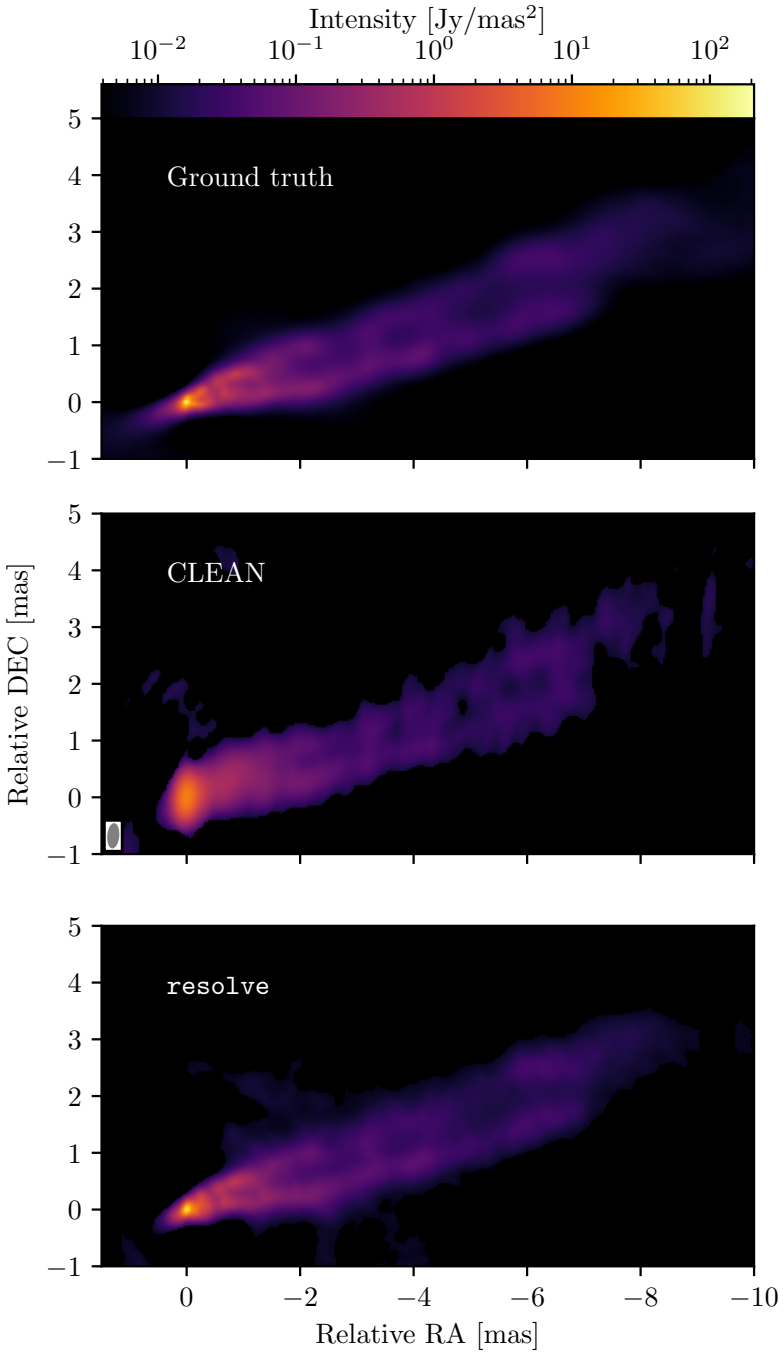

Figure 4.1: Synthetic data: ground truth (top) and reconstructed images obtained using `CLEAN` (middle) and `resolve` (bottom) self-calibration. The restoring `CLEAN` beam illustrated in the bottom left corner of the plot is 0.5×0.2 mas, P.A. $= -5°$. All images in the figure were masked at $3\sigma_{\rm rms}$ level of a corresponding image. The unified colour bar on the top of the figure shows an intensity range of the ground truth (GT) image, where maximum intensity is $I^{\rm GT}_{\rm max} = 209\,{\rm Jy\,mas^{-2}}$, the rms noise level is $\sigma^{\rm GT}_{\rm rms} = 1\,{\rm mJy\,mas^{-2}}$. The noise level of the reconstructed images are $\sigma^{\texttt{CLEAN}}_{\rm rms} = 3\,{\rm mJy\,mas^{-2}}$, $\sigma^{\texttt{resolve}}_{\rm rms} = 2\,{\rm mJy\,mas^{-2}}$. Maximum intensity values are $I^{\texttt{CLEAN}}_{\rm max} = 10\,{\rm Jy\,mas^{-2}}$, $I^{\texttt{resolve}}_{\rm max} = 111\,{\rm Jy\,mas^{-2}}$ correspondingly.

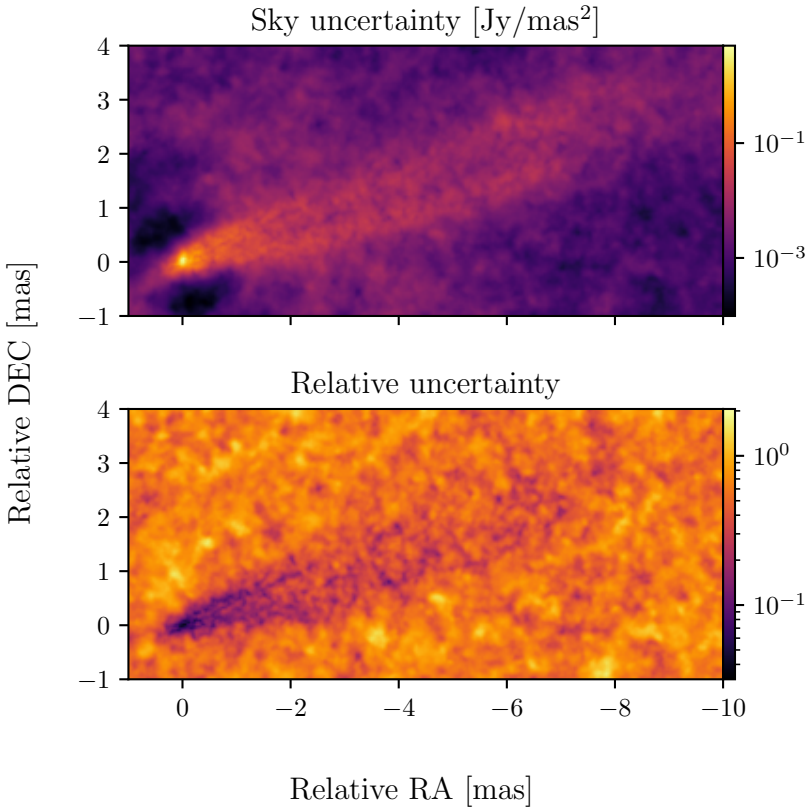

Figure 4.2: Synthetic data: sky posterior pixel-wise standard deviation (top) and relative uncertainty, which is the sky posterior standard deviation normalized by the posterior mean (bottom) by `resolve` reconstruction from the bottom panel of Figure 4.1.

the beam area, which is calculated as $\pi(4\log 2)^{-1}\cdot$ BMAJ $\cdot$ BMIN, where BMAJ and BMIN represent the major and minor axes of the beam, respectively.

For Bayesian self-calibration and imaging by `resolve`, a resolution of 2048×1024 pixels for the Stokes I image with a field of view 30 mas $\times$ 15 mas was chosen. The reduced χ^2 of the `resolve` reconstruction with the synthetic data is 0.6. The hyper parameters of the log-sky prior ψ, log-amplitude gain prior λ, and phase gain prior ϕ for the synthetic data are shown in Tables 4.1 and 4.2. However, for all the antenna and their polarisation modes, individual temporal correlation kernels for the amplitude and phase gains were employed for the synthetic data in order to infer gain corruptions with different correlation structures.

The posterior mean and standard deviation of amplitude and phase gains per each antenna and polarisation mode are shown in Figure 4.3 and Figure 4.4. The posterior samples estimate the uncertainty of the amplitude and phase gain solutions. Therefore, we can quantify the reliability of the amplitude and phase gain solutions by the Bayesian self-calibration method.

Figure 4.1 shows a comparison of images of ground truth, `CLEAN` reconstruction, and `resolve` reconstruction. The `CLEAN` algorithm tends to reconstruct a knotty extended structure since `CLEAN` reconstructs a collection of delta components, and the delta components are convolved with the `CLEAN` beam to visualise the image. We note that multi-scale `CLEAN` might recover the extended jet structure with a better-resolved core. However, iterative user-dependent self-calibration steps are still required to obtain high-fidelity images. In the `resolve` image, the core and the extended jet structure in the ground truth image are recovered better than the `CLEAN` reconstruction.

The ground truth gain corruption and recovered `resolve` gain solution figures for the synthetic data are archived on zenodo [3]. The Bayesian self-calibration's reconstructed amplitude and phase gain solutions in the time coverage with data are reasonably consistent with the ground truth.

In conclusion, this example illustrates that a high-fidelity image with robust amplitude and phase gain solutions with different correlation structures can be reconstructed from the corrupted synthetic data set by the Bayesian self-calibration and imaging method. Bayesian self-calibration may be utilised for inhomogeneous arrays, such as global mm-VLBI array (GMVA) and EVN (European VLBI network), to reconstruct reliable images and gain solutions with uncertainty estimation in the future.

[3] `https://zenodo.org/uploads/10190800`

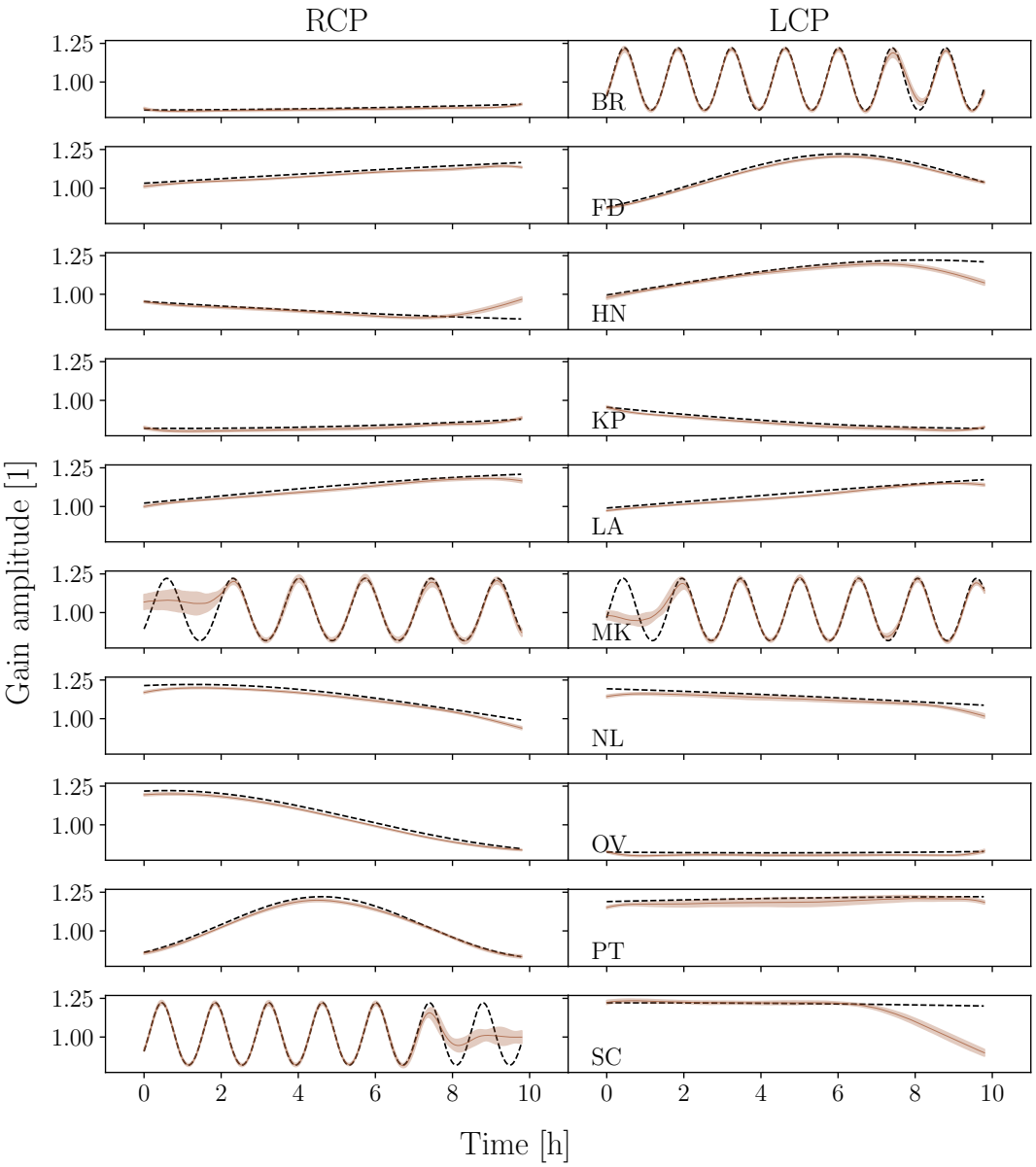

Figure 4.3: Ground truth and posterior amplitude gains from the synthetic data. The left and right columns of the figure show amplitude gains from the right (RCP) and left (LCP) circular polarisations correspondingly. Each row represents an individual antenna whose abbreviated name is indicated in the bottom left corner of each LCP plot. The black dashed lines denote the ground truth amplitude gain corruptions. The posterior mean amplitude gains and their standard deviations by `resolve` are presented as a solid brown line with shades. The visible discrepancies between the ground truth and reconstructed amplitude gains in the several baselines at specific time intervals (BR 7–8h, HN >8h, MK <2h, NL >9h, and SC >7h) are due to data gaps there.

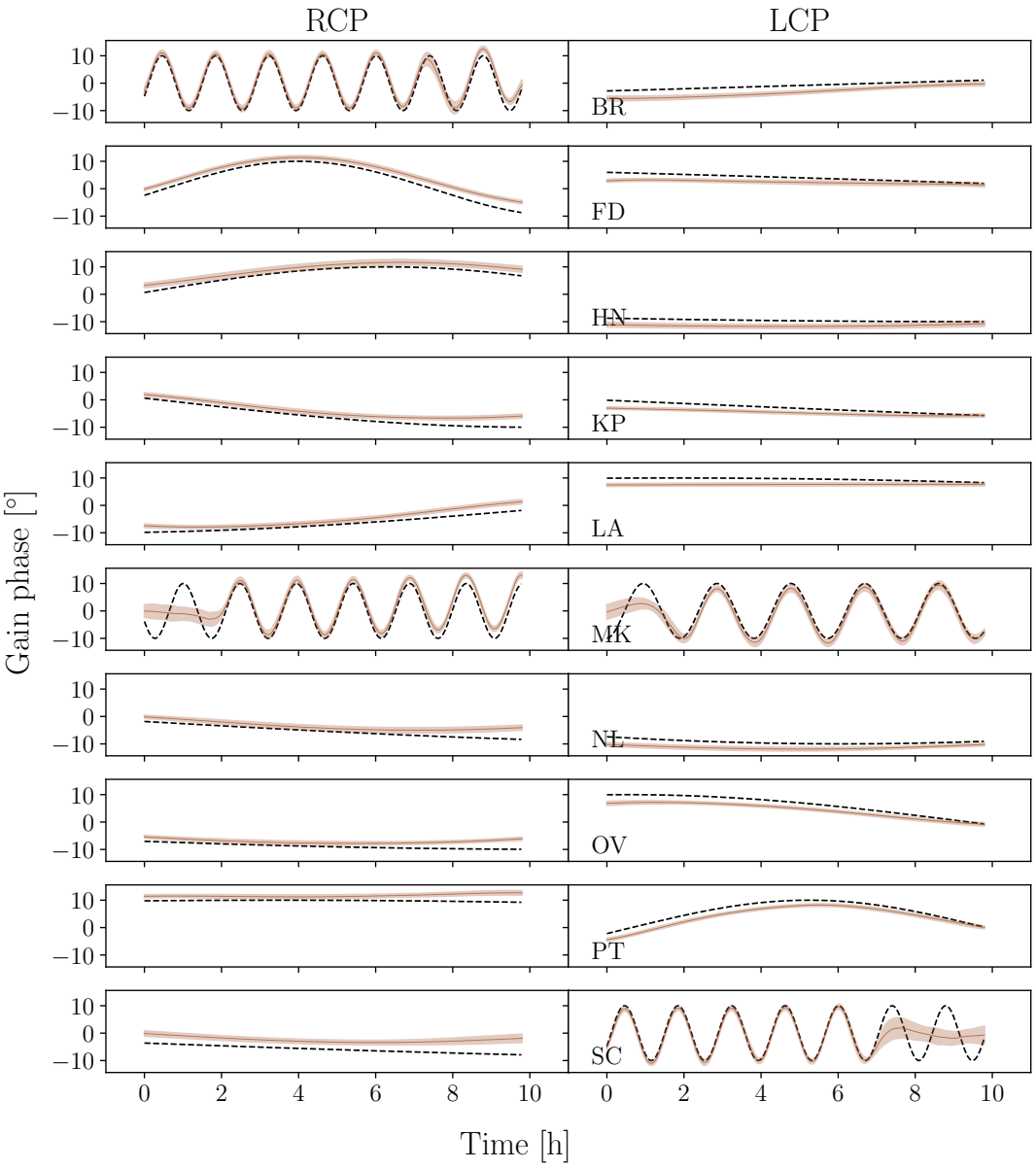

Figure 4.4: Ground truth and posterior phase gains from the synthetic data. The left and right columns of the figure show phase gains from the right (RCP) and left (LCP) circular polarisations correspondingly. Each row represents an individual antenna whose abbreviated name is indicated in the bottom left corner of each LCP plot. The black dashed lines denote the ground truth phase gain corruptions, and posterior mean phase gains and their standard deviations by `resolve` are presented as a brown solid line with shades. The visible discrepancies between the ground truth and reconstructed phase gains in the several baselines at specific time intervals (BR 7–8h, HN >8h, MK <2h, NL >9h, and SC >7h) are due to data gaps there.

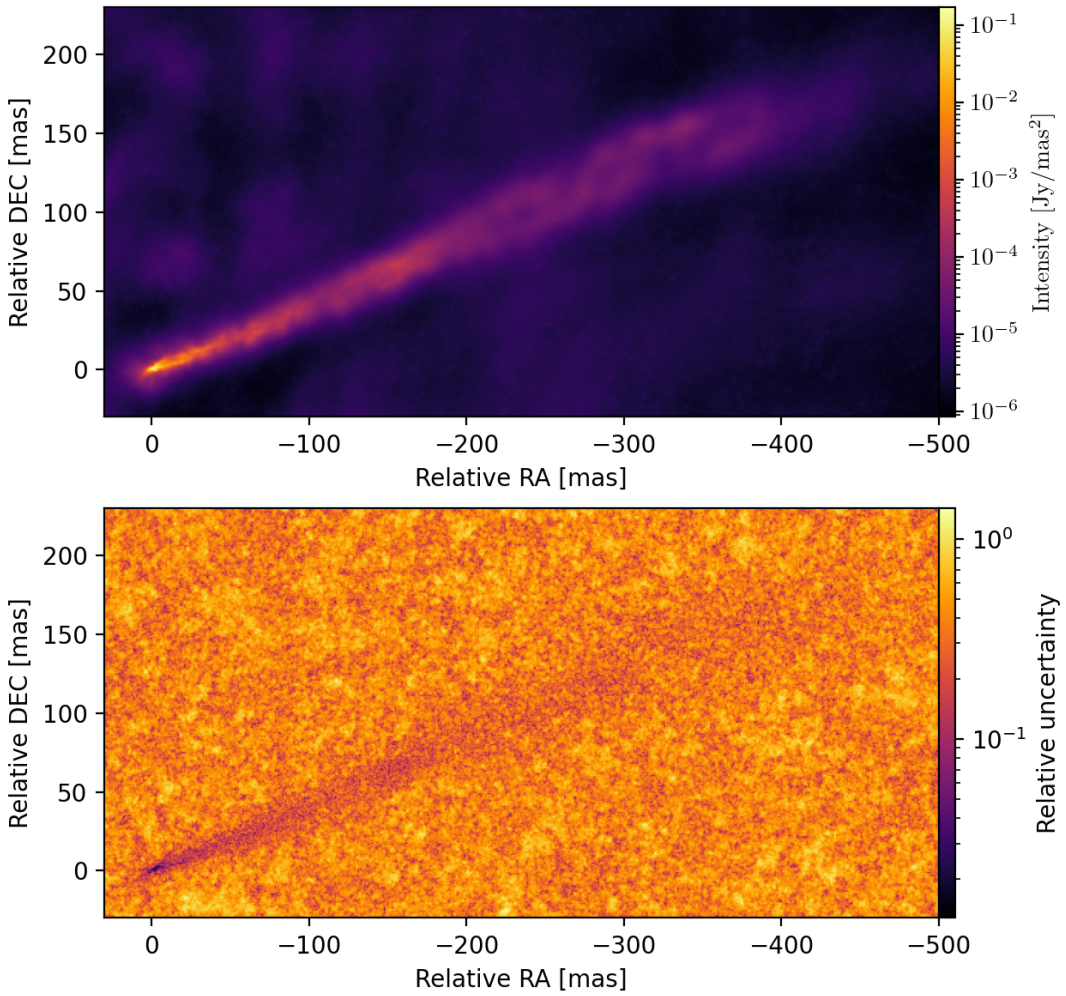

Figure 4.5: Top: RadioAstron M87 jet image at 2 GHz: the posterior mean image by Bayesian self-calibration. Bottom: The relative uncertainty of the M87 jet image is the sky posterior standard deviation normalized by the posterior mean.

4.4 Image reconstruction: real RadioAstron data

In Figures 4.5, 4.6, and 4.7, the posterior mean of 4 sample sky images and their relative uncertainties are displayed. The `resolve` image is reconstructed with a spatial domain of 1024 × 512 pixels and a field of view of 1024 mas × 512 mas. The visibilities were time-averaged with a time interval of 10 seconds and frequency-averaged. The flagging was done before the imaging to remove ambiguities and breaks in the visibility data between the ground and space baselines. In addition, the systematic error budget of approximately $\approx 10\%$ was used. Such underestimation of visibility errors in the apriori calibration is assumed to originate from the unaccounted-for various effects coming from space baselines. All this provided convergence in the algorithm and a $\chi^2 \sim 1$.

The hyperparameter setup for log-sky ψ, log amplitude gain λ, and phase gain ϕ priors is described in Appendix 4.5. Four temporal correlation kernels

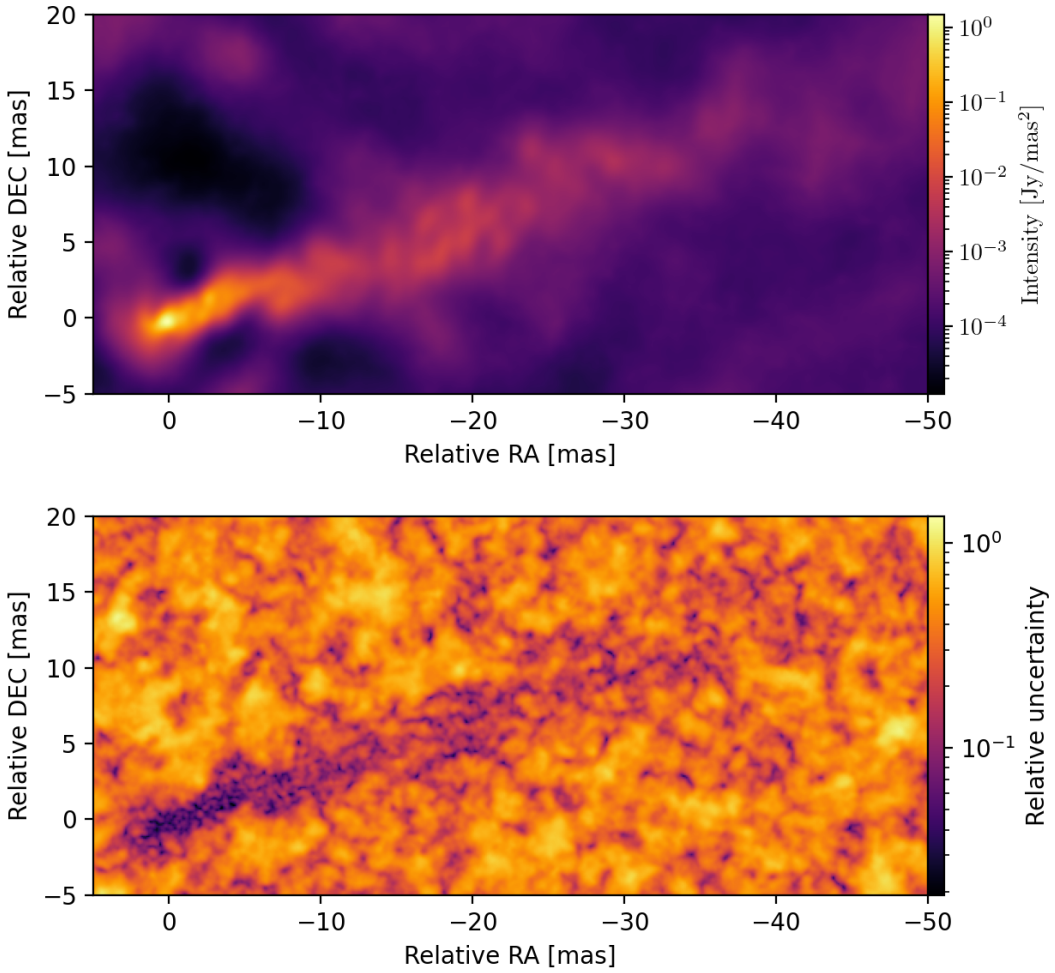

Figure 4.6: Top: RadioAstron M87 jet image at 5 GHz: the posterior mean image by Bayesian self-calibration. Bottom: The relative uncertainty of the M87 jet image is the sky posterior standard deviation normalized by the posterior mean.

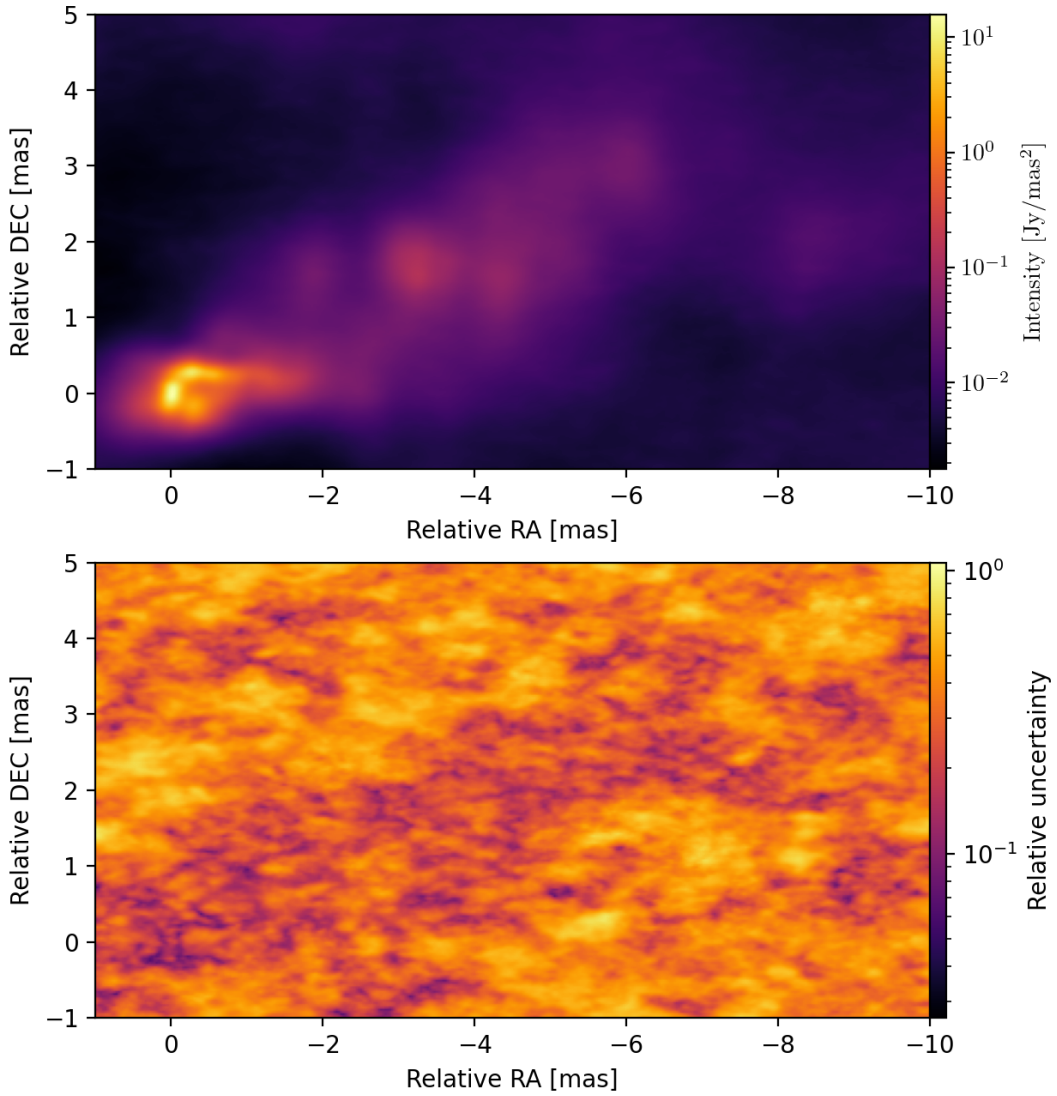

Figure 4.7: Top: RadioAstron M87 jet image at 22 GHz: the posterior mean image by Bayesian self-calibration. Bottom: The relative uncertainty of the M87 jet image is the sky posterior standard deviation normalized by the posterior mean.

Table 4.1: Hyperparameters for the log-sky prior ψ.

Parameter	ψ Mean	ψ Std
Offset	35	—
Zero mode variance	1	0.1
Fluctuations	3	1
Flexibility	1.2	0.4
Asperity	0.4	0.4
Average slope	-3	1

Notes. All hyperparameters are unitless. A detailed description of each parameter can be found in Section 3.4 of Arras et al. (2021b).

(amplitude gain and the phase gain for RCP and LCP mode, respectively) are inferred, assuming antennas have different amplitude and phase gain correlation structures per polarisation mode. This was intentionally used in the case of Space-VLBI observations since the space antenna has a different nature of gain variations. We note that the time interval in gains is not directly related to the solution interval in `CLEAN` self-calibration method since the correlation structure is learned from the data automatically instead of using a fixed solution interval in `resolve`. We infer gain terms with two times the observation time interval and crop only the first half since the Fast Fourier Transforms (FFT), which assumes periodicity, is utilized.

In order to obtain high-fidelity image, it is crucial to distinguish the uncertainty of gains and image from the VLBI data. From the perspective of statistical integrity, self-calibration and imaging should be performed simultaneously. Conventional iterative self-calibration estimates gain as a point and often flag outliers on the fly manually. This can impose a strong effective prior and thereby hinder proper accounting of the uncertainty information in the data. Furthermore, a variety of different images result from different ways `CLEAN` boxes are placed or different solution interval are chosen for amplitude and phase gains. Bayesian self-calibration and imaging can reduce such biases and provides reasonable uncertainty estimation of the gain solutions and image. This example with RadioAstron data set demonstrates that `resolve` is not only able to reconstruct images from real VLBI data but perform robust joint self-calibration and image reconstruction from sparse VLBI data set without iterative manual procedures.

4.5 Hyperparameter setup for sky and gain

The hyperparameter setup for the log-sky prior ψ is listed in Table 4.1. The offset mean represents the mean value of the log-sky ψ; thus the mean of prior sky

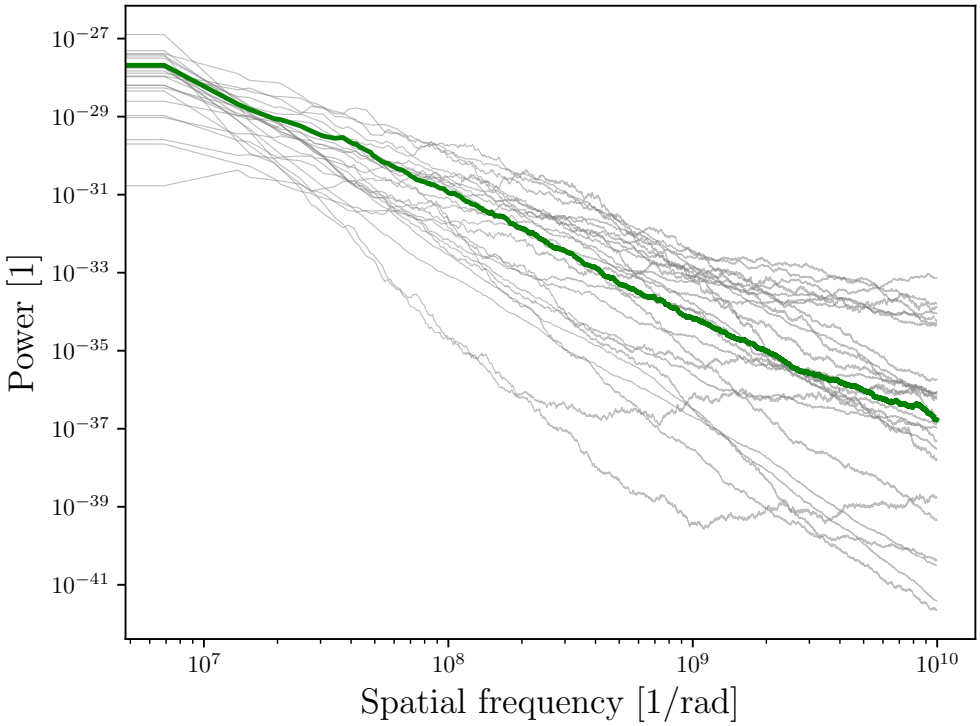

Figure 4.8: M87: posterior and prior power spectra of logarithmic sky brightness distribution ψ. The green line denotes the posterior mean power spectrum; grey lines denote prior power spectrum samples.

model $\exp(\psi)$ is $\exp(35) \approx 10^{15}$ Jy/sr ($\approx 10^{-2}$ Jy/mas^2). The value is allowed to vary two e-folds up and down in one standard deviation (std) of the prior. The zero mode variance mean describes the standard deviation of the offset and its standard deviation is therefore the standard deviation of the offset standard deviation.

The next four hyperparameters are model parameters for the spatial correlation power spectrum $P_\Psi(\xi_\Psi)$ in Eq. 4.2.4. The posterior and prior power spectra of the log-sky ψ are in Figure 4.8. The average slope mean and std denote the mean and standard deviation of the slope for amplitude spectrum, which is the square root of the power spectrum. In Figure 4.8, the prior power spectrum samples (grey lines) follow a power law with slope mean -6 and standard deviation 2. A steep prior power spectrum is chosen to suppress small scale structure in the early self-calibration stages. This prevents imprinting imaging artifacts from the noise to the final image. A relatively high standard deviation of the power spectrum is chosen to ensure flexibility of the prior model. Fluctuations and flexibility are non-trivial hyperparameters controlling the Wiener process and integrated Wiener process in the model, which determine fluctuation and flexibility of the power spectrum in a nonparametric fashion. Nonzero asperity can generate periodic

Table 4.2: Hyper parameters for the log-amplitude gain prior λ and the phase gain prior ϕ.

	λ mean	λ std	ϕ mean	ϕ std
Offset	0	—	0	—
Zero mode variance	0.2	0.1	1e-3	1e-6
Fluctuations	0.2	0.1	0.2	0.1
Flexibility	0.5	0.2	0.5	0.2
Asperity	None	None	None	None
Average slope	-3	1	-3	1

Notes. All hyperparameters are unitless. A detailed description of each parameter can be found in Section 3.4 of Arras et al. (2021b).

patterns in the image. Thus, we used relatively small asperity parameters for our log-sky model ψ. We note that the power spectrum model is flexible enough to capture different correlation structures. As a result, the flexibility of the prior model can reduce biases from strong prior assumptions.

For the self-calibration of the real data (see Section 4.4), four temporal correlation kernels (amplitude gain and the phase gain for RCP and LCP mode respectively) are inferred under the assumption that antennas from inhomogeneous array have different amplitude and phase gain correlation structures per polarisation mode. For the self-calibration of the synthetic data (see Section 4.3.2), 40 individual temporal correlation kernels for the amplitude and phase gains are inferred, one per antenna and polarisation mode, as the ground truth gain corruptions were generated with individual correlation structures. The mean of the amplitude gain prior model is obtained by exponentiating the offset mean of λ, which is $\exp(0) = 1$ and the mean of the phase gain prior model is the offset mean of ϕ, which is 0 radians. Model parameters for the zero mode variance, fluctuations, and flexibility are chosen to be small to suppress extremely high gain corrections. Asperity mean and std hyperparameters are set to None since the gain solutions are not periodic. The average slope mean is -3 for log-amplitude and phase gain, therefore the slope mean for the power spectrum is -6 with the standard deviataion 2. The broad range of the average slope parameter allows the prior model to describe different temporal correlation structures. As a result, the gain prior model is flexible enough to learn the temporal correlation structure from the data automatically. More details about prior model parameters are explained in Arras et al. (2021b).

4.6 Conclusions

We have presented a method for self-calibration and imaging of VLBI data based on the Bayesian imaging algorithm `resolve` and applied it to real and synthetic VLBI data. The data from RadioAstron observations of M87 at 2 GHz and 5 GHz used for this purpose were pre-calibrated in Savolainen et al. (in prep) and Kravchenko et al. (in prep), and imaging with self-calibration was performed by Bayesian imaging software `resolve`. The data flagging was performed manually, owing to the state-of-the-art nature of space VLBI observations, and the image and gain solutions with uncertainty estimation were reconstructed jointly in the `resolve` framework.

In Bayesian self-calibration, there is no ability to choose the solution interval of gain solutions but rather the time correlation structure of these solutions is inferred from the data. The synthetic data tests show that the Bayesian self-calibration method can successfully infer different correlation structures of gain solutions per antenna and polarisation mode, common in inhomogeneous VLBI arrays. Furthermore, in `resolve`, the uncertainty estimation of the gain solutions and the image is provided on top of the posterior mean gains and image, which is important for scientific analysis.

Images of the jet in M87 obtained with Bayesian imaging and self-calibration are consistent with those obtained using the traditional hybrid imaging approach and presented in Chapter 2. Further analysis of the helical threads is planned. Comparing the observed instability modes in frequency and time will be an important next step in the study of the development of KHI instability in the jet plasma.

Chapter 5

Summary and outlook

High angular resolution is key to understanding distant cosmic phenomena, such as AGN and relativistic jets. Quasars, Blazars, and Seyfert galaxies long held the title of mysterious objects until interferometry, and particularly the VLBI technique, revealed secrets about the structure of compact active regions. This pattern is repeating in the study of parsec-scale jets. Not long ago, VLBI observed relativistic jets as knotty structures, but with increased sensitivity and resolution, they now appear far more complex, featuring limb-brightening and helical filaments.

In this dissertation, a filamentary structure consisting of three helical threads in the parsec-scale jet of the M87 galaxy was discovered and analyzed. This phenomenon is interpreted as the result of Kelvin-Helmholtz instability (KHI) developing in the jet. Using an analytical model for the KHI, the jet structure was successfully explained, with three main instability modes identified: the helical surface mode, the elliptical surface mode and the elliptical first-order body mode. This identification allowed for the estimation of the basic physical properties of the jet plasma and their comparison to the results of the application of the KHI analysis to the jet structure observed on larger kiloparsec scales. The parameters of the instability modes in the parsec scale jet matched those of the kiloparsec scale jet. This, for the first time, confirms that the instability evolves on large scales, from the region near the black hole (in the collimation and acceleration zone) to the kinetic-dominated, conical kiloparsec scale jet. This conclusion is supported by the spectral index map between 8 and 15 GHz, which shows spectrum flattening at the intersections of the helical threads. The helical structure is also successfully identified in RadioAstron space VLBI images at 2 and 5 GHz, obtained using the novel Bayesian image reconstruction algorithm `resolve`. The consistent detection of the filamentary structures in all of the images and with two different imaging algorithms provides strong confirmation for the reliability of the reconstruction of the internal structure of the flow on scales of up to several dozens of parsecs.

At larger distances of about 100 parsecs, the prominent feature HST-1 is

believed to be related to the jet collimation, and yet its physical nature remains unclear. The spectral index maps of HST-1 obtained in this dissertation show a uniform structure and a steep spectrum, implying that the emitting plasma is optically thin. This contradicts the popular interpretation of HST-1 as a recollimation shock, typically assumed due to its proximity to the jet's geometry break, smaller-than-expected size, and relatively strong magnetic field. However, HST-1 exhibits non-ballistic motion, presenting puzzling observational results. Another possible interpretation proposed in this dissertation is that HST-1 could be an intersection of KHI threads, which would explain its spectral properties, non-ballistic motion, size, and strong magnetic fields.

The research presented in this dissertation opens several avenues for future studies. First, continuing the study of KHI in the M87 jet is crucial. Time- and frequency-dependent observations could reveal the evolution of the instability, improving the fidelity of the physical parameters obtained from modelling the observed structures. New instruments, such as the ngEHT and ngVLA, will provide unprecedented sensitivity, offering great prospects for investigating KHI in other AGN jets. These observations will refine models of jet dynamics and plasma evolution.

Second, while in this work, observations did not reach the turnover frequency in the radio spectrum of HST-1, in the near future, the international LOFAR array will have enough resolution to observe the HST-1 feature at low frequencies around 30 MHz, near which the turnover frequency is expected to be found. These future observations will provide deeper and more precise insights into the HST-1 spectrum. Finally, the high sensitivity of ngVLA and SKA will allow the mapping of hidden, low-intensity regions, potentially answering the question of the true physical nature of HST-1.

Chapter 6

Bibliography

Abbott, B. P., Abbott, R., Abbott, T. D., et al. 2016, Phys. Rev. D, 94, 064035

Abramowicz, M. A., Czerny, B., Lasota, J. P., & Szuszkiewicz, E. 1988, ApJ, 332, 646

Abramowicz, M. A. & Lasota, J. P. 1995, Comments on Astrophysics, 18, 141

Abramowski, A., Acero, F., Aharonian, F., et al. 2012, ApJ, 746, 151

Aharonian, F., Akhperjanian, A. G., Bazer-Bachi, A. R., et al. 2006, Science, 314, 1424

Alfvén, H. & Herlofson, N. 1950, Physical Review, 78, 616

Algaba, J. C., Nakamura, M., Asada, K., & Lee, S. S. 2017, ApJ, 834, 65

Allen, S. W., Dunn, R. J. H., Fabian, A. C., Taylor, G. B., & Reynolds, C. S. 2006, MNRAS, 372, 21

Antonucci, R. 1993, ARA&A, 31, 473

Antonucci, R. R. J. & Miller, J. S. 1985, ApJ, 297, 621

Appleyard, R. 1927, Electrical communication, 6, 66

Arnold, S. 2014, Getting Started in Radio Astronomy (Springer)

Arras, P., Baltac, M., Ensslin, T. A., et al. 2019a, NIFTy5: Numerical Information Field Theory v5, Astrophysics Source Code Library, record ascl:1903.008

Arras, P., Bester, H. L., Perley, R. A., et al. 2021a, A&A, 646, A84

Arras, P., Bester, H. L., Perley, R. A., et al. 2021b, A&A, 646, A84

Arras, P., Frank, P., Haim, P., et al. 2022, Nature Astronomy, 6, 259

Arras, P., Frank, P., Leike, R., Westermann, R., & Enßlin, T. A. 2019b, A&A, 627, A134

Arshakian, T. G., León-Tavares, J., Lobanov, A. P., et al. 2010, MNRAS, 401, 1231

Asada, K. & Nakamura, M. 2012a, ApJ, 745, L28

Asada, K. & Nakamura, M. 2012b, ApJ, 745, L28

Asada, K., Nakamura, M., & Pu, H.-Y. 2016, ApJ, 833, 56

Astropy Collaboration, Price-Whelan, A. M., Lim, P. L., et al. 2022, ApJ, 935, 167

Astropy Collaboration, Price-Whelan, A. M., Sipőcz, B. M., et al. 2018, AJ, 156, 123

Astropy Collaboration, Robitaille, T. P., Tollerud, E. J., et al. 2013, A&A, 558, A33

Avachat, S. S., Perlman, E. S., Adams, S. C., et al. 2016, ApJ, 832, 3

Avni, Y. 1976, ApJ, 210, 642

Baade, W. & Minkowski, R. 1954, ApJ, 119, 206

Baan, W. A., An, T., Henkel, C., et al. 2022, Nature Astronomy, 6, 976

Baczko, A. K., Ros, E., Kadler, M., et al. 2022, A&A, 658, A119

Bardeen, J. M. 1970, Nature, 226, 64

Bare, C., Clark, B. G., Kellermann, K. I., Cohen, M. H., & Jauncey, D. L. 1967, Science, 157, 189

Barthel, P. D. 1989, ApJ, 336, 606

Barvainis, R. 1987, ApJ, 320, 537

Batchelor, R., Jauncey, D. L., Johnston, K. J., et al. 1976, Soviet Astronomy Letters, 2, 181

Bayes, M. & Price, M. 1763, Philosophical Transactions of the Royal Society of London Series I, 53, 370

Bell, A. R. 1978, MNRAS, 182, 147

Beskin, V. S. & Nokhrina, E. E. 2006, MNRAS, 367, 375

Biretta, J. A., Sparks, W. B., & Macchetto, F. 1999, ApJ, 520, 621

Bisnovatyi-Kogan, G. S., Kazhdan, Y. M., Klypin, A. A., Lutskii, A. E., & Shakura, N. I. 1979, Soviet Ast., 23, 201

Blandford, R., Meier, D., & Readhead, A. 2019, ARA&A, 57, 467

Blandford, R. D. & Koenigl, A. 1979, Astrophys. Lett., 20, 15

Blandford, R. D. & Königl, A. 1979, ApJ, 232, 34

Blandford, R. D., Netzer, H., Woltjer, L., Courvoisier, T. J. L., & Mayor, M., eds. 1990, Active Galactic Nuclei

Blandford, R. D. & Payne, D. G. 1982, MNRAS, 199, 883

Blandford, R. D. & Rees, M. J. 1974, MNRAS, 169, 395

Blandford, R. D. & Znajek, R. L. 1977a, MNRAS, 179, 433

Blandford, R. D. & Znajek, R. L. 1977b, MNRAS, 179, 433

Boccardi, B., Krichbaum, T. P., Bach, U., Bremer, M., & Zensus, J. A. 2016, A&A, 588, L9

Boccardi, B., Krichbaum, T. P., Ros, E., & Zensus, J. A. 2017, A&A Rev., 25, 4

Boccardi, B., Perucho, M., Casadio, C., et al. 2021, A&A, 647, A67

Boettcher, M., Harris, D. E., & Krawczynski, H. 2012, Relativistic Jets from Active Galactic Nuclei (Wiley)

Boettcher, M., Harris, D. E., & Krawczynski, H. 2012, Relativistic Jets from Active Galactic Nuclei

Bolton, J. G., Stanley, G. J., & Slee, O. B. 1949, Nature, 164, 101

Bondi, H. 1952, MNRAS, 112, 195

Bonneau, D. 2019, Chapitre 2 Une idée : utiliser l'interférométrie pour mesurer le diamètre des étoiles (Les Ulis: EDP Sciences), 5–8

Bracewell, R. N. 1956, Australian Journal of Physics, 9, 297

Bracewell, R. N. & Roberts, J. A. 1954, Australian Journal of Physics, 7, 615

Braude, S. Y., Dubinskii, B. A., Kaidanovskii, N. L., et al., eds. 2012, Astrophysics and Space Science Library, Vol. 382, A Brief History of Radio Astronomy in the USSR: A Collection of Scientific Essays

Bridle, A. H., Hough, D. H., Lonsdale, C. J., Burns, J. O., & Laing, R. A. 1994, AJ, 108, 766

Bridle, A. H. & Perley, R. A. 1984, ARA&A, 22, 319

Bromberg, O. & Levinson, A. 2009, ApJ, 699, 1274

Broten, N. W., Locke, J. L., Legg, T. H., McLeish, C. W., & Richards, R. S. 1967, Nature, 215, 38

Bruni, G., Gómez, J. L., Vega-García, L., et al. 2021, A&A, 654, A27

Bruni, G., Savolainen, T., Gómez, J. L., et al. 2020, Advances in Space Research, 65, 712

Burbidge, E. M. 1967, ARA&A, 5, 399

Burke, B. F., Johnston, K. J., Efanov, V. A., et al. 1972, Soviet Ast., 16, 379

Burn, B. J. 1966, MNRAS, 133, 67

Buttiglione, S., Capetti, A., Celotti, A., et al. 2010, A&A, 509, A6

Butuzova, M. S. & Pushkarev, A. B. 2023, MNRAS, 520, 6335

Carter, B. 1971, Phys. Rev. Lett., 26, 331

CASA Team, Bean, B., Bhatnagar, S., et al. 2022, PASP, 134, 114501

Casadio, C., Gómez, J. L., Giroletti, M., et al. 2013, in European Physical Journal Web of Conferences, Vol. 61, European Physical Journal Web of Conferences, 06004

Cawthorne, T. V. 1991a, in Beams and Jets in Astrophysics, Vol. 19, 187

Cawthorne, T. V. 1991b, in Beams and Jets in Astrophysics, Vol. 19, 187

Chael, A. A., Johnson, M. D., Bouman, K. L., et al. 2018, ApJ, 857, 23

Chael, A. A., Johnson, M. D., Narayan, R., et al. 2016, ApJ, 829, 11

Chang, C. S., Ros, E., Kovalev, Y. Y., & Lister, M. L. 2010, A&A, 515, A38

Cheung, C. C., Harris, D. E., & Stawarz, Ł. 2007, ApJ, 663, L65

Cixin, L. 2008, The Three-Body Problem (Chongqing Press)

Clark, B. G. 1980, A&A, 89, 377

Clarke, D. A., Bridle, A. H., Burns, J. O., Perley, R. A., & Norman, M. L. 1992, ApJ, 385, 173

Clausen-Brown, E., Lyutikov, M., & Kharb, P. 2011, MNRAS, 415, 2081

Cohen, M. H., Meier, D. L., Arshakian, T. G., et al. 2014, ApJ, 787, 151

Combes, F. 2021, Active Galactic Nuclei: Fueling and Feedback (IOP Astronomy)

Condon, J. J. & Ransom, S. M. 2016, Essential Radio Astronomy (Princeton University Press)

Conway, R. G. & Kronberg, P. P. 1969, MNRAS, 142, 11

Cornwell, T. J. 2008, IEEE Journal of Selected Topics in Signal Processing, 2, 793

Cotton, W. D. 1993, AJ, 106, 1241

Cotton, W. D. 2012, Journal of Astronomical Instrumentation, 1, 1250001

Croke, S. M. & Gabuzda, D. C. 2008, MNRAS, 386, 619

Cui, Y., Hada, K., Kawashima, T., et al. 2023, NaturePortfolio

Curtis, H. D. 1918, Publications of the Lick Observatory, 13, 9

Davidson, W. & Davies, M. 1964, MNRAS, 127, 241

Davis, S. W. & Tchekhovskoy, A. 2020, ARA&A, 58, 407

De Young, D. S. & Axford, W. I. 1967, Nature, 216, 129

Deller, A. T., Brisken, W. F., Phillips, C. J., et al. 2011, PASP, 123, 275

Doeleman, S. S., Fish, V. L., Schenck, D. E., et al. 2012, Science, 338, 355

Eddington, A. S. 1924, Nature, 113, 192

Efstathiou, A. & Rowan-Robinson, M. 1995, MNRAS, 273, 649

Eichler, D. & Smith, M. 1983, Nature, 303, 779

Einstein, A. 1916, Annalen der Physik, 354, 769

Enßlin, T. A. 2019, Annalen der Physik, 531, 1800127

Event Horizon Telescope Collaboration, Akiyama, K., Alberdi, A., et al. 2024, ApJ, 964, L25

Event Horizon Telescope Collaboration, Akiyama, K., Alberdi, A., et al. 2023, ApJ, 957, L20

Event Horizon Telescope Collaboration, Akiyama, K., Alberdi, A., et al. 2022, ApJ, 930, L12

Event Horizon Telescope Collaboration, Akiyama, K., Alberdi, A., et al. 2019a, ApJ, 875, L5

Event Horizon Telescope Collaboration, Akiyama, K., Alberdi, A., et al. 2019b, ApJ, 875, L1

Event Horizon Telescope Collaboration, Akiyama, K., Alberdi, A., et al. 2019c, ApJ, 875, L1

Event Horizon Telescope Collaboration, Akiyama, K., Algaba, J. C., et al. 2021, ApJ, 910, L12

Ewen, H. I. & Purcell, E. M. 1951, Nature, 168, 356

Fanaroff, B. L. & Riley, J. M. 1974, MNRAS, 167, 31P

Fath, E. A. 1909, Lick Observatory Bulletin, 149, 71

Feng, J. & Wu, Q. 2017, MNRAS, 470, 612

Finkelstein, D. 1958, Physical Review, 110, 965

Frank, P., Leike, R., & Enßlin, T. A. 2021a, Annalen der Physik, 533, 2000486

Frank, P., Leike, R., & Enßlin, T. A. 2021b, Entropy, 23, 853

Franzen, T. M. O., Vernstrom, T., Jackson, C. A., et al. 2019, PASA, 36, e004

Fritz, J., Franceschini, A., & Hatziminaoglou, E. 2006, MNRAS, 366, 767

Frolova, V. A., Nokhrina, E. E., & Pashchenko, I. N. 2023, MNRAS, 523, 887

Fromm, C. M., Ros, E., Perucho, M., et al. 2013, A&A, 557, A105

Fuentes, A., Gómez, J. L., Martí, J. M., & Perucho, M. 2018, ApJ, 860, 121

Fuentes, A., Gómez, J. L., Martí, J. M., et al. 2023, Nature Astronomy, 7, 1359

Gabuzda, D. C. 2003, New A Rev., 47, 599

Gabuzda, D. C. 2021, Galaxies, 9, 58

Galilei, G. 1632, Dialogo di Galileo Galilei Linceo matematico sopraordinario. (Giovanni Battista Landini)

Gámez Rosas, V., Isbell, J. W., Jaffe, W., et al. 2022, Nature, 602, 403

Genzel, R., Eckart, A., Ott, T., & Eisenhauer, F. 1997, MNRAS, 291, 219

Georgelin, Y. & Lequeux, J. 2021, Journal of Astronomical History and Heritage, 24, 247

Gerwin, R. A. 1968, Reviews of Modern Physics, 40, 652

Ghez, A. M., Klein, B. L., Morris, M., & Becklin, E. E. 1998, ApJ, 509, 678

Ghisellini, G. & Celotti, A. 2001, A&A, 379, L1

Ginzburg, V. & Syrovatsk, S. 1969, Annual Review of Astronomy and Astrophysics, 7, 375

Ginzburg, V. L. 1951, Akademiia Nauk SSSR Doklady, 76, 377

Ginzburg, V. L. & Syrovatskii, S. I. 1965, ARA&A, 3, 297

Giovannini, G., Savolainen, T., Orienti, M., et al. 2018, Nature Astronomy, 2, 472

Giroletti, M., Hada, K., Giovannini, G., et al. 2012, A&A, 538, L10

Gómez, J. L., Lobanov, A. P., Bruni, G., et al. 2016, ApJ, 817, 96

Goulding, A. D., Alexander, D. M., Bauer, F. E., et al. 2012, ApJ, 755, 5

Gower, J. F. R. 1966, MNRAS, 133, 151

Gracia, J., Vlahakis, N., Agudo, I., Tsinganos, K., & Bogovalov, S. V. 2009, ApJ, 695, 503

Greenstein, J. L. 1963, Nature, 197, 1041

Greenstein, J. L. & Schmidt, M. 1964, ApJ, 140, 1

Greisen, E. W. 2003a, in Astrophysics and Space Science Library, Vol. 285, Information Handling in Astronomy - Historical Vistas, ed. A. Heck, 109

Greisen, E. W. 2003b, in Astrophysics and Space Science Library, Vol. 285, Information Handling in Astronomy - Historical Vistas, 109

Gurvits, L. I. 2023, arXiv e-prints, arXiv:2306.17647

Hada, K. 2017, Galaxies, 5, 2

Hada, K., Doi, A., Kino, M., et al. 2011a, Nature, 477, 185

Hada, K., Doi, A., Kino, M., et al. 2011b, Nature, 477, 185

Hamaker, J. P., Bregman, J. D., & Sault, R. J. 1996a, A&AS, 117, 137

Hamaker, J. P., Bregman, J. D., & Sault, R. J. 1996b, A&AS, 117, 137

Hardcastle, M. J., Alexander, P., Pooley, G. G., & Riley, J. M. 1999, MNRAS, 304, 135

Hardcastle, M. J. & Croston, J. H. 2020, New A Rev., 88, 101539

Hardee, P., Mizuno, Y., & Nishikawa, K.-I. 2007, Ap&SS, 311, 281

Hardee, P. E. 2000, ApJ, 533, 176

Hardee, P. E. 2003, ApJ, 597, 798

Hardee, P. E. 2007, ApJ, 664, 26

Hardee, P. E. & Eilek, J. A. 2011, ApJ, 735, 61

Hardee, P. E. & Norman, M. L. 1988, ApJ, 334, 70

Hardee, P. E. & Rosen, A. 1999, ApJ, 524, 650

Harris, C. R., Millman, K. J., van der Walt, S. J., et al. 2020, Nature, 585, 357

Harris, D. E., Biretta, J. A., Junor, W., et al. 2003, ApJ, 586, L41

Harris, D. E., Cheung, C. C., Biretta, J. A., et al. 2006, ApJ, 640, 211

Harris, D. E., Cheung, C. C., Stawarz, Ł., Biretta, J. A., & Perlman, E. S. 2009, ApJ, 699, 305

Hawking, S. W. 1972, Communications in Mathematical Physics, 25, 152

Herrnstein, J. R., Moran, J. M., Greenhill, L. J., et al. 1999, Nature, 400, 539

Hertz, H. 1887, Sitzungsber. d. Berl. Akad. d. Wiss.(10 November 1887)

Hewish, A., Bell, S. J., Pilkington, J. D. H., Scott, P. F., & Collins, R. A. 1968, Nature, 217, 709

Hewish, A. & Ryle, M. 1955, MmRAS, 67, 97

Hirabayashi, H., Edwards, P. G., Wehrle, A. E., et al. 2000, Advances in Space Research, 26, 689

Hirabayashi, H., Hirosawa, H., Kobayashi, H., et al. 1998, Science, 281, 1825

Hirotani, K., Shang, H., Krasnopolsky, R., & Nishikawa, K. 2024, ApJ, 965, 50

Ho, L. C., Filippenko, A. V., & Sargent, W. L. 1995, ApJS, 98, 477

Hodgson, J. A., Krichbaum, T. P., Marscher, A. P., et al. 2017, A&A, 597, A80

Högbom, J. A. 1974, A&AS, 15, 417

Hovatta, T., Lister, M. L., Aller, M. F., et al. 2012, AJ, 144, 105

Hovatta, T. et al. 2014, AJ, 147, 143

Hoyle, F. & Lyttleton, R. A. 1941, MNRAS, 101, 227

Hu, J. 2018, IOP Conference Series: Materials Science and Engineering, 452, 042052

Hubble, E. P. 1926, ApJ, 64, 321

Humason, M. L. 1932, PASP, 44, 267

Hunter, J. D. 2007, Computing in Science & Engineering, 9, 90

IceCube Collaboration, Aartsen, M. G., Ackermann, M., et al. 2018, Science, 361, 147

Israel, W. 1967, Physical Review, 164, 1776

Israelian, G. 1997, BAAS, 29, 1466

James, O., Tunzelmann, E. v., Franklin, P., & Thorne, K. S. 2015, Classical and Quantum Gravity, 32, 065001

Jansky, K. G. 1933, Nature, 132, 66

Janssen, M., Falcke, H., Kadler, M., et al. 2021a, Nature Astronomy, 5, 1017

Janssen, M., Falcke, H., Kadler, M., et al. 2021b, Nature Astronomy, 5, 1017

Janssen, M., Goddi, C., van Bemmel, I. M., et al. 2019, A&A, 626, A75

Jauncey, D. L. 1975, ARA&A, 13, 23

Jones, R. C. 1941, Journal of the Optical Society of America (1917-1983), 31, 488

Junklewitz, H., Bell, M. R., & Enßlin, T. 2015, A&A, 581, A59

Junklewitz, H., Bell, M. R., Selig, M., & Enßlin, T. A. 2016, A&A, 586, A76

Junor, W., Biretta, J. A., & Livio, M. 1999, Nature, 401, 891

Kardashev, N. S. 1962, Soviet Astronomy, 6, 317

Kardashev, N. S., Khartov, V. V., Abramov, V. V., et al. 2013, Astronomy Reports, 57, 153

Kellermann, K. I. 2015, in IAU Symposium, Vol. 313, Extragalactic Jets from Every Angle, ed. F. Massaro, C. C. Cheung, E. Lopez, & A. Siemiginowska, 190–195

Kellermann, K. I. & Moran, J. M. 2001, ARA&A, 39, 457

Kellermann, K. I., Sramek, R., Schmidt, M., Shaffer, D. B., & Green, R. 1989, AJ, 98, 1195

Khinchin, A. 1934, Mathematische Annalen, 109, 604

Kiepenheuer, K. O. 1950, Physical Review, 79, 738

Kim, J.-S., Nikonov, A. S., Roth, J., et al. 2024, arXiv e-prints, arXiv:2407.14873

Kim, J. Y., Krichbaum, T. P., Lu, R. S., et al. 2018, A&A, 616, A188

Kim, J.-Y., Savolainen, T., Voitsik, P., et al. 2023, ApJ, 952, 34

Kino, M., Takahashi, M., Kawashima, T., et al. 2022, ApJ, 939, 83

Kishimoto, M., Hönig, S. F., Antonucci, R., et al. 2011, A&A, 527, A121

Kishimoto, M., Hönig, S. F., Antonucci, R., et al. 2013, ApJ, 775, L36

Klebesadel, R. W., Strong, I. B., & Olson, R. A. 1973, ApJ, 182, L85

Knollmüller, J. & Enßlin, T. A. 2018, arXiv e-prints, arXiv:1812.04403

Knollmüller, J. & Enßlin, T. A. 2019, arXiv e-prints, arXiv:1901.11033

Komissarov, S. S., Barkov, M. V., Vlahakis, N., & Königl, A. 2007, MNRAS, 380, 51

Konigl, A. 1981, ApJ, 243, 700

Kovalev, Y. Y. 2008, in ASP Conference Series, Vol. 386, Extragalactic Jets: Theory and Observation from Radio to Gamma Ray, ed. T. A. Rector & D. S. De Young, 155

Kovalev, Y. Y., Lister, M. L., Homan, D. C., & Kellermann, K. I. 2007, ApJ, 668, L27

Kovalev, Y. Y., Lobanov, A. P., Pushkarev, A. B., & Zensus, J. A. 2008, A&A, 483, 759

Kovalev, Y. Y., Pushkarev, A. B., Nokhrina, E. E., et al. 2020a, MNRAS, 495, 3576

Kovalev, Y. Y., Pushkarev, A. B., Nokhrina, E. E., et al. 2020b, MNRAS, 495, 3576

Kramer, J. A. & MacDonald, N. R. 2021, A&A, 656, A143

Kravchenko, E., Giroletti, M., Hada, K., et al. 2020a, A&A, 637, L6

Kravchenko, E. V., Gómez, J. L., Kovalev, Y. Y., et al. 2020b, ApJ, 893, 68

Kravchenko, E. V., Kovalev, Y. Y., & Sokolovsky, K. V. 2017, MNRAS, 467, 83

Landau, L. D. 1932, Phys. Zs. Sowjet, 1, 285

Laplace, P. S. 1799, Allgemeine Geographische Ephemeriden, 4, 1

Laplace, P. S. 1813, Exposition du système du monde, Vol. 1 (Courcier)

Lemaître, G. 1933, in Annales de la Société scientifique de Bruxelles, Vol. 53, 51

Lemaître, G. A. & MacCallum, M. A. H. 1997, General Relativity and Gravitation, 29, 641

Lense, J. & Thirring, H. 1918, Zeitschrift für Physik, 19, 47

León-Tavares, J., Lobanov, A. P., Chavushyan, V. H., et al. 2010, ApJ, 715, 355

Leppanen, K. J., Zensus, J. A., & Diamond, P. J. 1995, AJ, 110, 2479

Levy, G. S., Linfield, R. P., Ulvestad, J. S., et al. 1986, Science, 234, 187

Lewis, J. P. 1995, Proceedings of Vision Interface, 120–123

Lisakov, M. M., Kovalev, Y. Y., Savolainen, T., Hovatta, T., & Kutkin, A. M. 2017, MNRAS, 468, 4478

Lister, M. L., Aller, M. F., Aller, H. D., et al. 2018, ApJS, 234, 12

Lister, M. L., Cohen, M. H., Homan, D. C., et al. 2009, AJ, 138, 1874

Lobanov, A., Hardee, P., & Eilek, J. 2003, New A Rev., 47, 629

Lobanov, A. P. 1998a, A&AS, 132, 261

Lobanov, A. P. 1998b, A&AS, 132, 261

Lobanov, A. P. 1998c, A&A, 330, 79

Lobanov, A. P. & Zensus, J. A. 1999, ApJ, 521, 509

Lobanov, A. P. & Zensus, J. A. 2001, Science, 294, 128–131

Longair, M. S. 1966, MNRAS, 133, 421

Longair, M. S., Ryle, M., & Scheuer, P. A. G. 1973, MNRAS, 164, 243

Lu, R.-S., Asada, K., Krichbaum, T. P., et al. 2023, Nature, 616, 686

Lu, R.-S., Asada, K., Krichbaum, T. P., et al. 2023, Nature, 616, 686

Lucchini, M., Krauß, F., & Markoff, S. 2019, MNRAS, 489, 1633

Luminet, J. P. 1979, A&A, 75, 228

Ly, C., Walker, R. C., & Junor, W. 2007, ApJ, 660, 200

Lynden-Bell, D. 1969a, Nature, 223, 690

Lynden-Bell, D. 1969b, Nature, 223, 690

Lynden-Bell, D. & Pringle, J. E. 1974, MNRAS, 168, 603

Lyutikov, M., Pariev, V. I., & Gabuzda, D. C. 2005, MNRAS, 360, 869

Madrid, J. P. 2009, AJ, 137, 3864

Markarian, B. E. 1963, Communications of the Byurakan Astrophysical Observatory, 34, 3

Markarian, B. E. 1967, Astrofizika, 3, 24

Markowitz, A. G., Krumpe, M., & Nikutta, R. 2014, MNRAS, 439, 1403

Marscher, A. P. 2008, in Astronomical Society of the Pacific Conference Series, Vol. 386, Extragalactic Jets: Theory and Observation from Radio to Gamma Ray, ed. T. A. Rector & D. S. De Young, 437

Marscher, A. P. 2014, ApJ, 780, 87

Marscher, A. P. & Jorstad, S. G. 2022, Universe, 8, 644

Marshall, H. L., Miller, B. P., Davis, D. S., et al. 2002, ApJ, 564, 683

Martel, A. R., Ford, H. C., Tran, H. D., et al. 2003, AJ, 125, 2964

Martí-Vidal, I. & Marcaide, J. M. 2008, A&A, 480, 289

Martí-Vidal, I., Mus, A., Janssen, M., de Vicente, P., & González, J. 2021, A&A, 646, A52

Matthews, A. M., Condon, J. J., Cotton, W. D., & Mauch, T. 2021, ApJ, 909, 193

Matthews, T. A. & Sandage, A. R. 1963, ApJ, 138, 30

Matveenko, L. I., Kardashev, N. S., & Sholomitskii, G. B. 1965, Radiophysics and Quantum Electronics, 8, 461

Mayall, N. U. 1934, PASP, 46, 134

McLean, I. S. 2008, Electronic Imaging in Astronomy: Detectors and Instrumentation (Second Edition) (Wiley)

Mei, S., Blakeslee, J. P., Côté, P., et al. 2007, ApJ, 655, 144

Meier, D. L. 2003, New A Rev., 47, 667

Mertens, F., Lobanov, A. P., Walker, R. C., & Hardee, P. E. 2016a, A&A, 595, A54

Mertens, F., Lobanov, A. P., Walker, R. C., & Hardee, P. E. 2016b, A&A, 595, A54

Michell, J. 1784, Philosophical transactions of the Royal Society of London, 35

Michelson, A. A. 1891, Nature, 45, 160

Michelson, A. A. & Pease, F. G. 1921, ApJ, 53, 249

Mizuno, Y., Gómez, J. L., Nishikawa, K.-I., et al. 2015, ApJ, 809, 38

Montesinos, M. 2012, arXiv e-prints, arXiv:1203.6851

Montgomery, C., Orchiston, W., & Whittingham, I. 2009, Journal of Astronomical History and Heritage, 12, 90

Morgan, W. W., Keenan, P. C., & Kellman, E. 1943, An atlas of stellar spectra, with an outline of spectral classification (Univ. Chicago Press)

Morganti, R. 2017, Frontiers in Astronomy and Space Sciences, 4, 42

Morris, D., Palmer, H. P., & Thompson, A. R. 1957, The Observatory, 77, 103

Müller, H. & Lobanov, A. P. 2022, A&A, 666, A137

Müller, H. & Lobanov, A. P. 2023, A&A, 672, A26

Murphy, E., Cawthorne, T. V., & Gabuzda, D. C. 2013, MNRAS, 430, 1504

Murphy, E. J., Bolatto, A., Chatterjee, S., et al. 2018, in Astronomical Society of the Pacific Conference Series, Vol. 517, Science with a Next Generation Very Large Array, ed. E. Murphy, 3

Nakahara, S., Doi, A., Murata, Y., et al. 2020, AJ, 159, 14

Nakamura, M., Asada, K., Hada, K., et al. 2018, ApJ, 868, 146

Nakamura, M., Garofalo, D., & Meier, D. L. 2010, ApJ, 721, 1783

Narayan, R., Quataert, E., Igumenshchev, I. V., & Abramowicz, M. A. 2002, ApJ, 577, 295

Narayan, R. & Yi, I. 1994, ApJ, 428, L13

Nenkova, M., Ivezić, Ž., & Elitzur, M. 2002, ApJ, 570, L9

Nikonov, A. S., Kovalev, Y. Y., Kravchenko, E. V., Pashchenko, I. N., & Lobanov, A. P. 2023, MNRAS, 526, 5949

Nokhrina, E. E., Gurvits, L. I., Beskin, V. S., et al. 2019, MNRAS, 489, 1197

Nokhrina, E. E., Kovalev, Y. Y., & Pushkarev, A. B. 2020, MNRAS, 498, 2532

Nokhrina, E. E., Pashchenko, I. N., & Kutkin, A. M. 2022, MNRAS, 509, 1899

Nokhrina, E. E. & Pushkarev, A. B. 2024, MNRAS, 528, 2523

Norman, M. L. & Hardee, P. E. 1988, ApJ, 334, 80

Novikov, I. D. & Thorne, K. S. 1973, in Black Holes (Les Astres Occlus), ed. C. Dewitt & B. S. Dewitt, 343–450

Oei, M. S. S. L., Hardcastle, M. J., Timmerman, R., et al. 2024, Nature, 633, 537–541

Ogihara, T., Takahashi, K., & Toma, K. 2019, ApJ, 877, 19

Oppenheimer, J. R. & Snyder, H. 1939, Physical Review, 56, 455

Oppenheimer, J. R. & Volkoff, G. M. 1939, Physical Review, 55, 374

Ortega-Rodríguez, M., Solís-Sánchez, H., Boza-Oviedo, E., et al. 2017, Physics in Perspective, 19, 60

Osterbrock, D. E. 1981, ApJ, 249, 462

Owen, F. N., Hardee, P. E., & Cornwell, T. J. 1989, ApJ, 340, 698

Pacholczyk, A. 1970, Radio astrophysics: A series of books in astronomy and astrophysics

Pacholczyk, A. G. 1970, Radio astrophysics. Nonthermal processes in galactic and extragalactic sources

Packham, C., Radomski, J. T., Roche, P. F., et al. 2005, ApJ, 618, L17

Padovani, P. 2016, A&A Rev., 24, 13

Padovani, P. 2017, Nature Astronomy, 1, 0194

Paraschos, G. F., Kim, J. Y., Wielgus, M., et al. 2024, A&A, 682, L3

Park, J., Byun, D.-Y., Asada, K., & Yun, Y. 2021, ApJ, 906, 85

Park, J., Hada, K., Kino, M., et al. 2019, ApJ, 887, 147

Park, J., Hada, K., Nakamura, M., et al. 2021, ApJ, 909, 76

Park, J., Zhao, G.-Y., Nakamura, M., et al. 2024, ApJ, 973, L45

Park, J. et al. 2019, ApJ, 871, 257

Pasetto, A., Carrasco-González, C., Gómez, J. L., et al. 2021a, ApJ, 923, L5

Pasetto, A., Carrasco-González, C., Gómez, J. L., et al. 2021b, ApJ, 923, L5

Pashchenko, I. N., Kravchenko, E. V., Nokhrina, E. E., & Nikonov, A. S. 2023, MNRAS, 523, 1247

Penrose, R. 1965, Phys. Rev. Lett., 14, 57

Penrose, R. 1969, Nuovo Cimento Rivista Serie, 1, 252

Penzias, A. A. & Wilson, R. W. 1965, ApJ, 142, 419

Perlman, E. S., Biretta, J. A., Zhou, F., Sparks, W. B., & Macchetto, F. D. 1999, AJ, 117, 2185

Perlman, E. S., Harris, D. E., Biretta, J. A., Sparks, W. B., & Macchetto, F. D. 2003, ApJ, 599, L65

Perlman, E. S., Sparks, W. B., Radomski, J., et al. 2001, ApJ, 561, L51

Perucho, M., Lobanov, A. P., & Martí, J. M. 2005, Mem. Soc. Astron. Italiana, 76, 110

Perucho, M., Lobanov, A. P., Martí, J. M., & Hardee, P. E. 2006, A&A, 456, 493

Perucho, M. & Martí, J. M. 2007, MNRAS, 382, 526

Pier, E. A. & Krolik, J. H. 1992, ApJ, 401, 99

Plavin, A., Kovalev, Y. Y., Kovalev, Y. A., & Troitsky, S. 2020, ApJ, 894, 101

Plavin, A. V., Kovalev, Y. Y., & Pushkarev, A. B. 2022, ApJS, 260, 4

Plavin, A. V., Kovalev, Y. Y., Pushkarev, A. B., & Lobanov, A. P. 2019, MNRAS, 485, 1822

Polko, P., Meier, D. L., & Markoff, S. 2010, ApJ, 723, 1343

Popkov, A. V., Kovalev, Y. Y., Petrov, L. Y., & Kovalev, Y. A. 2021, AJ, 161, 88

Prieto, M. A., Fernández-Ontiveros, J. A., Markoff, S., Espada, D., & González-Martín, O. 2016, MNRAS, 457, 3801

Punsly, B. 2022, ApJ, 936, 79

Punsly, B. 2023, A&A, 677, A180

Pushkarev, A. B., Aller, H. D., Aller, M. F., et al. 2023, MNRAS, 520, 6053

Pushkarev, A. B., Hovatta, T., Kovalev, Y. Y., et al. 2012, A&A, 545, A113

Pushkarev, A. B., Kovalev, Y. Y., Lister, M. L., & Savolainen, T. 2017a, MNRAS, 468, 4992

Pushkarev, A. B., Kovalev, Y. Y., Lister, M. L., & Savolainen, T. 2017b, MNRAS, 468, 4992

Qian, S.-j. 1983, Chinese Astron. Astrophys., 7, 251

Quataert, E. & Gruzinov, A. 2000, ApJ, 539, 809

Rampadarath, H., Garrett, M. A., & Polatidis, A. 2009, A&A, 500, 1327

Reber, G. 1944, ApJ, 100, 279

Reber, G. 1946, Nature, 158, 945

Rees, M. J. 1966, Nature, 211, 468

Rees, M. J. 1971, Nature, 229, 312

Ricci, L., Boccardi, B., Nokhrina, E., et al. 2022, A&A, 664, A166

Ro, H., Kino, M., Sohn, B. W., et al. 2023a, A&A, 673, A159

Ro, H., Yi, K., Cui, Y., et al. 2023b, Galaxies, 11, 33

Robinson, D. C. 1975, Phys. Rev. Lett., 34, 905

Rossi, P., Mignone, A., Bodo, G., Massaglia, S., & Ferrari, A. 2008, A&A, 488, 795

Ryle, M. 1968, ARA&A, 6, 249

Ryle, M., Smith, F. G., & Elsmore, B. 1950, MNRAS, 110, 508

Salpeter, E. E. 1964, ApJ, 140, 796

Savolainen, T. 2021, in 43rd COSPAR Scientific Assembly, Vol. 43, 1398

Savolainen, T., Giovannini, G., Kovalev, Y. Y., et al. 2021, arXiv e-prints, arXiv:2111.04481

Savolainen, T., Giovannini, G., Kovalev, Y. Y., et al. 2023, A&A, 676, A114

Schartmann, M., Wada, K., Prieto, M. A., Burkert, A., & Tristram, K. R. W. 2014, MNRAS, 445, 3878

Scheuer, P. A. G. 1974, MNRAS, 166, 513

Scheuer, P. A. G. & Readhead, A. C. S. 1979, Nature, 277, 182

Schmidt, M. 1963, Nature, 197, 1040

Schmitt, J. L. 1968, Nature, 218, 663

Schwab, F. R. & Cotton, W. D. 1983, AJ, 88, 688

Schwarzschild, K. 1916, Abh. Konigl. Preuss. Akad. Wissenschaften Jahre 1906,92, Berlin,1907, 1916, 189

Selina, R. J., Murphy, E. J., McKinnon, M., et al. 2018, in Astronomical Society of the Pacific Conference Series, Vol. 517, Science with a Next Generation Very Large Array, ed. E. Murphy, 15

Seyfert, C. K. 1943, ApJ, 97, 28

Shakura, N. I. & Sunyaev, R. A. 1973, A&A, 24, 337

Shepherd, M. C. 1997, in Astronomical Society of the Pacific Conference Series, Vol. 125, Astronomical Data Analysis Software and Systems VI, ed. G. Hunt & H. Payne, 77

Shepherd, M. C., Pearson, T. J., & Taylor, G. B. 1994, in Bulletin of the American Astronomical Society, Vol. 26, 987–989

Shields, G. A. 1999, PASP, 111, 661

Shklovskii, I. S. 1961, Soviet Ast., 4, 885

Shklovskii, I. S. 1963a, AZh, 40, 972

Shklovskii, I. S. 1963b, Soviet Ast., 6, 465

Shklovskii, I. S. 1964, Soviet Ast., 8, 132

Shklovskii, I. S. 1966, Soviet Ast., 9, 683

Shklovskii, I. S. 1977, Soviet Ast., 21, 401

Shklovsky, I. S. 1957a, in IAU Symposium, Vol. 4, Radio astronomy, ed. H. C. van de Hulst, 205

Shklovsky, I. S. 1957b, in IAU Symposium, Vol. 4, Radio astronomy, ed. H. C. van de Hulst, 201

Shklovsky, I. S. 1967, ApJ, 148, L1

Shklovsky, J. S. 1954, in Liege International Astrophysical Colloquia, Vol. 5, Liege International Astrophysical Colloquia, 515

Sholomitsky, G. B. 1965, Information Bulletin on Variable Stars, 83, 1

Simard-Normandin, M., Kronberg, P. P., & Button, S. 1981, ApJS, 45, 97

Sjouwerman, L. O., Mioduszewski, A. J., & Greisen, E. W. 2005, in Astronomical Society of the Pacific Conference Series, Vol. 340, Future Directions in High Resolution Astronomy, ed. J. Romney & M. Reid, 613

Slipher, V. M. 1917, Lowell Observatory Bulletin, 3, 59

Slish, V. I. 1963, Nature, 199, 682

Slysh, V. I. 1966, Soviet Physics Uspekhi, 8, 852

Smirnov, O. M. 2011, A&A, 527, A106

Smith, F. G. 1951, Nature, 168, 555

Smith, R. J., Lucey, J. R., Hudson, M. J., Schlegel, D. J., & Davies, R. L. 2000, MNRAS, 313, 469

Sob'yanin, D. N. 2017, MNRAS, 471, 4121

Sokolovsky, K. V., Kovalev, Y. Y., Pushkarev, A. B., & Lobanov, A. P. 2011, A&A, 532, A38

Sparks, W. B., Biretta, J. A., & Macchetto, F. 1996, ApJ, 473, 254

Sparks, W. B., Fraix-Burnet, D., Macchetto, F., & Owen, F. N. 1992, Nature, 355, 804

Stawarz, Ł., Aharonian, F., Kataoka, J., et al. 2006, MNRAS, 370, 981

Stiavelli, M., Biretta, J., Møller, P., & Zeilinger, W. W. 1992, Nature, 355, 802

Strittmatter, P. A., Hill, P., Pauliny-Toth, I. I. K., Steppe, H., & Witzel, A. 1980, A&A, 88, L12

Sulentic, J. W., Arp, H., & Lorre, J. 1979, ApJ, 233, 44

Taylor, G. B. & Zavala, R. 2010, ApJ, 722, L183

Tchekhovskoy, A. & Bromberg, O. 2016, MNRAS, 461, L46

Tchekhovskoy, A., Narayan, R., & McKinney, J. C. 2011, MNRAS, 418, L79

Thompson, A. R., Moran, J. M., & Swenson, George W., J. 2017, Interferometry and Synthesis in Radio Astronomy, 3rd Edition (Springer)

Tolman, R. C. 1939, Physical Review, 55, 364

Urry, C. M. & Padovani, P. 1995, PASP, 107, 803

van der Laan, H. & Perola, G. C. 1969, A&A, 3, 468

van Haarlem, M. P., Wise, M. W., Gunst, A. W., et al. 2013, A&A, 556, A2

Van Rossum, G. & Drake, F. L. 2009, Python 3 Reference Manual (Scotts Valley, CA: CreateSpace)

Vega-García, L., Perucho, M., & Lobanov, A. P. 2019, A&A, 627, A79

Vermeulen, R. C. & Cohen, M. H. 1994, ApJ, 430, 467

Virtanen, P., Gommers, R., Oliphant, T. E., et al. 2020, Nature Methods, 17, 261

Vlahakis, N. & Königl, A. 2003a, ApJ, 596, 1080

Vlahakis, N. & Königl, A. 2003b, ApJ, 596, 1104

Vlahakis, N. & Königl, A. 2004, ApJ, 605, 656

Wakker, B. P. & Schwarz, U. J. 1988, A&A, 200, 312

Walker, R. C., Dhawan, V., Romney, J. D., Kellermann, K. I., & Vermeulen, R. C. 2000, ApJ, 530, 233

Walker, R. C., Hardee, P. E., Davies, F. B., Ly, C., & Junor, W. 2018, ApJ, 855, 128

Wiener, H. 1949, Extrapolation, interpolation, and smoothing of stationary time series, with engineering applications (MIT Press)

Wu, X.-B., Wang, F., Fan, X., et al. 2015, Nature, 518, 512

Young, T. 1802, Philosophical Transactions of the Royal Society of London, 92, 12

Yuan, F., Wang, H., & Yang, H. 2022, ApJ, 924, 124

Zavala, R. T. & Taylor, G. B. 2002, ApJ, 566, L9

Zel'dovich, Y. B. 1964, Soviet Physics Doklady, 9, 195

Zel'dovich, Y. B. & Novikov, I. D. 1967, Soviet Ast., 10, 602

Zeldovich, Y. B. & Novikov, I. D. 1971, Relativistic astrophysics. Vol.1: Stars and relativity (University of Chicago Press)

I am grateful to my official supervisor Prof. Dr. J. Anton Zensus, and my day-to-day supervisor Dr. Andrei Lobanov, for the opportunity and honor of being employed at the Max Planck Institute for Radio Astronomy and for being their student. I would like to thank Prof. Dr. Andreas Eckart, as well, for having followed my progress over the years. I also thank my Thesis Advisory Committee, Prof. Dr. Ros Eduardo Ibarra and Dr. Nicholas Roy MacDonald. My appreciation extends to Prof. Dr. Bülent Tezkan for chairing the examination committee and to Dr. Ana Brás Würschig for contributing as an assessor of the examination committee.

I acknowledge, with gratitude, the financial support received for this research from the International Max Planck Research School (IMPRS) for Astronomy and Astrophysics at the Universities of Bonn and Cologne. Special thanks go to Dr. Gunther Witzel, Dr. habil. Rainer Mauersberger, and Arne Hoyer for their outstanding organizational efforts in IMPRS and for supporting all PhD students.

I am grateful to my friends and colleagues A. Tursunov, P. Benke, S. D. von Fellenberg, H. Müller, J. Kramer, G. F. Paraschos, J. Röder, J. Kim and my aunt J. I. Nikonova for careful reading and important comments on the dissertation.

I thank all my collaborators P. Arras, E. Bazanova, T. A. Ensslin, V. Frolova, M. Giroletti, L. I. Gurvits, J. A. Hodgson, D. C. Homan, M. Janssen, S. Jorstad, D. Kim, J. Kim, J.-Y. Kim, K. I. Kellermann, J. Knollmueller, Y. Y. Kovalev, E. V. Kravchenko, M. L. Lister, M. M. Lisakov, J. Livingston, A. P. Lobanov, R.-S. Lu, E. E. Nokhrina, I. N. Pashchenko, A. B. Pushkarev, J. Röder, J. Roth, T. Savolainen, P. A. Voitsik, M. Wielgus, and G.-Y. Zhao for useful discussions and collaborative work.

This work is part of the M2FINDERS project, which has received funding from the European Research Council (ERC) under the European Union's Horizon 2020 Research and Innovation Programme (grant agreement No 101018682).

The National Radio Astronomy Observatory is a facility of the National Science Foundation operated under cooperative agreement by Associated Universities, Inc.

This work is partly based on the observations with the 100-m telescope of the MPIfR (Max-Planck-Institut für Radioastronomie) at Effelsberg. This research has made use of the data from the University of Michigan Radio Astronomy Observatory which has been supported by the University of Michigan and by a series of grants from the National Science Foundation, most recently AST-0607523.

The RadioAstron project was led by the Astro Space Center of the Lebedev Physical Institute of the Russian Academy of Sciences and the Lavochkin Scientific and Production Association under a contract with the Russian Federal Space Agency, in collaboration with partner organizations in Russia and other countries. The National Radio Astronomy Observatory is a facility of the National Science

Foundation operated under cooperative agreement by Associated Universities, Inc. The European VLBI Network is a joint facility of independent European, African, Asian, and North American radio astronomy institutes. This research is based on observations correlated at the Bonn Correlator, jointly operated by the Max Planck Institute for Radio Astronomy (MPIfR), and the Federal Agency for Cartography and Geodesy (BKG). The Australia Telescope Compact Array and Mopra telescope are part of the Australia Telescope National Facility (https://ror.org/05qajvd42), which is funded by the Australian Government for operation as a National Facility managed by CSIRO.

Facilities: VLBA - Very Long Baseline Array, EVN - European VLBI Network, VLA - Very Large Array, GBT - Green Bank Telescope, Effelsberg Telescope, SRT (RadioAstron Space Radio Telescope (Spektr-R)).

Software: AIPS (Greisen 2003a), DIFMAP (Shepherd et al. 1994), eht-imaging (Chael et al. 2018, 2016), resolve (Junklewitz et al. 2016), rPicard (Janssen et al. 2019), Astropy (Astropy Collaboration et al. 2022, 2018, 2013), Matplotlib (Hunter 2007), Numpy (Harris et al. 2020), Python (Van Rossum & Drake 2009), Scipy (Virtanen et al. 2020), Grammarly, Overleaf.

First of all, I would like to sincerely thank my academic advisors and mentors: Andrei Lobanov and Yuri Kovalev. I am extremely proud to be a student of true giants of modern radio astronomy and astrophysics. This dissertation is the result of work carried out on their shoulders. In addition to academic support, Andrei and Yuri have been like fathers to me over the years, sharing not only their knowledge but also their life experience. I am infinitely grateful to them for their care and the warm relationship we share. They taught me to be critical, attentive to details without losing sight of the bigger picture, and not to worry too much about everyday difficulties. The only thing I would like to apologise for is my occasional reticence, which was due to my shyness and the importance I placed on their opinions of me.

I would like to extend special gratitude to the director, Anton Zensus. Despite his busy schedule, he always found time for important conversations with students. I deeply admire his genuine care for each member of the group and his sincere interest in their careers. It was especially heartwarming when Anton brought all the students together for heartfelt discussions, sharing his experience and advice.

Special thanks go to my academic "brothers" and "sisters" — Aleksandr Plavin, Mikhail Lisakov, Evgeniya Kravchenko, Aleksandr Popkov, Tatyana Koryukova, Darya Zobnina, Jongseo Kim, Hendrik Müller, Saurabh — for their mentorship, heart-to-heart conversations, and help in debugging code. A special thanks to Zhenya's daughter, Vasilisa, who, during difficult moments, brightened my day with her cuteness, smile, and carefree nature.

I am grateful to my colleagues from the Max Planck Institute for Radio Astronomy: Silke Britzen, Sergio A. Dzib-Quijano, Thomas P. Krichbaum, Anne-Kathrin Baczko, Florian Eppel, Florian Rösch, Jonas Heßdörfer, Luca Ricci, Galina Lipunova, Rainer Mauersberger, Eduardo Ros, Gunther Witzel, Guang-Yao Zhao, DaeWon Kim, Jack Livingston, Jan Röder, Sebastiano D. von Fellenberg, Lena S. Debbrecht, Prathamesh Ingale, Biagina Boccardi, Vieri Bartolini, Asmita Gupta, Helge Rottmann, Alan L. Roy, Arezu Witzel-Dehghanfar, Richard W. Porcas, Eftychia Madika, Georgios F. Paraschos, Cecilia Degli Agosti, Hui-Hshuan Chung, Joana Kramer, Brissa Gomez, Vanessa Pinto, Eva Martinez, Michael Janßen. I am very glad to have met such outstanding people. The time spent with you, the observations at the Effelsberg radio telescope, and, of course, our shared lunches were an unforgettable pleasure.

I would also like to thank the administrative team of the Max Planck Institute for Radio Astronomy: Siân Adey, Tuyet-Le Tran, Barbara Menten, and Silvia Mertens. Without you, the bureaucratic processes would have become a real headache.

Among my colleagues from the CIS countries, I would like to thank Aspan,

Amaliya and Arman Tursunov, Vladislav Makeev, Andrey Kazantsev, Aleksandr Batrakov, and Konstantin Grishunin. Our meetings and board games helped me relax and take my mind off problems. I knew I could turn to each of you for support. Special thanks to Amaliya and Arman, who took care of me during my illness and spoiled me with delicious food.

I would also like to thank my colleagues Maria Cywinska and Petra Benke, as well as their families, who hosted me in Poland and Hungary. Thanks to Csaba Benke, Júlia Benkéné Velkei, Réka Benke, Peter Gyarfas, Bogdan Cywinski, Ewa Cywinska, Paweł Cywinski for their warm, homely, and family hospitality. Spending a long time abroad, it was especially important for me to feel at home.

I would also like to extend my special thanks to my school mentors who prepared me for olympiads and guided me toward astronomy: Aitalina Protodyakonova, Mikhail Usov, Timofey Solovyov, Mikhail Gavrilov, Oleg Ugolnikov, Evgeny Fadeyev, and Boris Eskin. Additionally, I am grateful to my school teachers: Elena Kryuchkova, Alena Naumova, Marina Morozyuk, Galina Shimanova, Tatyana Barinova, Elena Makarova, Elena Bubyakina, Sajida Mukhametova, Tuyaara Zhirkova, Izolda Kirillina, Lyutsia Anisimova, Natalia Indeeva, Innokenty Koltovsky, Maria Koryakina, Alena Zamyatina, Ivan Sidorov, and Lyudmila Povedskaya.

Special gratitude goes to Dr. Jeroen Vleggaar[1], who inspired me with his sense of humor and simplicity in explaining complex concepts necessary for understanding interference and optics.

I would like to conclude with thanks to my family, my beloved parents — Alena Nikolaevna and Sergey Ivanovich Nikonov. Dear Mom and Dad, I am infinitely grateful for everything you have done for me. Your love, wisdom, and understanding gave me invaluable freedom, which not everyone has. I understand how difficult it must have been to let me go to study first in Moscow, and then in Germany. Not every parent could have done that. But I think the result was worth it. Special thanks to my younger sister, Irina Sergeevna Nikonova, for her support and care. You are always there and helping all of us, and I am proud of you as I watch you become an independent adult.

I would also like to thank my grandparents — Tamara, Kappa, Ivan, and Nikolay. It is a pity that you did not live to see my defense, but I am sure you would have rejoiced with me. Now I often think back to the time spent with you and realize how much I underappreciated it before.

I am grateful to all my relatives, especially Julia Nikonova, Pavel Nikonov, Aleksandra Nikonova, Lyudmila Ivanova, Lidia Pavlova, Valeriy Pavlov, Zhanna Ivanova, Nyurguyana Pavlova, Nikolay Pavlov, Vladimir Ivanov, Svetlana Ivanova,

[1] `https://www.huygensoptics.com/`

Vasiliy Ivanov, and Viktor Ivanov. My entire childhood and personal development happened alongside you.

I would especially like to thank my best childhood friend and distant relative, Aleksandr Fedorov. From our early school days to the present, we have gone through so much together and have supported each other. This dissertation is partly your achievement as well because you were the one who always asked important and difficult questions about space and physics. You were the driving force behind our childhood fantasies about space travel and story creation. Thanks to you, we had days dedicated to "Star Wars," where we got lost in that galaxy far, far away together. I would also like to thank your family, which I consider my own. Thanks to Aunt Zina, Uncle Volodya, Marina, Semyon, Maksim, Nastya, Kristian, Sonya, and Natasha for their warm relationship. Special thanks to Asya and Ira — the little ones who warmed my heart despite the distance of half a world between us.

In conclusion, I would like to express my gratitude to my former wife, Nadezhda, for whom my love has not faded over time. Dear Nadezhda, I want to thank you, first and foremost, for being the reason I ended up in the Max Planck Institute's PhD program. It was entirely your idea, and before we met, I could never have imagined that such a path was even possible for me. You taught me to believe in myself. Moreover, I am grateful to you for the invaluable experience of family life and the important life lessons I have learned. We went through a lot together, and that journey helped me understand myself better, become stronger, and gain more confidence. I sincerely cherish all the joyful moments we shared and remember them with warmth. I would also like to extend my gratitude to Nadezhda Sergeevna, Nadezhda Nikolaevna, Zhenya, Olya, Dasha, and Arisha for their kindness, support, and care.

Прежде всего, я хотел бы искренне поблагодарить моих научных руководителей и наставников: Андрея Петровича Лобанова и Юрия Юрьевича Ковалева. Я очень горд быть студентом настоящих гигантов современной радиоастрономии и астрофизики. Эта диссертация — результат работы, выполненной на их плечах. Помимо научной поддержки, Андрей и Юрий все эти годы были для меня как отцы, делясь не только знаниями, но и жизненным опытом. Я бесконечно благодарен им за заботу и теплые отношения. Они научили меня быть критичным, внимательным к деталям, не забывая при этом о глобальной картине, и не слишком беспокоиться о повседневных трудностях. Единственное, за что хотел бы извиниться, — за мою порой немногословность, вызванную застенчивостью и важностью их мнения для меня.

Особую благодарность хочу выразить директору Антону Ценсусу. Несмотря на плотный график, он всегда находил время для важных разговоров со

студентами. Мне очень импонирует его неравнодушие к каждому члену группы и искренний интерес к их карьерам. Было особенно приятно, когда Антон собирал всех студентов для душевных бесед, делясь своим опытом и советами.

Отдельное спасибо научным «братьям» и «сестрам» — Александру Плавину, Михаилу Лисакову, Евгении Кравченко, Александру Попкову, Татьяне Корюковой, Дарье Зобниной, Дьонсо Киму, Хендрику Мюллеру, Саурабу — за менторство, задушевные разговоры и помощь в поиске ошибок в коде. Особая благодарность дочке Жени — Василисе, которая в трудные моменты выручала меня своей милотой, улыбкой и беззаботностью.

Спасибо коллегам из Института радиоастрономии Макса Планка: Сильке Бритцен, Серхио А. Дзиб-Кихано, Томасу П. Крихбауму, Анне-Катрин Бацко, Флориану Эппелю, Флориану Решу, Йонасу Хессдорферу, Луке Риччи, Галине Липуновой, Райнеру Маурсбергеру, Эдуардо Росу, Гюнтеру Витцелю, Гуан-Яо Чжао, ДэВону Киму, Джеку Ливингстону, Яну Рёдеру, Себастьяно Д. фон Фелленбергу, Лене С. Деббрехт, Пратхамешу Ингале, Биаджине Боккарди, Вьери Бартолини, Асмите Гупте, Хельге Роттману, Алану Л. Рою, Арезу Витцель-Дехганфар, Ричарду В. Поркасу, Эфтии Мадике, Георгиосу Ф. Парасхосу, Чечилии Дегли Агости, Хуэй-Шуань Чунгу, Йоане Крамер, Бриссе Гомес, Ванессе Пинто, Еве Мартинес, Михаэлю Янссену. Я очень рад был познакомиться с такими выдающимися людьми. Время, проведенное с вами, наблюдения на радиотелескопе Эффельсберг и, конечно, совместные обеды — это незабываемое удовольствие.

Хотел бы выразить благодарность административной команде Института радиоастрономии Макса Планка: Шиан Эдди, Туйет-Ле Чан, Барбаре Ментен и Сильвии Мертенс. Без вас бюрократические вопросы стали бы настоящей головной болью.

Среди коллег из стран СНГ хотелось бы поблагодарить Аспана, Амалию и Армана Турсуновых, Владислава Макеева, Андрея Казанцева, Александра Батракова и Константина Гришунина. Наши встречи, игры в настольные игры помогали мне расслабиться и отвлечься от проблем. Я знал, что могу обратиться к каждому из вас за поддержкой. Особая благодарность Амалии и Арману, которые заботились обо мне во время болезни и баловали вкуснейшей едой.

Также хочу поблагодарить коллег Марию Цивинскую и Петру Бенке, а также их семьи, которые приглашали меня в гости в Польшу и Венгрию. Спасибо Чабе Бенке, Юлии Бенкене Велкеи, Реке Бенке, Петера Дьёрфашу, Богдану Цивинскому, Еве Цивинской, Павлу Цивинскому за тёплый, домашний и семейный приём. Находясь долгое время за границей, для меня было

особенно важно почувствовать себя как дома.

Отдельно хочу поблагодарить моих школьных наставников, которые готовили меня к олимпиадам, благодаря которым я пришёл в астрономию: Айталину Протодьяконову, Михаила Усова и Тимофея Соловьёва, Михаила Гаврилова, Олега Угольникова, Евгения Фадеева и Бориса Эскина. Моих школьных учителей: Елену Крючкову, Алену Наумову, Марину Морозюк, Галину Шиманову, Татьяну Баринову, Елену Макарову, Елену Бубякину, Сажиду Мухаметову, Туйаару Жиркову, Изольду Кириллину, Люцию Анисимову, Наталию Индееву, Иннокентия Колтовского, Марии Корякиной, Алену Замятину, Ивана Сидорова, Людмилу Поведскую.

Особую благодарность выражаю доктору Йероену Влеггару[2], который вдохновлял своим чувством юмора и простотой объяснений сложных вещей, необходимых для понимания интерференции и оптики.

Я хотел бы завершить благодарностями моей семье, любимым родителям — Алёне Николаевне и Сергею Ивановичу Никоновым. Дорогие мама и папа, я бесконечно благодарен за всё, что вы для меня сделали. Ваши любовь, мудрость и понимание подарили мне бесценную свободу, которую имеют далеко не все. Я понимаю, как тяжело было отпустить меня учиться сначала в Москву, а затем в Германию. Не каждый родитель смог бы на это решиться. Но, думаю, результат стоил того. Отдельная благодарность моей младшей сестре Ирине Сергеевне Никоновой за её поддержку и заботу. Ты всегда рядом и помогаешь нам всем, и я горжусь тобой, наблюдая, как ты становишься самостоятельным взрослым человеком.

Также хочу поблагодарить моих бабушек и дедушек — Тамару, Капитолину, Ивана и Николая. Жаль, что вы не дожили до момента моей защиты, но я уверен, что вы бы радовались вместе со мной. Сейчас я всё чаще вспоминаю время, проведённое с вами, и понимаю, как недооценивал это раньше.

Я благодарен всем родственникам, особенно Юлии Никоновой, Павлу Никонову, Александре Никоновой, Людмиле Ивановой, Лидии Павловой, Валерию Павлову, Жанне Ивановой, Нюргуяне Павловой, Николаю Павлову, Владимиру Иванову, Светлане Ивановой, Василию Иванову и Виктору Иванову. Всё моё детство и формирование как личности прошло рядом с вами.

Особенно хочу поблагодарить моего лучшего друга детства и по совместительству дальнего родственника Александра Фёдорова. С самого школьного времени и до сегодняшнего дня мы прошли через многое и поддерживали друг друга. Эта диссертация отчасти твоя заслуга, ведь именно ты задавал мне важные и сложные вопросы о космосе и физике, именно ты был двигателем наших фантазий о космических путешествиях и создании рассказов. Благодаря тебе

[2] `https://www.huygensoptics.com/`

у нас были дни, посвящённые «Звёздным войнам», где мы вместе увлекались той далёкой-далёкой галактикой. Я благодарю также и твою семью, которую считаю своей. Спасибо тёте Зине, дяде Володе, Марине, Семёну, Максиму, Насте, Кристиану, Соне и Наташе за тёплые отношения. Особое спасибо Асе и Ире — маленьким человечкам, которые согревали моё сердце, несмотря на расстояние в полмира между нами.

В заключение, я хотел бы поблагодарить мою бывшую жену Надежду, к которой моя любовь не ослабла со временем. Дорогая Надежда, хочу поблагодарить тебя, прежде всего, за то, что именно благодаря тебе я оказался в аспирантуре Института Макса Планка. Это была полностью твоя идея, и до нашей встречи я даже не мог представить, что такой путь для меня возможен. Ты научила меня верить в себя. Кроме того, я благодарен тебе за бесценный опыт семейной жизни и важные жизненные уроки. Вместе мы прошли через многое, и этот путь помог мне лучше понять себя, стать сильнее и увереннее. Я искренне ценю все радостные моменты, которые мы разделили, и вспоминаю их с теплотой. Также хочу сказать спасибо Надежде Сергеевне, Надежде Николаевне, Жене, Оле, Даше и Арише за вашу доброту, поддержку и заботу.